Thèse de Doctorat

Pour obtenir le titre de

Docteur

En Science des Matériaux

Présentée à

L'Université de Lille

École Doctorale Sciences de la Matière, du Rayonnement et de l'Environnement (EDSMRE)

Par

Isadora Maria OLIVEIRA ANICIO COSTA

Ingénieur Métallurgiste diplômée de l'Universidade Federal de Minas Gerais (UFMG), Brésil

Relations entre la microstructure, les propriétés mécaniques et électromagnétiques de fils d'acier au carbone traités thermomécaniquement

Thèse soutenue publiquement le 27 Novembre 2020 devant le jury composé de :

Marie-Laurence GIORGI	Professeur, CentraleSupélec, France	Président
Eric HUG	Professeur, Normandie Université, France	Rapporteur
Roumen PETROV	Professeur, Ghent University, Belgique	Rapporteur
Abdelkader BENABOU	Maître de conférences, Université de Lille, France	Examinateur
Jean-Bernard VOGT	Professeur, Centrale Lille, France	Directeur
Jérémie BOUQUEREL	Maître de conférences, Centrale Lille, France	Co-encadrant
Christophe MESPLONT	Dr. R&D Expert, Bekaert, Belgique	Invité

Unité Matériaux Et Transformations
Univ. Lille, CNRS, INRA, Centrale Lille, UMR 8207

NV Bekaert SA
Bekaertstraat 2, 8550 Zwevegem, Belgique

Ph.D. Thesis

To obtain the title of

Doctor of Philosophy

In Materials Sciences

At

Université de Lille

École Doctorale Sciences de la Matière, du Rayonnement et de l'Environnement (EDSMRE)

By

Isadora Maria OLIVEIRA ANICIO COSTA

Metallurgical Engineer of the Universidade Federal de Minas Gerais (UFMG), Brazil

Relations between microstructure, mechanical and electromagnetic properties of carbon steel wires after thermomechanical treatments

Thesis publicly defended on November 27, 2020 in front of the jury composed of:

Marie-Laurence GIORGI	Full Professor, CentraleSupélec, France	President
Eric HUG	Full Professor, Normandy University, France	Reviewer
Roumen PETROV	Full Professor, Ghent University, Belgium	Reviewer
Abdelkader BENABOU	Associate Professor, Lille University, France	Examiner
Jean-Bernard VOGT	Full Professor, Centrale Lille, France	Supervisor
Jérémie BOUQUEREL	Assistant Professor, Centrale Lille, France	Co-supervisor
Christophe MESPLONT	Dr. R&D Expert, Bekaert, Belgium	Industrial partner

Unité Matériaux Et Transformations
Univ. Lille, CNRS, INRA, Centrale Lille, UMR 8207

NV Bekaert SA
Bekaertstraat 2, 8550 Zwevegem, Belgium

Aos meus pais, Rachel e Aloísio,
todo o meu amor e a minha eterna gratidão.

ACKNOWLEDGMENTS

This Ph.D. research is the result of ten years of an invaluable formation in Metallurgical and Materials Science that will not be without consequences for the steps I will take from now on. During this period, one of the most beautiful things I have learned is that a doctoral thesis or any other work is, in a certain way, the extension of the author's life. For something of value to be produced, we must create something of value in ourselves. No ideal is easily and effortlessly accomplished. I have deeply invested myself in this project, but fortunately, I did not get here alone. For this reason, I would like to thank all those who contributed in different ways and at different levels throughout the development of the works which has culminated in the conclusion of this doctorate. Even though I know that there are no words that can express how grateful I am, I venture to say some, those that the memory brought to my mind at the time of writing.

My acknowledgments could not begin any other way than by expressing my deepest gratitude to the person who saw a light in me seven years ago when I was still an engineering student, and has completely changed my life since then, to my research supervisor, Dr. Jean-Bernard Vogt, Professor at Centrale Lille Institut. I am extremely grateful for the opportunity he has offered me to do research, for the competent, timely and intelligent criticisms that contributed to the improvement of the theoretical content, and for the invaluable guidance throughout this thesis work. His passion for teaching, dynamism, enormous engagement and intellectual incentive have always inspired me. It was a great privilege and honor to work under his direction within his team. He always wanted to make sure that all the conditions were right for the thesis to go well, for my stay in France to go well. I have learned a lot about materials science but also about listening and understanding, about empathy and trust, and of course, about beer! After all these years, Prof. Dr. Jean-Bernard Vogt, or simply JB as everyone says, have become a dear friend to me. I hope to continue learning with him.

I wish to show my gratitude to the company NV Bekaert SA and the Flemish governmental organization, the Agency for Innovation and Entrepreneurship (VLAIO), for the financial support to this industrial research. I would like to pay my special regards to my industrial supervisor, Dr. Christophe Mesplont, R&D Expert

Heat Treatment, for his trust and guidance. Also, thanks to Dr. Pascal Antoine, Senior R&D Expert Physical Metallurgy, and Veerle Van Wassenhove, Senior Technology Manager, for offering me the opportunity to work at Bekaert. What a challenge it was to complete a project in partnership with the metallurgical industry, building scientific knowledge and contributing to the development of more effective and sustainable practices.

I am immensely grateful to have had the opportunity to work with incredible professionals who welcomed me with great affection in Belgium. I would like to recognize the invaluable assistance that they have provided during my study. I wish to thank the teams from Bekaert Technology Center (BTC), notably the Wire Technologies group, and all the people whose assistance was a milestone in the completion of this project. I would particularly like to thank Renaat Vandemeulebroecke, Jan Holvoet, Franky Beyens, Nico Clement, Filiep Vanhee, Eddy Meersschaert, Rik Bossuyt, and Jan Lust for their support with thermal treatments tests performed in the pilot plants; Christophe Degraer, Peter Saelens, and Joris Verbrugge for their help with cold-drawing tests; Filip Nevejans for machining the fatigue specimens; Elisabete Pinto da Silva, Sabine Storme, Hans Vandeputte, Bas Werbrouck, Davey Henderickx, Nathalie Calis, and Dick Lambrecht for their expertise on many techniques related to material characterization; Tony Defoor and Christophe Noppe for the tensile and torsion tests; Bart Vanlandeghem, Hans Vandenbussche, Johan De Pontieu, and Liang Ma for their assistance with sensor applications. Appreciation is also extended to the Bekaert Qingdao Wire Products (BQWP) for their collaboration with experimental tests performed in China. I am grateful to people from WH4 for providing a very positive work atmosphere. A big thanks to André Lins, Sven Van Royen, and Steven Vanhaesebrouck for the welcome they gave me from the start and permanent encouragement. I am very proud of have been part of the #bettertogether team!

I take this opportunity to thank my colleagues from the Unité Matériaux et Transformations (UMET) that welcomed me to their laboratory, in particular to the Métallurgie Physique et Génie des Matériaux group (MPGM) for all the technical support and cooperation. This laboratory is a multicultural place, where people work who are both very competent and very accessible. To my co-supervisor, Dr. Jérémie Bouquerel, Assistant Professor at Centrale Lille Institut, who helped me in innumerable ways, I would like to thank him for his care and kindness. His vision,

critical thinking, and didactic skills, especially concerning microscopy analysis, were decisive for the development of this work. My gratitude to Damien Creton, not only for this technical support that greatly aided with metallographic characterization, but for his great sense of humor, his beautiful heart and constant care. I really appreciate his way of doing things and his simplicity and I will keep it with me for the future. I would extend my thanks to Jocelyn Golek for his help with the fatigue test machines and to Ahmed Addad for his expertise with transmission electron microscopy and imaging techniques. I would also like to mention Isabelle Samain, Corinne Henry, Anne-Marie Blanchenet, and Ingrid Proriol Serre. I thank the intern students Cédric Bouallag, Bárbara Alves Srica, Dóris Corsi Ribas d'Ávila, Florian Raffin, Guilherme Adinolfi Colpaert, Diana Tsvyd, Ana Beatriz Belletti Lopes Aires, and Ana Clara Amado Dolabella for the help they have given me and for the opportunities to learn jointly. I would like to thank the doctors Gabriel Franck Bouobda Moladje, Devadas Bhat Panemangalore, Romain Candela, Gulzar Seidametova, Kaotar Naji, and the almost doctors Sabrina Macaluso and Arthur Boidot for all the funny moments spent together during the past three years. To my Brazilian girls, Laís Ávila de Oliveira Silva and Mahira Adna Cota Araújo, with whom I had the chance to share the 227 office for a while, I am thankful for the scientific discussions and relentless help in daily life, for all the moments of complicity and great laughs.

The realization and conclusion of my doctorate were only possible thanks to the partnership and collaboration of a network of professionals and institutions in both France and abroad, to whom I would like to extend my deepest gratitude. I wish to express my sincere appreciation to Dr. Ivan Batko *in memorian* and Dr. Marianna Batkova from the Institute of Experimental Physics of the Slovak Academy of Sciences (IEP SAS), for performing the magnetic force microscopy analysis (MFM), without which an important part of the interpretation about the microstructural and electromagnetic interactions within carbon steels would not have existed. Their cutting-edge insightfulness and comprehensive view contributed very much to development of this thesis. I will never forget their hospitality and great affection during our visit to Košice. Many thanks to Dr. Gabriel Pristas and Dr. Slavomir Gabani from the IEP SAS, who carried out a high-quality work during resistivity measurements down to 2 K. I want to thank the collaboration of the Laboratoire d'Electrotechnique et d'Electronique de Puissance de Lille (L2EP) for making available all the devices and equipment necessary for bulk electrical and magnetic

characterization of steel wires. Thanks also to Christoph Adelmann, Kristof Moors and Diogo Costa from the Interuniversity Microelectronics Centre (IMEC) for the interesting discussions and their help with the first resistivity measurements.

To all the members of my thesis committee, my gratitude to the president of jury, Dr. Marie-Laurence Giorgi, Professor at CentraleSuperléc Paris; to the reviewers, Dr. Eric Hug, Professor at Normandy University and Dr. Roumen Petrov, Professor at University of Gent; and to the examiner, Dr. Abdelkader Benabou, Associate Professor at University of Lille, for agreeing to evaluate my thesis work and for their critical analysis, relevant comments and advices to this study. A special thanks to Dr. Abdelkader Benabou for the contributions concerning bulk electric and magnetic characterizations and the very constructive discussions, above all the help with finite-elements simulations. I also wish to thank the persons outside the jury for making my Ph.D. defense an enjoyable and memorable moment.

I could not fail to mention here the Universidade Federal de Minas Gerais and the Escola de Engenharia from which I graduated in Metallurgical Engineering. This place has provided me with unique experiences and countless opportunities until I got to where I am today. I am very proud and grateful to be a former student at UFMG. Special thanks also to all the professors of the Department of Metallurgical and Materials Engineering for their dedication and willingness to share their passion with the students. Among the persons of great importance in my journey, I would like to highlight my eternal teacher and friend, Dr. Vicente Tadeu Lopes Buono, Professor at UFMG, who taught me much more than Physical and Mechanical Metallurgy. In 2012, he offered me my first opportunity to work in research within his team, introducing me to this fascinating world of R&D. He has been by my side ever since. I would like to thank Vicente for his trust, for the long and relevant discussions and advices, for sharing knowledge, for the teachings for life.

I thank all my friends, in Brazil and elsewhere, without whom this adventure would not have been so special to me. Many thanks to the ones I have known since I was a kid, Tamara, Stefânia and Marcela, and to those who were in college with me, Hugo and Rodolfo, for sharing the good and bad moments, for not letting the distance reduce the importance we have in each other's lives. My gratitude to the lovely people I have found on my way along all these years that I have spent abroad – from Lille, Villeneuve D'Ascq, Maizières-Les-Metz, Isbergues, Grenay, Paris, Zwevegem, Croix, who with a little attention, a friendly word or a genuine smile made me feel at home.

I cherish this collection of great memories with me and all these good people that I loved having around and I will never forget. I also thank my Brazilian friends coming from the various regions of Brazil I was lucky to find in Lille at different moments, in particular to Charles, Beatriz, Victor, Marcos, Raido, Patrícia, Pedro, who have become family for me here, and have therefore contributed to this work.

To Damien, my companion, my gratitude for his love, listening, understanding, and continuing support to complete this research work. He did everything to ensure that I could do this job in the best possible way, especially at the time of writing. He cooked, he cleaned our house, he took care of our cats, and now he knows almost everything about pearlitic steels! With him I am happy and that is reflected in what I present here. I am extending my heartfelt thanks to the Descamps-Goudal family, my French family, who also did a lot to make sure that the end of my thesis went well. I am grateful to my parents-in-law, Marie-Françoise and Bernard, for making me feel so welcome into their home, sharing the daily life and so many moments of joy together. My appreciation to Juliette and Hervé, Laetitia, Emma and Marc, Heidi and Arnaud, Guillaume, Xavier, their care and affection have inspired me and made my defense even more meaningful.

I am deeply indebted to my parents, Rachel and Aloísio, for their unconditional love. The greatest strength in the world is the love parents feel. It is the strength of care, forgiveness and patience, the strength to heal everything without needing science, the strength of soul. Words will never be enough to thank them for all the effort and sacrifices they have made for educating me and made me who I am, for giving me this strength to reach for the stars and chase my dreams. Even with the distance, they have been always there to listening and advise me, they kept me going on, and this work would never have been possible if not for them. I wish to acknowledge all the support of my loved brothers, Alexandre and Guilherme, that have always believed in me, being by my side through good and bad times, and teaching me so much! I could never ever imagine my life without them in it. My most sincere thanks to my entire family, my grandparents, Geralda and João, Lourdes and José, my uncles and aunts, Maria de Lourdes, Darlene and Mauro, Socorro and Haroldo, Creusa and Eduardo, all my loved cousins, my sisters-in-law, for the wonderful memories. I love you to infinity and beyond!

Finally, I thank my God and Our Lady of Lourdes for the protection and for all the blessings granted. Deus é bom, o tempo todo.

Se Traduire	*Traduzir-se*
Une partie de moi	*Uma parte de mim*
est tout le monde :	*é todo mundo:*
l'autre partie est personne :	*outra parte é ninguém:*
fond sans fond.	*fundo sem fundo.*
Une partie de moi	*Uma parte de mim*
est multitude :	*é multidão:*
l'autre partie l'étrangeté	*outra parte estranheza*
et la solitude.	*e solidão.*
Une partie de moi	*Uma parte de mim*
pèse, pondère :	*pesa, pondera:*
l'autre partie	*outra parte*
délire.	*delira.*
Une partie de moi	*Uma parte de mim*
déjeune et dîne :	*almoça e janta:*
l'autre partie	*outra parte*
s'effraie.	*se espanta.*
Une partie de moi	*Uma parte de mim*
est permanente :	*é permanente:*
l'autre partie	*outra parte*
tout soudain se sait.	*se sabe de repente.*
Une partie de moi	*Uma parte de mim*
n'est que vertige :	*é só vertigem:*
l'autre partie,	*outra parte,*
langage.	*linguagem.*
Traduire une partie	*Traduzir uma parte*
dans l'autre partie	*na outra parte*
— qui est une question	*— que é uma questão*
de vie ou de mort —	*de vida ou morte —*
serait-il de l'art ?	*será arte?*
Ferreira Gullar	*Ferreira Gullar*

PREFACE

Thirty-six months ago, I started this Ph.D. as an exciting metallurgical project, but it turned out to be a long battle against free electrons and magnetic domain structures. How could I imagine that the subject I hated the most during my graduation in Metallurgical Engineering would become an essential piece for this Ph.D., and the worst, that I would love it? Oersted accidentally discovered electromagnetism in 1820, and since then, the world has continued spinning. This paper is the report of this passionate process. It cannot express the long days spent in the lab or the numerous nights and weekends working at home (long before Coronavirus), the hope for good results, the sadness and tiredness with each failed attempt, and the joy for an accomplished goal. It goes not even close to demonstrating all my gratitude for the excellent guidance of my dear supervisors and colleagues (UMET, Bekaert, IEP SAS Košice, L2EP, IMEC...), and the support of my family throughout this course. However, this writing does represent everything I have learned and all knowledge we built together along with this singular experience. During the route and its many winding curves, I ended up enjoying the road, and the most challenging step becomes then to put a term to it. This moment has finally arrived. In the end, thanks to you, dear reader. If you are reading this line after the others, you at least read one page of my thesis! I am very proud to share my work with you, and I hope you enjoy your reading.

Isadora Costa

TABLE OF CONTENTS

LIST OF FIGURES

LIST OF TABLES

NOMENCLATURE

Notations and units

d_i	[m]	Diameter
L_i	[m]	Length
A_i	[m^2]	Area
V_i	[m^3]	Volume
T	[K] [°C + 273]	Temperature
t	[s]	Time
π	Dimensionless	Pi number (3.141592…)
wt.	[%]	Atomic weight percent
A_1	[°C]	Critical eutectoid temperature
A_2	[°C]	Curie temperature
A_3	[°C]	Critical γ-α transformation temperature
A_4	[°C]	Critical γ-δ transformation temperature
A_{cm}	[°C]	Critical γ-Fe_3C transformation temperature
$\vec{b}$	Unitless	Burgers vector
D_C^{γ}	[$cm^2.s^{-1}$]	Average diffusion coefficient
R	[8.32 J. $mol^{-1}.K^{-1}$] [1.98 $cal.mol^{-1}.K^{-1}$]	Universal gas constant
G	[J]	Free energy
H	[J]	Enthalpy
S	[$J.K^{-1}$]	Entropy
d_g	[µm]	Grain diameter
S_P	[nm]	Interlamellar spacing
$\bar{S}$	[nm]	Mean true interlamellar spacing
F	[N]	Force
σ	[MPa]	Stress
σ_{UTS}	[MPa]	Ultimate tensile strength
ε	[%]	Strain
$\Delta\varepsilon_t$	[%]	Total strain range

$\Delta\varepsilon_e$	[%]	Elastic strain range
$\Delta\varepsilon_p$	[%]	Plastic strain range
r	Unitless	Drawing reduction
α	[°]	Die semi-angle or half-angle
ε/ ε_d	Unitless	Drawing strain
σ_d	[Pa]	Drawing stress
σ_b	[Pa]	Drawing back stress
σ_a	[Pa]	Average flow stress
P	[Pa]	Average die pressure
μP	[Pa]	Frictional shear stress
w_u	[J]	Uniform work
w_r	[J]	Redundant work
w_f	[J]	Friction work
Φ	Unitless	Redundant work factor
Δ	Unitless	Drawing die deformation zone shape
n	Unitless	Principal quantum number
ℓ	Unitless	Azimuthal quantum number
m_ℓ	Unitless	Magnetic quantum number
m_s	Unitless	Spin quantum number
e	[1.60 x 10.$^{-19}$ C]	Electron charge
m	[kg]	Electron mass
v	[m.s^{-1}]	Electron velocity
$\bar{v}$	[m.s^{-1}]	Electron average velocity
τ	[s]	Relaxation time
N	[m^{-3}]	Electron number density
μ	[m^2.(V.s)$^{-1}$]	Electron mobility
E_f	[eV]	Fermi energy
V	[V]	Voltage
emf	[V]	Electromotive force
$\mathcal{E}$	[V]	Induced electromotive force
I	[A]	Current
$\vec{J}$	[A.m^{-2}]	Current density
R	[Ω]	Resistance

ρ	[Ω·m]	Electric resistivity
ρ_0	[Ω·m]	Residual resistivity
ρ_i	[Ω·m]	Thermal resistivity
G	[S] [Ω^{-1}]	Conductance
σ	[$S.m^{-1}$]	Conductivity
m	[$A.m^2$]	Magnetic moments
M	[$A.m^{-1}$]	Magnetization
H	[$A.m^{-1}$]	Magnetic field strength
H_c	[$A.m^{-1}$]	Coercivity
Φ_B	[Wb]	Magnetic flux
B/ Φ	[T] [$Wb.m^{-2}$]	Magnetic flux density
B_s/ S	[T] [$Wb.m^{-2}$]	Magnetic saturation
B_r	[T] [$Wb.m^{-2}$]	Remanence
μ	[$H.m^{-1}$]	Magnetic permeability
μ_0	[1.26×10^{-6} $H.m^{-1}$]	Magnetic permeability in free space
μ_r	Unitless	Relative magnetic permeability
χ_m	Unitless	Magnetic susceptibility
L	[H]	Inductance
Z	[Ω]	Impedance
X_L	[Ω]	Inductive reactance
V_T	[V]	Total voltage
V_R	[V]	Resistive voltage
V_L	[V]	Inductive voltage
ϕ	[°]	Phase angle
N	Unitless	Number of turns
f	[Hz]	Frequency
δ	[mm]	Depth of penetration (skin depth)
$\bar{x}$	-	Arithmetic mean
s	-	Standard deviation
s^2	-	Variance
R^2	-	Coefficient of determination

Acronyms

AFM	Atomic force microscopy	ANOVA	Analysis of variance
AISI	American Iron and Steel Institute	BCC	Body-centered cubic
BCT	Body-centered tetragonal	BQWP	Bekaert Qingdao Wire Products
BSE	Back-scattered electron	BTC	Bekaert Technology Center
CCT	Continuous cooling transformation diagram	CF	Courant de Foucault
DF	Degree of freedom	EBSD	Electron backscatter diffraction
ECCI	Electron channelling contrast imaging	ECT	Eddy current testing
EDSMRE	École Doctorale Sciences de la Matière, du Rayonnement et de l'Environnement	FCC	Face-centered cubic
FEG	Field emitter gun	FE-SEM	Field-emission scanning electron microscope
FIB	Focused ion beam	FSM	Fatigue slip marking
HV	Vickers hardness number	IEP SAS	Institute of Experimental Physics of the Slovak Academy of Sciences
IMEC	Interuniversity Microelectronics Centre	L2EP	Laboratoire d'Electrotechnique et d'Electronique de Puissance de Lille
LOM	Light optical microscopy	MAE	Magneto-acoustic emission
MBN	Magnetic Barkhausen noise	MFM	Magnetic force microscopy
MPGM	Métallurgie Physique et Génie des Matériaux	MS	Mean square
MSA	Measurement system analysis	NDT	Non-destructive testing
PAGS	Prior austenite grain size	PSB	Persistent slip band
SI	International System	SEM	Scanning electron microscopy
SPM	Scanning probe microscopy	SS	Sum of squares
STM	Scanning tunneling microscopy	TEM	Transmission electron microscopy
TTT	Time-temperature-transformation diagram	UFMG	Universidade Federal de Minas Gerais
UMET	Unité Matériaux et Transformations	VLAIO	Agency for Innovation and Entrepreneurship

INTRODUCTION

INTRODUCTION

I. CONTEXT

The work presented in this thesis manuscript was carried out in a partnership between the UMET laboratory and the worldwide company NV Bekaert SA, whose Technology Center is located in Deerlijk, Belgium. Based on the site of the scientific campus of the University of Lille in France, UMET deals with specific themes on physical and mechanical metallurgy, and numerical methods. Bekaert's primary interests revolve around steel wire transformation and coatings technologies for multiple applications. Proposed by Bekaert, this study was financed by the company and by the Agency for Innovation and Entrepreneurship – VLAIO, a Flemish governmental organization that encourages and supports strategic and industrial research. As a part of a broader project on the advanced characterization techniques for wires, it attempts to provide solutions around applying non-destructive methods for the in-situ characterization of processed steel wires for oil and gas, construction, and advanced automotive applications. On this basis, the present research relies on the understanding of physical and mechanical properties related to the microstructure of pearlitic steels.

Pearlite is a common constituent of a large variety of high strength steel grades typically used in many structural engineering applications, including cables for suspensions bridges, steel cords for automobile tires, rails, hoses, wire ropes and springs. The Akashi-Kaikyō Bridge (Figure 1) that connects the city of Kobe and Awaji Island in Japan is the longest suspension bridge in the world, with a total length of 3911 m. With steel cables containing 300000 km of high strength wires made of pearlitic steel, the bridge was designed to withstand up to 286 km/h wind speeds and 8.5 magnitude earthquakes. Each main cable of 112 cm in diameter contains 290 parallel wire strands, comprised of 127 galvanized wires of 5.23 mm in diameter, with a tensile strength of about 1.8 GPa, used for the stiffening truss of the structure that experiences significant live and dynamic loads [1,2]. It is an appropriate example of high-performance pearlitic steel applications, whose requirements concerning toughness and formability are quite demanding.

First observed by Sorby in 1864 [3], pearlite is a lamellar composite consisting of alternated layers of α-iron ferrite and cementite. Ferrite is an interstitial solid

solution of carbon in a body-centered cubic iron and cementite, an iron carbide of Fe_3C composition, and a complex orthorhombic structure. Pearlite forms by a eutectoid reaction, as the result of the austenite decomposition. It nucleates heterogeneously on the adjacent side of the prior-austenite grain, where ferrite and cementite lamellae cooperatively grow arranged in colonies and nodules. Owing to the excellent combination of ductility, provided by the ferrite phase, and of strength, determined by the lamellar cementite structure, the remarkable mechanical behavior of pearlitic steels has since attracted considerable interest. Cold drawing is a metal forming process that refines the pearlitic microstructure, improving the wire strength while maintaining a satisfactory ductility. Advanced research still ongoing to further enhance the strength of cold-drawn pearlitic steel wires, reaching ultra-high-strength values that may attain above 7 GPa [4].

(a) **(b)**

Figure 1: (a) Top view of the world's longest suspension bridge, the Akashi-Kaikyō Bridge in Japan [5]; and (b) in detail, a steel cable section containing strands of high-tensile wires made from pearlitic steels [6]

Microstructural transformations taking place during heat treatments or under plastic deformation by drawing operation occur with considerable changes in the physical and mechanical properties of pearlitic steels. Also, undesirable phase transformations can produce deleterious microstructures (e.g., martensite or bainite), and severe plastic deformation can favor mechanisms such as cementite decomposition during the cold-work of pearlitic steels, which can strongly impact their functional properties. Hence, the adequate control of microstructural parameters developed during manufacturing processes of steels, such as grain size, phase balance, and precipitates, is critical for maintaining the consistency of mechanical properties. Microstructural changes in steels are usually characterized using conventional

methods, including light and electron microscopy, hardness measurement, and mechanical testing. However, these methods are destructive, costly, and do not allow adjustments of processing parameters or deviations on time. With the increasing quality requirements and low production costs demands, non-destructive techniques (NDT) had gained even more importance for the characterization of engineering materials.

Electromagnetic methods have been widely used for inspection defects and discontinuities [7], and in the last decades, it has become an up-and-coming tool for monitoring microstructural variations of ferromagnetic materials as steels and alloys [8,9]. Many studies have shown that electromagnetic properties of a material can provide useful information about their microstructure and mechanical properties, demonstrating the enormous potential of non-destructive testing techniques, including magnetic Barkhausen noise and eddy current testing. Nevertheless, among the numerous works on NDTs, only a few investigations proposed a broader comprehension of the electromagnetic behavior of steels and even less numerous concerning pearlitic steels. For the sake of explaining the interactions between the crystalline and micromagnetic structures of such materials, a first nano- and microscopic approaches must be considered.

In this context, the present research aims to study several microstructural aspects that can strongly influence the mechanical and physical properties of carbon steels. Among them, some parameters are particularly significant: phase balance and morphology, and applied stresses. Eddy current testing (ECT) is used to investigate the condition of materials by non-destructive means. This thesis manuscript completes this approach providing an extensive interpretation of the fundamental physical mechanisms that cause measurable variations on the electrical and magnetic properties of several carbon steel grades, and particularly of pearlitic steel wires. Besides, the two-phase nature of pearlite is a strong asset for such research. Indeed, due to a different crystallographic structure between ferrite and cementite phases, certain structure-properties interactions are very complex. An extensive study on carbon steel wires, which allow relating material characteristics to their physical behavior, would be useful for quality improvement efforts, extending the potential applications of electromagnetic non-destructive methods for the in-situ characterization of such industrial materials.

II. OBJECTIVES

Product quality and efficient manufacturing of steel wires, involving thermal processing and cold-drawing, demand continuous quality practices that are of particular interest in this research. Hence, the first objective of this manuscript is to assess the ability and the limitations of eddy current technique for the evaluation of steel wire components, giving the means to further development of adequate non-destructive control of the product quality and installations.

Moreover, the understanding of the mechanisms that explain the electrical and magnetic behavior of steels may allow a better interpretation of the electromagnetic phenomena related to eddy current testing and the material responses. The influence of microstructural parameters on the electromagnetic responses of carbon steels is, however, not yet completely understood. In this context, this work seeks broader investigate the interactions between microstructural features of steels and the electricity and magnetism phenomena, often not very well explored when it comes to the study of non-alloyed steels. Next, focusing on the pearlitic microstructure, the strain hardening to which pearlitic steel wires are subjected during their processing by cold-drawing, and how such plastically deformed microstructures may affect the electrical and magnetic properties of steel wires is an object of this investigation.

Besides the assessment of microstructure and state of stress of carbon steels after thermomechanical processing, this manuscript is also interested in assessing the functional fatigue properties of pearlitic steels. As mentioned, cold-drawn pearlitic wires can achieve high strengths required for structural applications such as spring and cables, structural components that are generally subjected to cyclic loading in-service. The influence of the microstructure on the fatigue behavior of fully pearlitic steel wires is studied, in particular, the stress-strain response and fatigue crack initiation and propagation. Finally, the capability of eddy current testing for monitoring in-service fatigue reliability of pearlitic structures is investigated.

Considering the context and the issues hitherto introduced, the purposes of this research are listed as follows:

- Determine the feasibility of using an electromagnetic sensor for the non-destructive characterization of plain carbon steel wires;

- Study of the major microstructural parameters that can impact the mechanical and physical properties of heat-treated carbon steel wires, in particular, the effect of carbon concentration and phase morphology;
- Investigate the influence of work-hardening by cold-drawing processes of pearlitic steel wires with fine and coarse lamellar microstructures on their electrical and magnetic behavior;
- Assess the potential of eddy current technique in monitoring cyclic accommodation of pearlitic steels responding to fatigue-loading conditions to which manufactured components may be subjected in-service environments.

III. THESIS OUTLINE

In order to achieve these objectives, the study program is structured into two main approaches. The first part is focused on the study of relations between microstructure, mechanical, and electromagnetic properties of carbon steel wires through experimental research, drawing the utmost from the related theoretical literature. The second part is focused on the work hardening and the microstructure evolution resulted from manufacturing process and in-service solicitations. In parallel, the eddy current technique is explored for the development of non-destructive characterization of such wires. Figure 2 illustrates the experimental program of the presented in this manuscript divided into four main chapters.

In Chapter 1, a literature study introduces the various aspects of the metallurgy of pearlitic steels, wire manufacturing, and conventional and non-destructive characterization methods. Furthermore, it establishes the basis of electromagnetism phenomena to provide the elements necessary for the understanding of this particular type of material behavior and the origin of the interactions between microstructure and electrical and magnetic properties. A study framework is defined based on the mentioned approaches. Chapter 2 describes the different carbon steel grades and heat-treatment procedures employed for producing various materials for this study, the equipment, and the implemented methodologies for the microstructural analysis and electromagnetic investigation. Then, Chapters 3 and 4 present experimental results to assess the correspondence between the microstructure parameters and the physical properties of carbon steel wires. More specifically, Chapter 3 focuses on the microstructure and their influence on the electromagnetic performance of carbon steel

wires, either on a macroscopic scale, with mechanical, resistivity, and magnetic measurements, and on a microscopic scale, through microstructure investigation and magnetic domain imaging. Chapter 4 is particularly interested in the work hardening behavior, and the microstructure evolution resulted from the manufacturing of cold-drawn pearlitic steel wires. Besides, it investigates the fatigue behavior of these materials, also encompassing the impact of cyclic mechanical loadings on their electromagnetic performance. The feasibility of eddy current testing for NDT evaluation of steel wires is discussed in each chapter.

Every chapter ends with a summary that recapitulates and brings together the key topics, concepts, results, and ideas discussed throughout this manuscript. Ultimately, the general conclusion highlights the findings, limitations, and the major implications of this research: from the scientific point of view for understanding the electromagnetic phenomenon occurring in carbon steels; and from the industrial perspective for applying an electromagnetic sensor as an NDT characterization tool for processed steel wires.

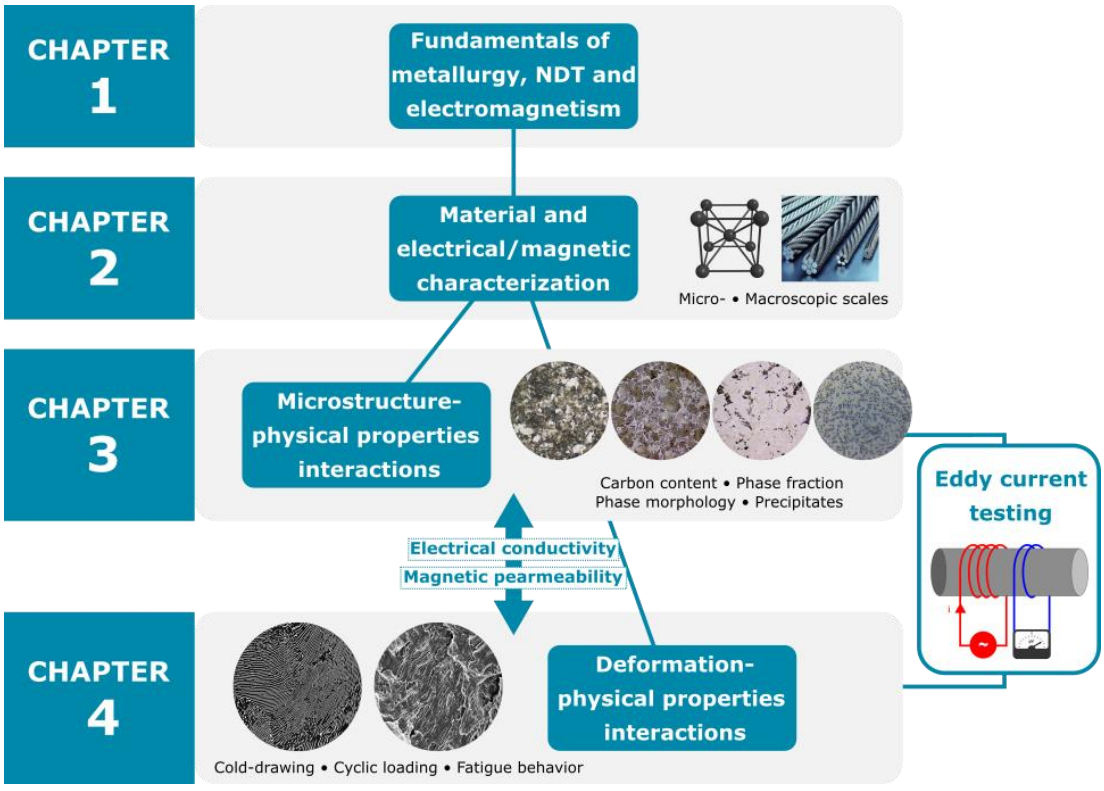

Figure 2: Schematic diagram of the experimental program of this manuscript, divided into four main chapters

CHAPTER 1

ELECTROMAGNETISM AND STEELS

CHAPTER 1

ELECTROMAGNETISM AND STEELS

This study addresses two distinct domains of knowledge of materials science: metallurgy and electromagnetism. More than merely evaluating their electromagnetic performance, this work aims to provide elements for a general understanding of the interactions between microstructure characteristics and physical properties of steels. The literature review present in this chapter purposes of laying the foundations in these fields for a complete appreciation of this study.

This chapter is, therefore, subdivided into two main parts. The first part covers the various aspects of the metallurgy of pearlitic steel wires. It begins with the notion of crystal structure and crystallographic defects in solids. Second, the definition of steel and its constituents are considered through the investigation of the iron-iron carbide and transformation-time-temperature diagrams. A particular focus is given to the mechanisms and kinetics of the formation of the pearlitic structure, its morphology, and mechanical characteristics. The wire manufacturing process is explained in-depth. Next, the state-of-the-art of non-destructive techniques developed for the evaluation of steels is reviewed, including magnetic Barkhausen noise and eddy current techniques.

In the second part, the basics of electricity and magnetism are approached in a way to introduce the necessary elements for elucidating the further understanding of the interaction mechanisms between the microstructure and electromagnetic properties of carbon steels. Also, the phenomena of electromagnetism and the principles of the eddy current method are described extensively. All the key elements considered, a precise experimental design for this research study is established at the end of the chapter.

I. METALLURGY OF PEARLITIC STEELS

Discovered by Sorby in 1864, pearlite is the product of decomposition of austenite by a eutectoid reaction and consists of ferrite and cementite phases arranged in alternating lamellae. The term pearlite refers to the appearance of its lamellar morphology when observed under an optical microscope, whose microstructure is similar to the nacre, or mother-of-pearl, a natural composite material produced by some mollusks (Figure 3). Pearlite is a common constituent of many common grades of steels used in a variety of applications that requires high strength and wear resistance, including cutting tools, high-strength wires for cables and ropes, rails, and tire cords. This section starts with a review on the iron crystal structures and lattice defects, and continues by describing the relevant metallurgical aspects of the pearlite microstructure: its components, kinetics of formation, morphology, and mechanical behavior. The wire manufacturing industrial processes and strengthening mechanisms of cold-drawn pearlitic steel wires are also described. Finally, to complete this metallurgical approach, an overview of the several techniques employed for microstructural and mechanical characterization of steels is presented.

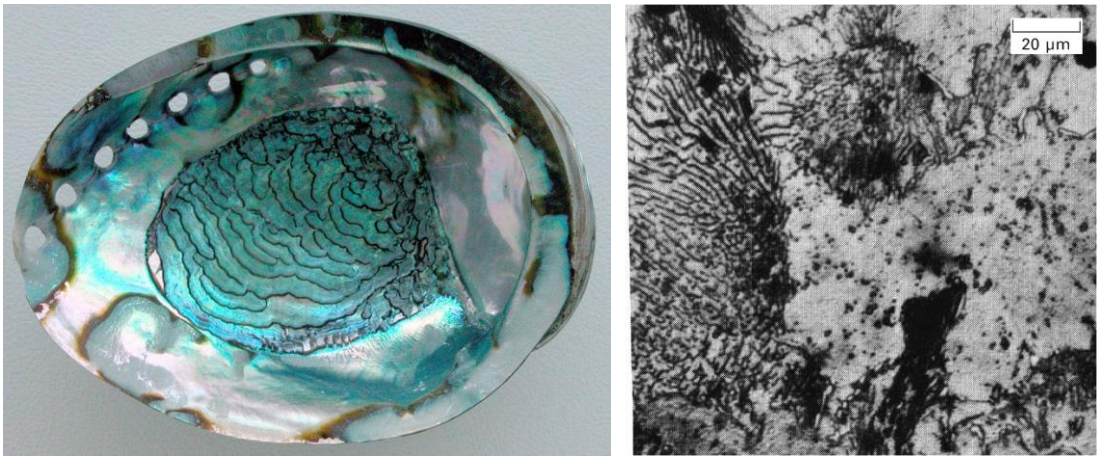

(a) **(b)**

Figure 3: (a) Iridescent effect of nacre in the inner shell of an abalone [10]; (b) pearlitic structure observed by Sorby in a heat-treated cast iron [3]

I.1. Crystal structures of iron and lattice imperfections

Solid materials can be classified into crystalline or amorphous according to the regularity and periodicity in which the atoms, ions, or molecules are spatially arranged with respect to another. All metals are crystalline materials in which the atoms distributed within their structure form periodic unit cells over large atomic distances,

configuring a three-dimensional crystalline lattice. The spatial arrangement at an atomic level is often reflected at a macroscopic level, affecting some physical properties of solids, including thermal conductivity, malleability, and ductility [11]. In order to understand the microstructural mechanisms controlling the physical and mechanical properties of steels at the atomic plane scale, it is capital to remember some notions of crystallography and crystal lattice defects.

The unit cell is thus the basic structural unit, whose geometry configuration defines the crystal structure. Seven different lattice systems are defined in terms of the lattice parameters of the crystal structure, that is, the lengths of the axes between lattice points and interaxial angles: cubic, tetragonal, orthorhombic, monoclinic, triclinic, hexagonal, and rhombohedral. Each crystal system has different lattice types, representing the possibilities of centering in the unit cell: simple, body-centered, face-centered, and base-centered. In three dimensions, there are in total 14 different unit cells, the Bravais lattices. Concerning the study of iron and its alloys, the body-centered and face-centered cubic crystal structures are of particular interest.

Pure iron is a particular element that has different allotropic forms depending mainly on the temperature. This allotropic variation is imperative in metallurgical processes, as it allows the change of specific properties of steel through heat treatments [12]. Typically, iron can have two crystal structures: α-iron or ferrite, which has a body-centered cubic lattice (BCC) from all temperatures up to 912°C; and γ-iron or austenite with a face-centered cubic lattice (FCC), stable between 912 and 1396°C. Next, the austenite transforms to a high-temperature body-centered cubic crystal structure, δ-ferrite, until melts around 1538°C. Austenite is non-magnetic. Ferrite is ferromagnetic at temperatures below 768°C, the Curie point, and above 768°C, it loses its magnetic properties. Ferrite is a soft and ductile phase at room temperature.

The BCC crystal structure has a unit cell of cubic geometry with atoms located at each corner and a single atom at the cube center. The FCC unit cell has atoms located at each corner and the centers of all the cube faces. Figure 4 shows both cubic lattice geometries. As observed, each atom of the BCC structure is shared among the eight-unit cells surrounding it, contributing one atom to the cell that, together with the one located at the cell center. Therefore, each BCC unit cell contains two lattice points. In this arrangement, each atom has eight near neighbors and a coordination number of 8. The FCC lattice, however, has an atom in the center of each face that belongs to two-unit cells, contributing with three atoms to each cell, besides the eight corner atoms

that contribute one atom to the cell. Four atoms are associated with each FCC unit cell that has a coordination number equal to 12. In an FCC structure, Fe atoms contact each other across the diagonal of each face, corresponding to <110> directions, and can be built up from the stacking of a closed-packed plane of atoms. Atoms in a BCC structure are assumed to touch along with the body diagonals of the unit cell in <111> directions. Atoms in FCC arrangements are more efficiently packed, occupying about 74% of the total volume rather than 68% in BCC unit cells.

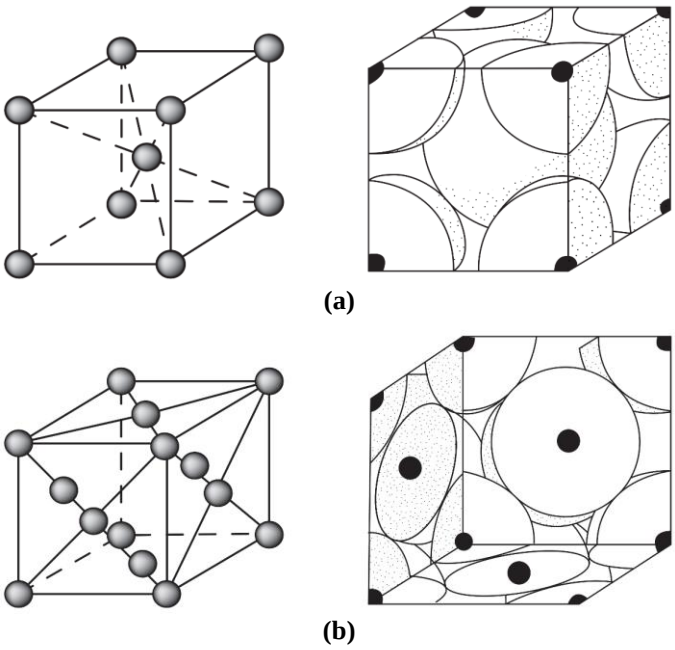

Figure 4: Schematic illustration of (a) BCC and (b) FCC unit cells [12]

The perfect crystal lattices hitherto described are an idealized system simplified to understand the constitutive behavior of crystalline solids. Real crystals contain large numbers of defects or imperfections in the regular periodic arrangement of atoms in the lattice. Many engineering properties of steels and alloys are controlled by crystallographic defects, including plasticity, corrosion resistance, and electric and thermal conductivity. According to their spatial dimension, lattice imperfections are usually classified into:

- Point defects: localized zero-dimensional irregularities that extend over only a few atoms in the lattice structure. It includes vacancies, interstitial and substitutional impurity atoms, self-interstitial atoms, Frenkel and Schottky defects. Figure 5 illustrates some types of point defects. Vacancies correspond to an atomic position in which an atom is missing. The equilibrium concentration of vacancies in a metal increases exponentially with the increase

of temperature, playing an important role in atomic diffusion processes in the solid-state. They are also introduced by plastic deformation and rapid cooling heat treatment. In a solid solution, atoms of foreign elements (impurity or solute) integrate neatly within the crystal lattice of a perfect crystalline element (solvent). Some of these impurity atoms exist as crystalline point defects as substitutional and interstitial atoms in the lattice. The presence of a small-sized atom (e.g., H, B, C, N, O) in an interstitial void occupies a position that does not belong to the structure of the crystal matrix. In iron-carbon (Fe–C) solid solutions, for instance, the size of carbon atoms is larger than the interstitial iron sites they occupy. Consequently, the surrounding lattice is compressed and distorted due to the mismatch caused by the presence of this interstitial defect. A substitutional defect is produced when an impurity atom replaces one of the bulk atoms in the lattice. These atoms may be either smaller or larger than bulk atoms, distorting the surrounding lattice, respectively, by compression or tension. Such defects are introduced to the lattice structure as impurities or by alloying addition, being relatively independent of temperature.

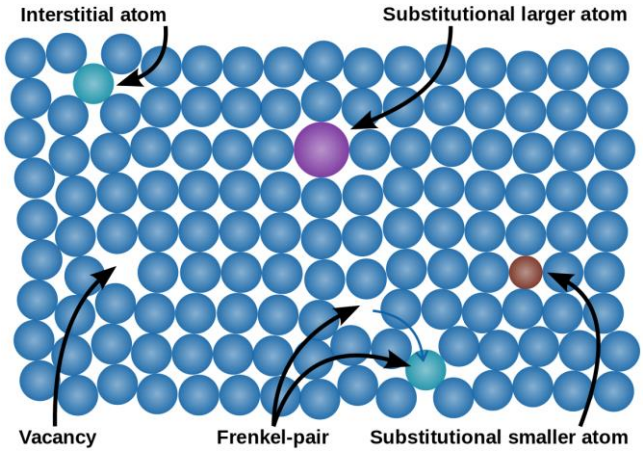

Figure 5: Types of point defects include vacancies, interstitial atoms, and substitutions impurities [13]

- Linear defects: one-dimensional defects that distort the lattice along with a row of atoms, also called dislocations. There are two types of dislocations shown in Figure 6, the edge and screw dislocations. The combination of them gives rise to mixed dislocations, which have both components. Edge dislocation is an extra half-plane of atoms that is not continued in the lattice structure, whereas the atomic planes of a screw dislocation produce a spiral or helical path around the dislocation line. The motion of both edge and screw dislocation

is a result of shear stress. However, the defect line movement of a screw dislocation is perpendicular to the stress direction and atom displacement, rather than parallel in an edge dislocation. The displacement of atoms around the dislocation, the Burgers vector $\vec{b}$ or slip vector, is associated with the magnitude and direction of the lattice distortion. The Burgers vector is perpendicular to edge dislocations and parallel to screw dislocations. Deformation occurs when a dislocation propagates across the crystal in the process of slipping one atomic plane at a time. Linear defects are mainly responsible for the plastic behavior and ductility of metals.

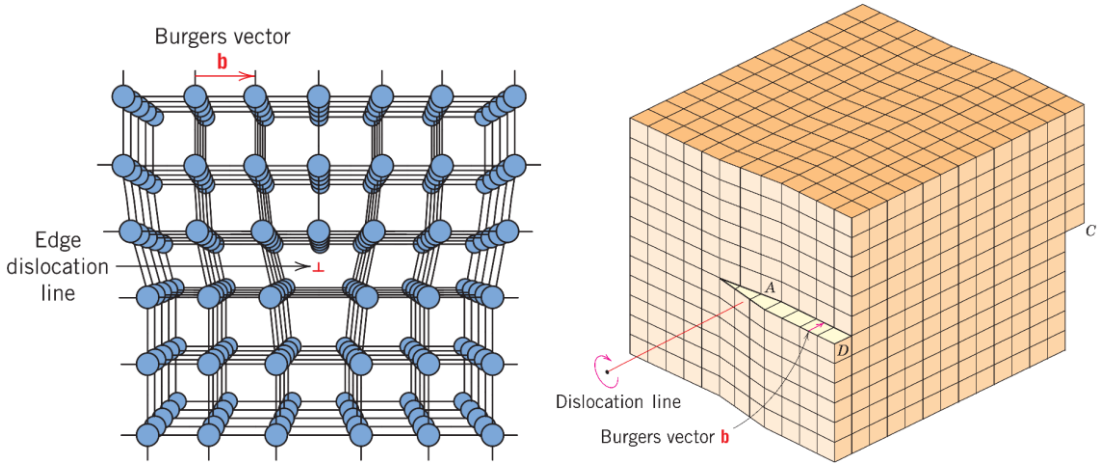

Figure 6: Three-dimension view of (a) an atomic arrangement in a plane normal to edge dislocation and (b) a screw dislocation within a crystal [11]

- Planar defects: two-dimensional defects that extend through a plane of atoms, which may be high angle and low-angle boundaries (<15°), twin grain boundaries, phase boundaries, and stacking faults. Grain boundaries delimit to regions within the crystal that presents a uniform spatial lattice orientation. Phase boundaries, however, refer to the interfaces between areas that differ in the lattice structure and chemical composition. Stacking faults are defects in the stacking sequence of crystallographic planes that interrupt the regularity of a perfect crystal lattice.
- Bulk defects: three-dimensional defects that occur on a macroscopic scale, including voids, pores, cracks, precipitates, second-phase particles, and inclusions. Many of these volumetric defects are introduced during solidification and thermomechanical processing of metals, including defects related to strain localizations and fractures.

Once the crystallographic defects are introduced, it becomes easier to understand how the unit cell geometry of α-iron and γ-iron crystal structures is significant to the formation of an interstitial solid solution of carbon in iron, and also determinant to the plastic deformation behavior of steels. The maximum solubility of carbon in austenite reaches 2.11 wt. % C at 1148°C, while in ferrite, the solubility limit is 0.02 wt. % C at 727°C. Figure 7 shows the interstitial sites in BCC and FCC lattices.

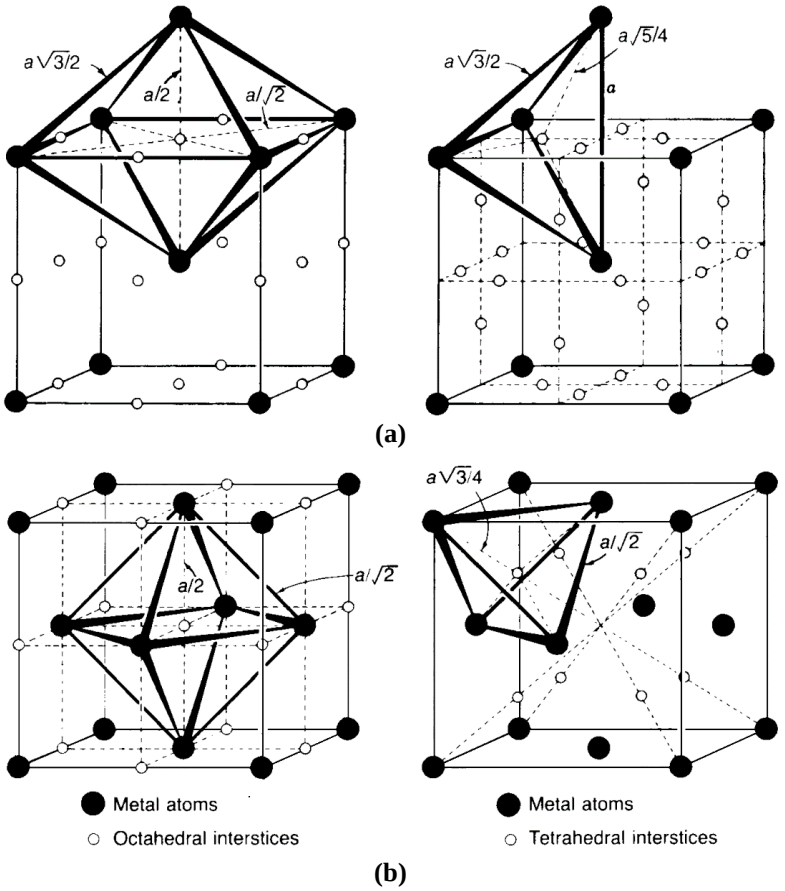

Figure 7: Octahedral and tetrahedral interstices in (a) BCC and (b) FCC lattices [14]

The higher solid solubility of carbon in austenite is due to the larger octahedral interstices (0.52 Å in radius) available in FCC crystal that allows the accommodation of carbon atoms of 0.77 Å in radius with a relatively small lattice strain, even though some lattice expansion is necessary. The γ-iron tetrahedral voids (0.28 Å in radius) cannot fit carbon atoms. In α-iron, the interstitial sites are much smaller, with tetrahedral sites that can accommodate an atom of 0.35 Å in radius and octahedral sites of only 0.19 Å in radius. Despite the smaller interstices, C atoms occupy octahedral sites, which causes a displacement of two adjacent Fe atoms rather than four iron atoms in tetrahedral sites, producing a less severe distortion of the lattice [14]. As the number of carbon is very limited in BCC, their lattice remains essentially cubic.

The introduction of carbon atoms into the interstitial voids of ferrite and austenite solid solutions modifies their lattice structures. Also, it contributes to the formation of cementite in Fe–C alloys when the solubility of carbon in both phases is exceeded up to 6.7 wt. % C. Cementite is an intermetallic iron carbide compound, a hard and generally admitted a brittle phase with a complex orthorhombic crystal structure. The orthorhombic unit cell of cementite (a≠b≠c) illustrated in Figure 8 consists of four Fe_3C formula units, with 12 atoms of iron and four of carbon. Four of the Fe atoms occupy mirror positions (4c), and the other eight atoms are at general locations (8d). Carbon atoms are located at prismatic and octahedral interstices, of which there are four centers per cell. Cementite is metallic and ferromagnetic at room temperature, becoming paramagnetic beyond the Curie temperature of 186°C. [15]

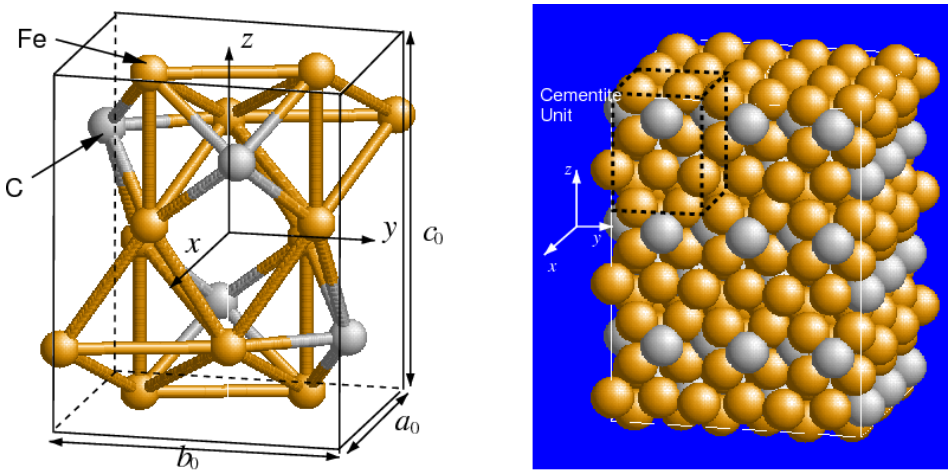

(a) **(b)**

Figure 8: Orthorhombic crystal lattice of cementite: (a) unit cell; (b) Fe_3C block [15]

I.2. Pearlite and its microstructures

I.2.1. The iron-carbon system: pearlite and its constituents

The study of the constituents and phases, microstructures, and properties of steels usually begins with the understanding of the iron-carbon phase diagram. Also called the equilibrium diagram, it defines the temperature-composition regions of stability of various phases found in Fe-C alloys under equilibrium conditions. The iron-iron carbide (Fe–Fe_3C) phase diagram shown in Figure 9 extends from pure iron to only 6.67 wt. % C, the composition of cementite. Although graphite is a more stable form of carbon than cementite, the Fe–Fe_3C phase diagram is more appropriate for studying iron and its alloys under equilibrium. Compositions are conventionally expressed in weight or mass percent (wt. %) in Fe–C phase diagrams. Iron carbon alloys containing

less than 2.11 wt. % C are arbitrarily classed as steels, while alloys containing between 2.11 and 6.67 wt. % C are designed as cast irons.

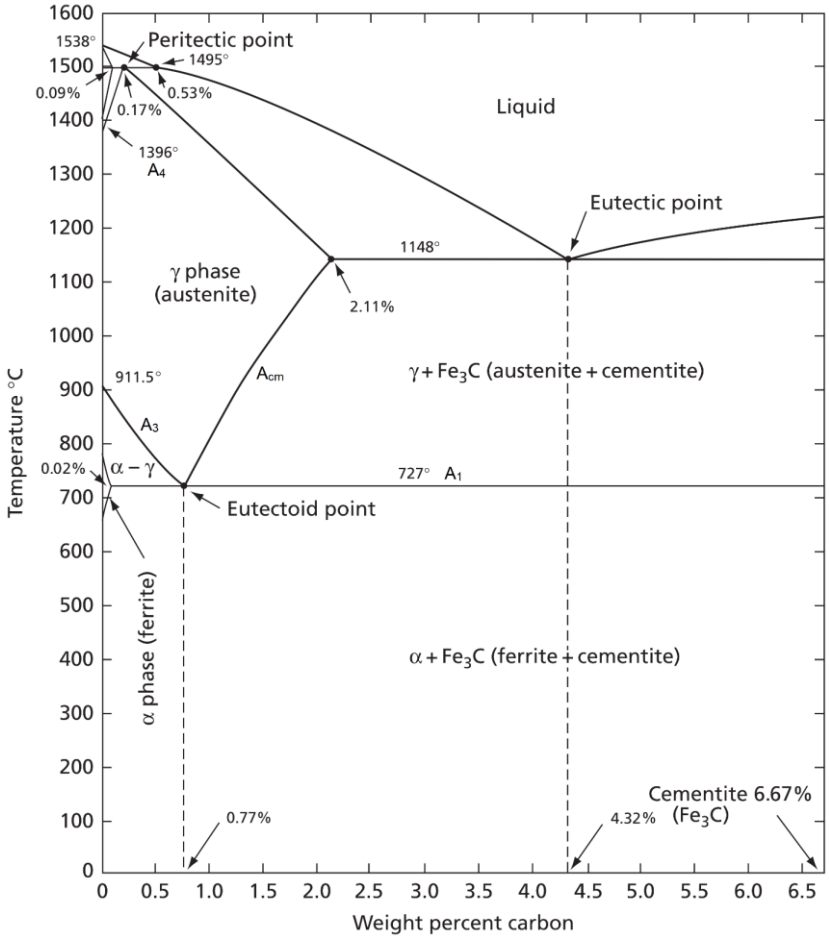

Figure 9: The Fe-Fe_3C phase diagram [12]

There are three invariant points in Fe–Fe_3C diagram describing phase transformations that occur at precise temperatures and alloy compositions: the peritectic point at 0.17 wt. % C and 1495°C (L+δ-iron→γ-iron), the eutectic point at 4.32 wt. % C and 1148°C (L→γ-iron+Fe_3C,), and the eutectoid point at 0.77 wt. % C and 727°C (γ-iron→α-iron+Fe_3C). Phase transformation temperatures are generally referred to as critical temperatures, corresponding to the boundary between the phase fields named A_1, A_2, A_3, A_4, and A_{cm}. A_1 is the eutectoid temperature, 727°C, below which the eutectoid reaction occurs. A_2 is the Curie temperature, 768°C, above which ferromagnetic α-iron becomes a paramagnetic phase. Next, A_3 is the temperature at which transformation of α-iron to γ-iron is completed, while A_4, the transformation temperature from γ-iron to δ-iron, 1396◦C. Finally, A_{cm} refers to the temperature at which the dissolution of Fe_3C in γ-iron is completed during heating. These critical temperatures are sensitive to steel composition, heat-treatment parameters, and heating

and cooling rates. Thus, it alters not only the transformation temperatures but also the phase balance in the steel. In regards to the present study, the phase transformations occurring at A_1, A_3, and A_{cm} are of primary interest and are dealt in more detail below.

As mentioned, the microstructure obtained during cooling under equilibrium depends on the carbon concentration of the steel. A fully pearlitic structure forms in eutectoid steels (0.77 wt. % C) below the eutectoid temperature. It contains about 88% by mass of α-iron and 12% of Fe_3C in a layered structure, whose relative thickness is approximately 8 to 1. Hypoeutectoid steels (< 0.77 wt. % C) form two primary constituents during slow cooling: proeutectoid ferrite and pearlite. In the case of hypereutectoid steels (> 0.77 wt. % C), the final microstructure contains proeutectoid cementite and pearlite. Ferrite grains can develop on a few different morphologies, including allotriomorphic, idiomorphic ferrite, and Widmanstätten ferrite.

The allotriomorphic ferrite nucleates at prior austenite grain boundaries and tends to grow along the parent phase grain boundary, while the idiomorphic ferrite is an equiaxed crystal that usually forms at inclusions or other heterogeneous nucleation sites inside the austenite grain. The Widmanstätten ferrite may be nucleated directly on grain boundaries or on grain boundary allotriomorphs, growing along well-defined austenite planes and forming thin elongated plates. [14,23] In its turn, in high-carbon steels, the proeutectoid cementite nucleate preferentially on the austenite grain boundaries, and tends to form as a layer that lies on one side of a boundary. Under certain conditions, it may create a continuous grain boundary network. Figure 10 shows the microstructure of hypo- and hypereutectoid steels.

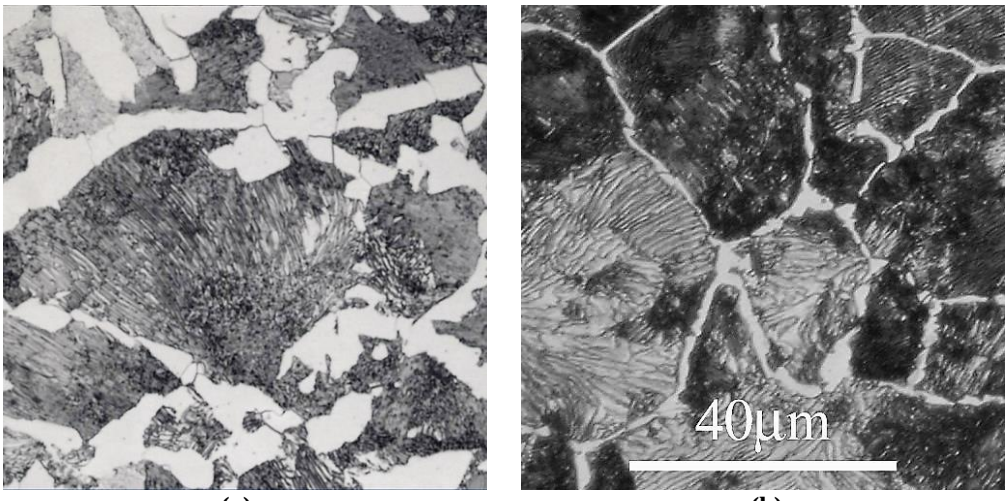

(a) **(b)**

Figure 10: Optical micrographs of pearlite, proeutectoid ferrite, and cementite phases (in white) of, respectively, (a) 0.4 wt. % C and (b) 1.0 wt. % C steels [16]

I.2.2. The pearlite formation

The phase transformation of austenite to pearlite occurs by nucleation and growth. This reconstructive transformation relies on the diffusion of carbon atoms that leads to the reconstruction of FCC austenite crystal lattice into a new and more complex crystal structure: BCC lattice of ferrite and orthorhombic lattice of cementite. The active nuclei for the formation of pearlite may be either a ferrite or cementite lamella, depending on the carbon content and transformation conditions. In the case of hypo- or hypereutectoid steels, the nucleation of pearlite takes place preferentially at the boundary layer of the respectively proeutectoid phase, which continues to grow with the same crystallographic orientation during the pearlite formation. In eutectoid steels, the pearlite nucleation sites are assumed to occur at the grain boundaries of austenite.

The mechanism of pearlite growth has been the subject of many works over the years. The theories of Zener-Hillert [17,18] established that the diffusion of carbon atoms governs the rate-controlling mechanism of growth. The growth of pearlite from austenite involves the redistribution of carbon atoms and the crystallographic change from the FCC austenite to the BCC and orthorhombic lattice structures of ferrite and cementite, respectively. The austenite-pearlite transformation kinetics is described by Kolmogorov-Johnson-Mehl-Avrami theory [19-22]. Figure 11 illustrates schematically the nucleation and grown processes occurring to form pearlite.

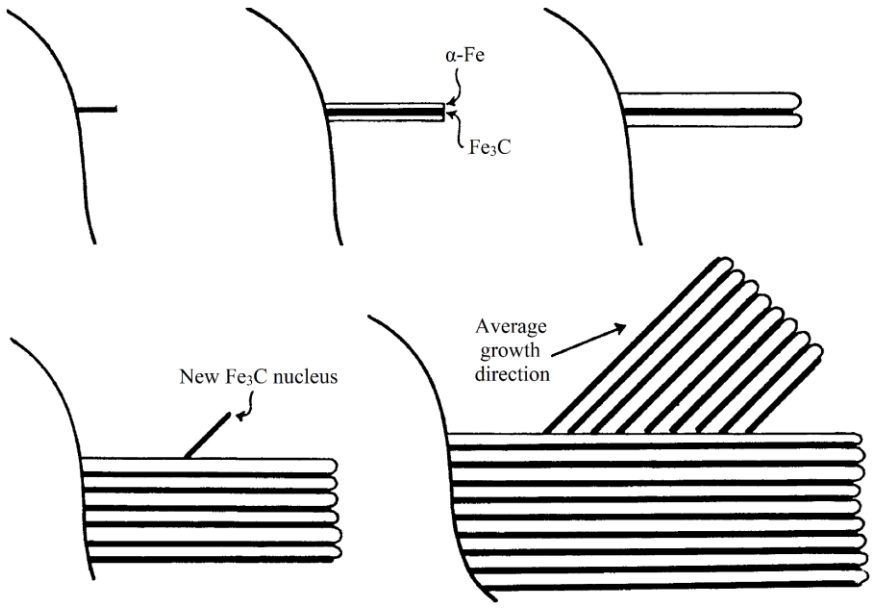

Figure 11: Successive stages in the formation of pearlite by nucleation and growth [22]

The nucleation process starts with the diffusion of carbon from the surrounding austenite grain to the formation of a nucleus of cementite, which grows into the

austenite grain γ_2 that has an incoherent high-energy interface with pearlite. Conversely, the boundaries formed at the site of nucleation between the adjacent austenite grain γ_1 and pearlite are low-energy interfaces with limited mobility. [12,23] As carbon diffuses into the iron carbide, the adjacent austenite is consequently impoverished in carbon atoms, and nucleation of a ferrite lamella begins. Simultaneously, the enrichment of carbon in the austenite vicinity promotes the nucleation of another cementite layer. Hence, the cooperative nucleation of alternating layers of cementite and ferrite takes place continuously along the austenite grain boundary. The pearlite grown occurs by extension of their edges due to the movement of the incoherent interface boundary into γ_2 and carbon diffusion. Moreover, it may further result from the branching of ferrite and cementite lamellae [24].

The continuous process of sympathetic nucleation, branching of lamellae, and edgewise growth of ferrite and cementite plates forms the microstructure of pearlite. The typical pearlite microstructure is illustrated in Figure 12. The distance between adjacent cementite lamellae is referred to as the interlamellar spacing of pearlite. Pearlite colony is commonly defined as the region in which alternated ferrite-cementite lamellae are aligned nearly parallel to each other due to a common direction of growth. Dippenaar and Honeycombe [25] found that the crystallographic orientations of both phase lamellae may be related to that of the adjacent austenite grain γ1, into which it does not grow. As the pearlite colony grows, new lamellae may nucleate from its sides at different growth directions. The set of colonies nucleated from the same adjacent austenite grain forms a pearlite nodule, also called a pearlite block. It refers to a region constituted of several colonies with similar crystallographic orientation and usually having fairly equal interlamellar spacing [12,22,26].

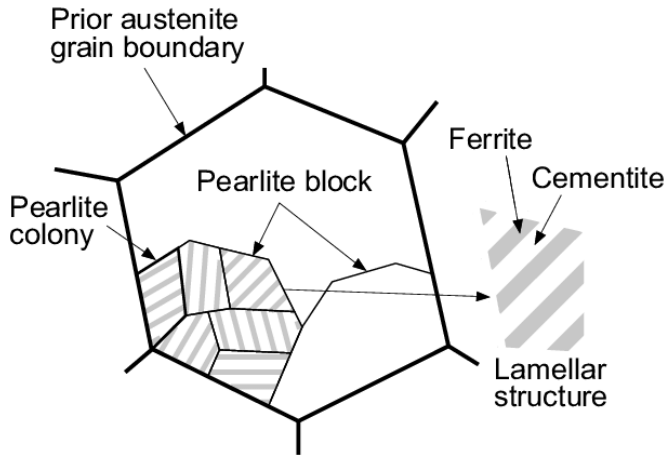

Figure 12: Schematic diagram of the pearlite microstructure [27]

The arrangement of the microstructure of pearlite in alternating layers of α-iron and Fe_3C phases is very complex. The commonly accepted definition of the pearlite colony is based on the cementite lamellae orientation, whereas the concept of a nodule is related to the crystallographic orientation of the ferrite matrix phase. Walentek et al. [28] reported the difficulty in determining mean perlite colony sizes by conventional metallography and electron backscatter diffraction (EBSD) techniques. The latter study is supported by Guo and Liu [29] that demonstrated the complexity of quantitatively assessing the mean colony size in the pearlite structure. Despite the many works in this field, the interface between adjacent colonies of pearlite is still not well defined for characterizing the pearlite microstructure based on two-dimension observations. However, they have shown that combining back-scattered electron (BSE) images with EBSD data (Figure 13) could bring additional information regarding the characterization of pearlitic steels.

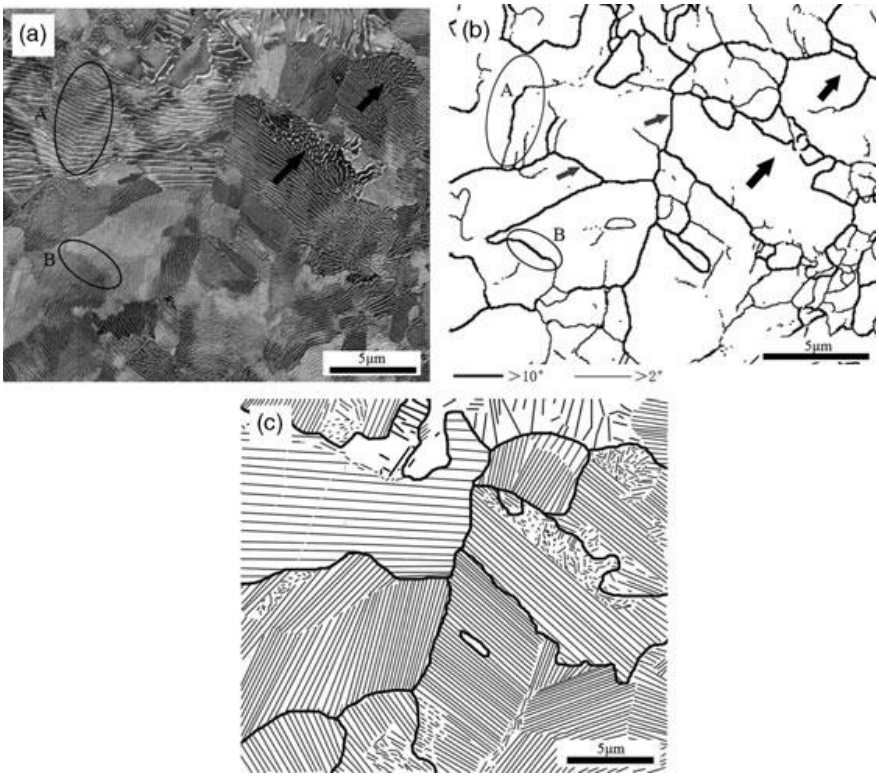

Figure 13: (a) BSE image, (b) EBSD grain boundary map, and (c) the corresponding BSE and EBSD combined image of a fully pearlitic microstructure, with coarse lines defining the nodule boundaries and fine lines the cementite lamellae [29]

I.2.3. The pearlite transformations kinetics

In the previous section, the pearlite formation has been described by a eutectoid reaction occurring at 727°C under very slow cooling rates. Nonetheless, considerably

long times are required for austenite decomposition into pearlite. Therefore, in current practice, the steel is cooled from the austenite phase and held at temperatures below A_1 for relatively short periods, which does not approach the equilibrium condition.

As the pearlite transformation is a diffusion-controlled process, temperature plays an essential role in its reaction kinetics. The diffusion of carbon in austenite is dependent on temperature, and its average diffusion coefficient D_C^γ is expressed below in $cm^2.s^{-1}$:

$$D_C^\gamma = 0.12e^{\frac{-32,000}{RT}} \quad (1)$$

where R is the universal gas constant (1.98 $cal.g\text{-}mol^{-1}.K^{-1}$), and T is the absolute temperature in K. The diffusion process decreases exponentially with decreasing temperature. At a constant transformation temperature, the initial reaction rate is relatively low due to the incubation period for the carbon atoms to diffuse and form the first nuclei. As the colonies grow, a greater surface area is available for nucleation, and the transformation rate accelerates. The transformed perlite colonies grow continuously, impinging on each other, and the rate of transformation is slowed until the full transformation. The interlamellar spacing within a pearlite colony is considered to be constant for a given transformation temperature. Although the rearrangement of carbon atoms is indispensable to accomplish the decomposition of austenite into pearlite, the rate of nucleation and growth of pearlite colonies increases with decreasing temperature. It is due to the antagonistic effects of the austenite decomposition driving force and the diffusion process on the phase transformation kinetics. The Gibbs free energy difference to provide the necessary driving force for the transformation of austenite to ferrite and cementite increases with decreasing temperatures, as follows:

$$\Delta G = \Delta H - T\Delta S \quad (2)$$

where G is the free energy, H is the enthalpy, T is the absolute temperature, and S the entropy. The higher the degree of undercooling, the greater the driving force for the austenite decomposition process, and the reaction rate accelerates, even if the carbon diffusion becomes sluggish. As a result, more pearlite colonies are produced, while the interlamellar spacing is progressively reduced to offset the decrease in diffusivity at lower temperatures by diminishing the diffusion distance of carbon atoms at the austenite-pearlite interface. [12,14] The temperature dependence of nucleation and growth rates of eutectoid steel is shown in Figure 14.

If the transformation occurs at temperatures slightly below A_1, the rate of nucleation is low compared to the rate of growth. A few pearlite nuclei form from austenite, each of which grows across austenite grain boundaries into large pearlite nodules. The percentage of transformed pearlite is relatively small, and an extended period is necessary for the transformation to complete. At relatively higher temperatures, around 650°C, carbon diffusion rates are relatively high, allowing its atoms to diffuse across longer distances, which results in the formation of a coarse pearlite structure with thicker ferrite and cementite lamellae. The incubation period decreases substantially with the lowering of the transformation temperature, reaching a minimum value in the nose of the transformation curve, generally at about 540°C. In its turn, fine pearlite with a thin-layered structure is produced, requiring only a few seconds for reaction completion. Therefore, the undercooling exerts a dominant effect on the reaction rate at high transformation temperatures, and, below the nose of the curve, the diffusion becomes the rate-limiting factor.

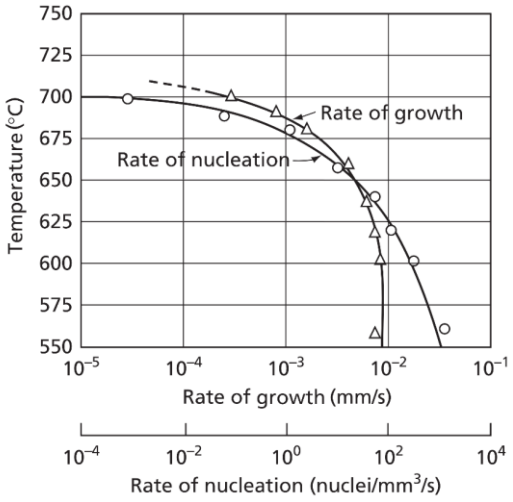

Figure 14: Nucleation and growth rates as a function of temperature in eutectoid steel (0.78 wt. % C, 0.63 wt. % Mn, ASTM No. 5) [12]

Most heat treatment processes applied to steels involve isothermal cooling (fast cooling and holding at a constant temperature) and continuous cooling (regular cooling rate) treatments. Isothermal and continuous cooling transformation diagrams represent both the time and temperature influence on the transformation kinetics of an alloy of specified composition in a more convenient way than phase diagrams, considering transformations under non-equilibrium conditions. Figure 15 shows the curves of an isothermal transformation diagram for eutectoid steel, also called the time-temperature-transformation (TTT) diagram. In continuous cooling transformation

(CCT) diagrams, a plot usually contains the beginning and ending reaction for each cooling rate curve of determined alloy composition, assessing the transformation progress concerning temperature changing. The TTT and CCT diagrams of hypo- and hypereutectoid steels differ from that of eutectoid steels with additional curves corresponding to their proeutectoid phases. Aspects such as prior-austenite grain size (PAGS), carbon content, and alloying elements can alter the morphology of pearlite [30-32], shifting the diagram curves to shorter or longer times or modifying its shape.

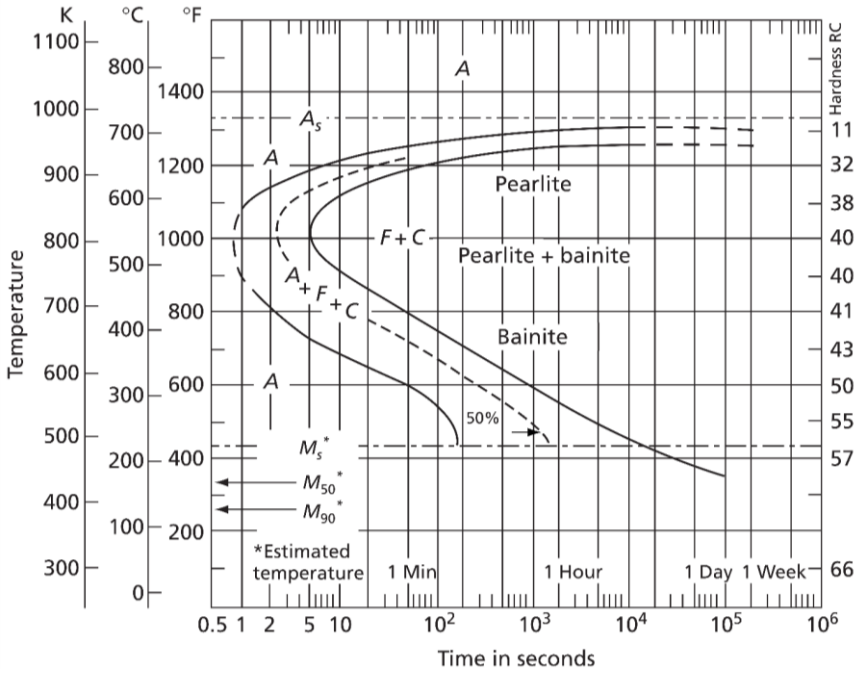

Figure 15: Complete isothermal transformation diagram for eutectoid steel; where A, C, F, and M are, respectively, austenite, cementite, ferrite, and martensite phases [12]

At a temperature range just below that at which pearlite forms, typically 550°C until approximately 250°C, the bainite is the transformation product of austenite. Bainite is a non-lamellar microstructure consisted of ferrite and iron-carbides, whose morphology is further classified as upper and lower bainite, depending mainly on its transformation temperature. The formation of bainite is intricate due to its dual nature, revealing typical characteristics of diffusion-controlled reconstructive transformation (nucleation and growth) and the displacive mechanism of transformation (shear displacements) [33,34].

Apart from bainite, a martensitic structure may be formed when iron-carbon alloys are quenched to temperatures below those where bainite would nucleate, usually below 200°C. The martensitic transformation is a diffusionless, displacive reaction that occurs when a diffusion-controlled transformation is suppressed by rapid cooling.

Large numbers of carbon atoms in the austenite lattice are trapped in their FCC octahedral sites, distorting the cubic structure by lattice shearing to a body-centered tetragonal (BCT) lattice structure supersaturated with carbon atoms [14]. The resultant morphology is characterized by a hierarchical structure of packet, block, and thin plates or laths. It allows minimizing the strains generated through shear and volume expansion during transformation. Martensite is an extremely hard and brittle phase, whose toughness can be significantly improved by tempering heat treatment. It involves heating at temperatures in the range of 250 to 650°C to alter the size and distribution of carbides and relieve internal stresses from quenching, resulting in a softer, more ductile, and malleable microstructure. The tempered martensite microstructure with very fine cementite precipitates is usually called sorbite.

Moreover, several microstructures may be produced by annealing processes that generally includes three stages, involving heating to a specified temperature below the critical point, holding at a temperature for a set length of time, and then cooling to room temperature, whose cooling medium depends on the size and composition of the heat-treated part and the final desired properties. When the austenite transformation products are heat-treated for an extended time at elevated temperatures close to A_1, the cementite emerges as a globular phase dispersed in a ferrite matrix, a very soft and ductile microstructure called spheroidite. A variety of annealing heat treatments can be performed to relieve internal stresses induced by heat treatments, casting, forming, or machining; to refine grain structure; to improve or restore mechanical properties such as ductility. Figure 16 shows light optical microscopy images of several microstructure features obtained from austenite decomposition in eutectoid steel.

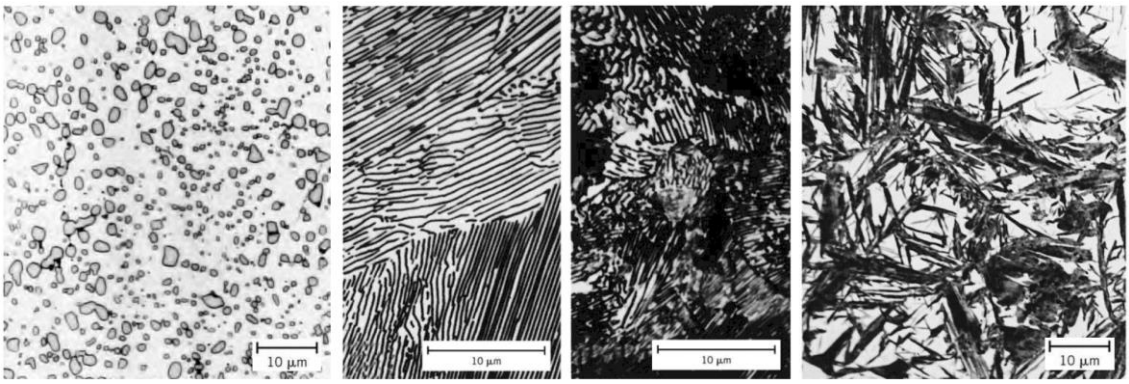

(a) **(b)** **(c)** **(d)**

Figure 16: Optical micrographs of the various microstructures in eutectoid steel: (a) spheroidized microstructure with globular cementite in a ferrite matrix; (b) coarse and (c) fine pearlite; (d) martensite needle-shaped grains and retained austenite [11]

I.3. The strength of pearlite

Structural materials may experience deformation processes during service, constantly subjected to a range of external loads. On a microscopic scale, these processes are generally associated with the movement of dislocations within crystalline solids in response to applied stresses. Plastic deformation involves slip and twinning deformations, and, eventually, martensitic transformations. Slip is the most important mechanism of deformation where crystal parts glide over one other along with specific slip systems, as a consequence of dislocations movement over particular crystallographic planes in certain directions within the crystal. It is usually due to pure shearing stresses acting across the material. Besides, crystal lattice imperfections, such as interstitial atoms, grain and phase boundaries, inclusions, and precipitates, represent significant obstacles to dislocation mobility into the lattice, also affecting the mechanical behavior of materials. The knowledge about the types of crystal defects, in particular, about the nature and the role of dislocations in deformation processes is imperative to the design of engineering materials.

Tensile and yield strength, ductility, toughness, and hardness are fundamental mechanical properties of most interest considering structural and engineering applications of steels. The yield strength determines the stress beyond which plastic deformation occurs, while ultimate tensile strength determines the maximum tensile stress from which crack initiation starts. Ductility is the ability of a material to withstand significant plastic deformation without fracturing. Toughness describes its ability to absorb energy in the plastic range up to fracture. In its turn, hardness is a measure of the resistance to localized plastic deformation induced by either indentation, scratching, or abrasion. [11,14] Accordingly, the mechanical performance of a material reflects its response to an applied load or force, which is directly related to the displacement of linear crystallographic defects within the crystal structure. In other words, the ability of a material to plastically deform depends on the faculty of dislocations to move in response to the applied stress.

In the case of carbon steels, it is well known that the carbon content present in iron-based solid solutions primarily controls their mechanical behavior. Gladman and Pickering [35] described the yield strength of hypoeutectoid steels as a function of ferrite and pearlite contributions, depending mainly on the volume fraction of proeutectoid ferrite and pearlite, but also the grain size of proeutectoid ferrite and the

interlamellar spacing of pearlite. The higher the carbon content, the more significant is the impact of pearlite interlamellar spacing on the strength and ductility of near-eutectoid steels. In hypereutectoid steels, the strength and hardness become even more elevated due to the precipitation of proeutectoid cementite, which consequently reduces both ductility and impact toughness properties. Concerning fully pearlitic structures, the spacing between ferrite and cementite lamellae is considered as the primary microstructural parameter controlling the material strength [35,36]. Besides the contribution of the interlamellar spacing, Hyzak and Bernstein [37] found that strength increases as the prior-austenite grain size decreases. On the other hand, the pearlite colony size has shown a minimal effect on the strength of fully pearlitic microstructures. The dependence of both yield and tensile strengths on the pearlite interlamellar spacing S_P has been reported to follow a Hall–Petch relationship:

$$\sigma_j = \sigma_0 + kS_P^{-\frac{1}{2}} \quad (3)$$

where σ_j indicates the yield or ultimate tensile strength, σ_0 is the friction stress, and the constant k is the strengthening coefficient [38-40]. The pearlite fineness has been considered the main factor responsible for the high strength of eutectoid steels, based on the assumption that dislocation sources are activated at ferrite-cementite interfaces and the dislocation pile-up model [40]. Although the lamellar spacing contributes to the ductility and toughness of pearlitic steels, these properties have been reported to be controlled by the prior-austenite grain size [41,42].

There are several types of dislocation-microstructure interactions that can be introduced into the lattice structure to enhance the material's mechanical properties, commonly defined as strengthening mechanisms. Solid solution and alloying strengthening, grain boundary strengthening, precipitation hardening, and work hardening are examples of strengthening mechanisms. As regards steel wires, work hardening by drawing processing allows obtaining wire products with ultra-high mechanical strengths. It is a metal forming process that leads to massive modifications to the microstructure and hence, on their mechanical properties through plastic deformation. As an external force is applied to the material, additional dislocations are increasingly generated. The higher dislocation density, the more obstacles that significantly impede the mobility of dislocations, which results in higher shear stress necessary to move them within the solid. The work hardening increases both yield and tensile strength, hardness, and subsequently decreases ductility. The effects of work

hardening may be reversed by annealing processes at high temperatures, reducing dislocation density, and recovering some ductility. The steel wire manufacturing processes, including drawing and heat treatments, are further described in the following paragraphs.

I.4. Steel wire manufacturing

Steel wires, bars, rods, and tubes are commonly fabricated by drawing operations, in which the shape and size of a metal piece are altered through plastic deformation induced by means of external forces. Thermo-processes are also carried out to improve formability and to obtain satisfactory mechanical characteristics for the final product. Figure 17 illustrates the principal wire processing operations.

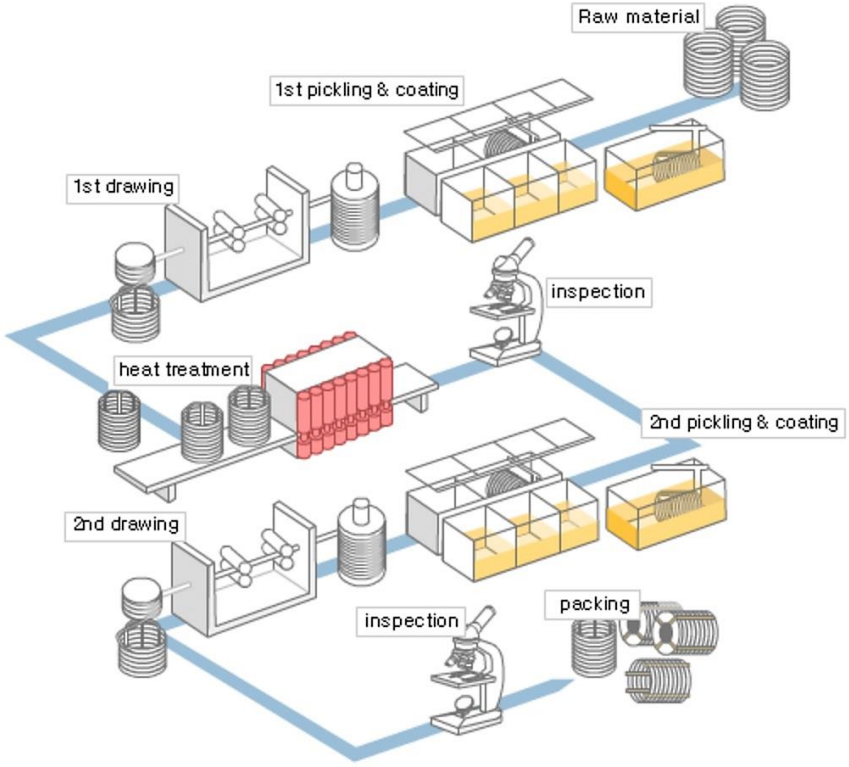

Figure 17: Schematic of typical wire manufacturing processes [42]

I.4.1. Wire drawing

Drawing is a metal forming process that allows obtaining excellent dimensional control and surface finish of long products in a continuous conformation processing. The concept of drawing involves pulling a metal workpiece through a single or a succession of multiple conical dies by applying tensile forces to the die outlet, resulting in a decrease of the cross-sectional area with a corresponding increase in the length of the material.

Drawing processes commonly begin with a coil of a hot-rolled rod that is the first chemical treated by pickling in an acid solution, usually sulfuric or hydrochloric acid, to remove any impurities, rust, or scale from the material surface. The surface treatment is commonly practiced after pickling, frequently with lime, borax, or phosphate acid solution. A solid-surface layer is then produced on the wire rod, which helps carry lubricants and prevents direct contact between the wire and the die, optimizing the manufacturing process [44]. Most drawing is conducted at room temperature by cold working, using a sequence of drawing passes with a set of dies of progressively reduced final diameters. At each pass, the wire is pulled through the die by a draw block or a capstan. The drawn wire is taken up like a coil, as illustrated in Figure 18. Drawing may also be performed at elevated temperatures to hot work materials of limited ductility.

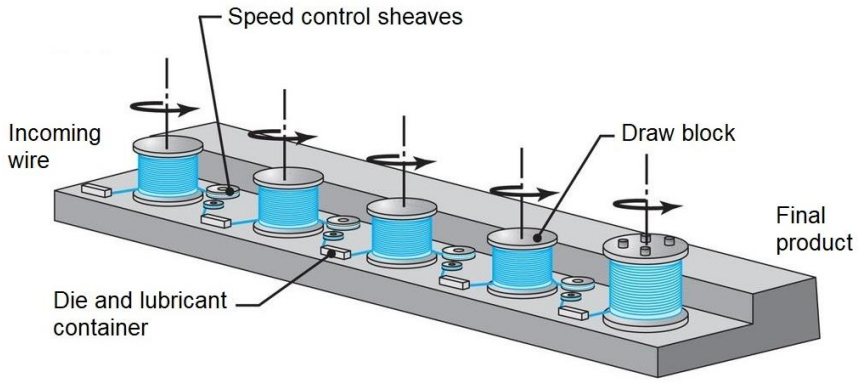

Figure 18: Schematic illustration of a multi-pass drawing machine [44]

Drawing dies are typically made of diamond or tungsten carbide in the form of inserts or nibs supported in a steel casting piece. The characteristic features of a die assembly are shown in Figure 19. The die is constituted of four regions: the entrance zone, a bell-shaped part to funnel the lubricant into the die-wire interfaces; the deformation zone, a cone-shaped area where the actual reduction in wire diameter occurs; the bearing or land zone, which determines the final size of the drawn wire; and the exit zone, a back relief region. Proper lubrication is essential to ensure an excellent surface finish and prevent excessively rapid die wear during drawing, reducing friction forces, and controlling temperature to a steady level. Lubrication takes place by spraying (dry drawing) or by immersion (wet drawing). In the dry drawing, powdered soaps are introduced in a container before the die entry and coat the die-wire interface when the wire rod passes through it. While in wet drawing, the drawing system is completely submerged in a lubricating fluid or an alkaline soap

solution. Critical parameters as die geometry, cross-sectional area reduction, number of passes, drawing speed, and lubricant selection, are decisive for reaching high-quality drawn products with great dimensional accuracy and surface finish. [45-47]

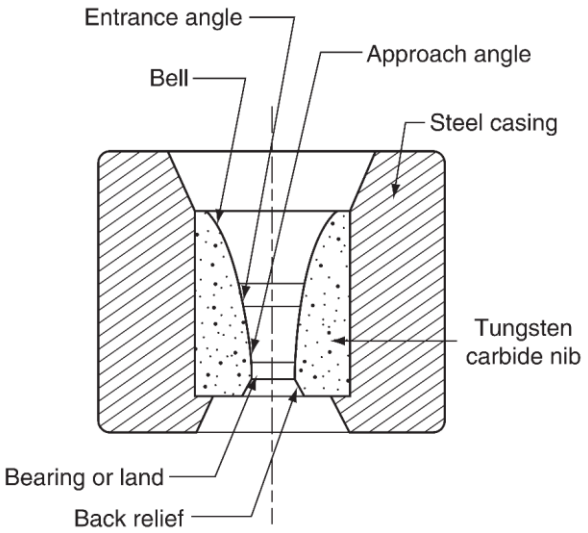

Figure 19: Cross-section geometry of a typical drawing die assembly [46]

Figure 20 illustrates the process variations in wire drawing operation. The cross-sectional area of wire before the drawing is designated as A_0, and it exits the die with a reduced cross-sectional area designated as A_1. The half die angle α, usually ranging from 6° to 10° [48], determines the reduction in the cross-sectional area after each pass and the final dimensions of the drawn product. Drawing deformations are frequently expressed as the fractional drawing reduction r, given by:

$$r = \frac{(A_0 - A_1)}{A_0} = 1 - \left(\frac{A_1}{A_0}\right) \quad (4)$$

It is convenient to recall that the workpiece volume should remain constant during the conformation. Therefore:

$$V_0 = A_0 l_0 = \left(\frac{\pi}{4} d_0^2\right) l_0 = V_1 = A_1 l_1 = \left(\frac{\pi}{4} d_1^2\right) l_1 \quad (5)$$

where l_0 and l_1 are, respectively, the initial and final length and d_0 and d_1 are correspondingly the starting and the finishing wire diameters. The true drawing strain ε_d, often used to indicate the level of reduction, can be determined as follows:

$$\varepsilon_d = ln\left(\frac{l_0}{l_1}\right) = 2ln\left(\frac{d_0}{d_1}\right) = ln\left(\frac{A_0}{A_1}\right) = ln\left(\frac{1}{1-r}\right) \quad (6)$$

Although the applied drawing force for wire stretching is tensile, the plastic deformation is effectively promoted by a combination of axial tensile and radial compressive forces, imposed by the conical die walls as the metal piece is squeezed down through it. The drawing stress σ_d is equal to the drawing force divided by A_1,

and the die pressure P represents the normal compressive force acting upon the wire in the deformation zone divided by the contact area between the wire and the die. As it is a continuous manufacturing process, tensile forces are applied both to the exit of the die (drawing force) and to the entry of the next one (back force). The back stress σ_b indicates the back force coming off the capstan divided by A_0. Besides, frictional forces generated from the interaction of the wire rod with the die are also present in the drawing system. The frictional shear stress in the opposite direction of wire drawing is indicated by μP, where μ is the coefficient of friction. [48]

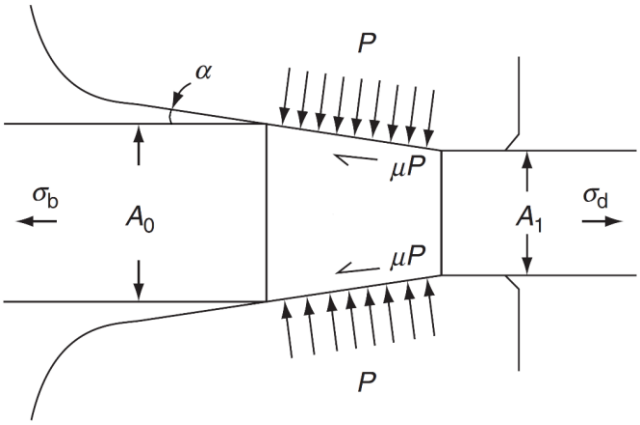

Figure 20: Primary forces operating in wire drawing [45]

It is a common practice to assume uniform the plastic flow of the workpiece, without considering any interaction between the workpiece and the die, for simplifying calculations of drawing forces and deformations. The drawing stress is equivalent to the plastic work per unit volume expended during drawing, involving the uniform work w_u required for stretching the wire, but also the contribution of the redundant w_r and friction w_f works that do not affect the wire dimension [46,47]. Redundant work arises from the shear related to the material flow deflection occurring when the wire passes through the die, whereas friction work represents the work required for overcoming frictional forces created by the wire-die wall interaction. The area reduction mainly determines uniform work. It is independent of the die geometry, unlike redundant and frictional works that are closely related to it. Figure 21 shows the components of drawing stress, determined by the sum of the necessary efforts to achieve homogeneous and redundant deformations and overcome friction, as follows:

$$\sigma_d = w_u + w_r + w_f = \sigma_a ln\left[\frac{1}{(1-r)}\right] + (\Phi - 1)\sigma_a ln\left[\frac{1}{(1-r)}\right] + \frac{4\mu\Phi\sigma_a}{\Delta} \qquad (7)$$

where σ_a is the average flow stress in the wire during drawing, and Φ is the redundant work factor. If back tension is considered in the system, it may lower the average die

pressure and the related frictional stress, reducing the overall drawing stress. In an ideal situation where drawing stress is homogeneous, the drawing limit is reached when drawing strain is equal to 1: r_{max}=63.2%. However, in practice, drawing limits involve reductions considerably below 63.2%, to about 35% per pass [46].

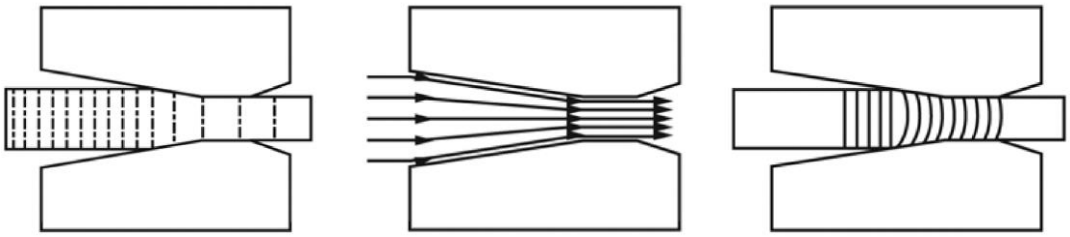

(a) **(b)** **(c)**

Figure 21: Components of plastic work that operate during wire drawing: (a) uniform, (b) redundant, and (c) frictional work [45]

The deformation zone, delimited by the wire and the die walls, forms an approximatively trapezoidal-shaped region in the longitudinal section, which can be characterized by the ratio Δ parameter:

$$\Delta = \left(\frac{\alpha}{r}\right)\left[1 + (1-r)^{\frac{1}{2}}\right]^2 \quad (8)$$

Lower Δ values correspond to higher reductions and lower die angles, which generally involves increasing frictional work. Higher Δ values are associated with lower reductions and higher die angles, which implicates a redundant work increase. Increased die wear is often associated with increasing of die pressure and Δ.

Hence, in addition to the half die angle and reduction of area, several factors may contribute to the total stress in the drawing process. It includes the deformation zone length and die contact length, friction coefficient, deformation speed, and temperature. The analysis of drawing process parameters and its relationship with the material characteristics is of great importance for the understanding and optimizing the manufacturing operation itself and the final properties of the drawn product.

I.4.2. Patenting

Annealing processes may be undertaken in combination with drawing to reach final mechanical property requirements. Specific annealing called patenting is usually adopted for medium and high carbon steels grades to achieve a pearlitic structure with a very fine lamellar spacing, which possesses excellent drawability and a high strength [49]. It is usually an intermediate step conducted in pre-drawn wires to recover its initial properties and allow continuing drawing to smaller diameters.

Patenting consists of heating at critical temperatures over A_3 or A_{cm} to ensure a complete and uniform austenite transformation, followed by a rapid cooling down below the A_1 point, where the austenite decomposition to pearlite is accomplished. Finally, the patented wires are cooled down to ambient temperature. It exists several kinds of cooling media, including lead, air, and fluidized sand-bed. In steel industries, isothermal cooling is usually carried out in a molten lead bath maintained at a constant temperature for the duration of the pearlitic transformation. Despite the excellent thermal properties of molten lead, the use of lead in the conventional patenting process has been considered environmentally dangerous and toxic for human health by current environmental regulations [50]. In the last decades, environmentally friendly alternatives have been developed, such as continuous cooling using high-velocity airflow or polymer solution baths [51,52].

Isothermal and continuous cooling patenting are processes that depend on several variables such as cooling rate, which involves temperature distribution into the wire and, therefore, possible variation in the microstructure. If the cooling rate is too slow, the transformation occurs at higher temperatures, leading to a coarser pearlite structure with a lower strength than a thinner microstructure. In contrast, faster rates lead to undesirable bainitic and even martensitic structures, as indicated in Figure 22. Quality control is thereby demanded to ensure uniform and fine microstructure of pearlite during wire manufacturing.

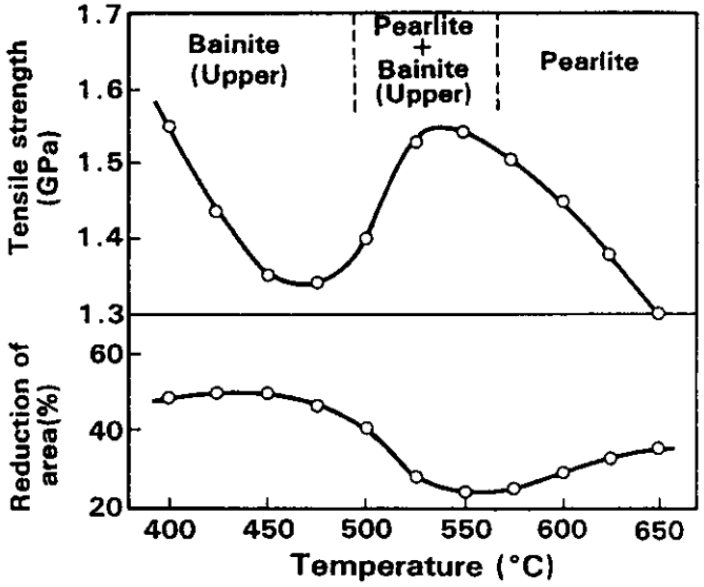

Figure 22: Tensile strength and reduction of area as a function of transformation temperature in patented hypereutectoid steels [14]

I.5. Experimental techniques for characterization of steels

As hitherto discussed, the adequate process control and characterization of microstructural and functional properties of processed wires are crucial for their further application in a wide range of engineering components. In this section, general aspects of the most relevant methods employed for the evaluation of microstructure and properties of steels are described. The current analysis techniques for inspection, monitoring, and in-situ characterization of steel wires, which involve non-destructive testing, are also discussed in this part.

I.5.1. Conventional characterization techniques

The existing methods for characterization of microstructure and mechanical properties of steels play an essential role in the development of advanced materials and applications in the final product validation and failure investigation.

Microscopy techniques are a powerful magnification and resolution imaging tool, providing detailed information on the element and compound structure, crystallographic data, composition, morphology, and topography. It includes light optical microscopy (LOM); electron microscopy, such as scanning electron microscopy (SEM) and transmission electron microscopy (TEM); scanning probe microscopy (SPM), which encompasses several types of microscopes – scanning tunneling microscope (STM), atomic force microscope (AFM), magnetic force microscope, among other techniques. In general, these are destructive techniques. Metallographic analysis requires a proper sample preparation, usually consisted of a succession of specific operations including cutting, mounting, grinding, and polishing, necessary to obtain a suitable examination surface for an accurate interpretation of the actual microstructure of the studied materials. Although microscopy instruments work very fast and accurately, these are usually quite expensive, require regular maintenance, and specialized training for specimen preparation and operation itself.

Tensile and compression tests, impact, torsion, bending, and fatigue tests are some of the standard tests used to evaluate mechanical properties, replicating as narrowly as possible materials service conditions. Mechanical tests are straightforward and rather inexpensive, providing information about the elastic limit, yield and ultimate tensile strengths, ductility, and toughness of materials operating under monotonic and cyclic loadings. However, these are destructive tests generally carried

out to failure, the specimen's shoulders are gripped to the claws of a specific testing machine, whereas the gauge section is progressively deformed during testing.

I.5.2. Non-destructive testing

Destructive testing has been around longer in engineering for a reliable and accurate evaluation of materials. Over the years, non-destructive testing methodologies have been developed to examine items without damaging the tested components [7-9]. Non-destructive testing, also referred to as non-destructive evaluation or inspection, consists of a variety of analysis techniques commonly used for inspecting raw materials, components, and end products, detecting the presence of defects or discontinuities (e.g., cracks, corrosion spots), and monitoring equipment in service and processing operations, as shown in Figure 23. It results in the quality improvement of components or products and major savings in time, scrap levels, and machinery.

The NDT methods are classified based on a particular physical principle, such as capillarity, emission of subatomic particles, electromagnetic waves, sound vibrations, or any type of test that does not alter the material under examination. Visual inspection is the simplest method of all. Surface imperfections invisible to the eye may be revealed by penetrant liquid or magnetic particle tests. Magnetic leakage flux is a method employed to detect corrosion and pitting in steel and other ferromagnetic structures. Radiography, ultrasonic and electromagnetic techniques can detect damage zones in the bulk material. There are several different methods for specialized applications, including acoustic emission, thermal and infrared tests, microwave techniques, and neutron radiography. [53]

(a) **(b)**

Figure 23: (a) Magnetic particle testing for inspecting a welded piece [54]; and (b) ultrasonic testing involving sound waves for defects detection in rail steels [55]

Recent advances in engineering have extended NDT applications to evaluate properties and physical characteristics that may affect the serviceability of materials. As far as microstructural characterization is concerned, electromagnetic techniques stand out, not only because of the sensitivity of electromagnetic properties to microstructural variations but also because of the simplicity of equipment installation and operations [53,56,57]. Based on the principles of electromagnetic induction, electromagnetic testing, such as magnetic Barkhausen noise analysis (MBN), magneto-acoustic emission (MAE), and eddy current testing, introduces electric currents or magnetic fields into the material under investigation in order to extract electromagnetic responses related to their physical properties.

Both MBN and MAE techniques rely on the irreversible and discontinuous movement of magnetic domain walls during the magnetization process, the Barkhausen effect, as shown in Figure 24. The abrupt domain walls jump affects the amplitude, peak, and width shape of the Barkhausen noise signal, which also depends on testing parameters, including the maximum applied magnetic field strength, measurement frequency range, and coil configuration.

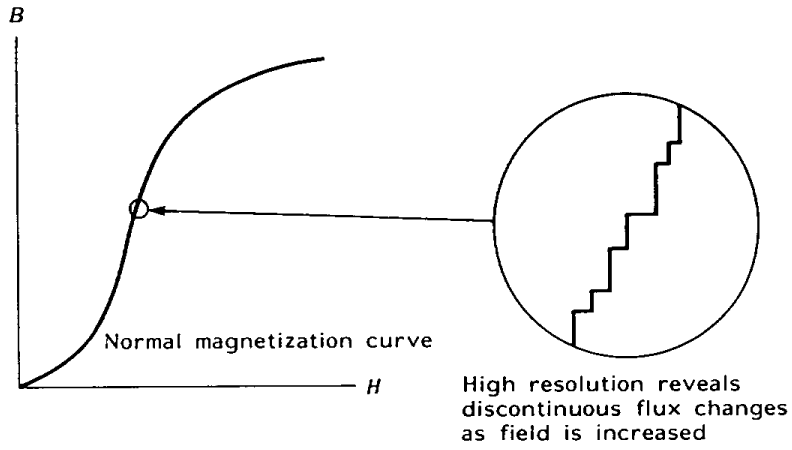

Figure 24: Barkhausen discontinuities along the initial magnetization curve [8]

Magnetic non-destructive methods such as magnetic hysteresis [58-62], acoustic [63,64] and magnetic Barkhausen analysis [65-73] have exhibited great potential for evaluation of microstructure and stresses in ferromagnetic steels. Relevant observations were obtained from these numerous studies. The increase in the strength and the number of pinning obstacles within the tested material leads to a rise in the MBN signals, and, as the structure becomes magnetically harder, the peak shifts to a higher value of the magnetic field. Moreover, evaluating steels with different carbon content and phases may produce different shapes of MBN profiles, revealing

considerable variation in the magnetization process between several microstructures features, as reported by Saquet et al. [65], and shown in Figure 25.

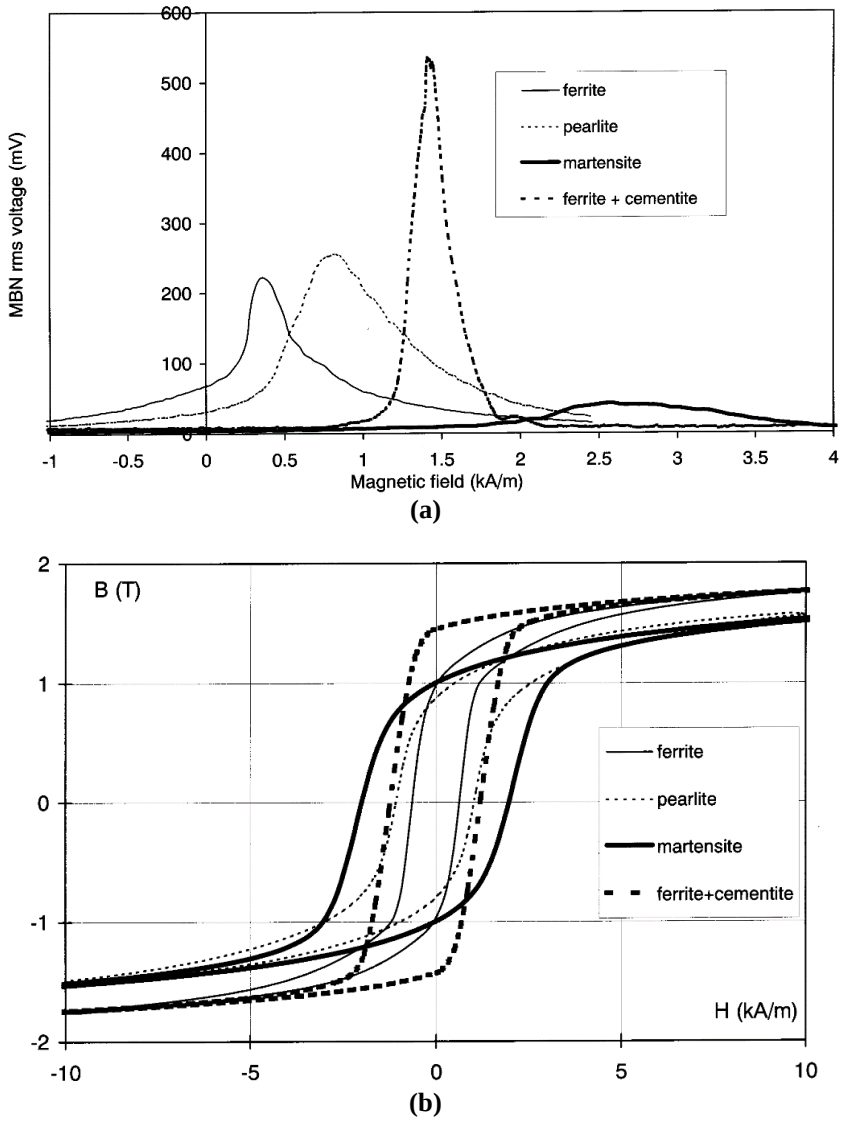

Figure 25: (a) MBN curves and (b) hysteresis cycles of ferrite (0.10 wt. % C), pearlite (0.80 wt. % C), martensite and sorbite (0.55 wt. % C) microstructures [65]

These results may be explained by the different mechanisms of interactions of magnetic domains within the crystal structure and lattice defects (e.g., grain boundaries, precipitates, and dislocations) of ferromagnetic materials. Thompson and Tanner [59] evaluated the effect of pearlite content on the magnetic and mechanical hardness of carbon steels. Domain wall displacements directly observed using Lorentz electron microscopy have been revealed to depend on the domain wall orientation with respect to the Fe_3C lamellae. Clapham et al. [66] reported that pearlite content has a significant influence on MBN outputs. In both studies, the magnetic responses were interpreted with respect to the domain wall pinning behavior in carbon steels, which

may be strongly pinned at Fe_3C lamellae. Batista et al. [74-76] studied the domain structure behavior in spheroidite structures, with globular cementite in a ferrite matrix, using hysteresis and MBN measurements. Also, MFM analysis combined with the EBSD technique was employed to determine the magnetic and crystallographic structures of carbon steels. The interactions between cementite precipitates and domain wall under an external magnetic field were investigated, as shown in Figure 26. It was observed that domain walls were anchored at Fe_3C precipitates during magnetization processes. At low magnetic fields, domain walls were observed to bend between two cementite particles before overcoming the pinning sites at higher fields, which generates a Barkhausen jump.

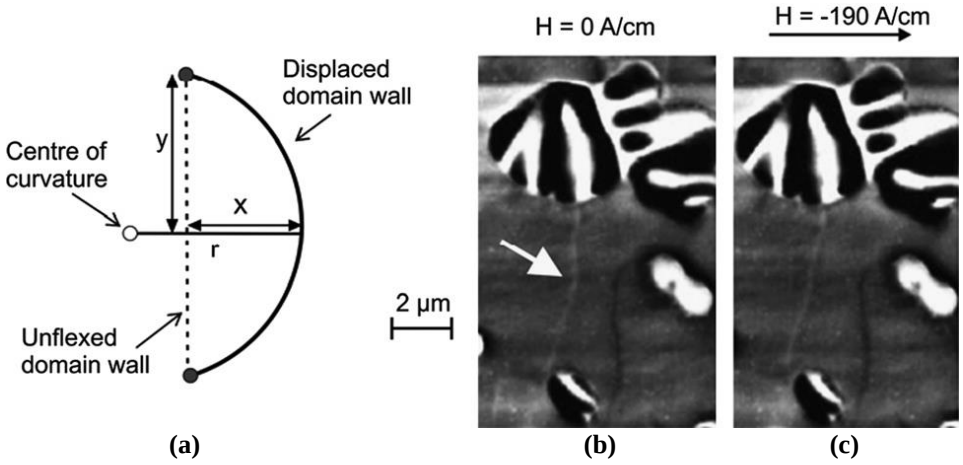

Figure 26: (a) Bending of a magnetic domain wall between two pinning sites; MFM images of domain walls in a hypereutectoid 1.5 %wt. C steel at (b) the remanence state, and (c) with an applied field of 190 A.cm^{-1} to the right [74]

Besides, Batista et al. [76] found that cementite has its own domain structure, whose configuration was observed to be influenced by their size, shape, and crystallographic orientation. These studies have shown that the magnetic domain structure of pearlitic steels is complicated to assess due to its complex lamellar microstructure. The interactions between the micromagnetic and the crystalline microstructures of such materials are still not wholly discerned, and only a few investigations proposed a more in-depth approach to this subject by nano- and microscopic evaluations.

The eddy current testing is a reliable inspection method based on the interaction between a coil sensor and the test material, which creates time-varying magnetic field that induces eddy currents in the piece. It utilizes the intrinsic electromagnetic properties of conductive materials for detection of surface and near-surface defects and

non-destructive evaluation of other variations in its characteristics by the analysis of the impedance changes in the inspection coil. Besides impedance signals (i.e., resistance, inductive reactance, phase angle), eddy current outputs can also be represented by coil's inductance or voltage signals. ECT allows automatic inspection and high-speed testing of up to 150 $m.s^{-1}$ under operating conditions. Any direct physical contact between the sensor and the inspected part is necessary for inspection. However, careful interpretation of signals is needed to distinguish between relevant and non-relevant responses. [53,56]

Some papers have reported impressive advances in monitoring austenite-ferrite phase transformation [77-79] and detecting the decarburization layer [80-82] during steel processing. Based on the differences in magnetic permeability between the surface ferrite and bulk pearlite, Hao et al. [81-82] showed that decarburization in steel rod samples can be measured using an electromagnetic sensor by experiments and modelling. As observed in Figure 27, the inductance values of the sensor at different test frequencies varied as a function of the decarburization depth. In order to optimize signal output, an appropriate frequency needs to be chosen in a way that the skin depth at the testing frequency is larger than the decarburization depth.

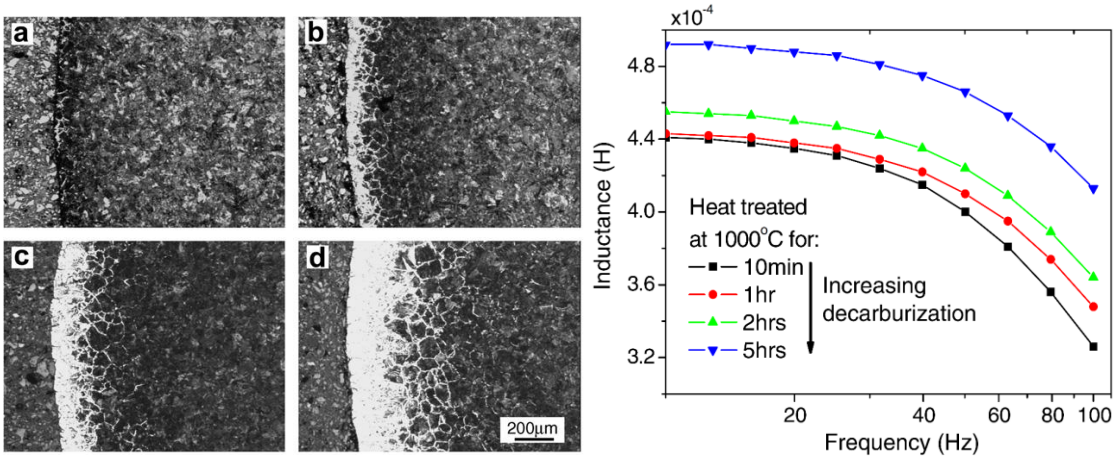

Figure 27: SEM micrographs of microstructures of Fe–0.8 wt.% C steel after decarburizing at 1000°C for (a) 10 min, (b) 1 h, (c) 2 h and (d) 5 h (left); and the respective measured inductance changes with frequency (right) [81]

ECT methods have also been used for assessing microstructural parameters, such as grain size [83,84] and phase fraction [84-86] of materials such carbon steels, dual phase steels and cast irons. Balamurugan et al. [87] demonstrated good correlations between inductance values and pearlite interlamellar spacing after patenting treatment of tire bead wires, as shown in Figure 28.

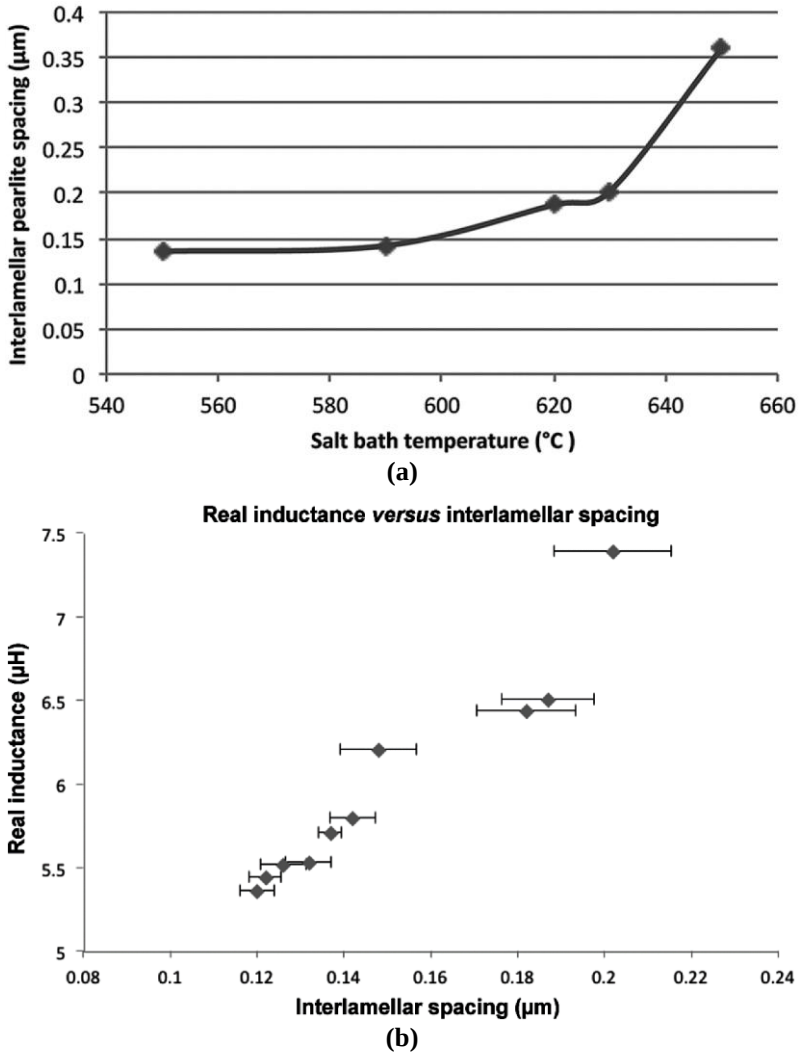

Figure 28: (a) Variations in the pearlite interlamellar spacing of tire bead wires after patenting at different salt bath treating temperatures, and (b) its respective correlation with inductance values obtained by ECT at low frequencies [87]

Mansoor and Ejaz [88] investigated the microstructural degradation of steels by the coarsening and spheroidizing of pearlite through eddy current measurements. It was observed that the eddy current phase angle has a linear relation with pearlite variations, from coarse lamellar carbides to uniformly dispersed spherical carbides in ferrite matrix, as shown in Figure 29. The degree of spheroidization of steels was also studied by Davut and Gür [89] by MBN method. MBN signals were found to be very sensitive to the degree of spheroidization of carbon steels, which, as a function of temperature and time, causes changes in the morphology and size of cementite. These results were attributed to the less effective pinning of domain walls by spherical cementite precipitates, and indicate the capability of such techniques for the characterization of the spheroidized steel components.

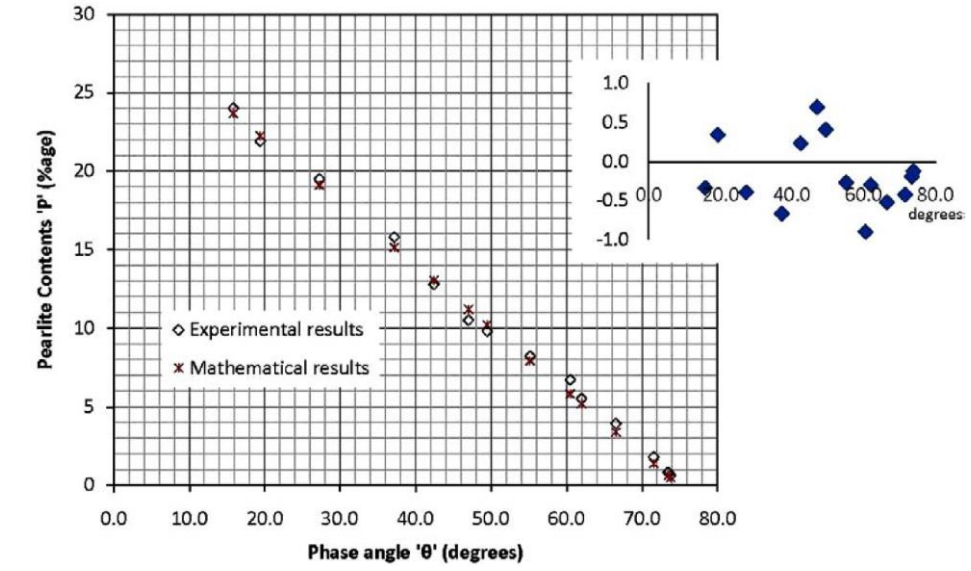

(a)

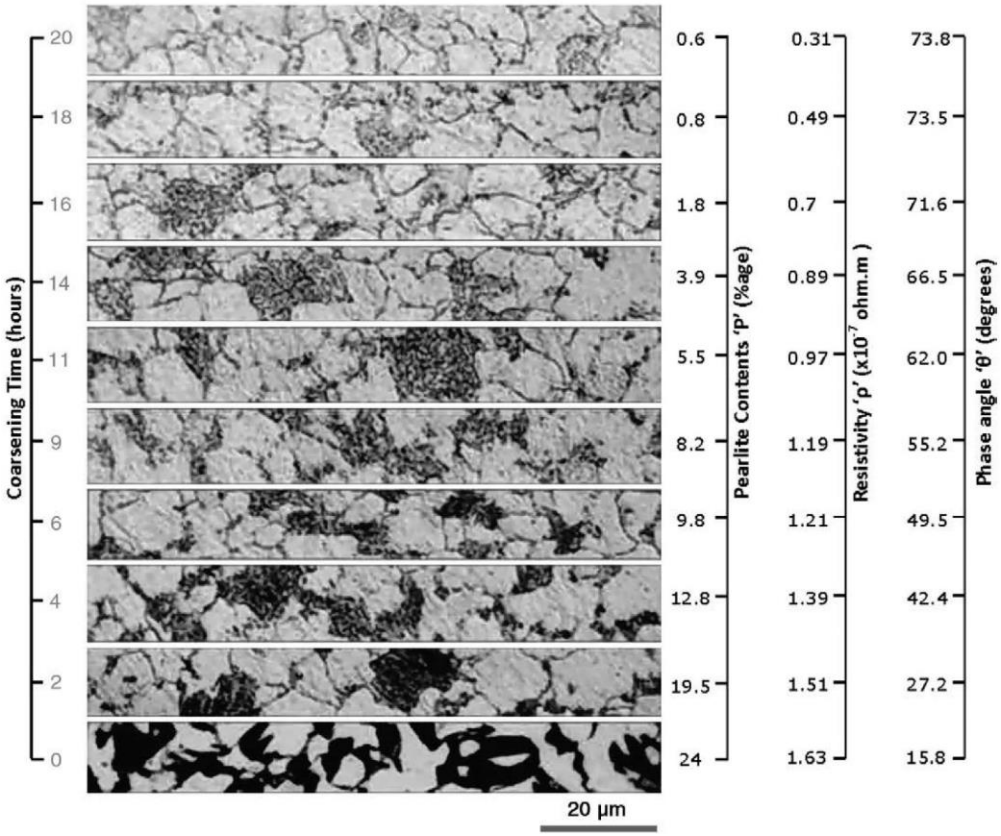

(b)

Figure 29: (a) Experimental and mathematical correlations between eddy current phase angle and pearlite fraction; (b) optical micrographs of the ferrite-pearlite samples showing the gradual coarsening of pearlite and the respective variations in pearlite content, resistivity and phase angle [88]

Also, the effect of applied stress and the mechanical characteristics of steels after thermomechanical treatments have been investigated [80,90-94]. Konoplyuk et al. [91] correlated the mechanical properties, including tensile strength, elongation,

and hardness, to the electromagnetic sensor outputs values of cast irons with changing ferrite-pearlite fractions. Ghanei et al. [94] published comparative experimental results on dual-phase steels with different ferrite-martensite phase balance, as shown in Figure 30. Normalized impedance was determined by dividing the impedance Z by the impedance of the empty coil Z_0, in order to disregard the effects of the electromagnetic sensor itself. Both studies have shown that the eddy current responses decreased with hardness, tensile, and yield strength and increased with elongation, demonstrating the sensitivity of ECT for predicting the mechanical properties of steels.

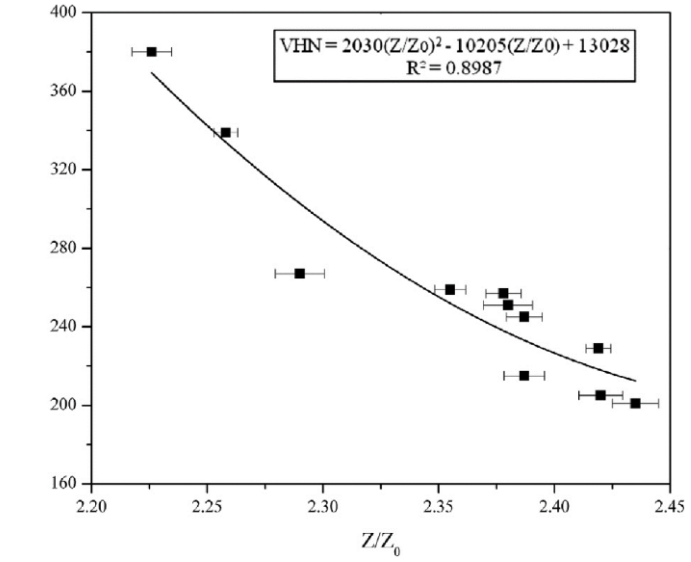

(a)

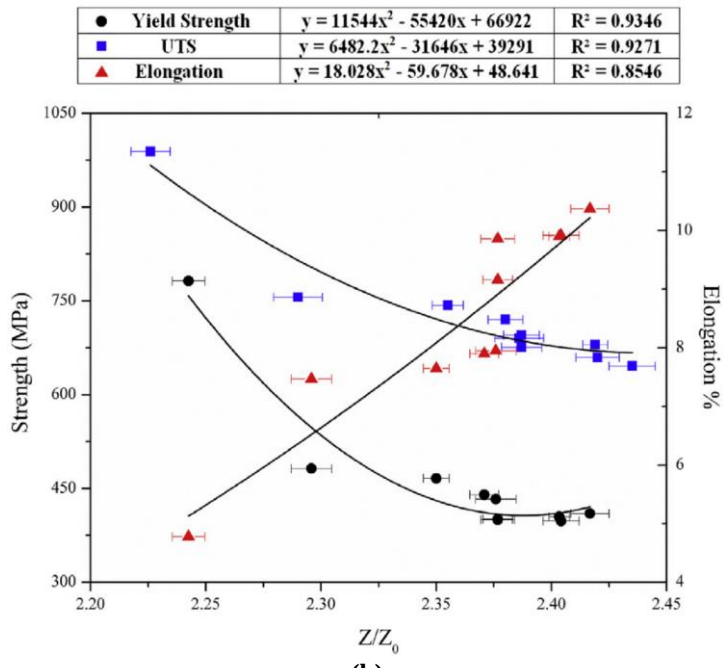

(b)

Figure 30: Relations between the (a) Vickers hardness and (b) tensile properties of heat-treated dual-phase steels with normalized impedance measured by ECT [94]

Despite the several works have demonstrated the accurate capability of electromagnetic NDT for the characterization of ferromagnetic materials such as steels and alloys, the fundamental evidence that allows relating microstructural variations of the studied materials to their electrical and magnetic properties, indirectly measured by these methods, is rarely mentioned. The studies found in this context are very scarce, in particular concerning ECT, and the interactions between microstructural parameters and electromagnetic properties is not yet fully understood.

The phenomenological understanding of electromagnetism and the relation to the microstructural aspects of steels is, therefore, necessary to extend the potential applications of non-destructive techniques. For this purpose, the second part of this chapter addresses an extensive study in this area.

II. INTRODUCTION TO ELECTROMAGNETISM

Electromagnetic techniques are widely used in non-destructive inspection to detect the presence of damage mechanisms, such as cracking or corrosion. Recent advances in microelectronics and sensing technology, mathematical modeling, signal, and image processing have considerably enhanced its capabilities, improving its use as an industrial tool for microstructural evaluations. Therefore, the second part of this chapter constitutes the first approach to electromagnetism in this manuscript, introducing general notions about electricity and magnetism, its origins, and fundamental concepts to understand and evaluate the sensitivity of these phenomena to microstructure characteristics ferromagnetic materials. Finally, relevant works from the literature exploring materials evaluation using electromagnetic NDT methods, including eddy current testing, are reviewed. It gives an overview of the main findings in this field, indicating aspects not very well explored in the literature for establishing the experimental program of the present research.

II.1. Principles of electricity

Electricity is a branch of physics involving the study of phenomena associated with electrical charges, which is divided into three main fields: the electrostatics that is the study of stationary electric charges; the electrodynamics that refers to electrical charges in motion; and electromagnetism, which studies the relationships between electrical and magnetic phenomena. The term electricity originates from the Greek *elektron* that refers to amber, a fossilized resin, due to its electrostatic attraction when rubbed with another material (Figure 31). Although considerable scientific advances have started from the 17th century, the electricity has been studied since antiquity.

Figure 31: The word electron means amber in Greek relative to the ability of this fossilized resin to bear a charge of static electricity [95]

II.1.1. Origin of electricity

All matter is constituted by atoms, which is the smallest constituent unit of the matter carrying the chemical properties of an element. Each atom is composed of protons and neutrons in the nucleus of respectively positive and neutral charges surrounded by negatively charged particles, called electrons. The electrons are in motion, rotating on their axes and orbiting the nucleus of the atom.

The electronic configuration describes the arrangement of electrons in energy levels around an atomic nucleus, whose distribution is subdivided into shells, sub-shells, and a set of orbitals. An atomic orbital is a particular spatial distribution of an electron in an atom. In other words, it can be understood as mathematically derived functions describing volumes of space in which there is a high probability of finding an electron within an atom. It is characterized by four quantum numbers describing the unique quantum state of an electron, and thus the energy states available to the atom. The principal quantum number n indicates the average relative distance of an electron from the nucleus, defining the size of the orbital and its general value of electronic energy. It is a set of positive integers n=1, 2, 3… to infinity, called K shell, L shell, M shell, and so it goes. The azimuthal quantum number ℓ determines its orbital angular momentum and describes the orbital shape. It may have integers ranging from 0 to n-1, corresponding to the s, p, d, f,…, n-1 subshells. The magnetic quantum number m_ℓ differentiates each one of the orbitals within a subshell, specifying its orientation in space. The number m_ℓ can take on integral values between $-\ell$ and $+\ell$. Electrons have a magnetic moment associated with the orbital angular momentum and an intrinsic angular momentum, called the electron spin. The fourth quantum number m_s is related to the direction of the intrinsic electron spinning, called the spin quantum number, which may have two values of +½ or -½. [96,97] The magnetic and spin quantum numbers are discussed in more detail in section II.2.

Each atomic state can then be identified by a set of four quantum numbers: n, ℓ, m_ℓ, m_s. According to the Pauli Exclusion Principle, each state can be occupied by no more than one electron. That is, no two electrons can have the same four quantum numbers. For a given atom, the electrons with the same energy level, shape, and orientation share the same orbital. Each orbital can be occupied by a maximum of two electrons of an opposite spin quantum number, each subshell comprises the electrons with the same values of both n and ℓ quantum numbers but differently oriented in space, while a shell contains all the electrons having the n same value. Electrons fill

the primary energy levels of lower energy to minimize the overall energy of the atom, as shown in Figure 32-a. For a given n value, ns orbitals always have lower energy than np orbitals, which are lower than the nd orbitals, and so forth. The different atomic orbital shapes are illustrated in Figure 32-b. The lobes indicate the regions of high electron density within an atom.

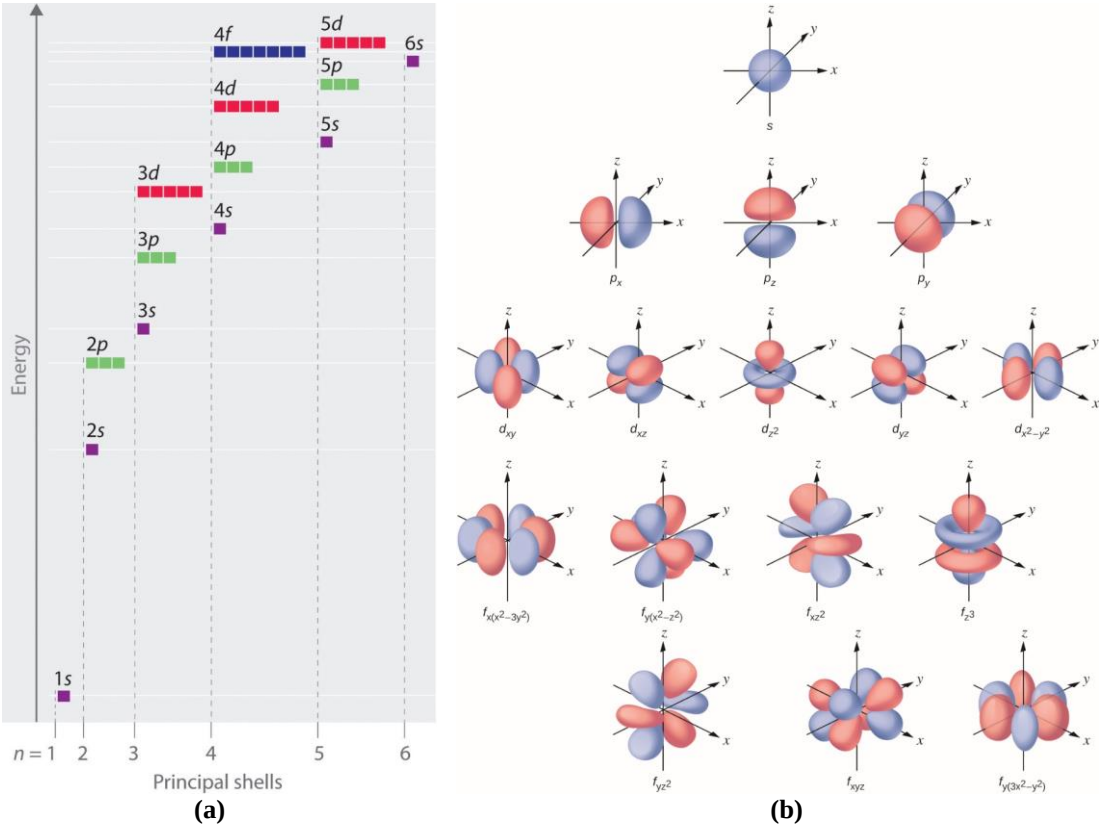

Figure 32: (a) Energy level diagram of an atom [73]; (b) orbital shapes characteristic of s, p, d, and f orbitals [98]

II.1.2. Electron energies in solids

As two or more atoms are bonded together into a molecule, the atomic orbitals occupied by electrons of each single atom overlap and, following the Pauli Exclusion Principle, each atomic energy level must split into multiple molecular levels to accommodate all the electrons that formerly were in similar isolated atomic orbitals. Thus, the electrons gradually change states, occupying new molecular orbitals of different energy. As the number of orbitals becomes excessively large, the difference between adjacent energy levels becomes minimal, forming continuous bands of energy states. Band gaps are regions where no electronic states can exist. The degree of overlap of electrons in similar states becomes more significant as higher their distance is from the nucleus. As a result, the outer states have progressively larger bands at

higher energies and narrower band gaps in between them. The core electrons occupy the inner states. The outer states are occupied by valence electrons, which participate in chemical bonding and electrical conductivity. [11,96]

A solid material consists of a massive number of atoms that, in its turn, are arranged in orderly repetitive patterns to form a crystalline structure. A similar electronic configuration can be found in a solid composed of N atoms and, thus, each atomic state splits into N discrete states, each of which may be occupied by pairs of electrons of opposite spins. The formation of energy bands in solid materials is illustrated in Figure 33. The bands are filled from the lowest energy states, and then successively higher states until all the electrons have been accommodated. The highest energy band filled with electrons is called the valence band, and the next available one is the conduction band. At 0 K, the energy corresponding to the highest filled state is called the Fermi energy E_f. In other words, all the available states in the material up to a certain energy level are filled by two electrons of opposite spin at absolute zero. [96,99] As temperature increases, electrons are more likely to be found in the higher energy states. The highest energy band filled with electrons is called the valence band, and the next available one is the conduction band. Only the electrons in that overcome the Fermi level are free to move and participate in the electrical conduction within the solid when an electromotive force is applied to it.

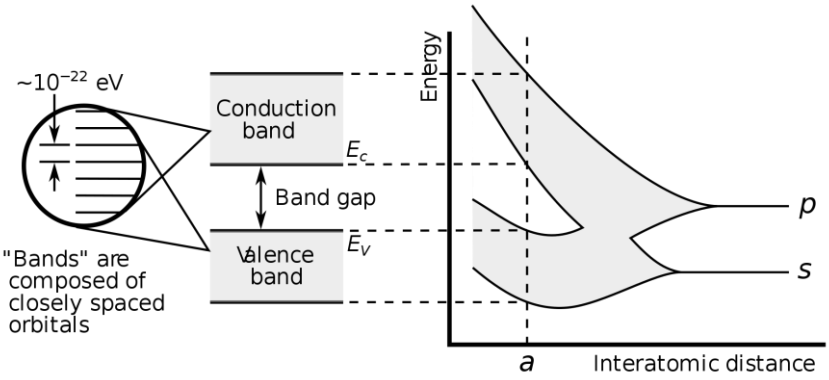

Figure 33: Formation of energy bands in a solid crystalline material [100]

In conductor materials such as metals, the valence band is generally partially filled and overlaps or is very close to the conduction band adjacent to the highest filled state at E_f. Thus, very little energy is required for the valence electrons to occupy the conduction band and becomes conductive. In its turn, insulators and semiconductors have the valence bands filled, and they are separated from the conductive bands by larges band gaps. Fermi levels are located in the band gaps, and higher energies are

then required for the electrons to jump up to the conduction band, approximately equal to the band gap energies. Insulators are non-conductive materials. In semiconductors, however, at relatively high temperatures, some electrons may gain enough thermal energy to overcome the energy gap and reach the conduction band. It creates few empty states in the valence band that allows more electrons to be excited, contributing the overall material's conductivity. The number of electrons of valence in the outermost shell of an atom and the Fermi level and band gaps is crucial factors in determining physical properties. The electrical conductivity of materials is a consequence of their electronic band structure, as represented in Figure 34.

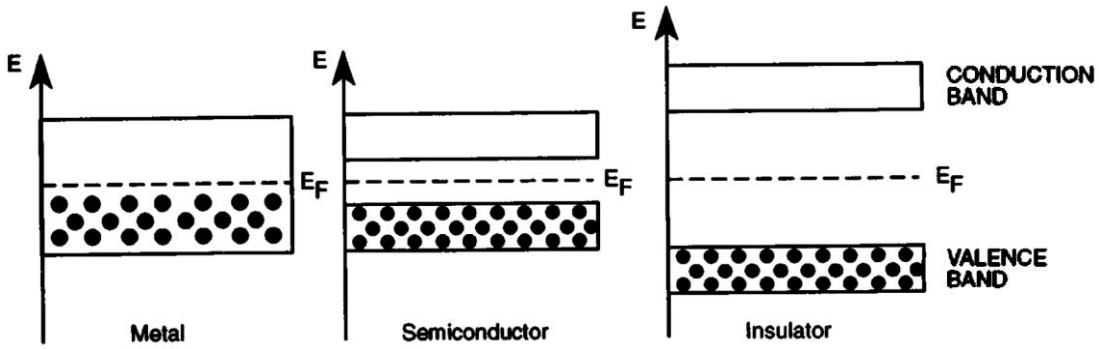

Figure 34: Electronic band structures of a conductor, semiconductor, and insulator [99]

II.1.3. Electrical conductivity

As hitherto designated, in response to an external applied electric field, the Fermi-level electrons, or free electrons, are accelerated and may move through the crystal. The motion of free electrons generates a flow of electrical charges called electric current. Ohm's law relates the current to the applied voltage, as follows:

$$V = IR \tag{9}$$

where V is the voltage in volts (V), I the current in amperes (A), and R is the resistance of the conductor material in ohms (Ω) in the International System of Units (SI). Although the electrons in a conductor can flow freely, there is always a certain opposition to the current that flows through it. The resistance is considered independent of the current, depending only on the specimen geometry and the material's resistivity at a given temperature, as expressed below:

$$R = \rho \frac{l}{A} \tag{10}$$

where A is the cross-sectional area and l the length of the specimen, and ρ the electrical resistivity in ohm-meter (Ω·m). Resistivity is an intrinsic property that can be understood as the ability of a material to oppose the electric current, which depends on

the purity and the number of lattice defects, besides the temperature. It is reciprocal to the conductivity:

$$\sigma = \frac{1}{\rho} \tag{11}$$

where σ is the conductivity in Siemens per meter ($S.m^{-1}$), defined as the measure of how well a material can transmit an electric current.

II.2. Principles of magnetism

Magnetism is a set of physical phenomena related to the attraction and repulsion force exerted by material upon another, particularly strong in magnets and ferromagnetic and conductive materials such as steels. The term magnetism originates from ancient Greece, in Magnesia, where a naturally magnetized form of the iron ore magnetite Fe_3O_4, called lodestone, was observed to attract small pieces of iron (Figure 35). Since then, several scientific works have collaborated with the advance of the theories of magnetism. Nowadays, many applications rely on magnetic properties and magnetic materials, including transformers, power generators, electric motors, optoelectronic components, and telecommunication devices.

Figure 35: Lodestone is a natural magnet mineral first observed in the city of Magnesia, in Greece, from which derives the terms magnet and magnetism [101,102]

II.2.1. Origin of magnetism

The macroscopic magnetic properties of materials result from the magnetic and intrinsic spin moments of electrons associated with m_ℓ and m_s quantum numbers. Each electron has magnetic dipole moments that originate from its total angular momentum, resulted from the orbital angular momentum of the electron's orbital movement around the atomic nucleus and from the intrinsic angular momentum of the electron spinning around its axes [97], as shown in Figure 36. The influence of electric current in magnetic properties is further discussed in section II.3.

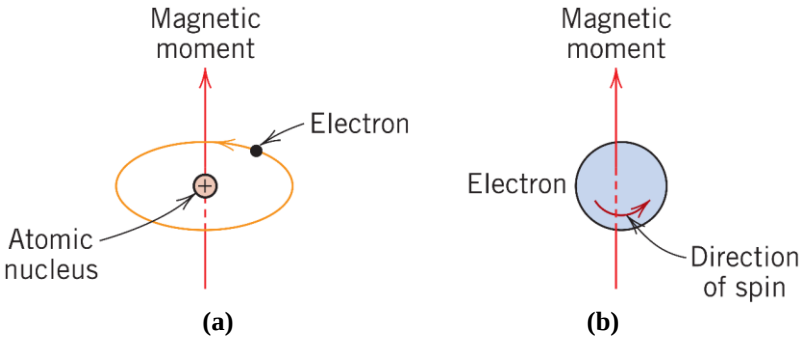

Figure 36: Magnetic dipole moment associated with (a) an orbiting electron around the atomic nucleus, and (b) a spinning electron [11]

The net magnetic moment for an atom is the sum of the contributions of each of its electrons, also considering the spin and orbital moment cancellation of electron pairs. Thus, each atom behaves like a magnetic dipole. At the crystal level, the sum of all elementary magnetic moments composes the magnetization of the material ($\vec{M}$). Magnetization expresses the density of permanent or induced magnetic dipole moments in a magnetic material, then:

$$\vec{M} = \frac{\vec{m}}{V} \tag{12}$$

where $\vec{m}$ is the vector sum of all magnetic moments in a unit volume V of a solid. The unit for $\vec{M}$ is in ampere per meter ($A.m^{-1}$). It depends not only on the intensity of each elementary magnetic moment but also on its orientation.

II.2.2. Magnetism at the macroscopic scale

From a macroscopic point of view, the magnetic behavior of a material is defined according to the type of magnetic response to the application of an external magnetic field, also called magnetic field strength $\vec{H}$, generated by an electrical current. The material's response is given by the magnetic induction or magnetic flux density $\vec{B}$, which represents the magnitude of the internal field strength within a material that is subjected to a field $\vec{H}$. The magnetic field and the induction are related according to:

$$\vec{B} = \mu\vec{H} \tag{13}$$

where μ is a physical property of a material called magnetic permeability. Permeability is the measure of a material's ability to be magnetized, that is, its ability to support the formation of a magnetic field within itself. In SI units, $\vec{H}$ is in $A.m^{-1}$. The unit for $\vec{B}$ is the tesla (T) or weber per square meter ($Wb.\ m^{-2}$), and μ is measured in henry per meter ($H.m^{-1}$).

In free space, a magnetic field $\vec{H}$ gives rise to a magnetic induction $\vec{B}$ through the equation:

$$\vec{B} = \mu_0 \vec{H} \tag{14}$$

where the constant μ_0 is the permeability in a vacuum and its value is $\mu_0 = 4\pi \times 10^{-7} H.m^{-1}$. The relative permeability μ_r of a medium is given by the ratio of the permeability in material and a vacuum, as follows:

$$\mu_r = \frac{\mu}{\mu_0} \tag{15}$$

Then,

$$\vec{B} = \mu \vec{H} = \mu_0 \mu_r \vec{H} \tag{16}$$

The magnetic induction also consists of a contribution from the magnetization of the material $\vec{M}$. As mentioned previously, the magnetization is generated by the resultant orbital angular and spin magnetic moments of electrons in an atom. In the presence of a field $\vec{H}$ the magnetic moments tend to align themselves with this field, reinforcing it through their magnetic fields. Hence, the magnetic induction is defined by the expression:

$$\vec{B} = \mu_0 \left(\vec{H} + \vec{M}\right) \tag{17}$$

The magnetic susceptibility $\chi_m$of a material expresses the faculty of a material to be magnetized under the action of magnetic excitation. Magnetic susceptibility is dimensionless and can be defined by the ratio of its magnetization and a magnetic excitation applied to it, or:

$$\chi_m = \frac{\vec{M}}{\vec{H}} = \mu_r - 1 \tag{18}$$

Therefore, the magnetic induction can also be described as a function of χ_m:

$$\vec{B} = \mu_0 (1 + \chi_m) \vec{H} \tag{19}$$

Materials may be classified as magnetic or non-magnetic. Among the magnetic materials, there are different types of magnetism classified according to their magnetic susceptibility: diamagnetism, paramagnetism, and ferromagnetism. Diamagnetic materials have all paired electrons in atomic orbitals, so there is no permanent net magnetic moment, presenting weak negative susceptibility. Paramagnetic materials have a small positive susceptibility due to the presence of some unpaired electrons in the atoms. It may have their magnetic moments aligned under the influence of an external magnetic field. However, when the external field is removed, the magnetic moments become again randomly orientated, and the material does not conserve any

magnetic behavior. In its turn, ferromagnetic materials have a significant positive susceptibility. Its magnetic moments spontaneously align with moments of adjacent atoms over relatively large volume regions of the crystal, called magnetic domains. Each of these domains containing elementary atomic moments presents random magnetization vectors within the crystal, resulting in a null global magnetization at the demagnetized state. [96,103] When a magnetizing force is applied, the magnetic domains with orientation close to the field tend to grow at the expense of others, aligning in the same direction of the external field, as observed in Figure 37. The organization inside matter in magnetic domains and domain walls constitutes the micromagnetic structure.

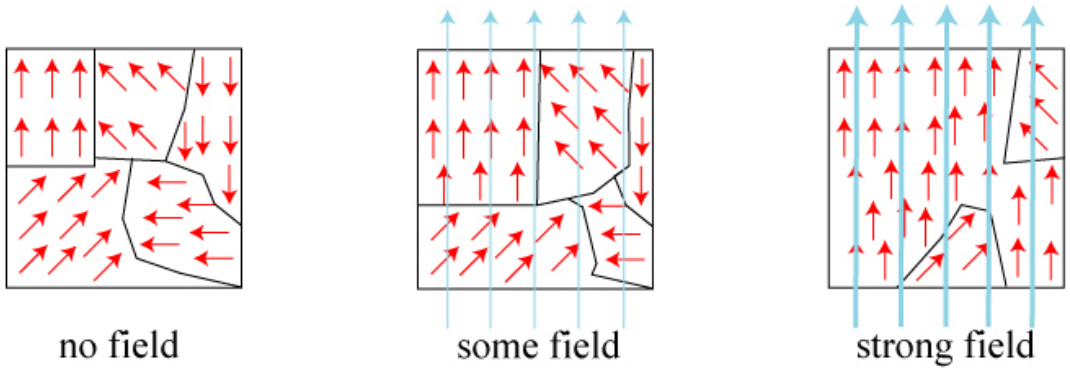

Figure 37: Magnetic domain structures of ferromagnetic materials: (a) randomly orientated domains in an unmagnetized state, (b) and (c) alignment of domains under an external field [104]

It is customary to plot the magnetization or the flux density of a material as a function of the applied magnetic field that drives the magnetization, as shown in Figure 38. For increasing levels of field strength, $\vec{B}$ follows the initial magnetization curve that increases rapidly due to the alignment of magnet domains within the material. The relative permeability is not a constant but a function of the magnetic field strength and can be determined from the initial magnetization curve. The initial relative permeability describes the permeability at shallow excitation levels, whereas the maximum relative permeability is the point where the B–H curve slope is the greatest. When the increase of $\vec{H}$ entails a very little increase in $\vec{B}$, the flux density reaches its limit and the magnetic saturation state S is attained.

From the saturation, the $\vec{H}$ field is reduced by field removal or reversal of field direction. The magnetization curve does not retrace its original path. This phenomenon

is known as magnetic hysteresis and refers to the irreversibility of both magnetization and demagnetization processes. At zero field strength ($\vec{H}$=0), the induced magnetic field that remains in the material is called remanence or retentivity B_r. The coercivity or coercive force H_c is defined as the magnetic field required to remove the residual magnetization, that is, $\vec{B}$=0. Ferromagnetic materials are usually distinguished as hard or soft, depending on the magnitude of their coercivity. A second reversal of the field to the point of the initial saturation completes the hysteresis loop. The energy losses correspond to the total area enclosed by the hysteresis loop.

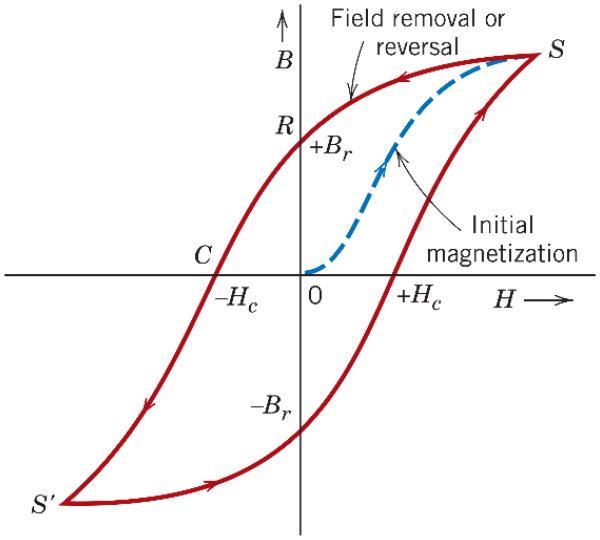

Figure 38: Typical hysteresis cycle for a ferromagnetic material [11]

Together with magnetic permeability, remanence and coercivity are properties that characterize the magnetic behavior of materials. Besides temperature, the magnetic characteristics depend on several factors that may hinder the movement of domain walls within the material, including the crystal lattice structure, preferred crystallography orientation, presence of lattice imperfections, and stress state [103].

II.3. Electromagnetism

Although electricity and magnetism are two distinct subjects, there is a strong connection between these physical phenomena. This interaction was first discovered by Oersted in 1820, who noticed that an electric current passing through a conductor caused a magnetic field to develop concentrically around it as if it were a magnet (Figure 39). In 1831, Faraday demonstrated that the variation in magnetic flux also generated electric current, a phenomenon known as Faraday's Law of induction. Finally, in 1873, the electromagnetic phenomena were described by a set of differential

equations formulated by Maxwell, a considerable contribution to modern physics. [53] Nowadays, several indispensable devices, in everyday life until research applications, exist due to the significant advances in the comprehension of electromagnetism, including magnetic cards, household appliances, telecommunication equipment and networks, induction heating, motors, generators, sensor, and actuator devices, advanced medical equipment, among many others.

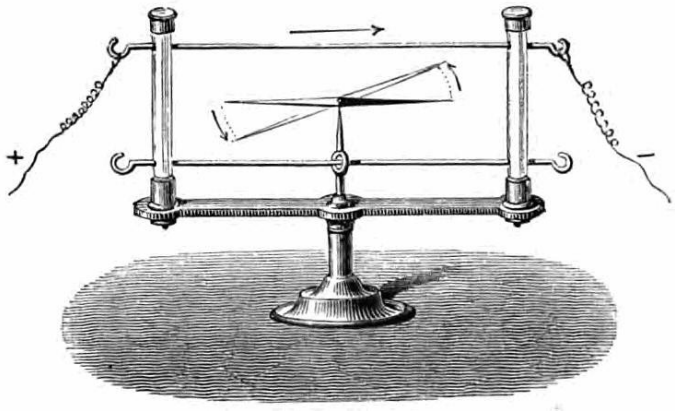

Figure 39: Oersted's experiment performed in 1820 demonstrated that electric currents create magnetic fields [105]

II.3.1. Electromagnetic induction

Consider a closed conducting loop placed in the magnetic field $\vec{B}$ assumed to be uniform, as shown in Figure 40. The magnetic flux Φ_B crosses its surface, as follows:

$$\Phi_B = \vec{B}\vec{A} = BA\cos\theta \qquad (20)$$

where $\vec{A}$ is the area vector given by $\vec{A} = A\hat{n}$, A is the surface area, and $\hat{n}$ the normal to the surface, θ indicates the angle between $\vec{B}$ and $\hat{n}$. The unit of Φ_B is Wb or T.m^2.

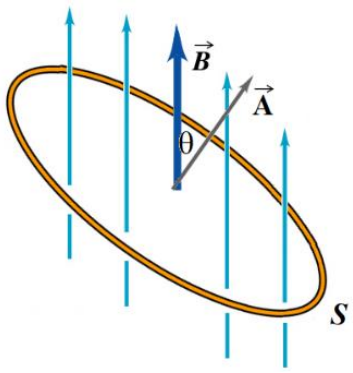

Figure 40: Magnetic flux through a surface [106]

The variation in the magnetic flux can occur due to changes in the magnetic environment in several ways, such as by changing the magnetic field strength with

time, by moving the conductor while it is exposed to a static magnetic field, or by moving the magnet. When a flow variation occurs, an electromotive force is induced around the loop. If the circuit is closed, an electric current circulates through it, named induced current. This phenomenon is called electromagnetic induction. Similarly, this resulting induced current generates, in its turn, an induced magnetic field into the conductor that opposes the change of magnetic field, as illustrated in Figure 41.

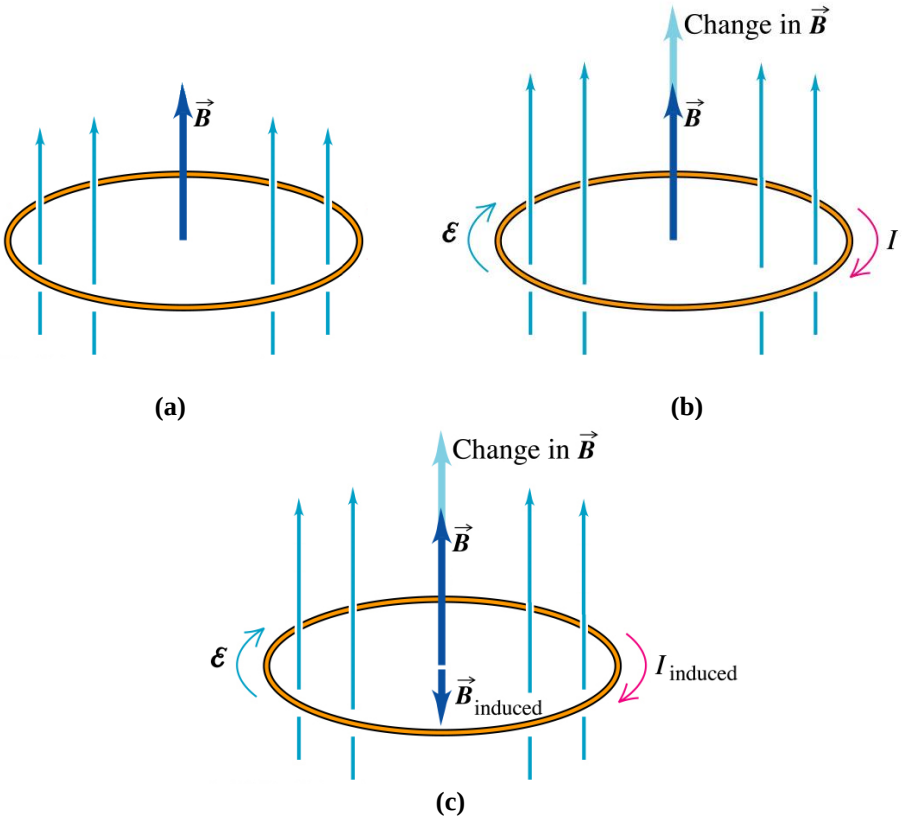

Figure 41: (a) A closed conducting loop placed perpendicular to a magnetic field, (b) generates an induced current to flow through it, (c) in such a direction to create a magnetic field opposing the variation in the magnetic flux [106]

According to Faraday's law, the electromotive force induced in the circuit is defined as the negative rate of change of the magnetic flux through the surface area, mathematically established by Neumann as follows:

$$\varepsilon = -\frac{d\phi_B}{dt} \tag{21}$$

where ε is the induced electromotive force in volts and t the time interval. The negative sign of the formula refers to the electromotive force polarity and, thus, to the generated current direction. In complement to Faraday-Neumann's law, Lenz's law defines the direction of the induced current is such that the magnetic field produced by it opposes the magnetic flux variation.

II.3.2. Eddy current testing

Discovered by Foucault in 1851, the eddy currents phenomenon is derived from the electromagnetic induction. Nonetheless, ECT was first performed for non-destructive tests by Hughes in 1879. Since then, it is one of the widely used electromagnetic methods for the detection of damaged zones, cracks, and discontinuities of a variety of industrial products, such as wires, bars, tubes, or profiles during fabrication and processing [53,107].

The elements of the eddy current system include power supplies, coil circuits, processing and recording devices. The alternating current generators can operate at a single fixed frequency or multiple frequencies simultaneously. There are many types of electromagnetic sensors for eddy current inspection such as surface coil probes for monitoring material surfaces, internal coils for in-service inspection of pipes and tubes, and encircling coil probes employed for the testing of cylindrically shaped parts such as rods, wires, and bars, as shown in Figure 42. The operation mode determines how the instrument interfaces with the test material, which can be by absolute or differential operations, or external reference coil configuration.

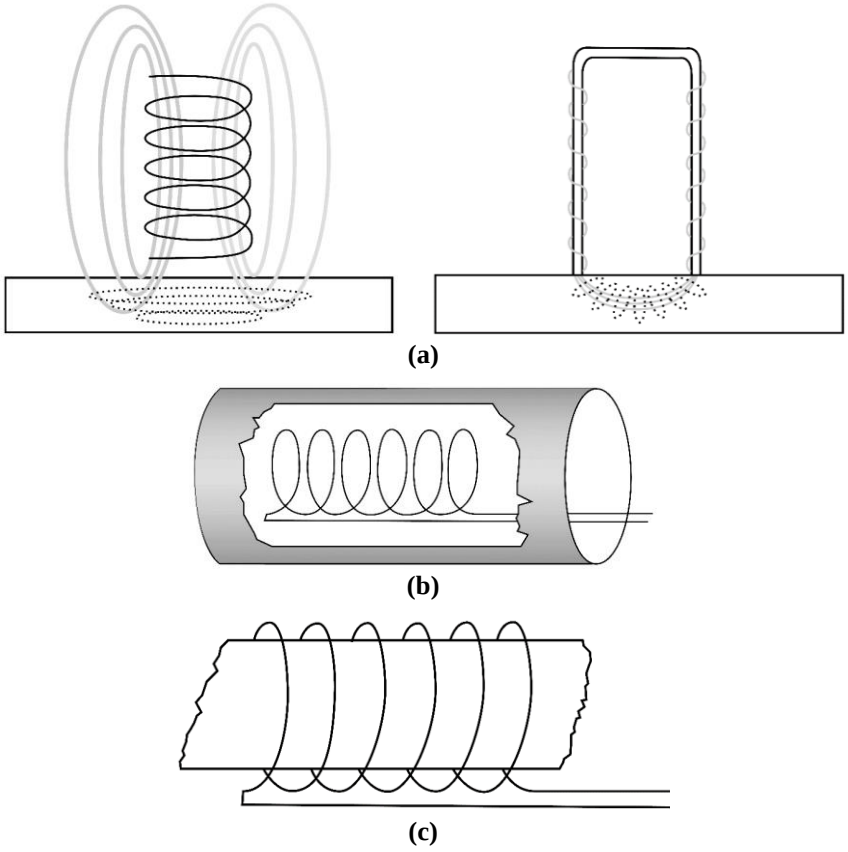

Figure 42: Schematic illustrations of various coil assemblies: (a) surface coils – bobbin-wound (left) and horseshoe probe (right), (b) internal coil, and (c) encircling coil [65]

As mentioned, the technique apparatus consists of an alternating current generator and a coil in a closed circuit. An alternating voltage is applied to the coil circuit, and thus, electrical current flows through it. The alternating current I causes an alternating magnetic field to develop around the coil in phase with the voltage V_R applied across the resistance of the coil and the primary current. Since the coil stands in the field of its varying magnetic flux, an electromotive force is induced into the circuit. It results in an additional voltage, the induced or back voltage V_L, which is 90° out of phase with the primary current and magnetic flux, as shown in Figure 43. This process is a particular form of electromagnetic induction known as self-induction.

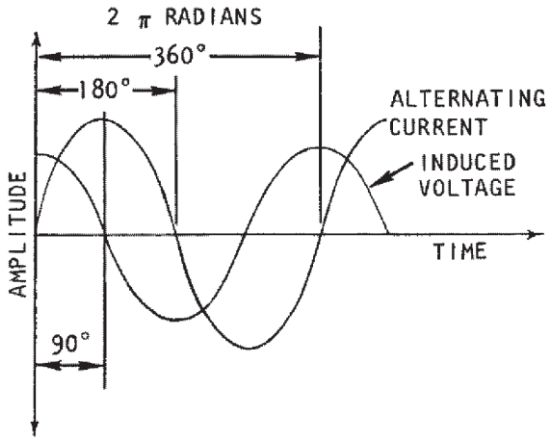

Figure 43: Sinusoidal variation of alternating current and induced voltage in a coil, out of phase by 90° with the current [108]

As stated by Faraday's law, the self-induced voltage in a coil circuit is proportional to the rate of the magnetic flux variation Φ and, thus, of the rate of current change. The coil geometry also influences the amplitude of the induced voltage V_L in the circuit, given by:

$$V_L = -N\frac{d\Phi}{dt} = L\frac{dI}{dt} \quad (22)$$

where N the number of turns in the coil and L the inductance of the coil. According to Lenz's law, the induced current flows through the coil in such a way to oppose the change in the primary alternating current that causes the magnetic flux to change. Therefore, the total voltage V_T in the coil circuit can be described as:

$$V_T = \sqrt{{V_R}^2 + V_L^2} \quad (23)$$

The coil impedance is characterized by a resistive component related to the current flow resistance, and an inductive term that indicates the opposition to the current flow variation, as expressed in the following equations:

$$Z = \frac{V_T}{I} = \sqrt{\left(\frac{V_R}{I}\right)^2 + \left(\frac{V_L}{I}\right)^2} = \sqrt{R^2 + X_L^2} \quad (24)$$

where the resistance R and the inductive reactance X_L represent, respectively, the real and the imaginary parts of the coil's impedance Z in ohms. The inductive reactance depends on the geometry of the coil and the test frequency, as described below:

$$X_L = 2\pi f L \quad (25)$$

$$L = \mu \frac{N^2 A}{l} = \mu_0 \mu_r \frac{N^2 A}{l} \quad (26)$$

where f is the test frequency in Hertz and L the inductance of the coil, which is defined by the relative permeability μ_r of the coil core (air core or ferromagnetic core) and the coil's turns, cross-sectional area, and length, respectively, N, A, and l.

The eddy current system can be represented as a typical resistor-inductor series circuit, or RL circuit, as demonstrated in Figure 44-a. The alternating current flows through both the resistance R and inductive reactance X_L of the circuit, influenced by both resistive voltage V_R and inductive voltage V_L, which constitute the total voltage V_T of the circuit. The impedance Z is the sum of the resistance and inductive reactance and represents the total opposition of the coil to the current flow. Since the inductive voltage is induced 90° out of phase with the current and the current is in phase with the resistive voltage, V_R and V_L have a phase difference of 90°. The two voltages combination results in a total voltage out of phase with the alternating current, but not by a full 90°, as it can be seen in Figure 44-b.

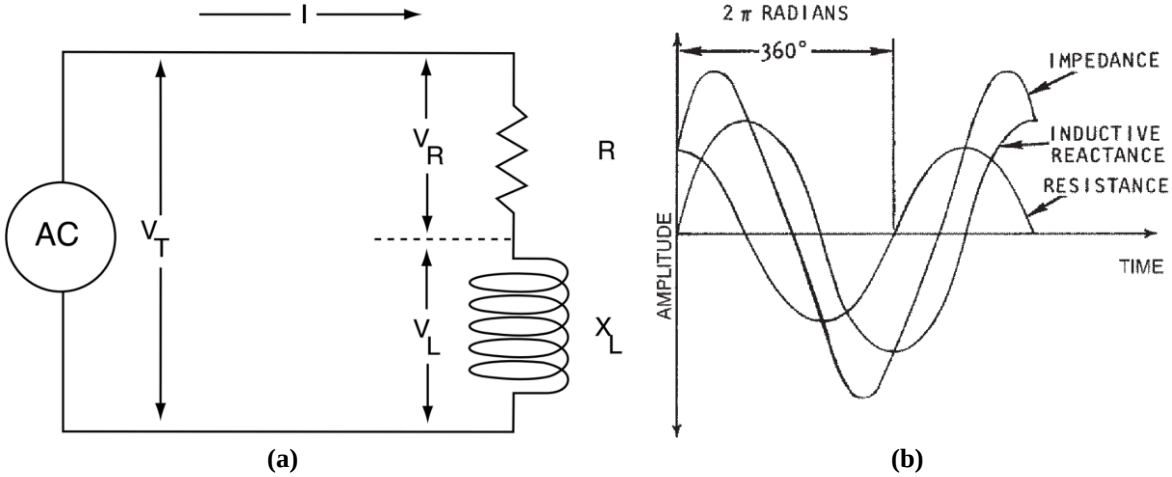

(a) **(b)**

Figure 44: Representation of (a) an RL circuit driven by alternating voltage [53]; and of (b) combining out-of-phase voltages [108]

If a conductive material is brought into the proximity to the primary alternating magnetic field, a voltage is induced, causing an electrical current to flow into it by

means of mutual induction. This induced current is named eddy current and flows in closed loops within the material. The orientation of the eddy current flow pattern is perpendicular to the axis of the magnetic field generated by the coil. Next, eddy currents cause a second alternating magnetic field to develop in the material. The secondary flux's polarity opposes that of the primary flux, as stated by Lenz's law. A change in the overall net magnetic flux results in a shift in the net magnetic flux variation rate, altering the coil's impedance. A schematic of the eddy current phenomena is illustrated in Figure 45.

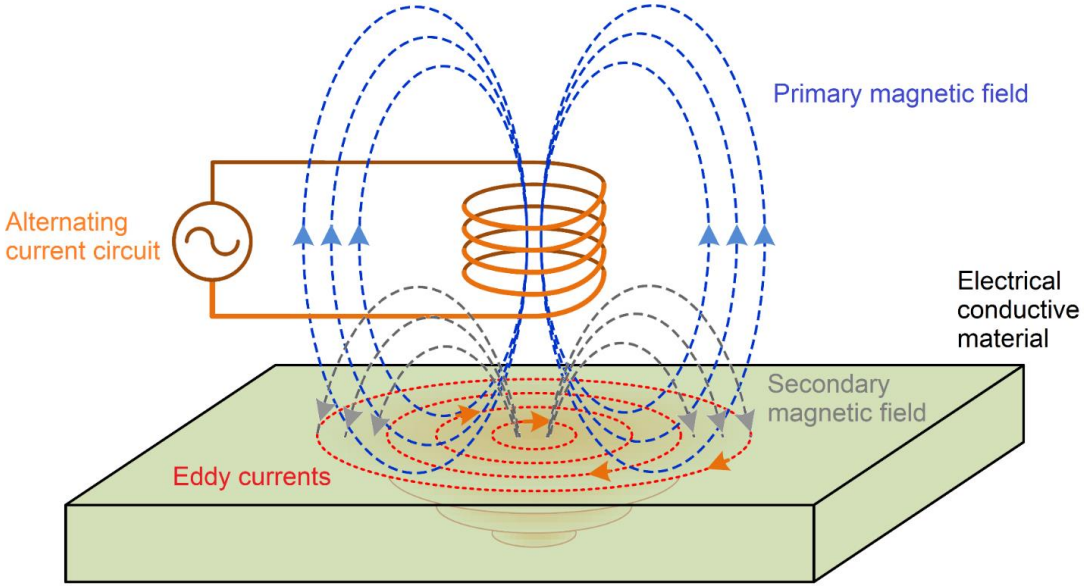

Figure 45: Eddy currents induced in a conductive material by an alternating current passing through a coil [109-adapted]

Information can be gathered about the test material by monitoring changes in the impedance of the excitation coil using a single coil arrangement or a separate measuring coil. The amplitude and phase of output signals amplified and converted are commonly displayed in the form of a complex impedance plane. Depending on the instrumentation, the signals can also be decomposed into its constituent frequencies and harmonic components by applying fast Fourier transformations. Although impedance plane is the convention for expressing eddy current outputs, inductance and voltage variations can be employed to characterize coil's impedance variations. In the latter case, the output information from eddy current testing is the total voltage magnitude, including resistive and inductive voltages, and the phase angle ϕ relative to the primary current. It can be simply displayed in voltage planes, as it can be seen on the plot representation in Figure 46.

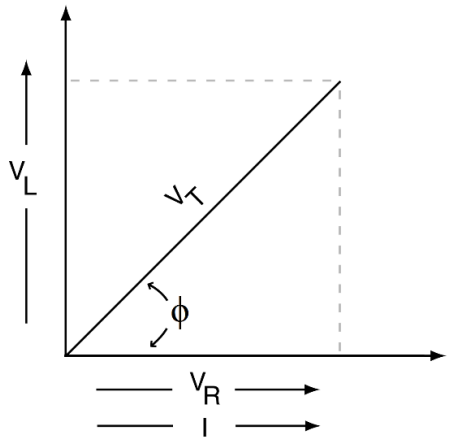

Figure 46: Eddy current voltage plane [53-adapted]

Eddy currents have particular flow characteristics. It flows in closed concentric loops within the material and their flow patterns are susceptible to material discontinuities and non-conducting boundaries, distorting itself to accommodate such interferences into their flow. As shown in Figure 47, the discontinuities are detected in proportion to the degree to which they disturb the flow pattern of eddy currents. The orientation of the coil to the test material determines the orientation of the eddy current flow paths induced inside the material, which circulate in planes perpendicular to the axis of the magnetic flux. Also, the frequency of alternation of the eddy currents depends on the frequency of alternation of the primary magnetic flux.

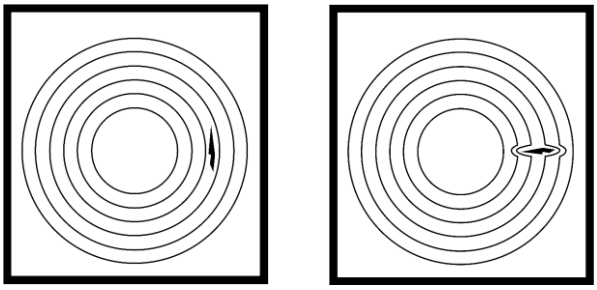

Figure 47: Discontinuities (a) parallel and (b) perpendicular to EC flow paths [53]

As observed in Figure 45, the eddy current density is not homogeneous within the material. It is maximum at the material surface, near the surface adjacent to an excitation coil and decreases exponentially with depth, exhibiting a skin effect. The standard depth of penetration δ, or skin depth, is defined as the depth at which eddy current density decreases to e^{-1} (i.e., 36.8%). It depends on the material's electric conductivity and magnetic permeability, and the test frequency, as follows:

$$\delta(mm) = \frac{1}{\sqrt{\pi f \mu \sigma}} = \sqrt{\frac{\rho}{\pi f \mu}} \qquad (27)$$

with the units of σ in $S.mm^{-1}$, ρ in Ω.mm, μ in $H.mm^{-1}$ and f in Hz. Beyond the third skin depth, the current density becomes too weak to give any meaningful information.

The magnitude of eddy currents is a function of the physical properties of the test material and of the testing parameters such as test frequency. Besides the conductivity and permeability of the test material, the test frequency affects the effective penetration of eddy currents into the material, as described in Figure 48. The optimum test frequency may be determined by experimentation.

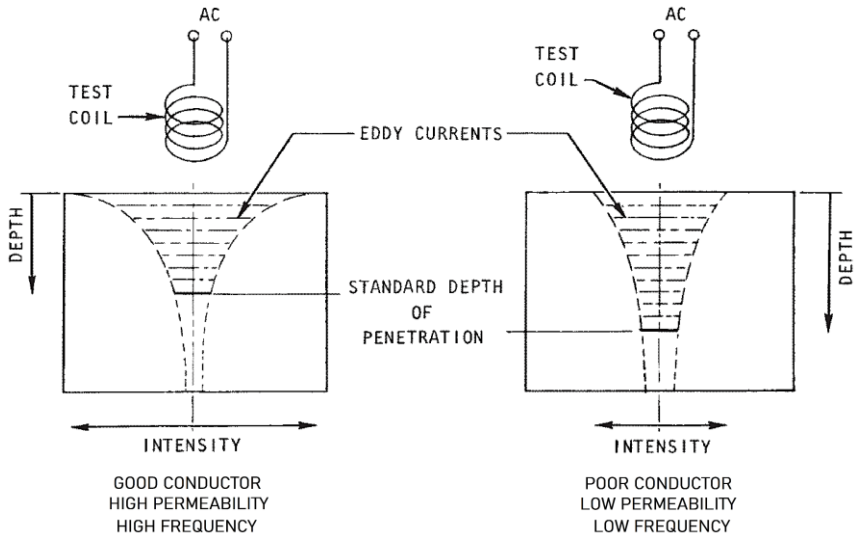

Figure 48: Relative magnitude and distribution of eddy currents depending on the test frequency, the material's conductivity and permeability [108-adapted]

Moreover, the electromagnetic coupling between the coil and the test material is influenced by the coil assembly design (i.e., probe geometry, number of turns and size of the coil), as well as the lift-off and the fill-factor, in the case of internal and encircling coil probes, which are the spacing between the coil and test material. The fill-factor is designated by the ratio of the squares of the cross-sectional areas of the test piece and the coil section, as indicated in Figure 49 below.

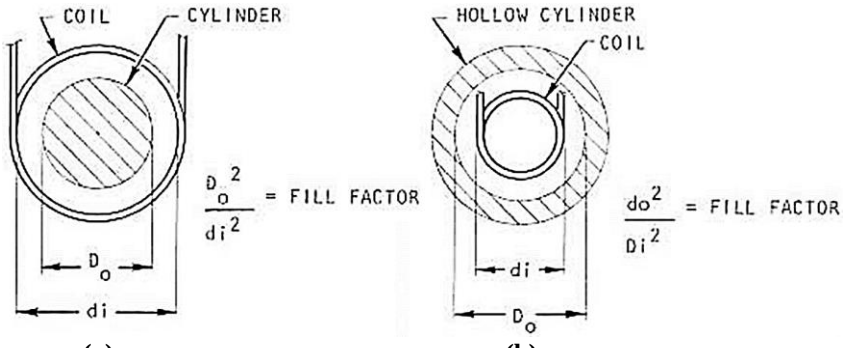

Figure 49: Fill-factor in an (a) encircling coil probe and (b) internal coil probe [108]

A suitable separation between the inspection coil and the sample is important to ensure a proper scanning of the material while generating sufficient eddy currents during the inspection. The greater the electromagnetic coupling, the denser the eddy current and the smaller its depth of penetration into the material, and thus, the more sensitive is the test to any material variable. This condition is demonstrated in Figure 50. The lift-off or fill-factor effect is used to measure non-conductive coating thickness. However, for defects detection or material evaluation it must be as constant as possible during testing to avoid impedance changes considered as a noise source. [53,56,108]

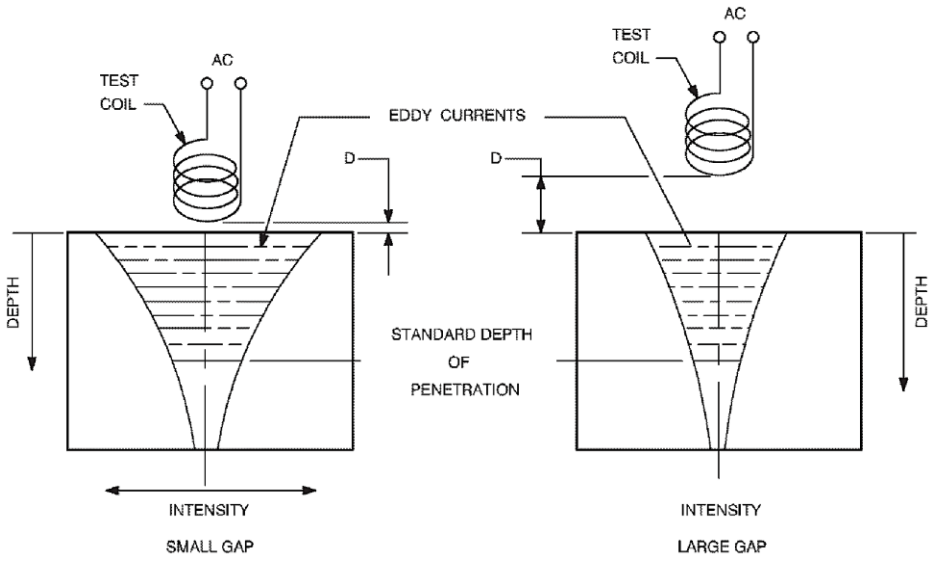

Figure 50: Relative intensity of eddy currents with variations in lift-off [109]

In summary, the generation and detection of eddy currents in a conductive part are largely dependent on the inspection system, the material properties of the sample, and the test conditions. Any factors that affect the flow pattern of eddy currents induced into the material, change the secondary magnetic field and the overall net magnetic flux accordingly. It affects the coil's inductance and so the inductive reactance, as well as the effective resistance of the coil circuit. Although the coil's resistance itself does not change, the dimensional and material property variations of the investigated sample may alter its resistance, affecting the effective resistance. In order to achieve optimum performance, the instrument sensitivity and resolution determined by the probe design, test frequency and EC instrumentation might be established from reference standards. The test parameters must be defined and adjusted according to the investigation purpose of a given material.

III. SUMMARY

This chapter introduced the fundamental concepts of metallurgy and electromagnetism fields, serving as the reference upon which the research scope of this thesis manuscript is based. The scope of this work can be represented by three principal axes, as illustrated schematically in Figure 51.

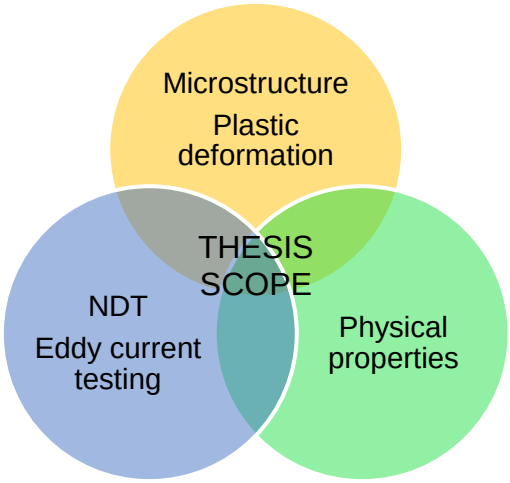

Figure 51: Research scope of the thesis manuscript

First, it is referred to the microstructure of carbon steels and the plastic deformation by cold-drawing processing of wires or by mechanical exposure in service operations. Second, to the physical properties that define the electrical and magnetic behaviors of these materials, which are closely related to their crystalline structure configuration. The third point concerns the non-destructive techniques, in the case of this research, the development of eddy current testing as a tool for the characterization of steel wires. The purpose of this thesis manuscript is thereby to understand the intersections between these different areas of knowledge, seeking to assess the microstructural parameters that affect the electromagnetic behavior of steel wires, which is, in turn, determinant for the comprehension of electromagnetic sensor responses obtained via eddy current testing.

CHAPTER 2

MATERIALS AND EXPERIMENTAL PROCEDURES

CHAPTER 2

MATERIALS AND EXPERIMENTAL PROCEDURES

This chapter is primarily dedicated to describing the various materials, equipment, and experimental techniques employed in the present research to be able to establish the relations between microstructure, mechanical, and physical properties of carbon steel wires, whether on a macroscopic scale and a microscopic level.

The first part of this chapter focuses on presenting the selection of the wire rod steel grades for the study. The several thermal and cold-working processing carried out to obtaining samples with various microstructure features and tensile strengths are detailed. Second, the equipment and experimental methods performed for material characterization are described, as well as the implemented methodologies for the evaluation of electrical and magnetic properties. Next, the eddy current testing equipment and test conditions for the non-destructive assessment of steel wires are discussed. Finally, relevant aspects of statistics and metrology are approached to ensure accurate and reliable measurement procedures. A synthesis of the materials and experimental methods to be studied is presented at the end of this chapter.

I. MATERIALS

I.1. Chemical composition

The samples examined in this study were obtained from AISI 1000 series plain carbon steel wire rods, with carbon content varying from 0.03 to 0.78 wt. % C, the chemical compositions of which are given in Table 1.

Table 1: Chemical composition of the AISI 1000 series plain carbon steels (wt. %)

AISI steel	C	Mn	Si	Cr	Ni	P	S	Fe
1000	0.033	0.150	0.014	0.023	0.022	0.006	0.014	Bal.
1020	0.201	0.726	0.215	0.019	0.015	0.013	0.011	Bal.
1035	0.346	0.607	0.209	0.015	0.015	0.015	0.010	Bal.
1050	0.498	0.590	0.208	0.018	0.020	0.013	0.005	Bal.
1055	0.520	0.607	0.210	0.016	0.015	0.015	0.005	Bal.
1060	0.583	0.607	0.189	0.009	0.013	0.009	0.008	Bal.
1065	0.647	0.613	0.183	0.014	0.014	0.017	0.014	Bal.
1080	0.776	0.587	0.235	0.020	0.020	0.014	0.009	Bal.

I.2. Material preparation: thermomechanical treatments

The wire rods had an initial diameter of 6.5 mm and were cold-drawn for obtaining wire samples of diameters 2, 4, and 6 mm that were posteriorly heat-treated. The cold-drawing and thermal processing were performed at the installations of the Bekaert Technology Center, shown in Figure 52.

(a) **(b)**

Figure 52: Pilot plants at the Bekaert Technology Center: (a) multi-pass drawing machine and (b) automated heat-treatment line

Several heat treatments were carried out to produce samples with different microstructures and strengths for the study of the influence of carbon content and phase morphology on the physical properties of carbon steels. Besides thermal processing, steel wires undergo mechanical stresses that affect the microstructure of the material and may also impact their electromagnetic properties. Therefore, the thermomechanical treatments here are divided into two transversal study axes: firstly, with respect to the microstructure, and second, to the plasticity. The samples were characterized by metallographic methods, mechanical tests, electrical and magnetic techniques described later in this chapter. A sufficient number of wire samples were produced for performing in-situ and offline eddy current analysis.

I.2.1. Samples for the study of microstructure

For investigating the microstructural characteristics, the wire rods were first cold-drawn from 6.5 mm to the three diameters wires of 2, 4, and 6 mm, as previously mentioned. Next, the cold-drawn wires were submitted to different heat treatments, according to each microstructural aspect studied. The obtained microstructures described in the following paragraphs are classified in groups A, B, and C.

At first, plain carbon steels varying from 0.03 to 0.78 wt. % C were selected for assessing the effects of changing the chemical composition, altering the volume fraction of ferrite and pearlite components in the steel. Each material was austenitized in an electric-powered furnace at 950°C in an inert atmosphere for 85 s and cooled in a molten lead bath at a constant temperature of 580°C for 35 s before final cooling at room temperature, as shown in Figure 53. Thus, the group A consists of different batches of steels with varying fractions of pearlite, as briefly described in Table 2.

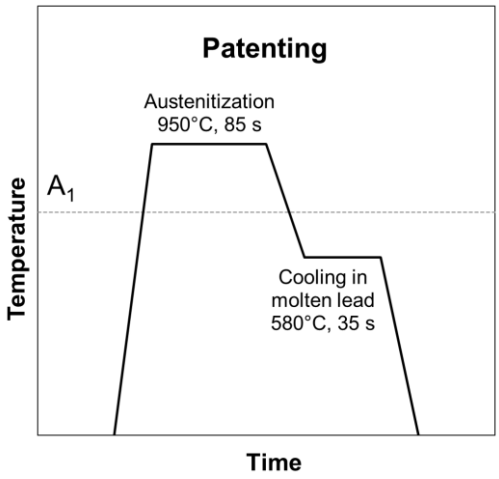

Figure 53: Thermal cycle employed for producing ferrite-pearlite samples (group A)

Table 2: Summary of the thermal treatments carried out on plain carbon steel wires

AISI steel	C (wt. %)	Heat treatments	Microstructure
1000	0.03		Fully ferrite
1020	0.20		Proeutectoid ferrite-pearlite
1035	0.35		Proeutectoid ferrite-pearlite
1050	0.50	Austenitizing at 950°C	Proeutectoid ferrite-pearlite
1055	0.52	Cooling at 580°C	Proeutectoid ferrite-pearlite
1060	0.58		Proeutectoid ferrite-pearlite
1065	0.65		Proeutectoid ferrite-pearlite
1080	0.78		Fully pearlite

Concerning the study of the pearlite microstructure, the 1080 steel wires were also employed for investigating the effect of prior-austenite grain size and interlamellar spacing. Therefore, the samples were obtained by varying the austenitization temperature at 950 and 1050°C in a furnace for about 85 s, and the cooling was performed in a molten lead bath at constant transformation temperatures of 540, 560, 580, 600, 620, and 640°C, followed by cooling in air for 35 s. The samples produced constitute the group B. Several thermal routes are illustrated in Figure 54.

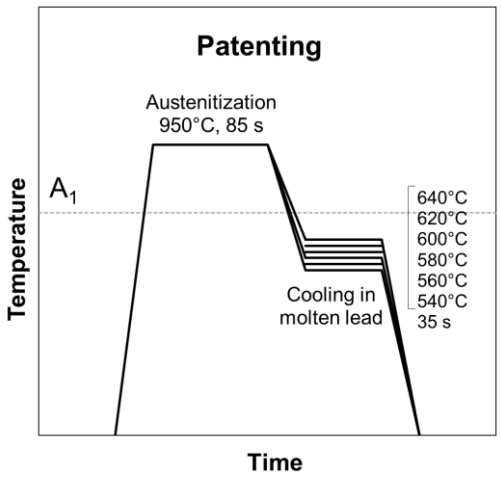

Figure 54: Patenting treatments for obtaining fully pearlitic steels with varying PAGS and interlamellar spacing (group B)

The group C includes the different types of microstructure features produced from the eutectoid 1080 steel. Lamellar pearlite, spheroidite, martensite, and sorbite microstructures were obtained through various heat treatments shown in Figure 55. The pearlitic samples with fine and coarse pearlite microstructures of group B that were austenitized at 950°C and cooled at 540 and 640°C also composed group C.

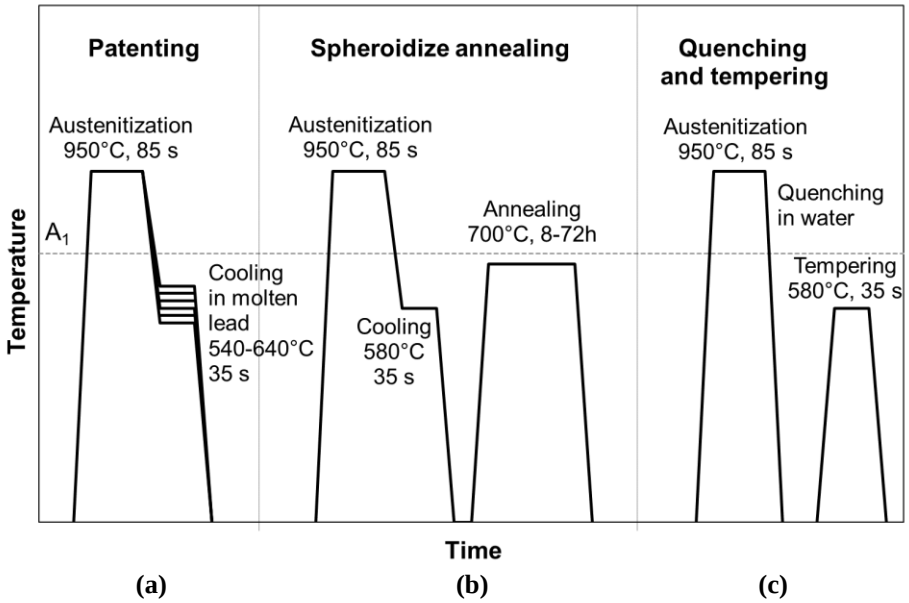

Figure 55: Schematic diagram of the heat treatments carried out on eutectoid steels of group C for producing (a) lamellar pearlite, (b) spheroidite, (c) martensite, and sorbite microstructures

In order to obtain a spheroidite microstructure, the pearlitic samples were annealed at a relatively high temperature of 700°C in an inert-atmosphere furnace for soaking times of 8, 24, and 72 h, and cooled in air. Besides, martensite was produced by austenitization in an oven at 950°C for 85 s and subsequent quench in a water bath at 25°C. Next, the sorbite microstructure was produced by tempering treatment of the martensitic samples in a molten lead bath at 580°C for 35 s. The samples were air-cooled after the transformation end. Table 3 lists the various samples of group C.

Table 3: Summary of the various heat treatments performed on eutectoid steel wires

AISI steel	C (wt. %)	Heat treatments	Microstructure
1080	0.78	Austenitizing at 950°C Cooling at 540°C	Fine lamellar pearlite
1080	0.78	Austenitizing at 950°C Cooling at 640°C	Coarse lamellar pearlite
1080	0.78	Annealing at 700°C for 8 h	Spheroidite
1080	0.78	Annealing at 700°C for 24 h	Spheroidite
1080	0.78	Annealing at 700°C for 72 h	Spheroidite
1080	0.78	Quenching in water at 25°C	Martensite
1080	0.78	Tempering at 580°C	Sorbite

I.2.2. Samples for investigation of plastic deformation

In order to study the contributions of plasticity to the physical properties of pearlitic steel wires, distinct types of forces were applied to the material by the cold-drawing process (shear, tension, and compression stresses) and cyclic loading testing (tension/compression stresses), resulting in different deformation phenomena. In this subsection, only the parameters involving cold-drawn processed steel wires are discussed. The sample preparation methods employed for the cyclic loading tests will be directly described in Chapter 4.

The initial 6.5 mm diameter wire rods of 1080 steel were first cold-drawn to wires of 6 mm diameter, which were posteriorly austenitized in an electric furnace at 950°C for 85 s and then cooled in a lead bath at constant temperatures of 540 and 640°C for 35 s for producing initial fine and coarse pearlite microstructures, respectively. Finally, the patented eutectoid steel wires were cold-drawn in a multi-pass dry drawing machine, from 6 to 2 mm in diameter in ten drawing passes. Samples were collected after each drawing pass for subsequent evaluation.

The thermomechanical processing for obtaining cold-drawn wires from both initial fine and coarse pearlite microstructures is summarized in Table 4.

Table 4: Summary of the multi-pass dry drawing processes on fully pearlitic steel wires

AISI steel	Initial diameter (mm)	Final diameter (mm)	Drawing pass	Reduction in area, r	Drawing strain, Ɛ
1080	6.00	5.23	1	0.24	0.27
1080	6.00	4.74	2	0.38	0.47
1080	6.00	4.33	3	0.48	0.65
1080	6.00	4.00	4	0.56	0.81
1080	6.00	3.49	5	0.66	1.08
1080	6.00	3.07	6	0.74	1.34
1080	6.00	2.72	7	0.79	1.58
1080	6.00	2.44	8	0.83	1.80
1080	6.00	2.20	9	0.87	2.01
1080	6.00	2.00	10	0.89	2.20

II. EXPERIMENTAL PROCEDURES

All the experimental procedures for the microstructure evaluation of the various produced steel wires were carried out in the UMET and BTC laboratories. The electromagnetic characterization presented in this work was performed in the Laboratoire d'Electrotechnique et d'Electronique de Puissance de Lille – L2EP of the University of Lille in France, and in the Institute of Experimental Physics of the Slovak Academy of Sciences – IEP SAS in Košice, Slovakia. The non-destructive eddy current tests were operated in the BTC installations.

II.1. Microstructure analysis techniques

II.1.1. Preparation of metallographic specimens

Before carrying out metallographic analysis by optical or electron microscopy, a succession of specific operations was necessary to obtain a suitable examination surface and an accurate interpretation of the real microstructure of the studied materials. The metallographic preparation of the carbon steel samples involved abrasive cutting in a Struers Labotom-3 cut-off machine, hot compression mounting in a Struers CitoPress-1 mounting press, followed by grinding using successively finer silicon carbide abrasive papers from 80 to 2400 grit in the automatic grinding and polishing machine Struers Tegramin-30. Next, to ensure the disappearance of scratches left by a coarse grinding, the samples were polished on soft cloths, on which were applied water-based diamond in suspensions of controlled sizes, from 9 to 0.25 µm. Finally, the last polishing step by colloidal silica-based slurry on a napless cloth was performed to eliminate as much as possible the micro-scratches and deformation layer consecutive to previous steps. The microstructural constituents were revealed by chemical etching using various reagents, depending on the investigation purpose.

II.1.2. Light optical microscopy

The various microstructures were observed on the Zeiss Axioplan 2 and Zeiss Axio Vert.A1 microscopes. Prior-austenite grain size and phase volume fraction were also determined experimentally based on LOM micrographs of sample transverse sections.

In addition to mechanical polishing, the sample preparation for grain size measurements included thermal etching with alkaline sodium picrate solution for a few seconds to reveal the prior-austenite grain boundaries [110,111]. LOM images were

taken from randomly selected fields under a magnification of 500 times, and grain sizes were quantified by the intercept procedure (ASTM E112) using the ImageJ/Fiji software. It involves counting the number of grain boundary intersections with a circular grid drawn through the micrograph [112], as shown in Figure 56. The average PAGS is calculated by dividing the number of crossings by the actual line length.

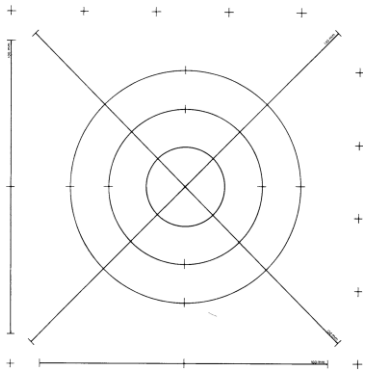

Figure 56: Pattern for intercept counting [87]

The quantification of proeutectoid ferrite and pearlite volume fractions was carried out by color etching of the samples with 3% Nital and 10% potassium metabisulfite solution [110] for reveling the proeutectoid ferrite grains in white areas (Figure 57-a). A considerable number of LOM micrographs under a magnification of 500 times was done along the specimen's transverse cross-sections. Considering that the area percentage of a phase of interest in a two-dimensional plane is equal to its volumetric rate, the volume fraction that phase could be determined using the image-processing program ImageJ/Fiji. It was possible to distinguish both the components using phase-contrast image analysis (Figure 57-b). The phase balance was estimated by the number of pixels related to each phase, divided by the total pixels of the images.

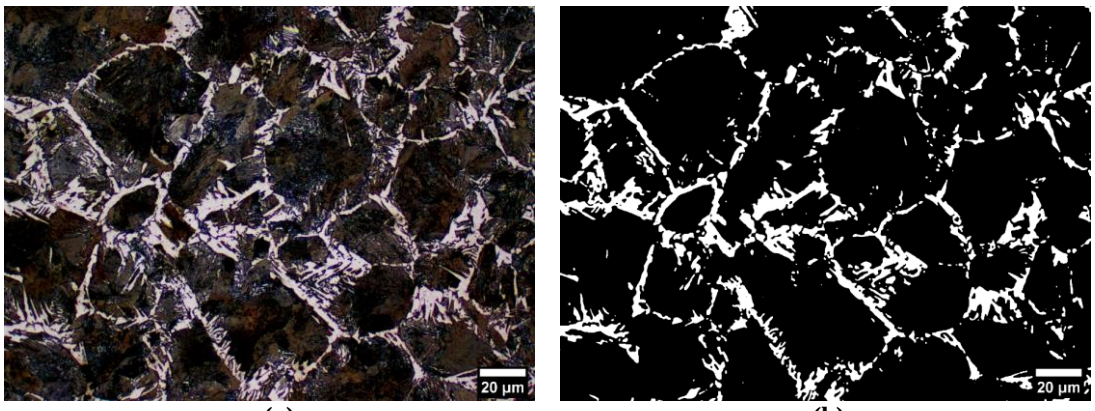

(a) **(b)**

Figure 57: (a) LOM image of a hypoeutectoid steel color etched with 3% Nital and 10% potassium metabisulfite, and (b) phase-contrast analysis for volume fraction estimation

II.1.3. Scanning electron microscopy

Several scanning electron microscopes shown in Figure 58 were employed in the present study. The Hitachi S4700 and FlexSEM 1000 Hitachi with tungsten filaments were used for basic microscopy, including low magnification images of various microstructure and fractographic analysis. The JEOL JSM-7200F FE-SEM was used for microstructure observations at higher magnifications and details, due to the field-emission gun to reach a nanometric spatial resolution. It was also employed for the estimation of pearlite interlamellar spacing, whose methodology is detailed below. The observations were made at an acceleration voltage of 20 kV.

(a) **(b)**

Figure 58: Scanning electron microscopes (a) Hitachi S4700 at UMET, and (b) JEOL JSM-7200F at BTC installations

The evaluation of average pearlite interlamellar spacing was carried out from FE-SEM observations at the transverse cross-sections of samples. As mentioned later, the microstructure of pearlite is very complex, and even the definition of a mean interlamellar spacing is not straightforward. The problem of measuring the apparent interlamellar spacing λ observed directly in the micrograph plane is that the lamellae are not necessarily orientated perpendicular to it, as illustrated in Figure 59.

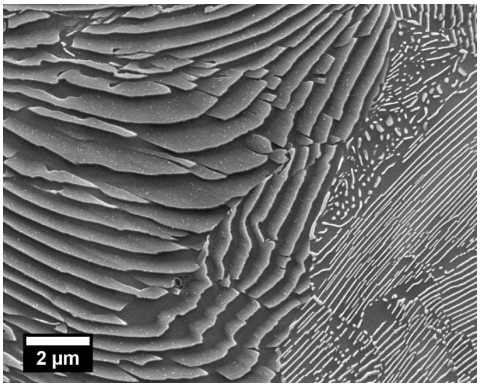

Figure 59: SEM image showing Fe_3C lamellae at different orientations in pearlite

Hence, the calculation of the average interlamellar spacing from the simple measurement of the apparent distance between the cementite layers does not provide a realistic view of the pearlitic microstructure with perlite colonies oriented randomly. For this reason, the true interlamellar spacing λ_0 should be considered to minimize the spatial issue. It corresponds to a distribution of spacing on a surface normal to the lamellae, as seen in Figure 60.

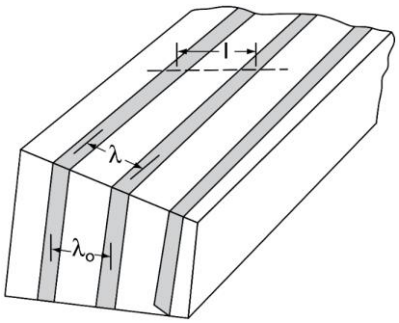

Figure 60: Parameters for interlamellar spacing estimation [12]

In this study, the mean true interlamellar spacing of pearlite was determined according to Underwood's method. It consisted of superimposing an intersection grid, as described previously for grain size measurements, in such a manner that the lines intersected the pearlite lamellae randomly in all directions. The mean intercept $\bar{l}$ is thus obtained by dividing the total line length by the number of the lamellae intercepted of each grid line [12,113]. The mean true value of interlamellar spacing $\bar{\lambda}_0$ is given by the equation below:

$$\bar{\lambda}_0 = \frac{\bar{l}}{2} \tag{28}$$

For this measurement, the samples were polished and etched in a 4% Picral solution. FE-SEM micrographs were captured at magnifications between 5000 and 10000 times, depending on the microstructure fineness, and at least 25 images of each sample were measured to ensure the data accuracy. The images were processed using the ImageJ/Fiji software, allowing better identification of the lamellae.

The cementite precipitate sizes of spheroidite microstructures were determined by the interception procedure using SEM images under magnetization of 5000 times.

II.2. Mechanical testing

The mechanical characteristics of the studied steel wires were determined via Vickers microhardness measurements and standard tensile tests. The equipment is shown in Figure 61.

Vickers microhardness tests were carried out on the transverse cross-section of the polished samples using a load of 0.5 kgf and a working time of 10 s in a Buehler and a Zwick Roell ZHμ microhardness testers. Two-line segments passing through the geometric center of the transverse cross-section were measured for each sample, each line segment assured ten measuring points, with the measurement interval depending on the sample diameter.

Conventional tensile tests were performed using a Zwick Roell test machine, coupled with an extensometer, at a constant crosshead speed of 30 mm/min and room temperature. The wire specimens had about 20 cm length, with a gauge section length of 10 cm, conforming to ASTM E8. At least two experiments were executed for each similar specimen.

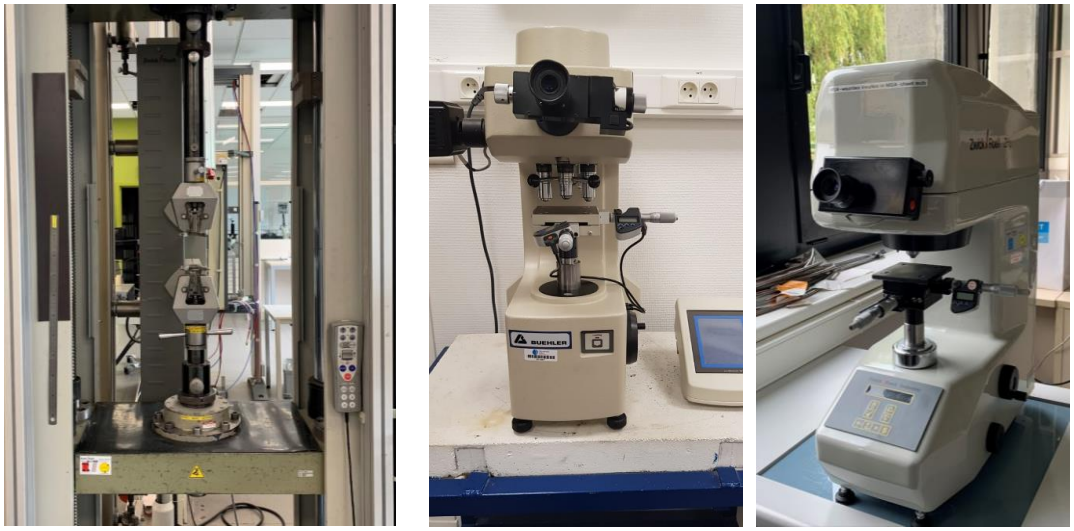

(a) **(b)**

Figure 61: (a) Zwick Roell test machine; (b) Buehler (left) and Zwick Roell ZHμ (right) microhardness machines

II.3. Electromagnetic characterization experiments

II.3.1. Characterization methods of electrical resistivity

Electrical resistivity measurements were performed in a temperature range from 2 K up to 300 K using the AC transport (ACT) option of the Physical Properties Measuring System (PPMS) from Quantum Design. The test leads for the four-probe setup were contacted by silver paste to rod-shaped specimens with a diameter of 2 mm and a length of 1 cm. The used measuring current was 5 mA. The electrical characterization was carried out at the IEP – SAS installations and the experimental device is shown in Figure 62.

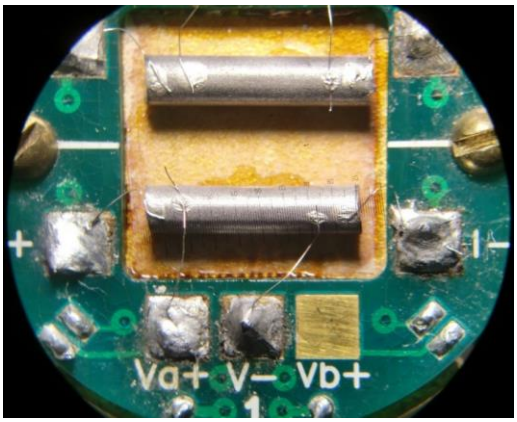

Figure 62: Experimental device for resistivity measurements at IEP SAS laboratory

Further resistivity measurements were performed utilizing the four-point probe method in micro-ohmmeter installed at the L2EP laboratory, as shown in Figure 63. The rod-shaped specimens of various diameters of 2, 4, and 6 mm and 2.5 cm in length were slightly ground with 2400 mesh abrasive paper to remove oxide layers of the conductive surface. The measurements were performed at a controlled temperature in a Binder stove at 35°C. The current was set to 1 A.

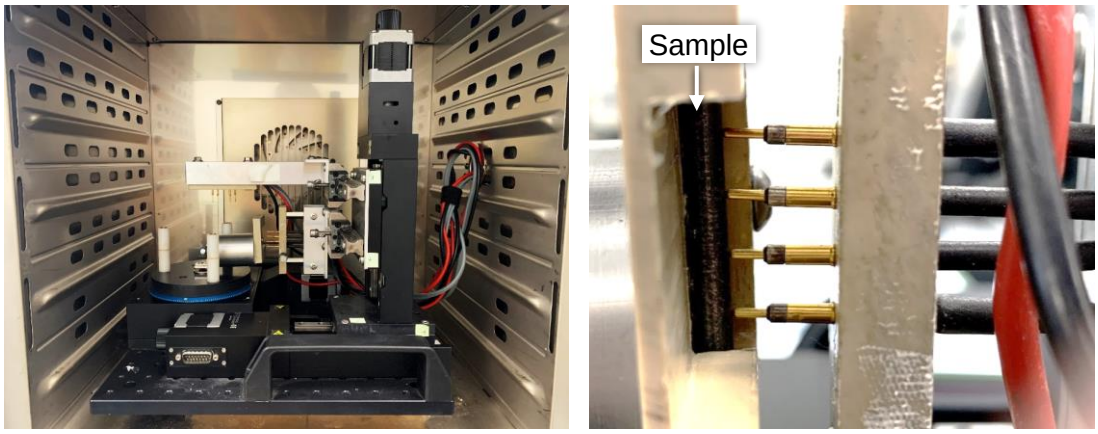

(a) **(b)**

Figure 63: (a) Experimental device for resistivity measurements placed inside the stove at L2EP laboratory, and (b) the four-point probe in contact with the sample with the help of a polymeric support

The resistivity values were calculated based on the measured resistance of each circuit and the dimensions of the specimens. In principle, conductivity measurements are straightforward to be performed. However, potential sources of errors can be manifold, including measurement devices (ohmmeter, digital pachymeter), possible irregularities in the specimen geometry, electromagnetic disturbances, temperature, and humidity variations. Each sample was measured quasi-statically at a stabilized temperature and repeated numerous times to increase measurement accuracy.

II.3.2. Macroscopic magnetic methods

The evaluation of bulk magnetic properties is an elaborate experiment, once it involves a set of variables that change according to the excitation field due to the hysteresis phenomenon, but also depends on the past magnetic history of the material. There was an additional difficulty related to the rod-shaped geometry of the steel samples, which configured an open magnetic circuit. In this circumstance, an experimental set-up was built at the L2EP installations using an electromagnet connected to an alternating current voltage source, as shown in Figure 64. The close magnetic circuit was constituted by the electromagnet and the cylindrical sample, ensuring a more uniform magnetic field and reducing the demagnetizing field magnitude.

The electromagnet is made of a ferromagnetic ferrite core. The carbon steel rod-shaped samples of 2, 4, and 6 mm in diameter and 2.5 cm length were placed between the electromagnet poles. A pick-up coil was carefully wound around each sample, made of copper wires of 0.20 mm in diameter, having 50 windings for the 6 mm-diameter specimens, and 100 windings for the steel samples with 2 and 4 mm in diameter. Four adjacent Hall probes were positioned at different positions perpendicular to the sample surface with a support stand.

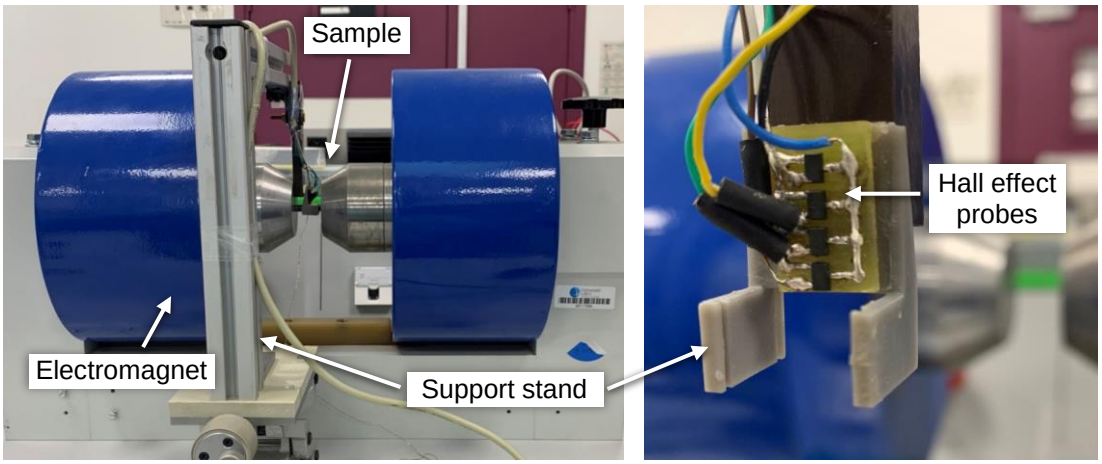

Figure 64: (a) Experimental device of bulk magnetic measurements at L2EP laboratory, and (b) in detail, the arrangement of four Hall effect probes

The close circuit was traversed by a constant current that generated a magnetic field, magnetizing the steel samples along their axial direction under magnetic field strengths ranging from -15 $kA.m^{-1}$ to -15 $kA.m^{-1}$. The magnetic measurements were carried out at a low excitation frequency of 0.5 Hz for reducing energy losses due to the macroscopic eddy currents induced in the ferromagnetic materials. The Hall effect

probes measured the tangential field strength at different positions in the air. Based on the continuity principle of the tangential field at an interface, it was possible to estimate the local magnetic excitation at the surface of a material. Also, the induced magnetization was measured by the pick-up coil surrounding the samples. Hence, the magnetic flux density was recorded as a function of the calculated excitation field at the surface of the tested specimens. At least two measurements were carried out in each sample. The system was degaussed before and after testing by an alternating current with a decreasing amplitude in time to avoid possible remanent magnetization within the specimens or the electromagnet, which would disturb the experiment. The magnetic properties of carbon steels were quantitatively calculated from the obtained hysteresis loops.

II.3.3. Magnetic force microscopy

Among the various scanning probe microscopy techniques developed for nanostructural analysis that have emerged in the last decades, magnetic force microscopy is a handy technique in investigating the magnetic properties of ferromagnetic materials. In this study, MFM analysis was employed for the observation of magnetic domains in the bulk material. It consists of a mechanical probe placed very close to the sample surface, a piezoelectric actuator that moves the sample laterally to the probe, and a monitoring system to detect the out-of-surface plane deflections in response to the magnetic interaction variations with the probe as it scans across the specimen surface. A computer receives and converts the signal data, generating a typical MFM image, as illustrated in Figure 65.

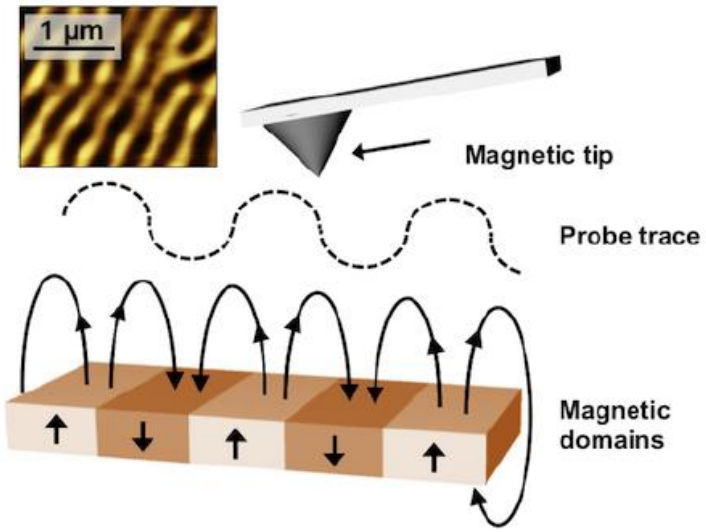

Figure 65: Schematic of magnetic force microscopy analysis [114]

MFM observations were carried out in the transverse cross-section of the 4 mm diameter and 5 mm thick samples. The sample surface was prepared using conventional metallographic techniques up to polishing with 0.025 µm colloidal silica suspension followed by etching in a 0.5% Nital solution. A final preparation step was added using focused ion beam (FIB) milling for obtaining a free-deformed layer. The MFM measurements were carried out at room temperature using an Agilent 5500 Atomic Force Microscope equipped with a magnetic cobalt-chromium (CoCr) coated tip with a nominal coercivity of 32 $kA.m^{-1}$ (medium). First, images of topography were acquired in the tapping mode. Subsequently, the domain structures were observed in the lift mode by mapping the magnetic forces resulting from the interactions between the magnetic tip and the sample surface at a distance of 100 nm.

II.4. Eddy current testing

An electromagnetic sensor connected to an electronic oscillator, an amplifier, and a data acquisition computer was employed to evaluate electromagnetic properties by eddy current testing, as shown in Figure 66. The ECT sensor system was composed of a encircling coil arrangement with excitation and receiver coils of copper.

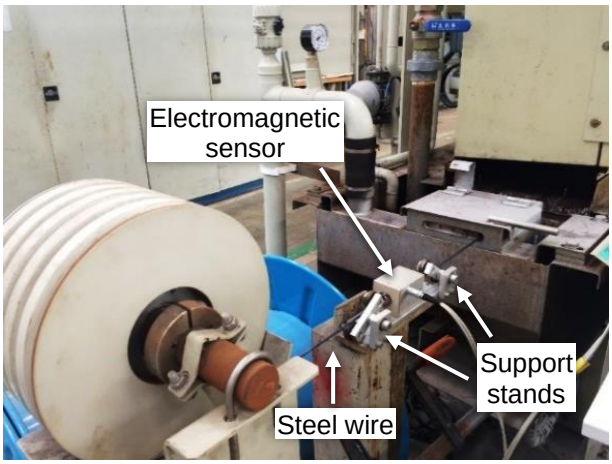

Figure 66: Eddy current equipment installed at the end of the heat-treatment line

As discussed in Chapter 1, the ECT performance depends on the material's physical properties of electrical conductivity and magnetic permeability, in addition to test parameters such as the test frequency, coil design, and fill-factor. Since the objective of this study is to characterize microstructures and functional properties in a non-destructive way, the test frequency and fill-factor effect were maintained constant in such a way to ensure that only the effective parameters affecting the material responses to the induced currents were directly related to its characteristics.

Figure 67 shows a cause-and-effect diagram, also known as Ishikawa diagram, used to help to identify and summarize the critical parameters and potential sources of errors involved with the non-destructive characterization by eddy current testing.

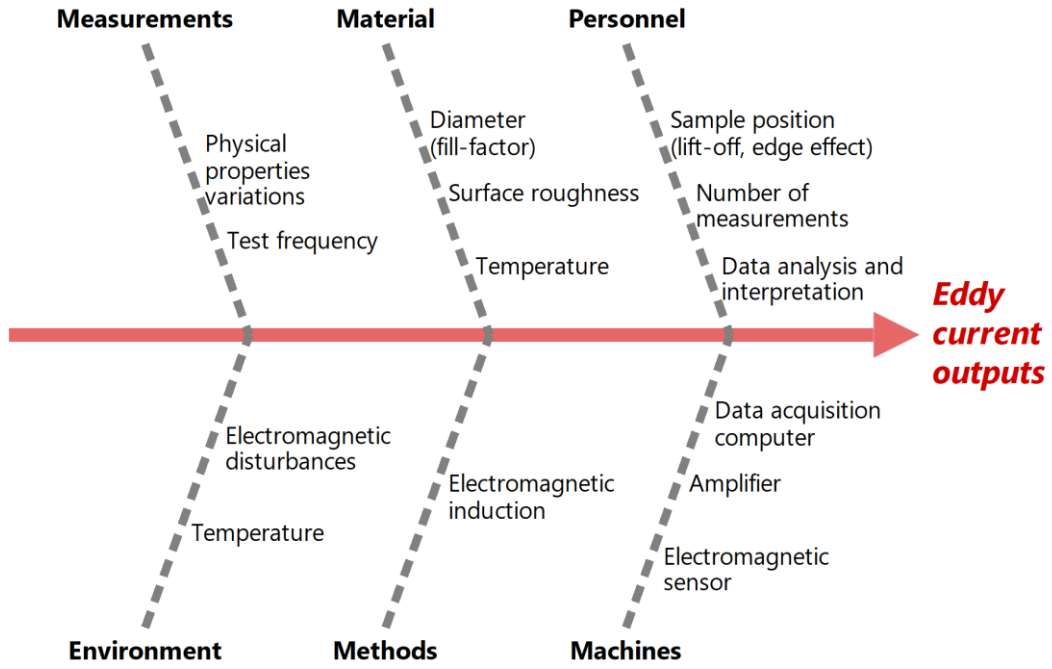

Figure 67: Ishikawa diagram of eddy current testing

The non-destructive eddy current evaluations described in this investigation were all carried out using the same electromagnetic sensor to prevent signal variations due to changes in the coil geometry. The experiments described in Chapter 3 for investigation of microstructure were all performed on 4-mm diameter wires. In Chapter 4, the study of cold-drawn steel wires after each drawing pass implies a significant reduction of cross-sectional diameter area. The diameter change of the test materials was taken into account for the electromagnetic evaluation. Moreover, to avoid errors linked to fill-factor variations, the specimen position inside the coil was maintained always centered using support stands positioned at the ends of the wire samples during testing. As eddy currents are very sensitive to any discontinuities within the material, measurements were not carried out at the end of test specimens to avoid current flow distortions due to the edge effect.

Before testing, a calibration is necessary to define an optimum test frequency concerning mainly the nature and dimensions of the materials to be tested. A test frequency of 200 Hz was chosen for eddy current evaluations in this study, aiming to obtain a considerable penetration depth that allows well distinguishing the different tested materials, also considering the diameter range of the steel wires investigated.

The excitation current was 0.5 A. All measurements were performed at room temperature. At such low frequency, no considerable temperature variation was observed within the material. Voltage variations were used to characterize the coil's impedance variations and thus the output information is displayed as the total voltage amplitude V_T, resistive voltage V_R, inductive voltage V_L, and phase angle ϕ relative to the primary current.

ECT was carried out online with the electromagnetic sensor positioned at the end of the automated heat-treatment line as illustrated in Figure 66, measuring the materials responses directly after thermal processes. In addition, multiple measurements were performed offline by measuring the correspondent signal outputs of collected wire samples after processing. A sufficient large dataset was produced for each different material.

II.5. Metrology and statistics

Metrology is the science of measurement and encompasses the theoretical and practical issues related to measures in any field of science and technology. Statistical science has a fundamental role as an instrument for the use of metrology. The need to study statistics stems from the random nature of the studied phenomenon and the measurement itself. This section covers the fundamental concepts of statistics useful for metrology science and applied to the physical experiments in the present research.

The result of a measurement is an estimate of the value of the measurand, that is, the measured physical quantity. The process of measurement is influenced by the isolated or combined action of several factors involving the measurement system (experimental devices), the measurement method (scientific fundamentals, calculation model, interpretation of results), the operator skills, in addition to the action of external disturbances (temperature, humidity, pressure) that can also introduce relevant uncertainty components into the result of a measurement. Hence, the results of a set of measures are usually affected by systematic errors that can be eliminated, often due to poor measurement quality involving unbalanced measuring instruments or inadequate procedures, but also due to intrinsic errors. These types of errors that cannot be evaded are called random errors and are usually related to the stability and precision of the measuring system, the environmental conditions, and other effects. However, it is still possible to obtain reliable information by identifying the sources of errors and calculating the measurement uncertainty based on statistical dataset analysis.

The measurement accuracy is the closeness of agreement between a measured value and the real value of the measurand. The accuracy has no numerical value because the actual value of a population cannot be determined. However, an accurate measurement is defined as a measurement that provides a smaller measurement error: the minor difference between the measured value and the real value. The uncertainty is a parameter that characterizes the statistical dispersion of the measurand to the true value. Hence, the uncertainty reflects the accuracy of a measurement system, addressing the total errors expressed by both systematic and random errors.

The definitions of accuracy and trueness of measurements are very similar. The trueness refers to the average value obtained from an extensive series of measures, whereas the accuracy is a property referent to a single measurement result. The trueness is quantified by the bias, which is related to systematic errors. Besides, the measurement of precision is the closeness of agreement between estimated values obtained by repeated individual measures under specified conditions. It can be achieved under conditions of repeatability and reproducibility. The first refers to the results of successive measurements of the same measurand with the same conditions and methods, evaluating the measurement device precision. In turn, the reproducibility assesses the precision of measures carried out under the same techniques, but varying the measurement conditions (e.g., operator, instruments, environment). The precision does not include systematic error, since it is not based on the true value of the measurand, but only on repeated individual estimations. It depends exclusively on random errors, which are usually reduced by increasing the number of observations.

Hence, accuracy includes the effect of both trueness and precision, as illustrated schematically in Figure 68.

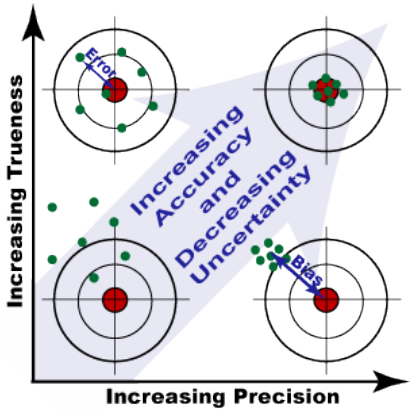

Figure 68: Target comparison illustrating trueness, precision, accuracy, and uncertainty of measurement results [115]

In statistics, a population is a global set of measures that have something in common. A sample is a subset of a population, referring to a small number of elements collected and analyzed to make inferences about that population. Therefore, the sample needs to be representative of the population. For this, it must be sufficiently large and collected randomly. The most likely value for a set of independent values x_1, x_2,…, x_N of a sample is expressed as the arithmetic mean $\bar{x}$ of the N individual values, which is defined by the expression:

$$\bar{x} = \frac{1}{N}(x_1 + x_2 + \cdots + x_N) = \frac{1}{N}\sum_{i=1}^{N} x_i \quad (29)$$

where X_i is the individual values, and n is the number of elements of the sample.

Besides, measures of dispersion are used to study the variability of a given distribution, which can be considered as a quantitative indicator of the measurement accuracy. Standard deviation and variance assess the degree of dispersion of the variable values concerning the arithmetic mean of the sample. The standard deviation s is defined as given below:

$$s = \sqrt{\frac{1}{N-1}\sum_{i=1}^{N}(x_i - \bar{x})^2} \quad (30)$$

The sample variance s^2 is equal to the square of the standard deviation, that is, the average of the sum of squares differences from the mean $\bar{x}$, as follows:

$$s^2 = \frac{1}{N-1}\sum_{i=1}^{N}(x_i - \bar{x})^2 \quad (31)$$

In probability theory, the central limit theorem establishes that the mean distribution of a random and sufficiently large sample is approximately normal. It signifies that the measurement values are distributed symmetrically around a central mean value. In a normal distribution, the confidence interval is a range of upper and lower values that is likely to include a population means, at a certain level of confidence α, usually 95 or 99%. Confidence intervals are employed to indicate the reliability of an estimate or, in a simpler way, how well a determined sample represents the population. The end of the intervals is calculated by an upper and lower score, using the z-score $z_{\alpha/2}$ characteristic of each confidence level. For instance, a confidence interval, with a confidence level of 95, or α=0.05, has a z-value of 1.96. Hence, this critical value defines the limit that separates values whose population means have a probability of 95% to be found between -1.96 and +1.96 concerning the sample mean, from the values that are unlikely to occur. These values lie outside the upper and lower confidence interval. Confidence intervals are determined as in the equation below:

$$\bar{x} \pm z_{\alpha/2} \frac{s}{\sqrt{N}} \quad (32)$$

where $z_{\alpha/2}$ is the z-score, α is the level of significance, s is the standard deviation, and N, the sample number. When the sample size is inferior to 30, the Student's $t_{\alpha/2}$ confidence coefficient is used, whose values are indicated in the t-Student table and depend on the degree of freedom (DF), equal to N-1. For an approximately normal distribution, with sample sizes equal or higher than 30, z and t have almost the same values. The margin of error is statistically expressed as half of the confidence interval.

Analysis of variance (ANOVA) is a statistical hypothesis-based test for determining whether there are any significant differences between the means of two or more groups of data in one or more distinguishing factors. One-way ANOVA is used to compare the means of groups in the function of one independent variable. It uses F-tests to evaluate the ratio of variances and determine whether the mean variances of groups within a sample are equal (null hypothesis, H_0: $\mu_1=\mu_2=...=\mu_j$), or if it exists differences between the means and groups (alternative hypothesis, H_1: the means are not all equal). The F-statistic ratio for one-way ANOVA is given as follows:

$$F = \frac{MS_{between-groups}}{MS_{within-groups}} = \frac{\frac{\sum_{j=1}^{k} n_j \left(\bar{x}_j - \bar{x}\right)^2}{k-1}}{\frac{\sum_{j=1}^{k} \sum_{i=1}^{n_j} \left(x_{ij} - \bar{x}_j\right)^2}{N-k}} \quad (33)$$

where the mean square (MS) between each group is calculated by the sum of squares (SS) deviation between each group mean $\bar{x}_j$ and the global mean $\bar{x}$ multiplied by each sample size n_j. The sum of squares is then divided by the DF between groups (i.e., the total number of groups minus 1, k-1). The mean square within-group variability is equal to the sum of squares of the differences between each data and its group mean, divided by the error DF: the total individual values minus the total number of groups (N-k). The p-value is the probability of obtaining a determined F-value. The null hypothesis is rejected when the p-value is smaller than the α-level; that is, the low likelihood suggests that not all group means are equal.

In addition to ANOVA, post hoc tests can be employed to complete statistical analysis of the sample data means. For instance, Levene's and Tukey's tests assess, respectively, the equality of variances and comparing the differences between all pairs of means. Moreover, two-way ANOVA considers the effect of two independent variables on a dependent variable and on each other for comparing means of groups. In contrast, factorial ANOVA is used to analyze the means of multiple independent variables that classify the sample in several groups. [116]

The measurement system analysis (MSA) improves measurement processes by quantifying characteristic parameters of uncertainty, precision, and stability. The most commonly used statistical tools to analyze the measured data quality are bias and variances. The bias refers to the location of data to an accepted reference value for the true value, which is determined based on a standard method or material, as follows:

$$Bias = \bar{x} - \mu_0 \quad (34)$$

where $\bar{x}$ is the sample mean, and μ_0 is the reference value. Systematic errors can be corrected by adjusting the bias.

The gage repeatability and reproducibility, or gage R&R, is an MSA technique for determining the variances associated with the measurement equipment, different methods, operators, or environments. Gage R&R allows distinguishing the measurement system variability from the process variation itself, evaluating the impact of one or more factors on the measure dispersion.

The evaluation of uncertainty measurement is divided into two categories, according to the method used to estimate its numerical values: type A, referring to the uncertainties determined by statistical analysis; and type B, which corresponds to evaluations by non-statistical means. In the present research, the measurement uncertainty was evaluated by statistical methods, including standard deviation, analysis of variance, and post hoc tests.

The experimental values relatives to material characterization are exhibited in terms of average, standard deviation, and confidence intervals. Besides, as it involves estimating microstructural states from information in two-dimensions images, several statistical hypothesis tests were performed for assessing individual and group means and variance homogeneity of the estimated microstructural parameters (i.e., phase volume fraction, interlamellar spacing, prior-austenite grain size, precipitate size). Besides numerical outputs from ANOVA, graphical interpretation was given in box-plot charts with the minimum and maximum data points, the median (Q2), and the first (Q1) and third (Q3) quartiles, which are the median of the lower and upper half of the dataset, respectively. The electrical resistivity measurements have provided enough data to allow statistical analysis of variances, which is relevant due to the multiple sources of errors involving conductivity measures. The mechanical and magnetic properties are presented in terms of the average and standard deviation values calculated from replicated experiments.

The eddy current outputs obtained for each material are displayed as average values and standard deviations. Gage R&R was used for assessing the measurement system accuracy of ECT. Also, ANOVA tests were conducted to verify significant differences between the mean signal responses of the various group material. Finally, regression analysis was used to assess the relationship between the investigated parameters and define the impact of one or more independent variables on a factor of interest.

III. SUMMARY

A precise study program was defined for investigating the fundamental effects of different microstructure parameters and plastic deformation on the electrical and magnetic properties of carbon steel wires and, hence, evaluate the sensitivity of eddy current testing for the non-destructive characterization of such materials. A certain number of microstructural parameters have been identified based on the literature review, and a selection of various grades of carbon steel rods was first made for the production of different steel microstructures by thermal and cold-work processing.

Figure 69 summarizes the overall thermomechanical treatments performed on carbon steel wires of different chemical composition, of diameters varying from 2 to 6 mm, to obtain the desired materials for the present research.

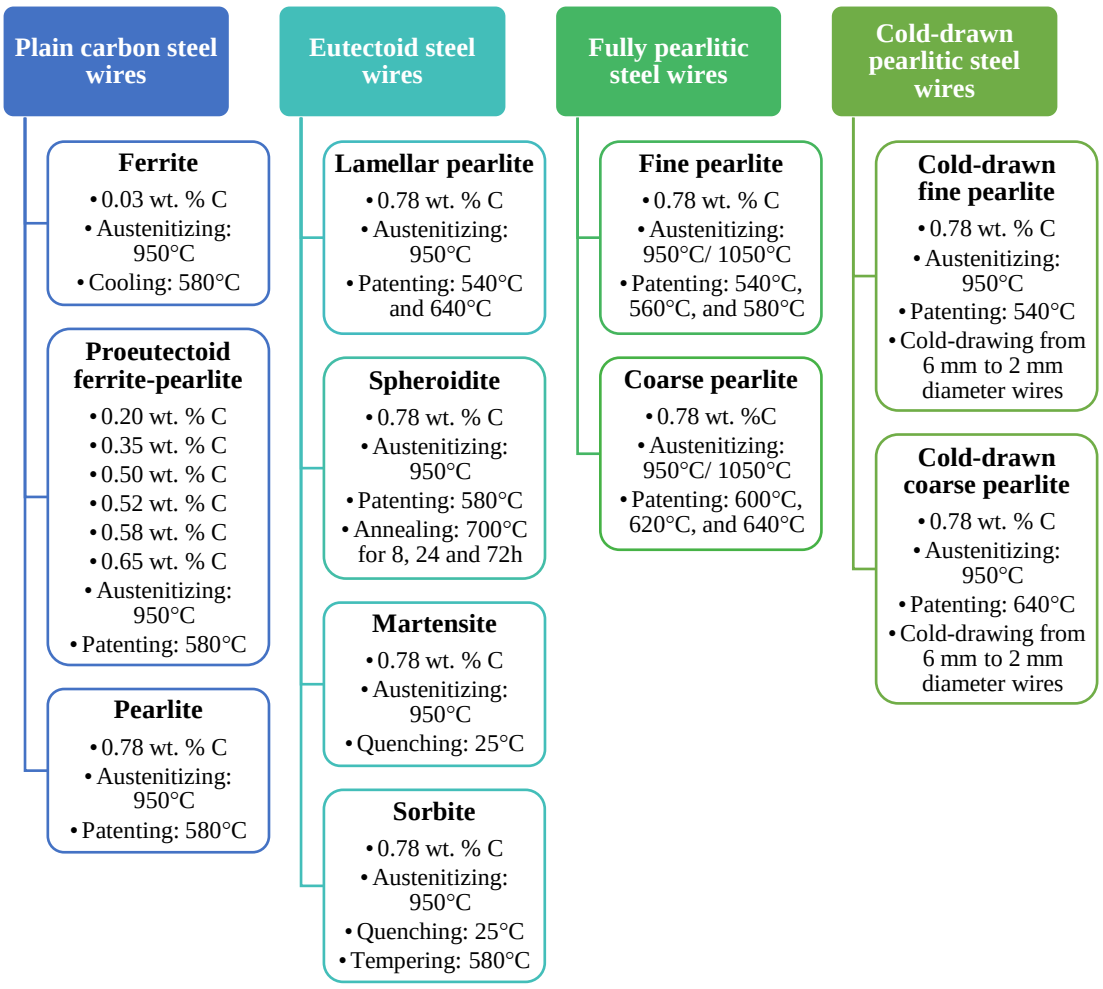

Figure 69: Schematic of the thermomechanical treatments carried out on various carbon steel wires

CHAPTER 3

MICROSTRUCTURE INFLUENCE ON THE PHYSICAL PROPERTIES OF CARBON STEELS

CHAPTER 3

MICROSTRUCTURE INFLUENCE ON THE PHYSICAL PROPERTIES OF CARBON STEELS

In the previous chapter, the various heat treatments performed to produce different structures for studying the relations between microstructure, mechanical and electromagnetic properties of steel wires were described. As the number of samples is considerably large, this chapter is simply divided according to the several microstructural aspects of carbon steels to be investigated:

- Effect of the carbon content on the AISI 1000 series plain carbon steels;
- Effect of the phase morphology of several microstructural produced from eutectoid AISI 1080 steel.

As previously mentioned, the microstructure and mechanical properties were characterized by conventional methods of metallography and static mechanical tests. Electrical resistivity measurements down to 2 K and magnetic characterization were also carried out to assess the dependence of such physical properties on microstructure characteristics of carbon steels. Eddy current testing was performed to investigate the sensibility of using a NDT for in-situ characterization of carbon steels, extending its application for industrial inspection of wire manufacturing. The main findings of this investigation conclude this chapter.

I. EFFECT OF CARBON CONTENT

I.1. Microstructure and mechanical properties

Plain carbon steel wires of 4 mm in diameter and carbon content varying from 0.03 to 0.78 wt. %C were selected to investigate the carbon effect on the microstructure and, consequently, on the mechanical and physical properties of steels. The heat treatment, including austenitization at 950°C and cooling at a constant temperature of 580°C for a few seconds, allowed to obtain the samples of group A.

The typical microstructures of ferrite, ferrite-pearlite, and pearlite samples are shown in the LOM and SEM micrographs of Figure 70. The samples were etched in 3% Nital and 10% potassium metabisulfite solution for revealing proeutectoid ferrite grains on the LOM and in 4% Picral solution for SEM observation. Ultra-low carbon steel with 0.03 wt. %C was used to produce a fully ferritic microstructure with grains that varied by a few tens of microns, as shown in Figure 70-a and Figure 70-i. Hypoeutectoid steels with the composition ranging from 0.20 to 0.65 wt. %C presented ferrite-pearlite microstructures with pearlite fractions varying from 33.0 to 98.9%. In the optical micrographs of Figure 70-b to Figure 70-g, a network of proeutectoid ferrite (bright regions) is observed along the grain boundaries surrounding areas of pearlite, which is a constituent consisted of alternate lamellae of eutectoid ferrite and cementite phases. Pearlite nodule sizes were observed to decrease with decreasing proeutectoid ferrite fraction. In SEM images of Figure 70-j to Figure 70-o, the dark regions are the α-phase that occurs both in pearlite and in simple ferrite grains, while the Fe_3C is white and sticks out of the ferrite matrix in pearlite. The eutectoid steel with 0.78 wt. %C exhibits a fully pearlitic microstructure, as shown in Figure 70-h and Figure 70-p.

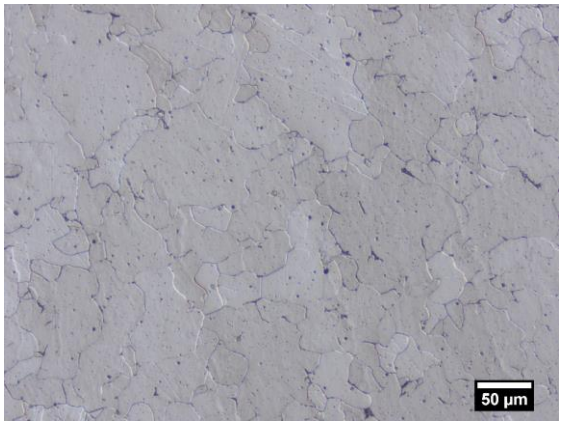

(a)

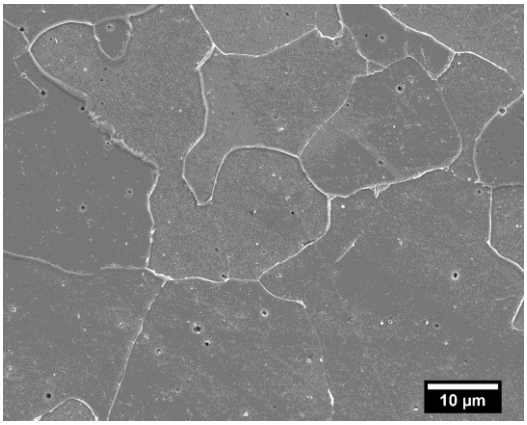

(i)

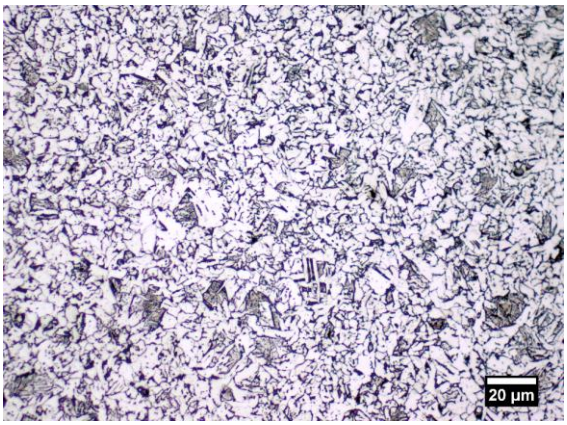

(b)

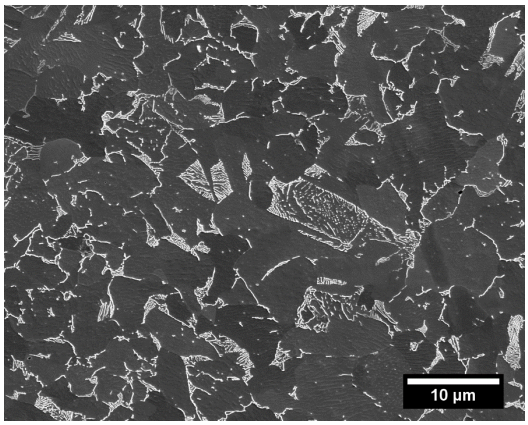

(j)

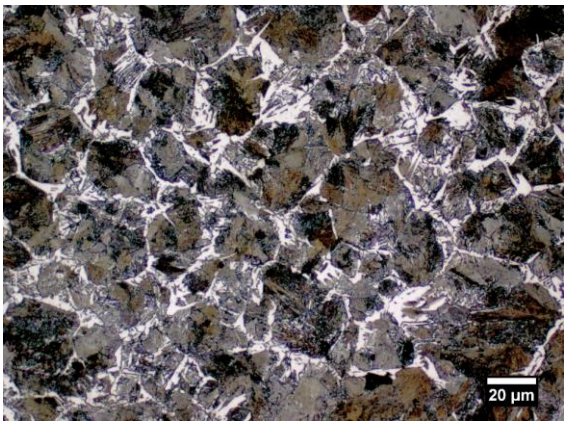

(c)

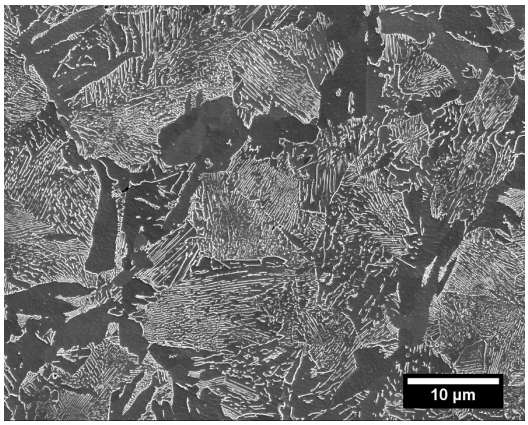

(k)

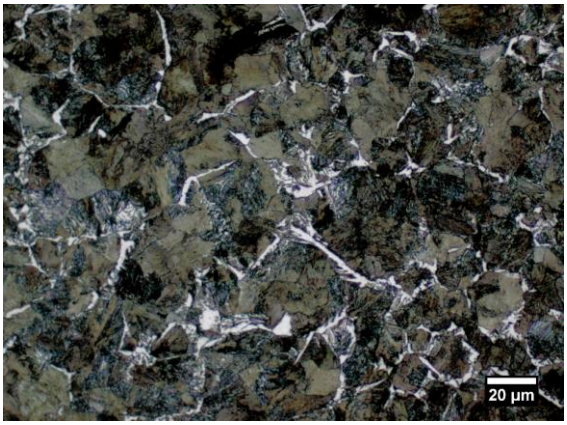

(d)

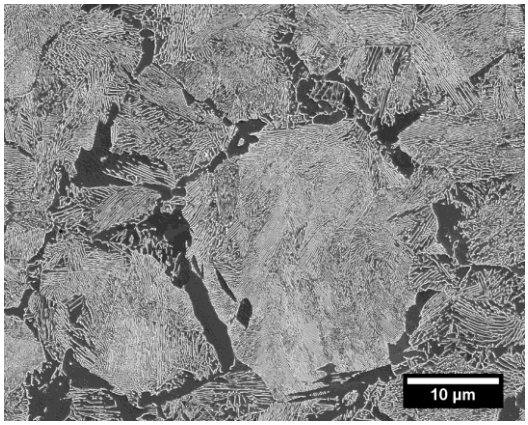

(l)

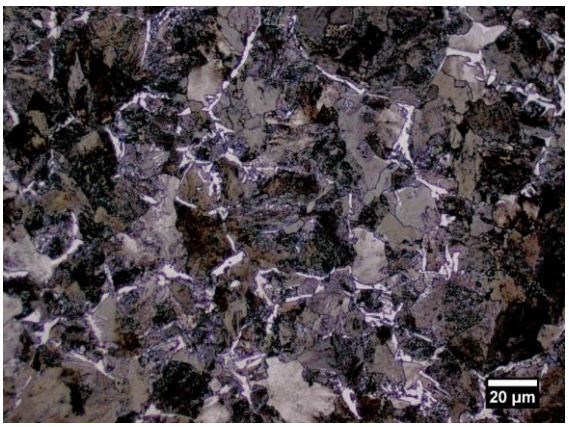

(e)

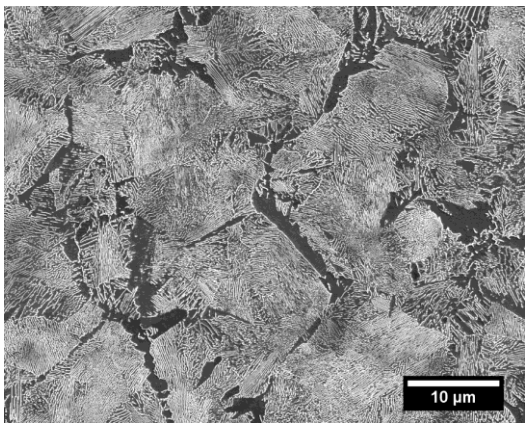

(m)

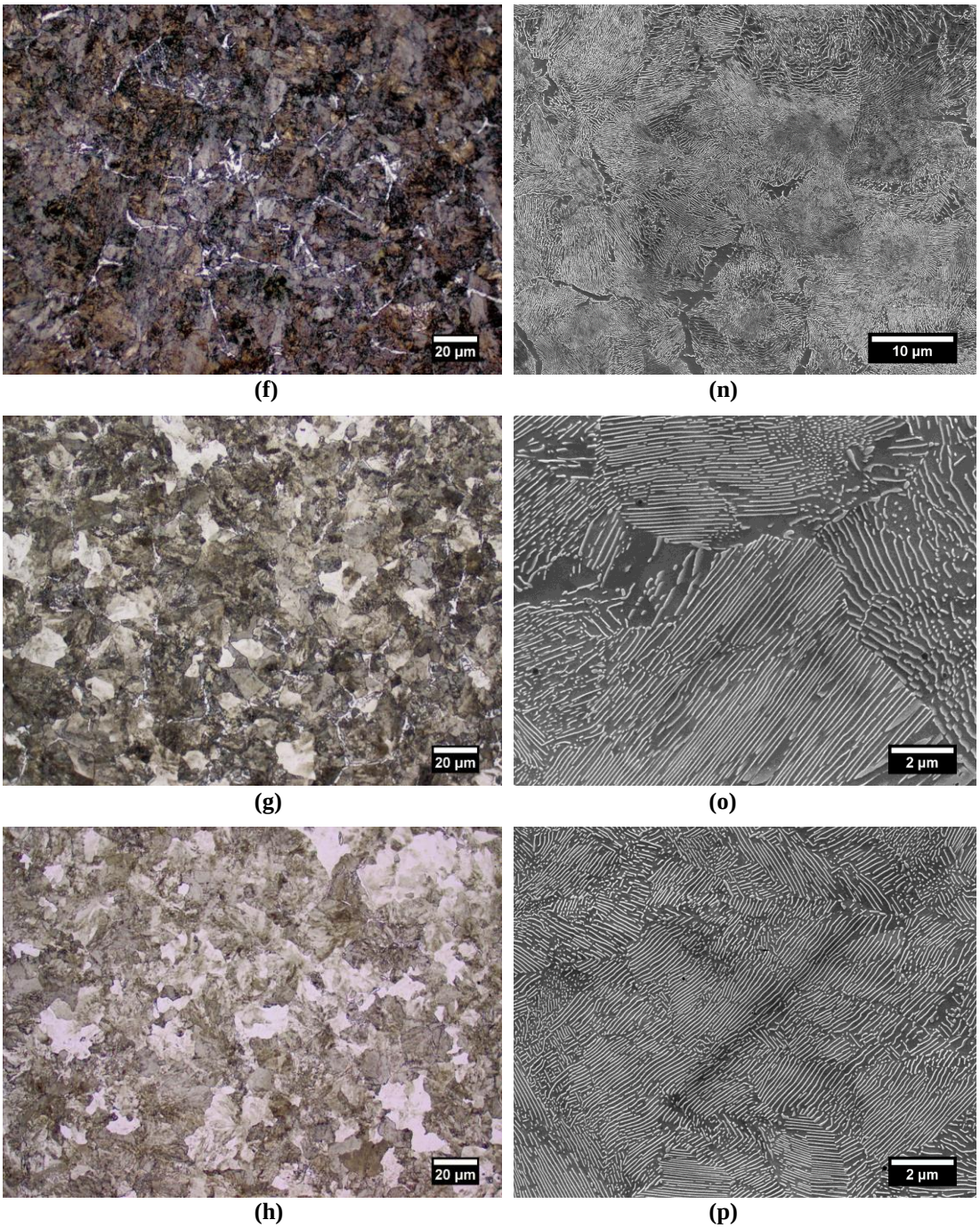

Figure 70: Optical (right) and SEM (left) micrographs of the AISI (a, i) 1000; (b, j) 1020; (c, k) 1035; (d, l) 1050; (e, m) 1055; (f, n) 1060; (g, o) 1065; and (h, p) 1080 steels

The main microstructural aspects were evaluated by metallographic analysis of the AISI 1000 series plain carbon steels. The volume fraction and interlamellar spacing of pearlite were determined from heat-treated samples hereto described, and the prior-austenite grain sizes were calculated from quenched samples of each steel grade. The descriptive statistics of the measured parameters, including the men, standard deviation, and 95% confidence interval are summarized in Table 5 and Table 6.

Table 5: Prior-austenite grain size values of samples of group A

AISI steel	Prior-austenite grain size (µm)			
	Mean	Standard deviation	95% confidence interval	
			Lower bound	Upper bound
1000	91.30	20.60	87.66	94.94
1020	73.61	9.04	61.07	86.16
1035	66.55	1.22	64.85	68.24
1050	60.63	6.18	52.05	69.21
1055	59.57	4.86	50.65	68.49
1060	48.66	2.50	45.16	52.13
1065	31.11	3.01	30.06	32.15
1080	37.14	4.12	35.31	38.18

Table 6: Average pearlite volume fraction and true interlamellar spacing of group A

AISI steel	Pearlite volume fraction (%)				True interlamellar spacing (nm)			
	Mean	Standard deviation	95% confidence interval		Mean	Standard deviation	95% confidence interval	
			Lower bound	Upper bound			Lower bound	Upper bound
1000	0.00	0.00	0.00	0.00	-	-	-	-
1020	33.03	6.56	31.03	35.02	212.50	50.63	204.64	220.35
1035	78.28	2.36	76.97	79.59	196.46	27.32	192.23	200.70
1050	94.70	0.69	94.26	95.14	157.00	20.35	153.84	160.16
1055	95.79	0.68	95.10	96.18	153.09	21.81	149.71	156.48
1060	98.07	0.51	97.73	98.41	145.51	16.34	142.98	148.05
1065	98.91	0.31	98.71	99.11	158.93	30.05	153.61	164.25
1080	99.92	0.08	99.87	99.98	125.50	20.16	121.93	129.07

As previously mentioned, the samples were thermally treated on a fast-cooling cycle. Consequently, the ratio of proeutectoid ferrite to pearlite within hypoeutectoid steels is smaller than that would be obtained on an equilibrium transformation. The increase of pearlite fraction cannot occur without a corresponding change in its composition ($\alpha + Fe_3C$), usually 87.5% ferrite and 12.5% cementite. Hence, the α-phase amount in pearlite structure increases, which leads to a decrease in the carbon content in pearlite [12,117], resulting in an increase of the pearlite interlamellar spacing, even though transformation temperature was maintained the same.

The one-way analysis of variance at a 0.05 level was used to determine whether there is any statistically significant difference between the means of these estimated variables, as shown in Figure 71. The prior-austenite grain size is found to decrease with increasing carbon content. The carbon content has a significant impact on the austenite grain size of the investigated samples, $F(7,191)=100.55$, $p=1.37.10^{-60}$. Smaller PAGS contributes to faster kinetics for both proeutectoid ferrite and pearlite formation, as it promotes an increase of the austenite grain boundary area, increasing the nucleation sites. Such an increase in carbon amount produces a significant change in the volume fraction of pearlite, $F(7,121)=1333$, $p=2.81.10^{-111}$.

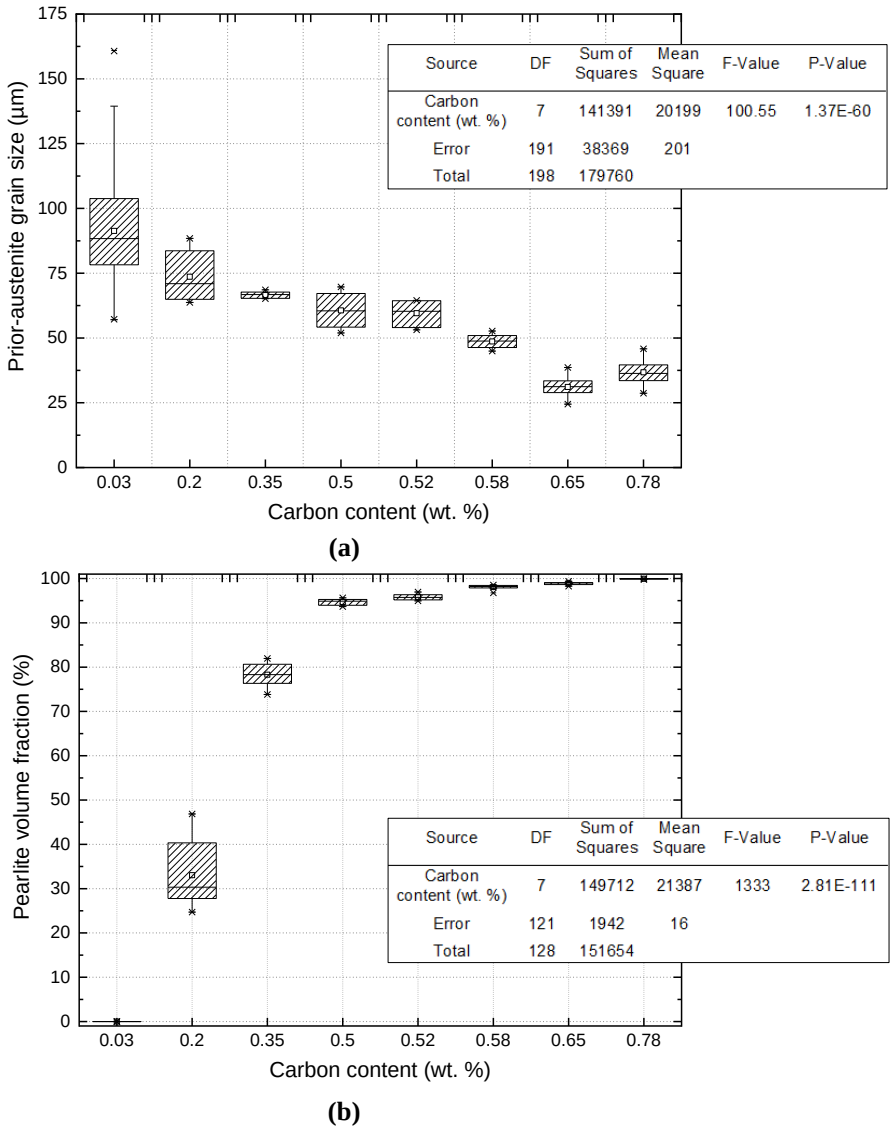

Figure 71: Box-plot charts of one-way ANOVA test (α=0.05) of the (a) prior-austenite grain size and (b) pearlite volume fraction for the AISI 1000 series plain carbon steels

As observed in Figure 72, there is also a significant difference in the average pearlite interlamellar spacing among the samples, $F(6, 1053)=164.43$, $p=2.24.10^{-147}$.

Besides, the Tukey's post hoc test was employed for comparing particular differences in the means between all possible group pairings of the studied steels. Notably, the means of low-carbon steels AISI 1020 and 1035 grades differ significantly from the other five groups. The pearlite structure observed in these specimens presents discontinuous cementite lamellae, as the amount and continuity of carbide layers depend on the carbon concentration of the steel. The difference between the means of the medium-carbon samples, the AISI 1050, 1055, 1060, and 1065 steels, are not significant at the 0.05 level. The eutectoid AISI 1080 steel presents a lamellar structure with a slightly lower average interlamellar spacing.

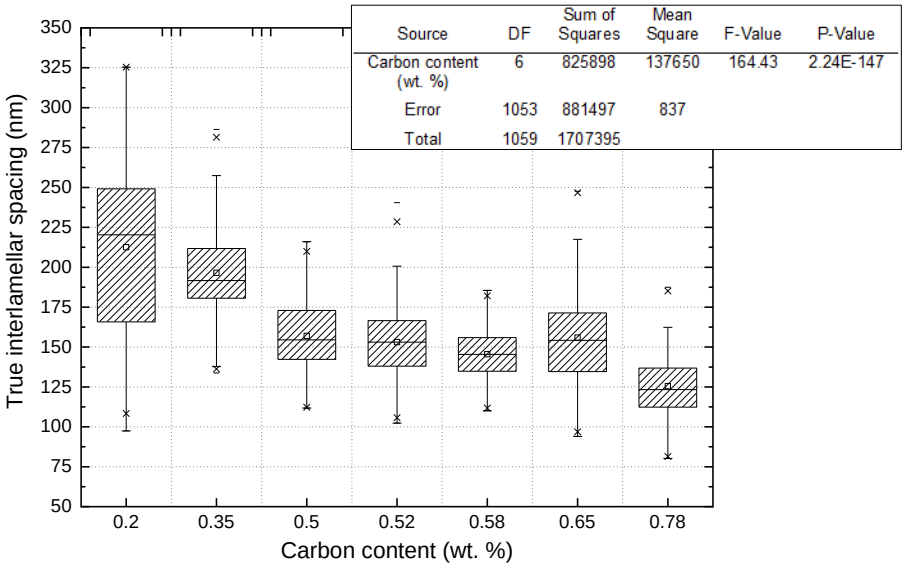

Figure 72: Box-plot chart of one-way ANOVA test of the estimated true interlamellar spacing values for AISI 1000 series samples, with a critical significance level of 0.05

The SEM images of Figure 73 illustrates the morphology of proeutectoid ferrite-pearlite microstructure observed in low-carbon AISI 1020 and 1035 steels.

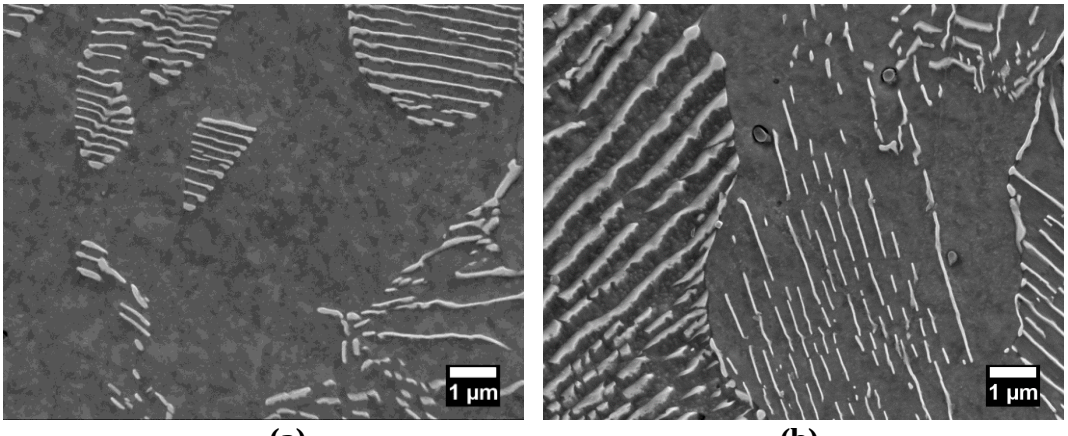

(a) **(b)**

Figure 73: SEM micrographs of the hypoeutectoid AISI (a) 1020 and (b) 1035 steels

The size of colonies and nodules of pearlite depends on several parameters of phase transformation and is likely to decrease with the transformation temperature and the previous austenitic grain size [32]. However, the mean colonies and nodules sizes were not determined in this study for the reason that their boundaries are quite difficult to be identified by the existing metallography and electron microscopy methods [28,29], and they do not significantly influence the properties of steel [37,38]. Possible variations of cementite lamellae thickness were not considered due to the difficulty in acquiring accurate values of such fine microstructures through metallographic observations.

The stress-strain curves of the AISI 1000 series are represented in Figure 74. The mechanical properties determined by tensile and microhardness tests are shown in Table 7, displayed as average values with respective standard deviations.

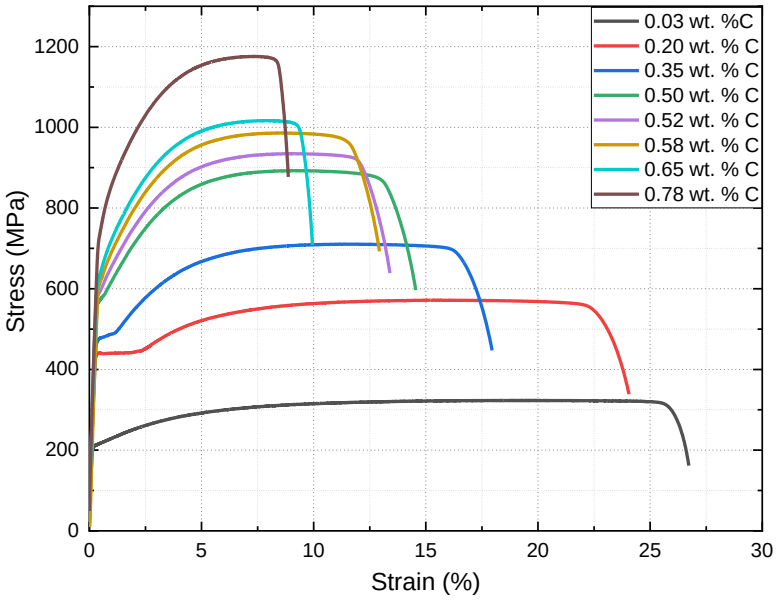

Figure 74: Stress-strain curves of the plain carbon steels (group A)

Table 7: Mechanical properties of the AISI 1000 series plain carbon steels

AISI steel	Yield strength (MPa)	Ultimate tensile strength (MPa)	Elongation (%)	Reduction of area (%)	Vickers hardness number (HV)
1000	210 ± 2	323 ± 0	27.4 ± 1.4	87 ± 0	102 ± 6
1020	438 ± 4	571 ± 0	23.6 ± 0.4	77 ± 0	170 ± 3
1035	478 ± 2	709 ± 1	18.1 ± 0.3	73 ± 1	209 ± 6
1050	573 ± 1	892 ± 1	14.3 ± 0.3	66 ± 1	266 ± 7
1052	593 ± 1	935 ± 0	13.6 ± 0.5	64 ± 1	272 ± 6

1058	625 ± 2	986 ± 1	13.3 ± 0.4	60 ± 1	295 ± 9
1065	642 ± 5	1019 ± 2	10.4 ± 0.4	61 ± 1	317 ± 11
1080	760 ± 0	1175 ± 1	9.3 ± 0.4	54 ± 2	354 ± 9

As the pearlite volume fraction increases, the proportion of cementite, which is a relatively hard phase, grown. In consequence, the strength and hardness of plain carbon steels raise accordingly. The elongation and reduction of area decrease linearly with increasing carbon concentration, indicating a decrease in ductility. Moreover, the refinements of prior-austenite grain and interlamellar spacing with carbon content also contribute to the increase of strength and ductility reduction of the studied steels.

Figure 75 shows the correlations between the main mechanical properties and the carbon concentration of the plain carbon steel samples of group A.

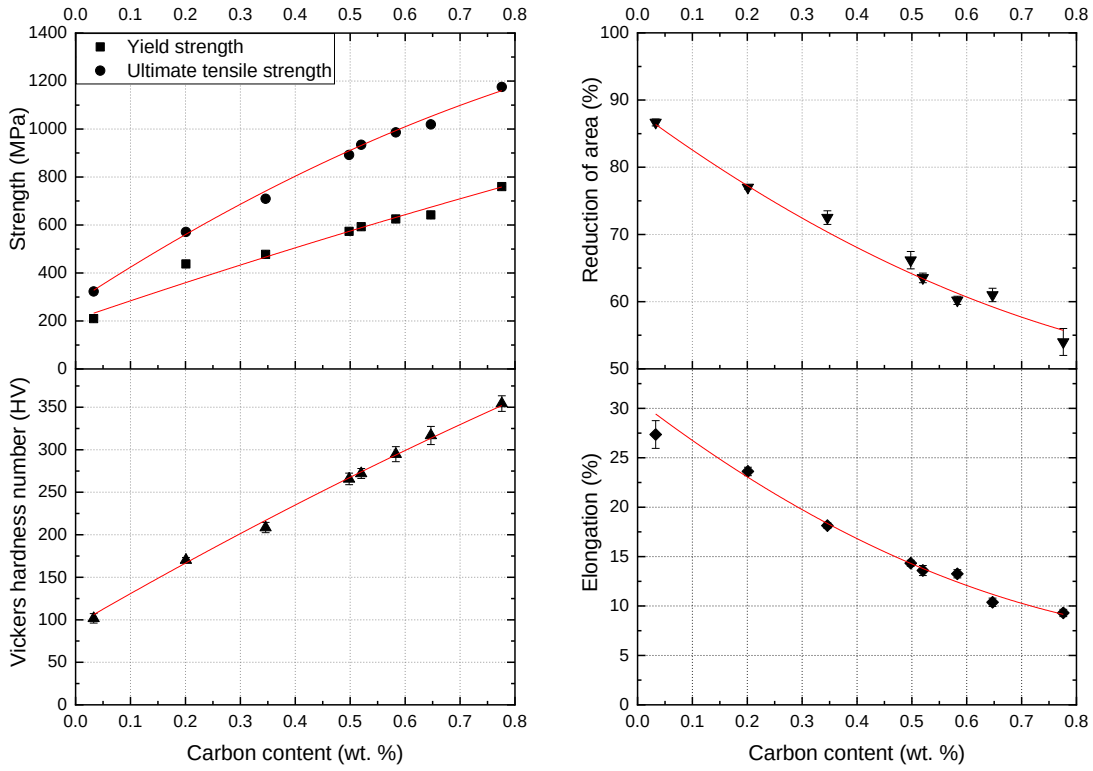

Figure 75: Correlations of tensile properties and Vickers hardness with the carbon concentration of the plain carbon steels of group A

As discussed, the increasing amount of carbon alters not only the proeutectoid ferrite and pearlite phase balance of plain carbon steels but also the prior-austenite grain size and the interlamellar spacing of pearlite. In order to study these microstructural parameters separately, samples of 1080 steel were austenitized at 950 and 1050°C for obtaining two different austenite grain sizes and then cooled at

constant temperatures from 540 to 640°C, producing pearlitic samples with different interlamellar spacing. These samples constitute the group B. The measured prior-austenite grain sizes are shown in Table 8. The volume fraction of proeutectoid ferrite is not significant, and thus the eutectoid samples of group B are considered to be entirely pearlitic. The true interlamellar spacing means are presented in Table 9.

Table 8: Prior-austenite grain size estimated values of samples of group B

AISI steel	Austenitization temperature (°C)	Prior-austenite grain size (µm)			
		Mean	Standard deviation	95% confidence interval	
				Lower bound	Upper bound
1080	950	37.14	4.12	35.31	38.18
1080	1050	49.15	5.30	47.32	50.97

Table 9: True interlamellar spacing of AISI 1080 steels patented at different transformation temperatures

Austenitization temperature (°C)	Transformation temperature (°C)	True interlamellar spacing (nm)			
		Mean	Standard deviation	95% confidence interval	
				Lower bound	Upper bound
950	540	95.40	9.13	93.78	97.01
950	560	103.42	12.22	101.25	105.58
950	580	125.50	20.16	121.93	129.07
950	600	128.94	22.21	125.01	132.87
950	620	153.46	27.94	148.52	158.41
950	640	185.50	37.48	178.86	192.13
1050	540	88.32	17.39	81.14	95.50
1050	560	99.60	26.40	88.70	110.49
1050	580	121.00	28.78	109.12	132.89
1050	600	126.88	30.05	121.68	146.49
1050	620	150.61	22.80	141.20	160.02
1050	640	180.78	31.76	167.67	193.89

Levene's test demonstrated that the population variances of the samples austenitized at 950 and 1050°C were equal. One-way ANOVA test determined the statistical significance between the mean PAGS obtained at 950 and 1050°C at a confidence level of 0.05, $F(1,68)=118.35$, $p=1.55.10^{-16}$, as shown in Figure 76.

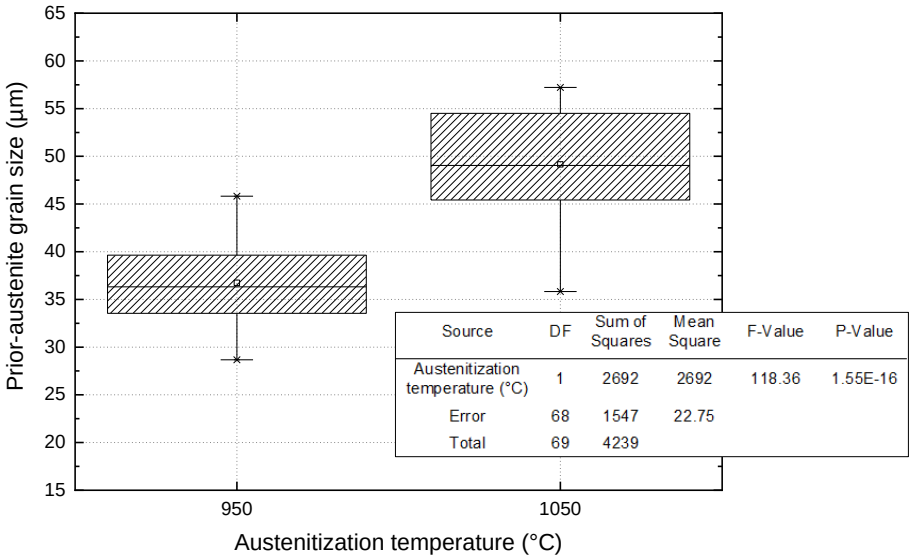

Figure 76: Box-plot chart of one-way ANOVA test (α=0.05) of the PAGS for the fully pearlitic samples obtained at two different austenitization temperatures

Concerning the estimated values of true interlamellar spacing, a two-way ANOVA test was performed considering both the austenitization and transformation temperature factors, as seen in Figure 77. At the 0.05 level, the true interlamellar spacing means are statistically significantly different concerning both the different austenitization temperatures (i.e., different PAGS), $F(1,898)=4.42$, $p=0.03$, and the various transformation temperatures, $F(5,894)=289.85$, $p=3.60.10^{-184}$. It evidences the primary influence of the transformation temperature on pearlite interlamellar spacing.

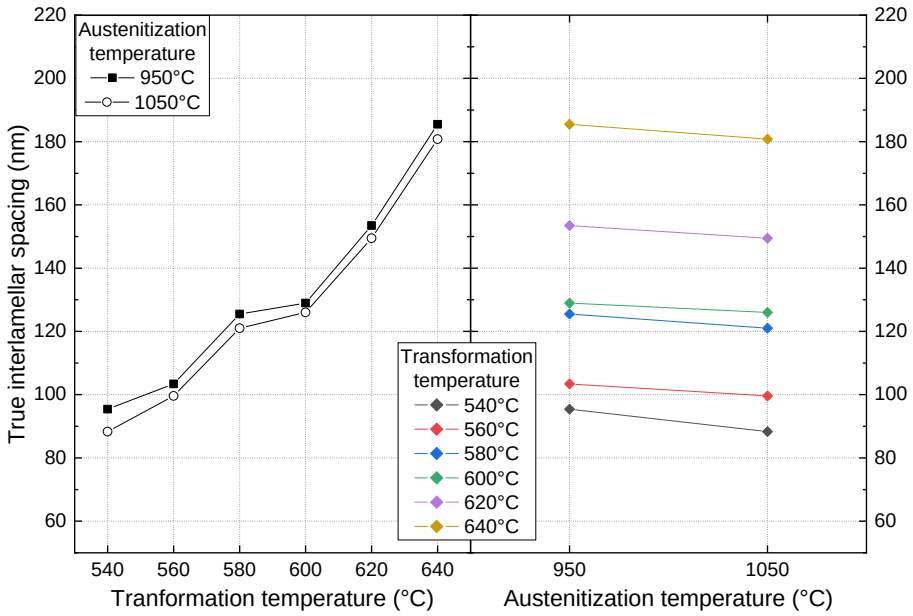

Figure 77: Two-way ANOVA test (α=0.05) of the determined true interlamellar spacing values for the group B samples heat-treated at different conditions

Figure 78 shows the cross-section SEM micrographs of the eutectoid steels with relatively fine and coarse pearlite microstructure.

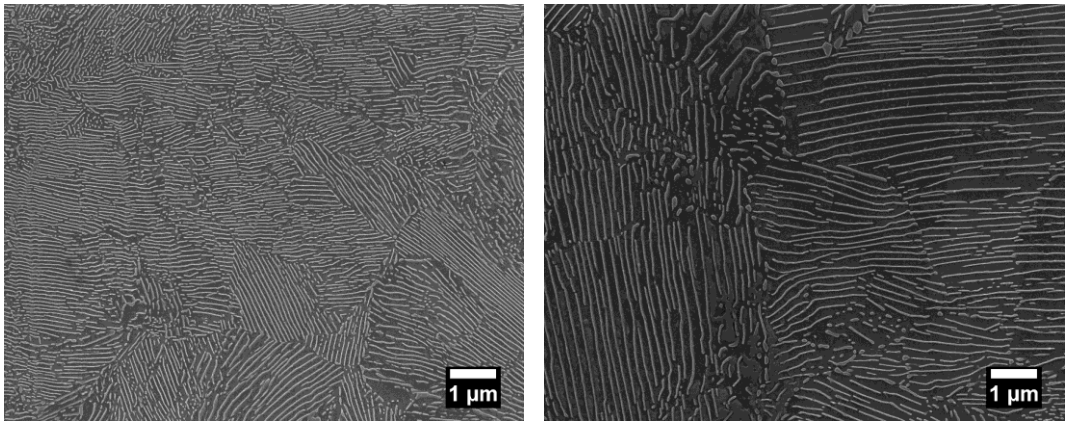

(a) **(b)**

Figure 78: SEM images showing fine and coarse lamellar pearlite microstructures of the 1080 steel heat-treated at, respectively, (a) 540°C and (b) 640°C

Table 10 shows the average and the corresponding standard deviations of the mechanical properties evaluated for group B.

Table 10: Mechanical properties of the AISI 1080 steels produced at different austenitization and transformation temperatures

Austenitization / Transformation temperatures (°C)	Yield strength (MPa)	Ultimate tensile strength (MPa)	Elongation (%)	Reduction of area (%)	Vickers hardness number (HV)
950 / 540	857 ± 5	1252 ± 2	8.2 ± 0.9	53 ± 0	374 ± 12
950 / 560	807 ± 5	1212 ± 1	9.3 ± 0.7	52 ± 0	370 ± 11
950 / 580	760 ± 0	1175 ± 1	9.3 ± 0.4	54 ± 2	354 ± 9
950 / 600	719 ± 6	1141 ± 1	9.8 ± 0.6	53 ± 0	350 ± 9
950 / 620	660 ± 5	1099 ± 1	10.5 ± 0.8	53 ± 0	328 ± 9
950 / 640	598 ± 2	1045 ± 1	10.9 ± 0.9	50 ± 1	322 ± 17
1050 / 540	883 ± 7	1272 ± 1	9.1 ± 0.5	52 ± 1	388 ± 10
1050 / 560	837 ± 1	1238 ± 1	9.3 ± 0.3	51 ± 0	368 ± 9
1050 / 580	798 ± 12	1201 ± 1	10.0 ± 0.2	49 ± 1	362 ± 6
1050 / 600	743 ± 5	1164 ± 1	9.9 ± 0.1	50 ± 0	353 ± 12
1050 / 620	964 ± 10	1121 ± 0	10.3 ± 0.2	48 ± 1	333 ± 10
1050 / 640	636 ± 14	1073 ± 1	10.5 ± 0.2	44 ± 0	321 ± 12

The pearlitic samples with a smaller PAGS present slightly lower yield strength and ultimate tensile strength values, and higher cross-sectional area reductions than

the samples with a larger austenite grain size. However, the differences in the PAGS values between these samples, estimated in the order of 15 µm, do not seem significant enough to effectively affect their mechanical properties, as shown in Figure 79. In the plots, the mean values and their respective standard deviations are displayed.

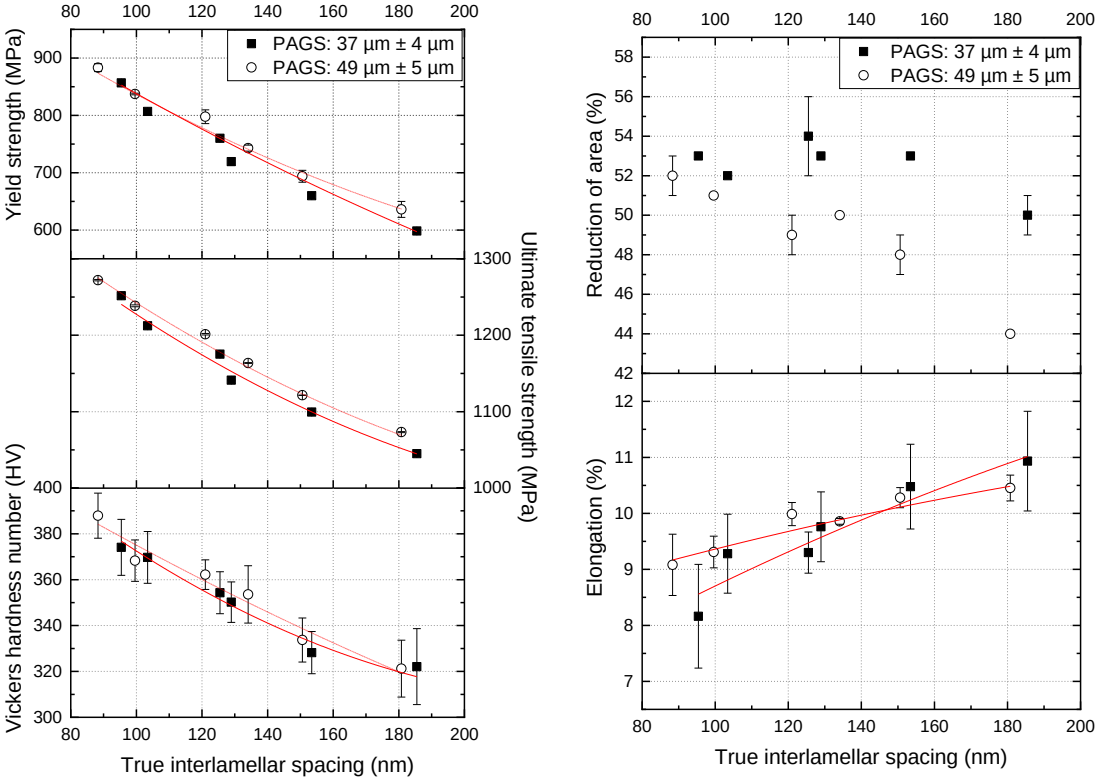

Figure 79: Tensile properties and Vickers hardness of group B samples

As indicated in the statistical analysis, the interlamellar spacing does not depend on the PAGS and is strongly affected by the austenite decomposition temperature. Among the investigated microstructural parameters, the interlamellar spacing variations significantly affect the mechanical properties of pearlitic steels. The interlamellar spacing decrease alters the mean free path of dislocations within the lamellae, restricting the mobility of dislocations, which results in an increase in the yield and ultimate tensile strengths and Vickers hardness values. Also, the elongation decreases, indicating a decrease in the ductility of the materials. Significant changes in the reduction of area are not observed.

I.2. Eddy current testing

Non-destructive eddy current tests were performed at a low frequency of 200 Hz and at room temperature, in the way to ensure that the microstructural parameters were the

only significant factors affecting the material response to the induced current during the test. Voltage variations were used to represent the impedance changes of the coil. It includes the resistance and inductive voltages, which are relative, respectively, to the resistive and inductive components of the coil's impedance. The magnitude of the total voltage is correspondent then to the primary current in the circuit and is related to the impedance amplitude that indicates the coil's total opposition to current flow. The measurements were carried out continuously during heat-treatments and off-line using the collected wire samples.

Gage R&R analysis was carried out to evaluate the impact of varying several parameters on the ECT precision, as shown in Figure 80. For this, repeated experiments were carried out in distinct reference materials, at various environments, for different operators, and reproduced on a three-week time scale. It is found that the measurements of varied materials (i.e., distinct physical properties) have a relevant effect on electromagnetic responses. The factors related to the repeatability and reproducibility (environment, operators) are practically irrelevant to explain measurement variations. It confirms the accuracy of the measurement system.

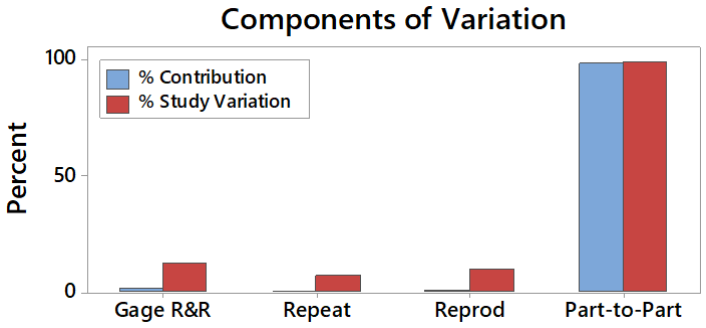

Figure 80: Gage R&R for eddy current measurement system

Levene's test showed that the population variances are not equal for eddy current signals between the tested samples. Because the sample size is roughly equal for each group, the assumption of variance can be ignored for running one-way ANOVA tests. As shown in Figure 81, significant differences are observed between the total voltage signal means of the tested samples at a 0.05 level, $F(7,13774)=372905$, $p=0$. Statistical significant differences are also achieved for resistive voltage means, $F(7,13774)=436006$, $p=0$, and inductive voltage means between the samples, $F(7,13774)=253083$, $p=0$. Also, Tukey's hoc tests indicated that all means are significantly different from each other. These results suggest that each of the studied materials exhibit a characteristic signal response to their carbon content.

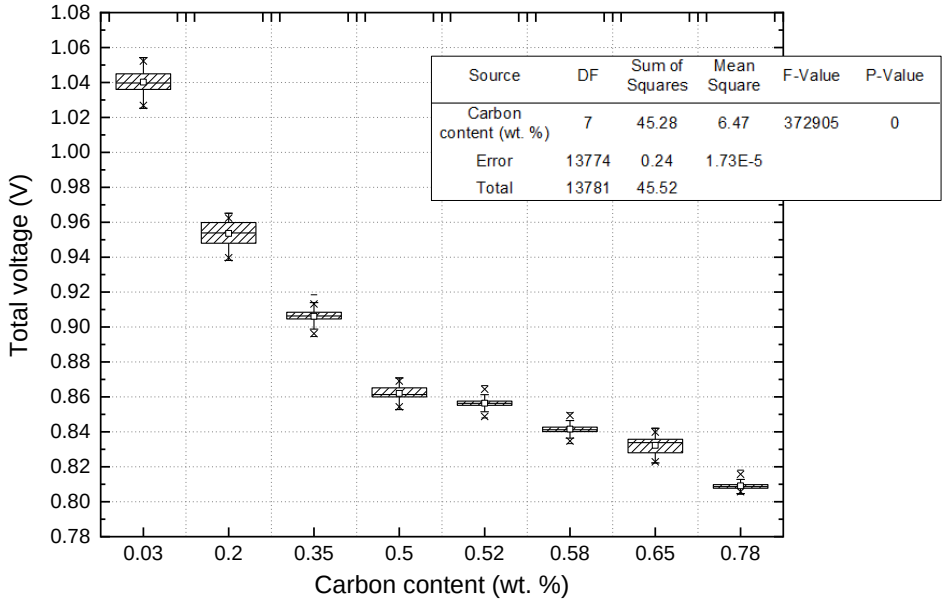

Figure 81: Box-plot result of one-way ANOVA (α=0.05) of the total voltage outputs for the various samples of group A

Figure 82 shows the eddy current voltage plane of the plain carbon samples of group A. It can be observed that the resistive voltage values increase while the inductive voltage decrease accordingly with the increasing carbon concentration.

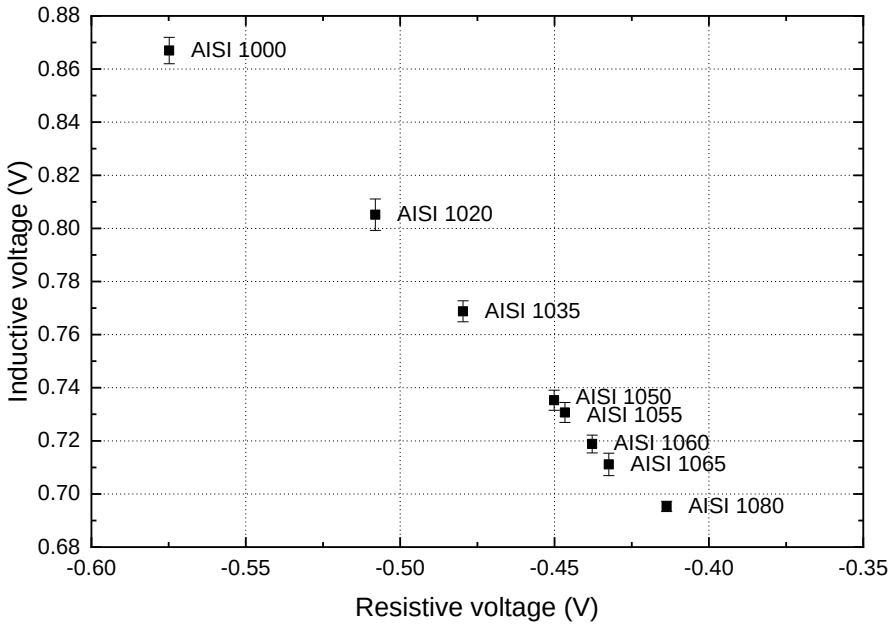

Figure 82: Eddy current voltage plane of the plain carbon steels of group A

The total voltage is expressed in the function of carbon content in Figure 83-a, displayed as average and standard deviations values. The ECT outputs correlate very well (R^2=0.99) with chemical composition variations. Figure 83-b shows the correlates the total voltage with the main microstructural parameters of plain carbon steels.

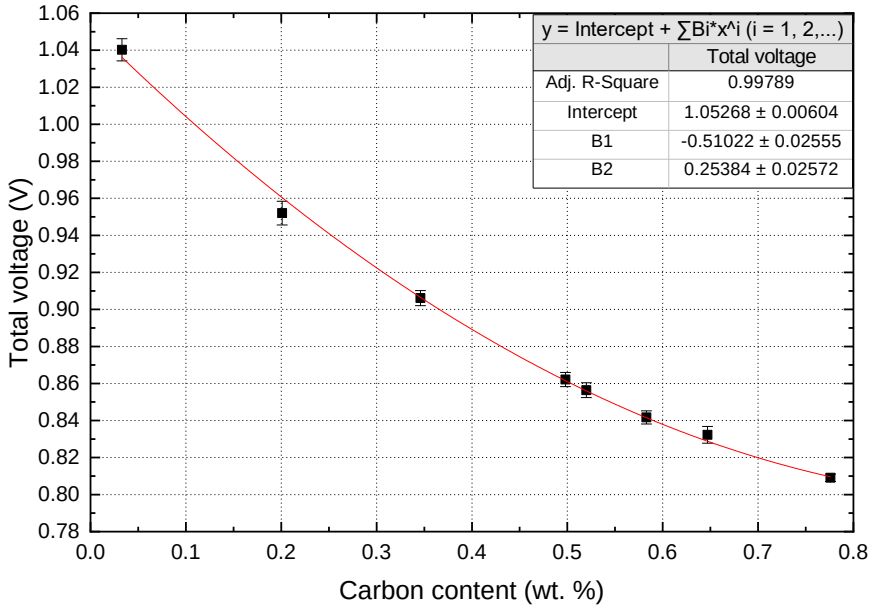

(a)

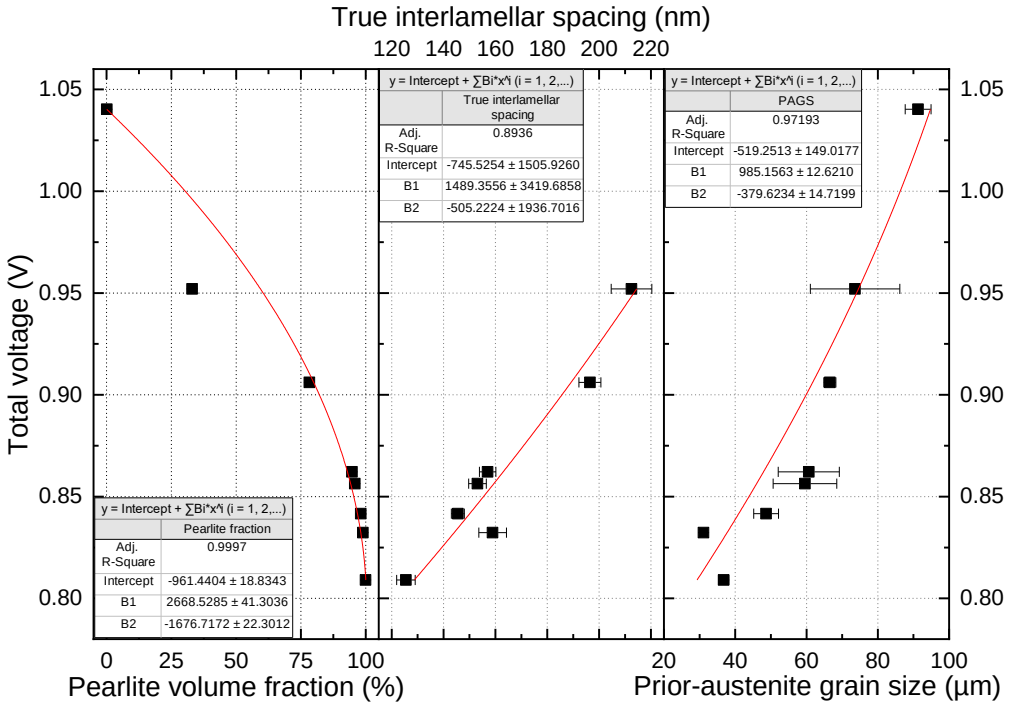

(b)

Figure 83: Relations between the eddy current responses and (a) the carbon content; and (b) the main microstructural parameters of plain carbon steels of group A

Good correlations are found between the total voltage responses obtained from ECT and the pearlite volume fraction (R^2=0.99), interlamellar spacing (R^2=0.89), and prior-austenite grain size (R^2=0.97).

The change in carbon amount alters the proeutectoid ferrite-pearlite phase balance, due to the formation of Fe_3C. Any change in the volume fraction of ferrite, which is a magnetically softer phase than pearlite, affects the magnetic characteristics

of the steel. Besides, it is known that the electromagnetic behavior of ferromagnetic materials may be affected by lattice defects, such as grain boundaries and secondary phase particles [9,96,99,118]. As the varying carbon content also affects the PAGS and interlamellar spacing of pearlite, these corresponding parameters might also contribute to the electromagnetic response variation of the carbon steels.

In order to determine more precisely the effects of prior-austenite grain size and interlamellar spacing of pearlite on the electromagnetic responses obtained for carbon steel wires, fully pearlitic steels of group B were also evaluated by eddy current technique. Figure 84 shows the results of the two-way ANOVA test for mean eddy current responses of the pearlitic samples of group B. The total voltage means signals are statistically different between the samples austenitized at 950 and 1050°C (i.e., different PAGS), F(1,7122)=7961, p=0, and between the patented steels at various transformation temperatures (i.e., different interlamellar spacing), F(5, 7118)=183191, p=0 at the 0.05 level. Similar results were found for the resistive and inductive voltage acquired during eddy current testing. It validates the assumed potential of this NDT for characterizing the principal microstructural parameters of pearlitic steel wires.

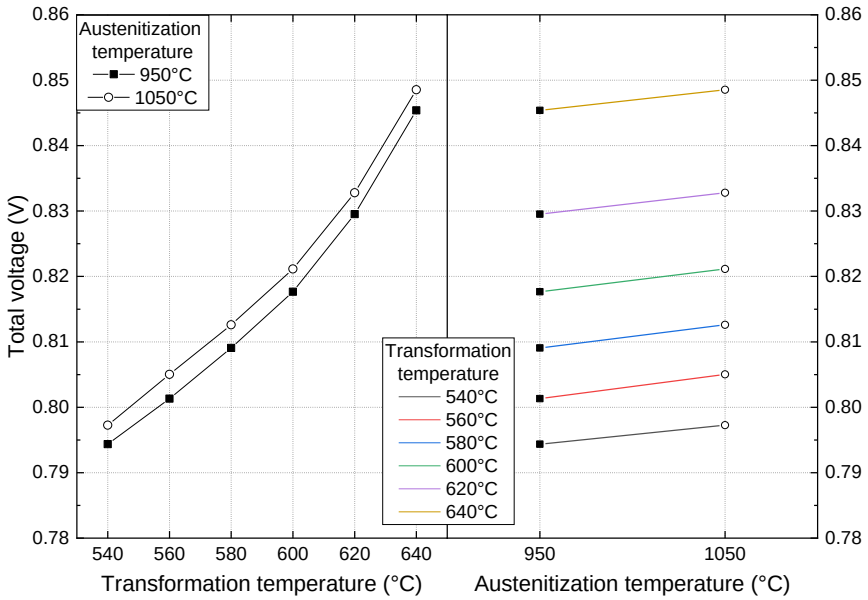

Figure 84: Two-way ANOVA test (α=0.05) of the total voltage for the group B samples

Figure 85 shows the measured eddy current voltage signals for the eutectoid samples of group B with different PAGS and interlamellar spacing. In the plots, average measurement values and standard deviations are represented. The different PAGS and pearlite interlamellar spacing ($\bar{S}$) ranges are reported according to the determined confidence interval at 95%.

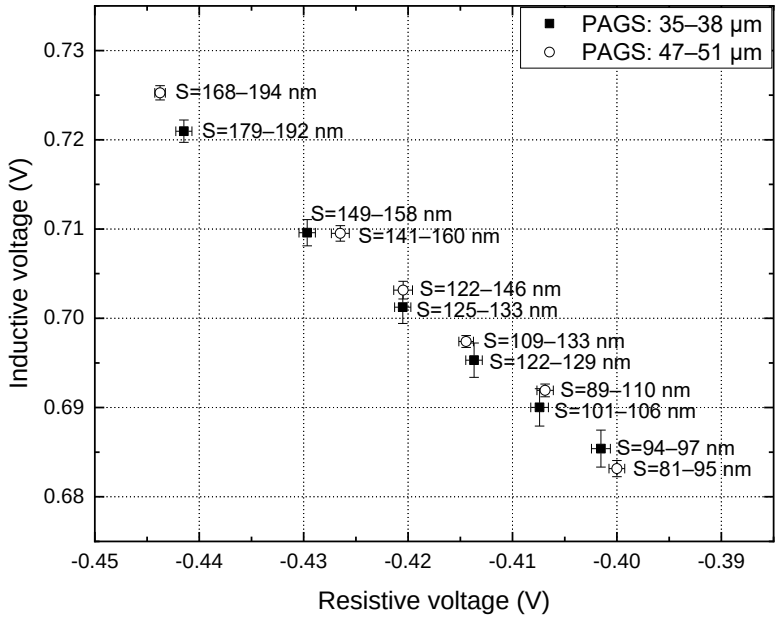

(a)

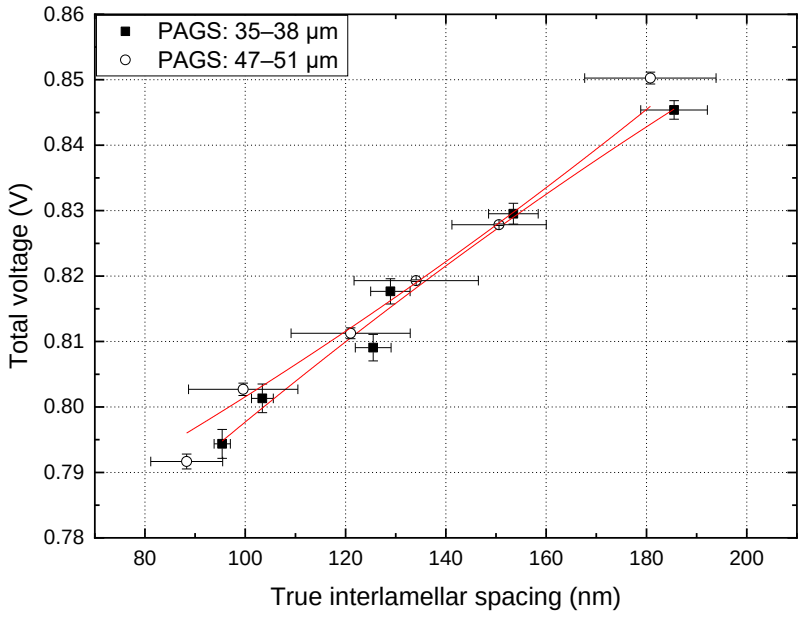

(b)

Figure 85: (a) Eddy current voltage plane, and (b) relations between the signal voltages and the interlamellar spacing of the group B eutectoid samples of two different PAGS

The samples with larger PAGS exhibited slightly higher signals, in the same was as found for tensile strength variations. In contrast, the ECT responses vary appreciably between the samples with varying interlamellar spacing. The resistive voltage increases, while the inductive and total voltage signals decrease with decreasing interlamellar spacing. The overall electromagnetic behavior in multiphase microstructures such as ferrite-pearlite and pearlite steels is observed to be a function of their different microstructural features, in particular proeutectoid ferrite-pearlite balance and width of ferrite lamellae. This result confirms that the prior-austenite grain

size has little effect on both the mechanical properties and the eddy current responses, at least within the grain size range investigated in this study. From this point on, only the samples with similar PAGS are discussed in this thesis manuscript.

Figure 86 shows the voltage plane corresponding to these samples of groups A and B. The effect of carbon content and transformation temperature on phase balance and interlamellar spacing of pearlite result in variations of the resistive and inductive voltages. It is possible to conclude that an increase in the volume fraction of cementite and a decrease of the distance between its lamellae in the pearlitic structure cause an increase in the resistive voltage and a reduction in the inductive voltage, and thus, the total voltage measured through eddy current testing. High-strength samples exhibit high resistive voltage and low inductive voltage. The more ductile the material, the lower is the resistive voltage, and the higher the inductive voltage signals.

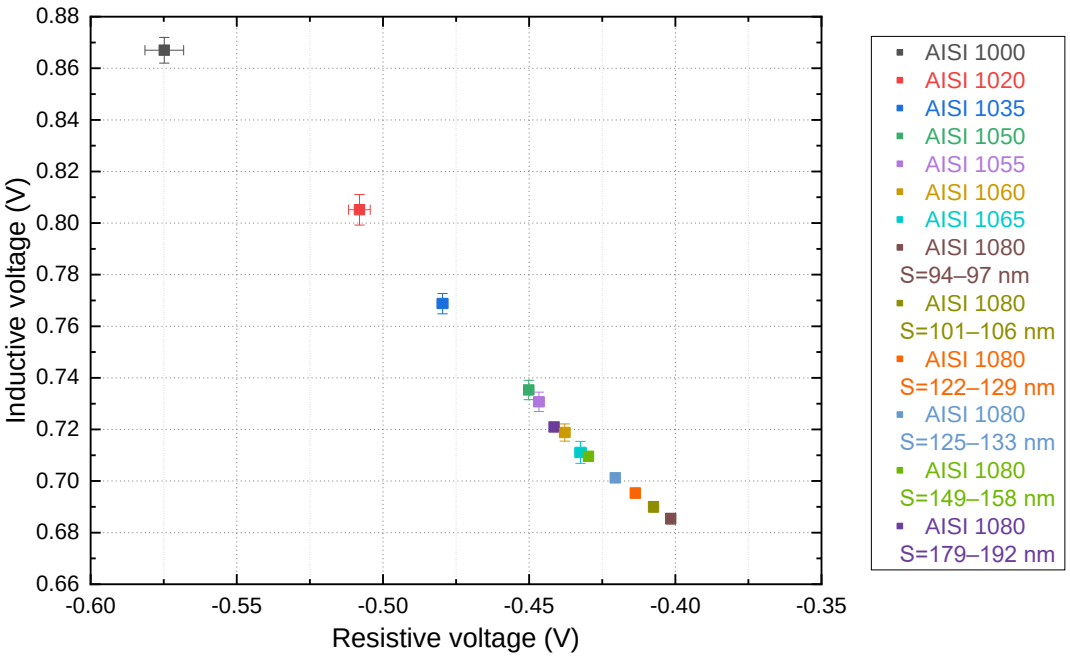

Figure 86: Eddy current voltage plane of groups A and B samples, with similar PAGS about 35–38 µm, and varying carbon content and pearlite interlamellar spacing

The potentiality of the eddy current method for characterizing mechanical properties of AISI 1000 series plain carbon steel wires is highlighted in Figure 87. A clear dependence was found between metallurgical and mechanical characteristics of the carbon steels and measured eddy current outputs. However, more profound knowledge about the relations between the microstructural, mechanical, and electromagnetic properties of steels is still necessary for a better interpretation of the material's responses.

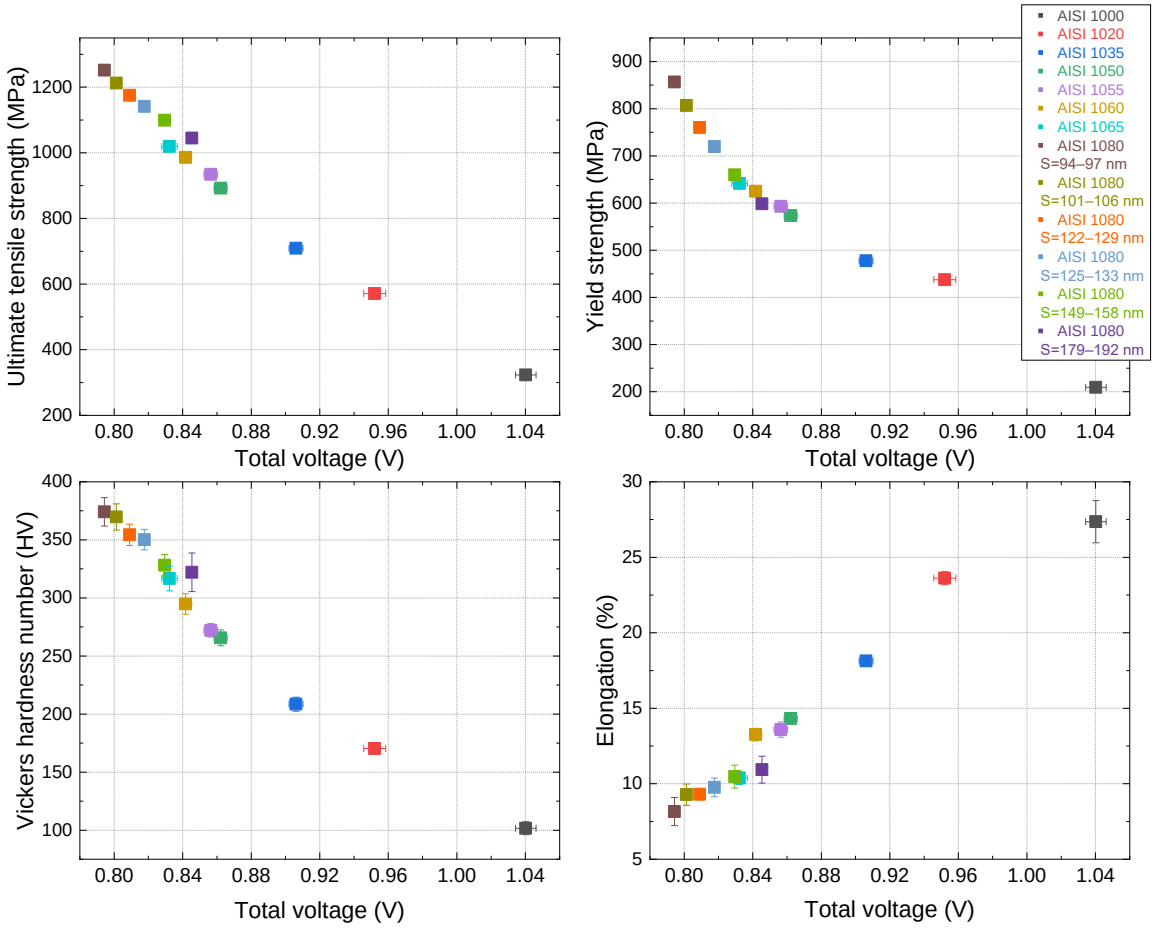

Figure 87: Relations between the eddy current signal voltages and the mechanical properties for the samples of groups A and B with similar PAGS

I.3. Electrical resistivity

Understanding the macroscopic measurable electrical properties of conductive materials, such as steels, goes through the comprehension of fundamental electronic properties on a microscopic scale and its relationship with their crystalline lattice structure.

In this context, carbon steel wires from the same batches of AISI 1020, 1035, and 1080 steels were heat-treated at the same conditions as groups A and B. AISI 1020 and 1035 steels were austenitized at 950°C and patented at 580°C for obtaining proeutectoid ferrite-pearlite samples, while the 1080 steel was patented at 540 and 640°C for producing fully pearlitic microstructures with different interlamellar spacing. The rod-shaped specimens with a diameter of 2 mm and a length of 1 cm were used to investigate the conductive behavior of ferrite-pearlite and pearlite steels. Their corresponding microstructures and mechanical properties are shown in Table 11, displaying average values and standard deviations.

Table 11: Microstructural and mechanical properties of the 2 mm diameter samples

AISI steel	Pearlite volume fraction (%)	Interlamellar spacing (nm)	Yield strength (MPa)	Ultimate tensile strength (MPa)	Elongation (%)	Vickers hardness values (HV)
1020	45 ± 4	211.7 ± 46.7	414 ± 1	604 ± 1	18.8 ± 0.7	179 ± 5
1035	83 ± 3	199.8 ± 34.3	488 ± 4	749 ± 1	13.8 ± 0.7	222 ± 6
1080	99 ± 1	91.4 ± 12.6	957 ± 4	1307 ± 1	9.8 ± 0.1	382 ± 10
1080	99 ± 1	136.1 ± 28.1	701 ± 2	1119 ± 1	10.6 ± 0.2	325 ± 12

Electrical resistivity measurements involved a four-probe setup connected to the samples by silver paste, as previously described in Chapter 2. The measuring current was set to 5 mA. The experiments were performed at temperatures ranging from 2 K up to 300 K. The results are shown in Figure 88.

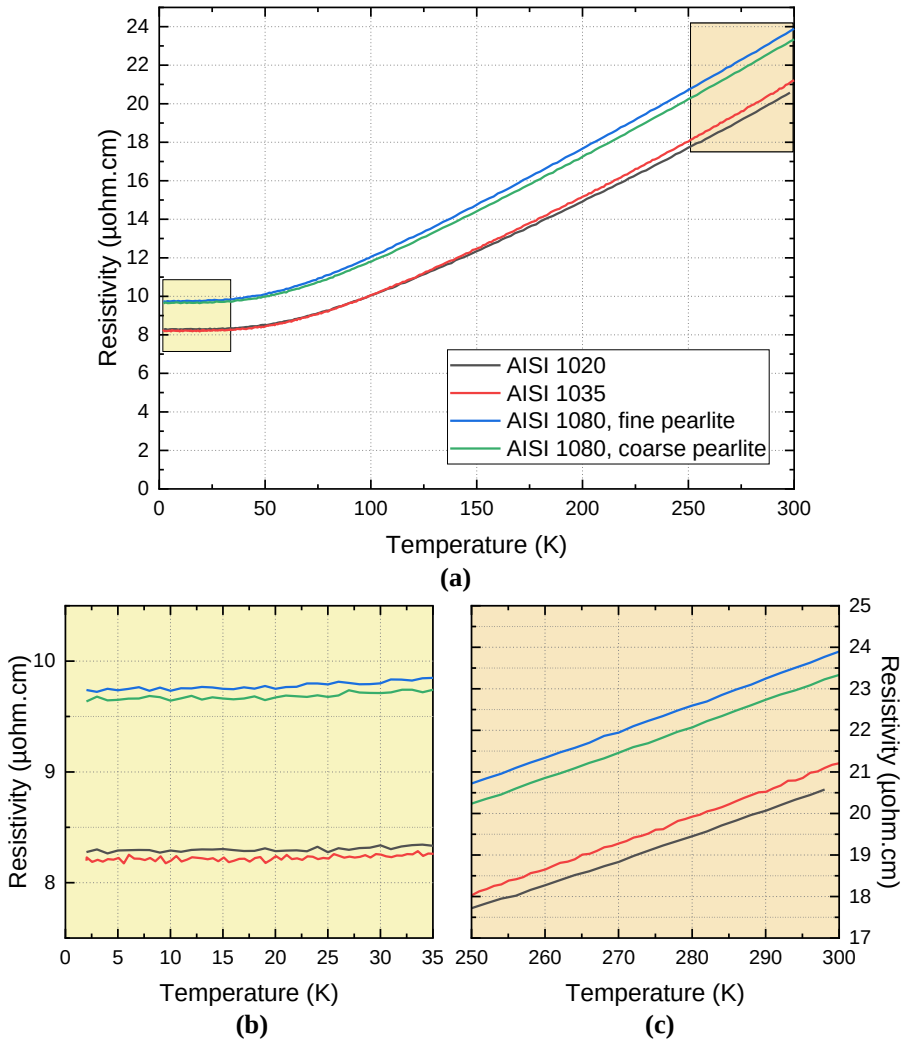

Figure 88: (a) Temperature dependence of electrical resistivity of ferrite-pearlite samples; in detail for temperature region (b) from 2 to 35 K and (c) from 250 to 300 K

As observed in Figure 88, the electrical resistivity of the carbon steels increases exponentially with increasing temperature. It indicates the metallic nature of the conductivity. The AISI 1020 and 1035 samples present lower resistivity than the eutectoid steels. The AISI 1080 sample with a narrower interlamellar spacing has slightly higher resistivity values than the sample with a coarser lamellar pearlite microstructure. The results demonstrate a decrease of conductivity with increasing pearlite fraction and decreasing interlamellar spacing.

The description of electron mobility in solids can be elucidated based on the classical free electron and wave-mechanical theories. The classical model assumes that an electron behaves as classical particles inside a solid. In the absence of an electric field, the free electrons in the valence band move randomly in different directions. When a potential difference is applied, a net flow of charge appears within the conductor, which constitute the electric current. Free electrons are accelerated, acquiring a drift velocity in the opposite direction to that of the electric field, as given:

$$\frac{dv}{dt} = \frac{e\varepsilon}{m} \tag{35}$$

where v is the velocity of the electrons, m and e are the mass and the charge of the electrons, and ε is the applied electric field. Their motion in a solid is constrained by instantaneous collisions between electrons and some lattice atoms, particularly crystal lattice imperfections, including vacancies, impurity atoms, dislocations, and grain boundaries. These successive collisions regularly reduce its kinetic energy, and the electrons may be accelerated until a finite drift velocity is eventually reached since it does not accelerate indefinitely. The electron average velocity $\bar{v}$ is given by:

$$\bar{v} = \frac{\tau e\varepsilon}{m} \tag{36}$$

where τ is the relaxation time, defined as the mean free time between a collision. Hence, the current density induced by an applied electrical field depends also on the average electron velocity, which is altered by the frequency of collisions with lattice atoms. The current density is induced by an applied electrical field, as described below:

$$J = \frac{\varepsilon}{\rho} = \sigma\varepsilon \tag{37}$$

where J is the current density, ρ is the resistivity, and σ is the conductivity. It is an equivalent form of expressing the Ohm's law, which defines a linear relationship between the voltage and the current in an electrical circuit determined by its resistance. The current density also depends on the average electron velocity, and it can be written in terms of the mobility of free electrons:

$$J = Ne\mu\varepsilon = Ne\bar{v} = \frac{Ne^2\tau\varepsilon}{m} \quad (38)$$

where N is the number density and μ is the mobility of electrons, defined as $\bar{v}.\varepsilon^{-1}$. By substituting Equation 38 on Equation 37, the electrical conductivity can be derived based on the classical free electron model, as given:

$$\sigma = \frac{1}{\rho} = \frac{Ne^2\tau}{m} \quad (39)$$

Ohm's law may be explained in terms of the interactions between electrons and crystallographic lattice imperfections. Although its simplicity and limitations, the classical model provides a useful insight into the electron motion in a solid, allowing to relate model parameters to measurable electronic properties such as electrical and thermal conductivity. [96,99] This approach can be extended by applying the quantum mechanical model, which considers the electrons as packets of energy with wave-like properties, according to the wave-particle duality. As hitherto designated, when in equilibrium, the free valence electrons of an atom are in random motion, with no preferential velocity and direction inside the solid. If an electric field is applied, not all the free electrons contribute to the current, as assumed by the classical model.

Regarding the quantum-mechanics principles, the number of electrons available to participate in conduction depends on the electronic band structure. The filling of bands occurs from the states of the lowest energy levels to the highest filled state, called the Fermi level. The valence band contains the highest occupied energy levels, and the uppermost band (conduction band) is the lowest range of vacant electronic states, located above the Fermi level. Only electrons that drift with a high velocity, close enough to the Fermi velocity, are free to move under the influence of an electric field and participate in conduction processes. The electrical conductivity depends then on the Fermi velocity and the population density of the electrons near the Fermi surface, besides the relaxation time after a scattering event.

Considering electrons to have a wave nature, its motion through an ideal crystal does not encounter any resistance, that is, without changing its intensity or direction. Elastic scattering thus occurs between electrons and lattice atoms with almost no energy loss. In real crystals, however, electrons may be inelastically scattered by any disturbance within its structure (e.g., lattice defects, impurities, phonons). The energy loss due to inelastic scattering causes a transition from an excited to a ground state, explaining the resistance to electric current transport. Figure 89 illustrates electron scattering events schematically.

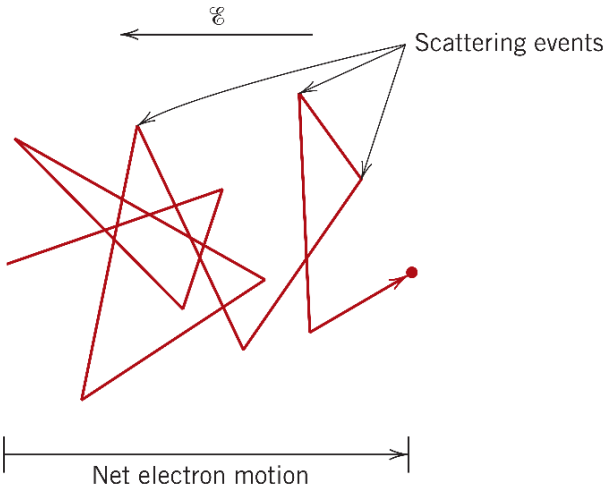

Figure 89: Electron path deflected by scattering events [11]

At temperatures close to the absolute zero, the electron-phonon scattering is almost negligible. The electrical resistance at these temperatures is due to the presence of lattice defects and impurities within a material, leading to a residual resistivity that is independent of temperature. The residual resistivity values measured at 2 and 35 K for each different sample are confirmed to be statistically significant at the 0.05 level via a one-way ANOVA test, $F(3, 166)=53279$, $p=2.19.10^{-247}$.

As shown in Figure 88-b, the residual resistivity of the ferrite-pearlite samples increases according to the increase of carbon content, mainly influenced by the increment of Fe_3C volume fraction with pearlite formation. The nucleation and growth of pearlite take place from the carbon redistribution from ferrite to cementite (6.67 wt. % C) and the depletion of carbon in the ferrite matrix (<0.03 wt. % C). The interstitial sites of cementite unit cell are illustrated in Figure 90.

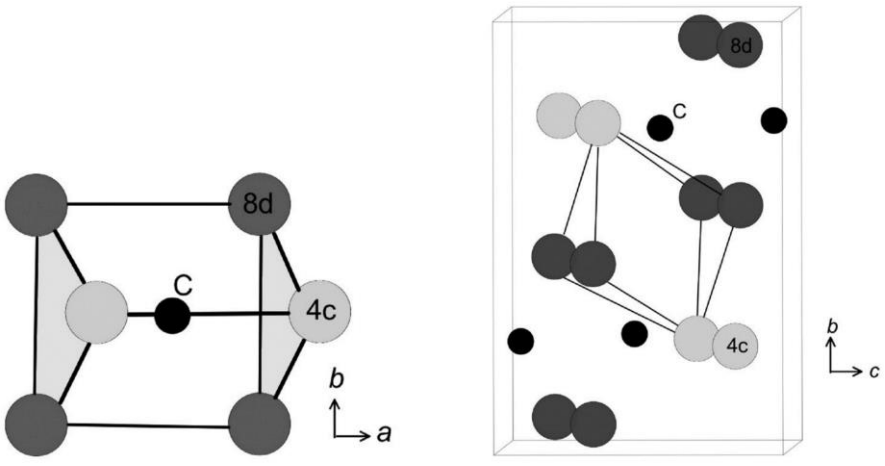

(a) **(b)**

Figure 90: Types of interstitial sites in cementite unit cell (a) prismatic and (b) octahedral, where C atoms are represented in black and Fe atoms in grey spheres [120]

In the orthorhombic unit cell of Fe_3C, carbon atoms occupy both trigonal prismatic sites of hexagonal close-packed basal planes of iron atoms (mirror planes) and octahedral interstices, as shown in. The tetrahedral positions of the orthorhombic structure are too small to be occupied by carbon atoms. [119,120]

Physical properties related to the electronic density of states of Fe_3C have been discussed by Häglund et al. [121], Chiou and Carter [122], Faraoun et al. [123], and Razumovskiy et al. [124]. It was found that states near the Fermi level are dominated by iron d states, whereas the low-lying states by carbon s and p contributions. The absence of a band gap indicates the metallic nature of Fe_3C, comparable to pure iron and other iron carbides. The iron atoms are held together by a metallic bonding. However, the interaction between iron and the interstitial carbon atoms involves a charge transfer from Fe to C and the covalent character of the Fe–C bonding [125,126]. Gavriljuk et al. [127,128] studied the effect of interstitial atoms in iron-based solid solutions on their electron structure and properties. It was observed that interstitial carbon assists the localization of electrons at the atomic sites, which decreases the number of free s-electrons. Consequently, the electron state density at the Fermi level is reduced, and thereby the concentration of conducting electrons in the iron lattice. It contributes to the covalent component of the interatomic bonds of Fe–C. Hence, the increase in carbon content and the subsequent formation of Fe_3C decrease the electrical conductivity of the steels as observed.

Besides the phase composition, the effect of the morphologic distribution and dimension of each phase is significant, as reported by Hasselman and Johnson [129] and Chen and Chen [130]. Indeed, pearlite microstructure can be compared to a metal matrix composite with a lamellar structure. The cementite layers represent effective interfacial barriers for electron and thermal conduction. As the spacing between cementite lamellae decreases, the number of α-Fe_3C interfaces increases, and so, the interfacial barrier resistance. It explains the higher resistivity values of the fine lamellar pearlite observed in Figure 88-b, compared to the coarser pearlitic microstructure. Also, the slight lower residual resistivity of the ferrite-pearlite 1035 steel in comparison with 1020 steel at absolute zero might be explained by the concurrent influence of increasing pearlite volume fraction and decreasing spacing of Fe_3C lamellae.

In addition to scattering on impurities, the electron mobility is also affected by scattering on phonons, which increases with increasing lattice vibrations at rising

temperatures. At finite temperatures, lattice vibrations distort the crystal and the scattering of electrons by phonons lead to a thermal resistivity component ρ_i. The total electrical resistivity can be thereby described as a sum of the residual resistivity and the thermally dependent resistivity components, given by the equation below, known as Matthiessen's rule:

$$\rho = \rho_0 + \rho_i \tag{40}$$

where ρ is the total resistivity, ρ_0 and ρ_i are, respectively, the residual and thermal resistivity in ohm-meter. In accordance with this scenario, the electrical resistivity of carbon steels increases continuously with the temperature, as shown in Figure 88-c.

In order to expand the understanding of the influence of the microstructure on the electrical properties of carbon steels, additional resistivity measurements were carried out using a four-point probe at a controlled temperature of 35°C on specimens of 4 mm in diameter 2.5 cm of length, corresponding to samples of groups A and B described in the previous sections. The current was set to 1 A. The average results and the respective standard deviation values are presented in Table 12.

Table 12: Electrical resistivity measurements of groups A and B samples carried out at a controlled temperature of 35°C

AISI steel	Electrical Resistivity (µohm.cm)
Group A	
1000	11.97 ± 0.03
1020	19.19 ± 0.02
1035	19.46 ± 0.01
1050	20.71 ± 0.00
1055	21.02 ± 0.02
1060	21.31 ± 0.10
1065	20.84 ± 0.02
1080	22.48 ± 0.01
Group B: AISI 1080	
$\bar{S}$=94–97 nm	22.74 ± 0.02
$\bar{S}$=101–106 nm	22.61 ± 0.01
$\bar{S}$=122–129 nm	22.48 ± 0.01
$\bar{S}$=125–133 nm	22.41 ± 0.04
$\bar{S}$=149–158 nm	22.37 ± 0.05
$\bar{S}$=179–192 nm	22.27 ± 0.02

The electrical resistivity is observed to increase with the rise of the carbon concentration of group A samples. This result is mainly attributed to the increase of the pearlite fraction in the steels, as discussed previously. The pearlitic steels of group B with several interlamellar spacing present slightly higher resistivity values with the decreased in the width of ferrite lamellae.

Statistical hypothesis tests were performed to evaluate measurement accuracy. Levene's test has assessed that the sample variances are significantly different at the 0.05 level. However, as the sample size is equal and quite extensive, the assumption of variance homogeneity can be disregarded to analyze variance. The one-way ANOVA has determined the significant difference between the resistivity means at the significance level of 0.05, F(12, 2587)=1152436, p=0, as shown in Figure 91. Moreover, through Tukey's post hoc test, all the resistivity mean of each heat-treated sample has been confirmed to be statistically different from another.

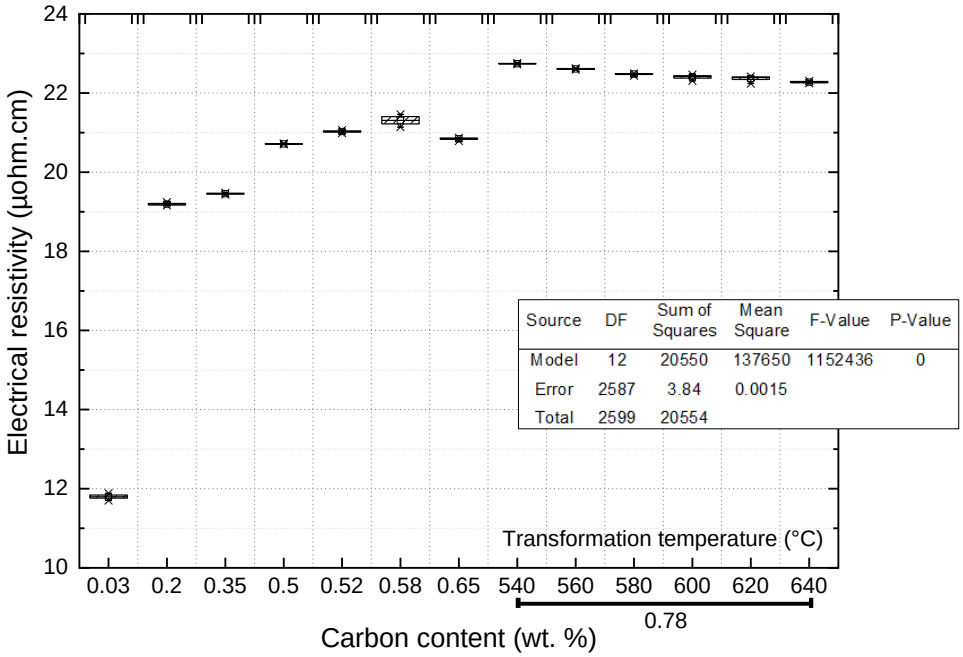

Figure 91: One-way ANOVA test (α=0.05) of the resistivity values for groups A and B

Figure 92 shows the evolution of the mean resistivity values with mechanical properties, including the standard deviations. It is observed that electrical resistivity decreases with an increase in the strength and hardness and a decrease in the ductility of carbon steels. The good correlations between the resistivity and yield strength (R^2=0.95), ultimate tensile strength (R^2=0.98), elongation (R^2=0.90), and hardness (R^2=0.97) confirm the influence of Fe_3C lamellae volume fraction on their electrical conductivity.

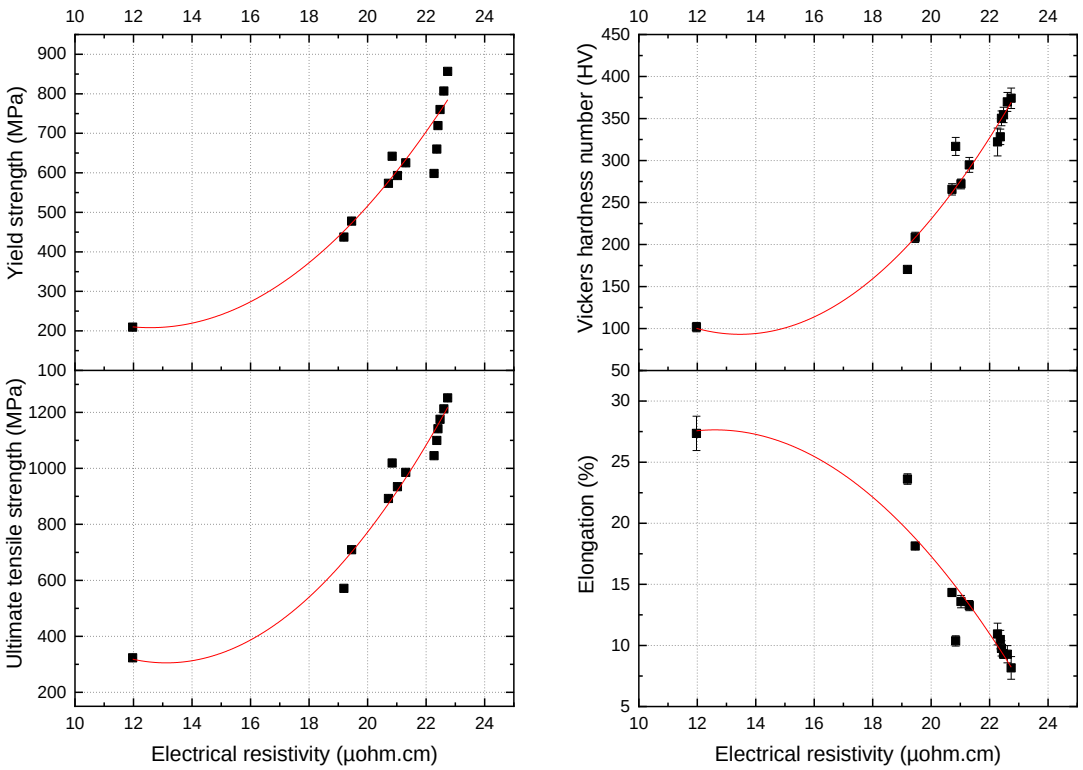

Figure 92: Relations between electrical resistivity and mechanical properties of carbon steels of groups A and B

Figure 93 shows the correlations between the resistivity values and the eddy current resistive voltage signals of the samples varying pearlite volume fraction and interlamellar spacing.

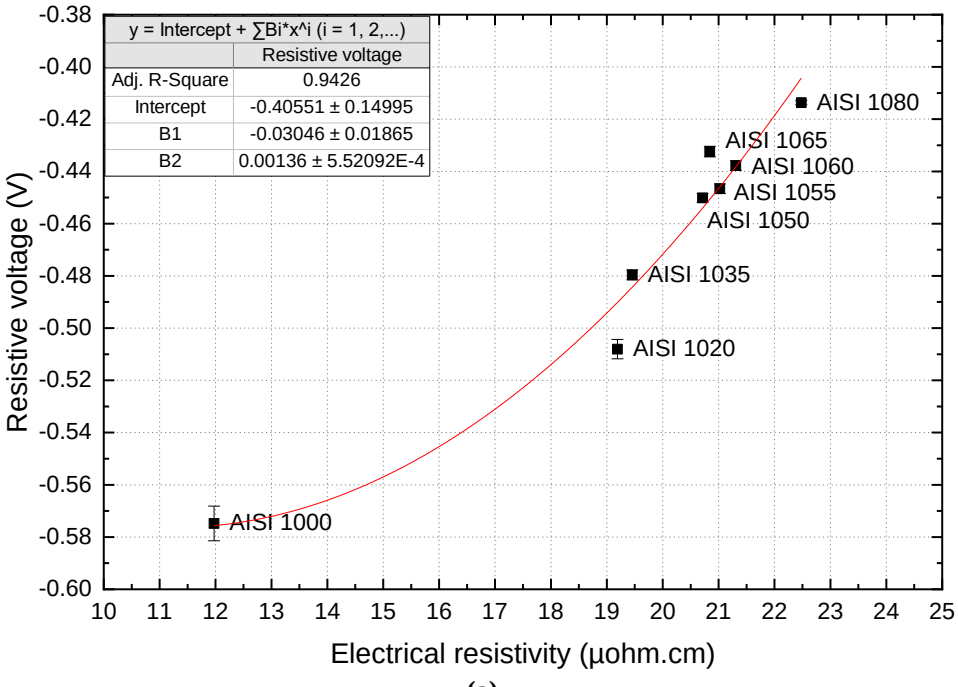

(a)

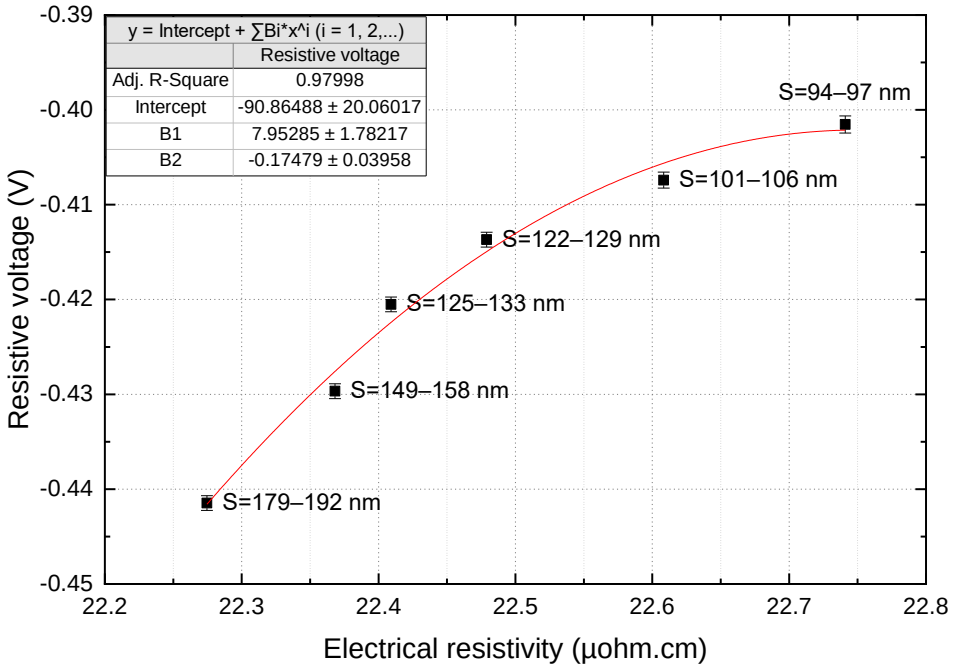

(b)

Figure 93: Correlation between the resistive voltage and the resistivity of the group A and B with varying the pearlite (a) volume fraction and (b) interlamellar spacing

The results show that the microstructural variations in the investigated materials directly affect the resistive voltage signals measured through the eddy current testing. The resistive voltage V_R is related to the resistive component R of impedance, which represents the effective resistance of the circuit to the current flow, as given in the equations below:

$$V_T = ZI = \sqrt{V_R^2 I + V_L^2 I} \tag{41}$$

$$V_R = RI \tag{42}$$

where V_T is the total voltage, V_L, the inductive voltage, Z, the impedance, and I, the current. As mentioned, the eddy current inspection system can be explained as a resistor-inductor series circuit driven by an alternating voltage. Although the resistance of the coil does not change itself, the resistance of the tested material varies, as it depends on their electrical resistivity, as described in the following equations:

$$R = R_{coil} + R_{material} = R_{coil} + \left(\rho \frac{l}{A}\right)_{material} \tag{43}$$

where ρ is the material's resistivity, and l and A, its geometry characteristics, respectively, the length and cross-section area. Hence, the ECT is assumed sensitive to the conductivity of carbon steel wires, which is mainly determined by the Fe_3C volume fraction and the finesses of the lamellar structure within the materials.

I.4. Magnetic properties

Limited information is available in the literature on the relationship between the microstructure and the magnetic domain structure of carbon steels, although the study of the micromagnetic structure evolution may help understand their electromagnetic responses. Particularly in this section, the effect of carbon and ferrite-cementite lamellar structure on the micromagnetic structure and the bulk magnetic behavior of carbon steels are investigated in detail.

Magnetic force microscopy experiments were performed on the transverse cross-sections of 4 mm diameter and 5 mm thick samples of AISI 1020, 1035, and 1080 steel grades, the latter with fine and coarse lamellar pearlite microstructures. The surface topography was obtained in tapping mode scan. Subsequently, MFM images were obtained in lift mode at 100 nm between the magnetic tip and the specimen surface. Typical topographic images and magnetic domain patterns of plain carbon steels obtained by MFM analysis are shown in Figure 94. The dark and bright contrasted regions in magnetic patterns correspond, respectively, to attractive and repulsive force derivatives between the magnetized tip and local magnetic moments of the ferromagnetic samples.

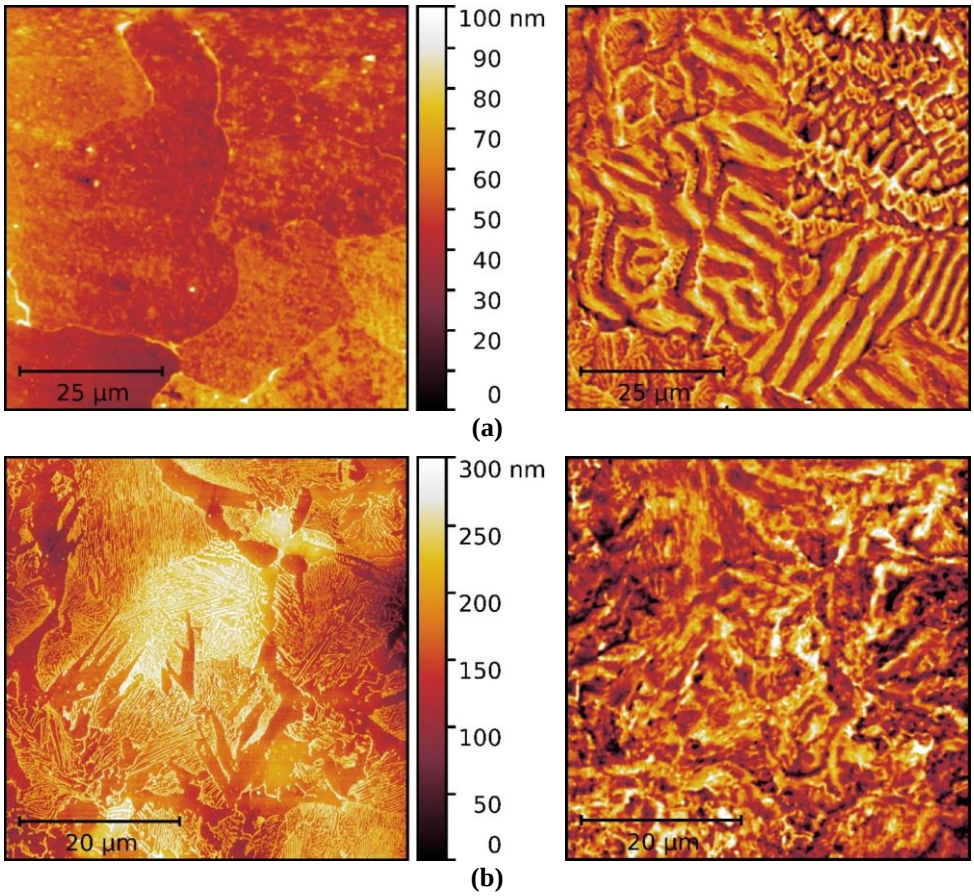

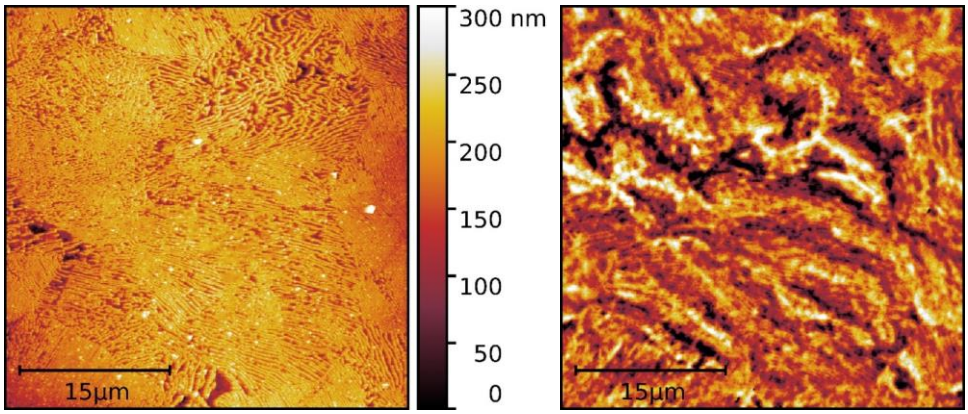

Figure 94: Topography (left) and magnetic domain pattern (right) images in bulk AISI (a) 1000, (b) 1035, and (c) 1080 carbon steel specimens

The magnetic domain distribution can be observed in the surface domain pattern of the fully ferritic AISI 1000 steel, as observed in Figure 94-a. The magnetic domains exhibit different patterns: striped domains within some grains, spike domains, and fine maze type domains in other grains. The magnetic domain patterns have changed with the increase of carbon concentration in the steels, as can be seen in Figure 94-b and Figure 94-c. It indicates that the presence of Fe_3C lamellae altered the micromagnetic structures in these materials. The width of striped domains in ferritic grains is observed to be about four µm, much larger than the domains imaged in ferrite-pearlite and pearlite steels on the order of hundreds of nanometers.

A brief introduction of domain theory might be complementary to domain observation in the present study of magnetic microstructures of carbon steels. The magnetic properties of solids originate from the permanent magnetic dipole moment of the atoms, associated with the electron's intrinsic properties of spin and electric charge. Ferromagnets present a magnetic ordering consisting of magnetic domains, each of which has their atomic magnetic moments aligned in parallel with one another. The existence of such domain structures within the material is a consequence of internal energy minimization, explained by a balance between four main energy terms: exchange, magnetostatic, magnetocrystalline, and magnetostrictive energies.

The exchange energy is at the origin of ferromagnetism, referred to as the quantum-mechanical interactions that occur between identical spins, as a result of Pauli's exclusion principle. In ferromagnetic materials, it favors electrons with parallel spins, reaching a minimum value when all individual atomic dipoles moments are aligned in a single domain. On the other hand, the surface magnetic charges associated

with the uniform magnetization configuration of a ferromagnetic crystal generates a demagnetizing field extending outside the material. This magnetic interaction results in the magnetostatic energy that tends to reverse the material's spontaneous magnetization. This energy is the main driving force for the arrangement of magnetic moments into domains, uniformly magnetized regions inside the material, reducing the external field. The magnetostatic energy is minimized with the formation of closure domains (90° walls) at the top and bottom of the crystal, as shown in Figure 95.

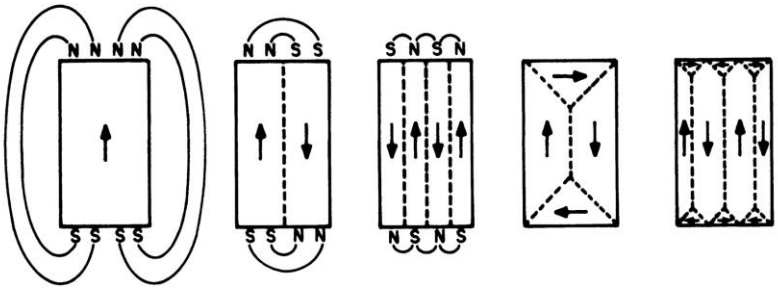

Figure 95: Subdivision of a single-domain crystal into magnetic domains, minimizing the demagnetizing energy by closure domains [118]

As the magnetic domains are randomly orientated, the material presents a null global magnetization on a macroscopic scale. A multiple-domain configuration is particularly favorable as it reduces to a minimum the magnetostatic energy within the crystal. However, the energy cost for creating a domain wall is a limiting factor for increasing the number of domains, determining either the size and shape of domains. Hence, the domain formation is favored as long as the required wall energy is less than the respective magnetostatic energy decrease.

Another characteristic of ferromagnetic materials is the magnetocrystalline anisotropy, that is, the preferential alignment of atomic magnetic moments along with certain directions than in others, due to the coupling between the spin and orbital moments. The magnetocrystalline anisotropy energy corresponds then to the energy required to magnetize the material in directions not favored by the crystal structure. In BCC iron, the easy magnetization directions are along the cube edges, which is the <100> directions. In cementite, the preferred direction of magnetization is the axis within the plane (001) [59,120]. The domain wall width corresponds to an equilibrium between exchange and magnetocrystalline energies. The first tends to make it thicker to minimize the orientation angle difference between adjacent spins, while the anisotropy energy acts to reduce the wall width to ensure the largest number of spins aligned along crystallographic equivalent axes.

Finally, the magnetostrictive energy is associated with small changes in the dimensions of a ferromagnetic material when it is subjected to an external field. It generates an elastic strain in the lattice that alters the magnetization direction to minimize the magnetocrystalline anisotropy energy. Inversely, the magnetoelastic effect characterizes the change of magnetic behavior when mechanical stresses are applied to the sample, leading to magnetic anisotropy. [96]

The minimum-energy configuration of magnetic domain structures is disturbed by external magnetic fields that introduce additional energies to the system, forcing these structures to rearrange under the new conditions. In real materials, magnetic behavior is also affected by the energetic interactions between domain walls and crystal lattice defects [118,131]. Néel [132] demonstrated that closure domains form about inclusions to reduce the magnetostatic energy arising from demagnetizing fields at its surface. These inclusions can be second-phase precipitates, impurity elements, or voids that are sufficiently large to act as nucleation sites for closure domains and to reverse magnetization domains by the closure domain rotation at a lattice defect.

MFM images acquired at higher magnification allow further examination of domain configurations of the various ferrite-pearlite steels, as shown in Figure 96.

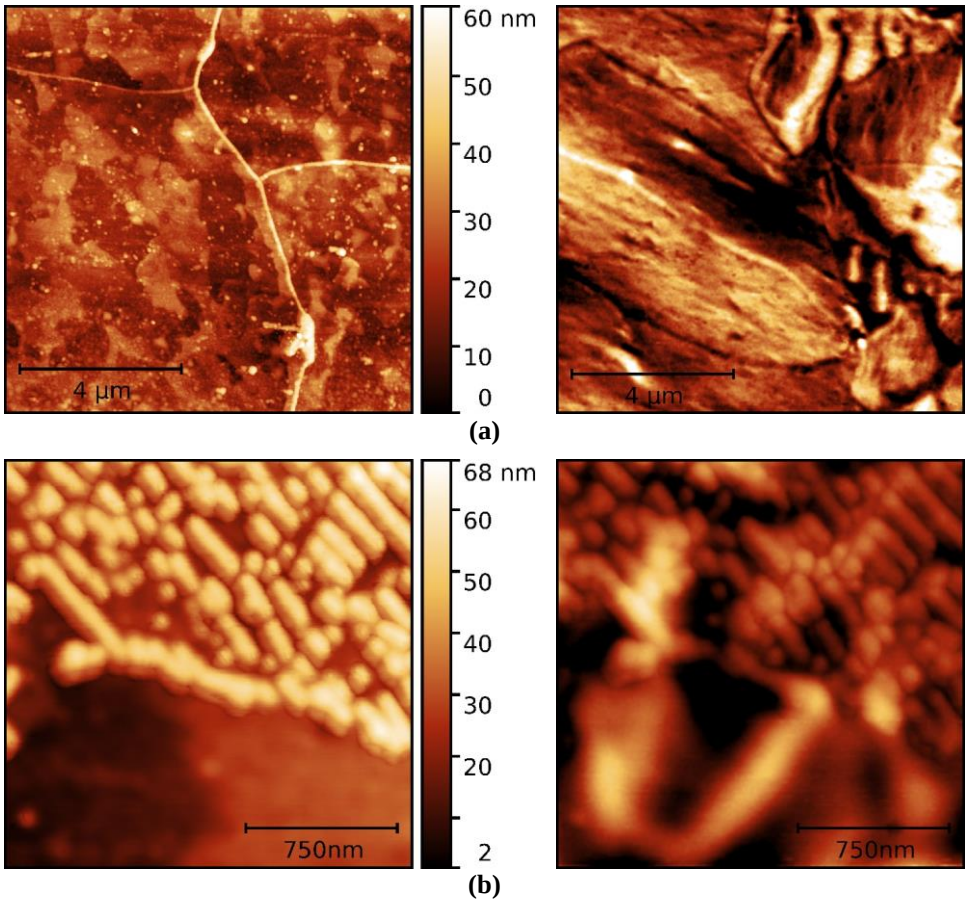

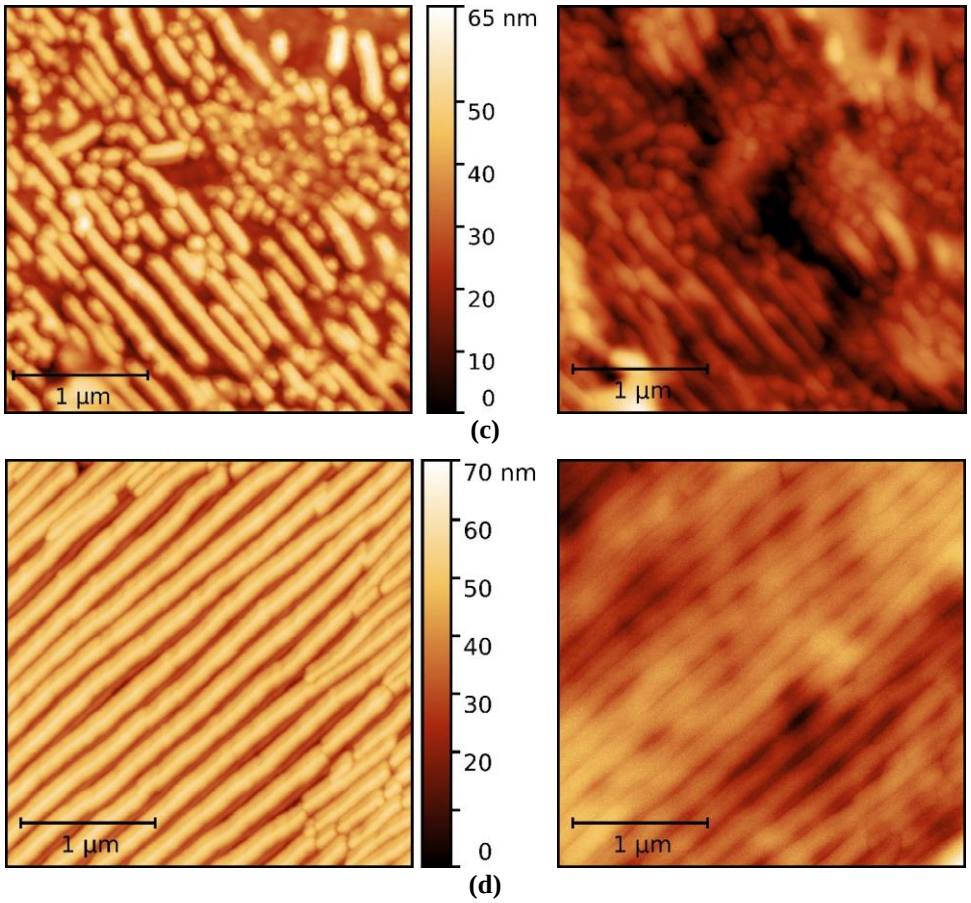

Figure 96: MFM observations of the topography (left) and magnetic domain patterns (right) of AISI (a) 1000, (b, c) 1035, and (d) 1080 samples

The different magnetic domain patterns in ferrite, observed at higher magnification in Figure 96-a, seem to be associated with misorientations between adjacent grains of ferrite and wall interactions at grain boundaries. Correlations with crystallographic orientations of the various investigated carbon steels were not attempted in the present study. However, the influence of crystallographic orientations on domain structures has been reported for ferromagnetic materials such as pure iron [133], stainless and electrical steels [134,135], exhibiting different contrast and width relative to their crystallographic orientations.

Besides, the work of Goodenough [136] shows the effectiveness of grain boundaries at pinning domain walls. Tobin and Paul [137] identified various types of domain structures formed at grain boundaries in soft iron. The free pole density that can occur at a grain boundary surface depends on the angle between the magnetization vectors of adjacent grains, among other factors such as the grain boundary nature, associated internal stresses, and local misorientations [136,137].

Figure 96-b shows the domain interactions at proeutectoid ferrite and pearlite boundaries in the AISI 1035 steel. The ferritic grain showed sharp striped type domains that become a more complex micromagnetic structure at pearlite grain boundaries. Considering the pearlite microstructures of hypoeutectoid AISI 1035 and eutectoid AISI 1080 steels, it is possible to perceive subtle differences in the domain patterns, even though both magnetic structures are very difficult to characterize. The domains seemed to be larger in regions where cementite presented discontinuous lamellae (Figure 96-c). In the fully pearlitic sample shown in Figure 96-d, the magnetic domains appeared to be arranged concerning the cementite lamellae. As observed, the magnetic domains in the full ferrite sample are considerably larger than the micromagnetic structures in the ferrite-pearlite and fully pearlitic steels, probably due to different energetic interactions. These results suggest that important obstacles are encountered by domain walls in moving through pearlite.

Although Fe_3C is ferromagnetic at room temperature, it is a relatively hard magnetic material, unlike the BCC ferritic matrix. Thompson and Tanner [59] observed that cementite lamellae restricted the domain wall movement in pearlitic steels. Cementite has high anisotropy energy with an easy (001) direction that does not coincide with that of ferrite. Hetherington et al. [138] pointed out that the domain configuration depended also on the domain wall orientation with respect to the Fe_3C lamellae. Besides, magnetization discontinuities across the α-Fe_3C interfaces generate surface magnetic free poles, causing demagnetizing effects [133,134]. Hence, Fe_3C lamellae may be considered as a magnetic inhomogeneity such as a second-phase precipitate in the ferritic matrix, altering the magnetic behavior by increasing the pinning sites density that hampers the wall motion when an external field is applied.

The lamellar structure of pearlite is considered a critical microstructural parameter affecting the magnetic domain arrangement of ferrite-pearlite and pearlitic samples. The straight-sided magnetic domains in the relatively fine lamellar pearlite are observed to lie along with the α-Fe_3C interfaces, as shown in Figure 97-a. In contrast, the domain width was observed to increase with increasing interlamellar spacing of pearlite, extending across several lamellae, as seen in Figure 97-b. Besides, some domains are seen with magnetization directions perpendicular to the Fe_3C lamellae. The finesse of the lamellar structure is also assumed to influence the domain configuration of pearlitic steels.

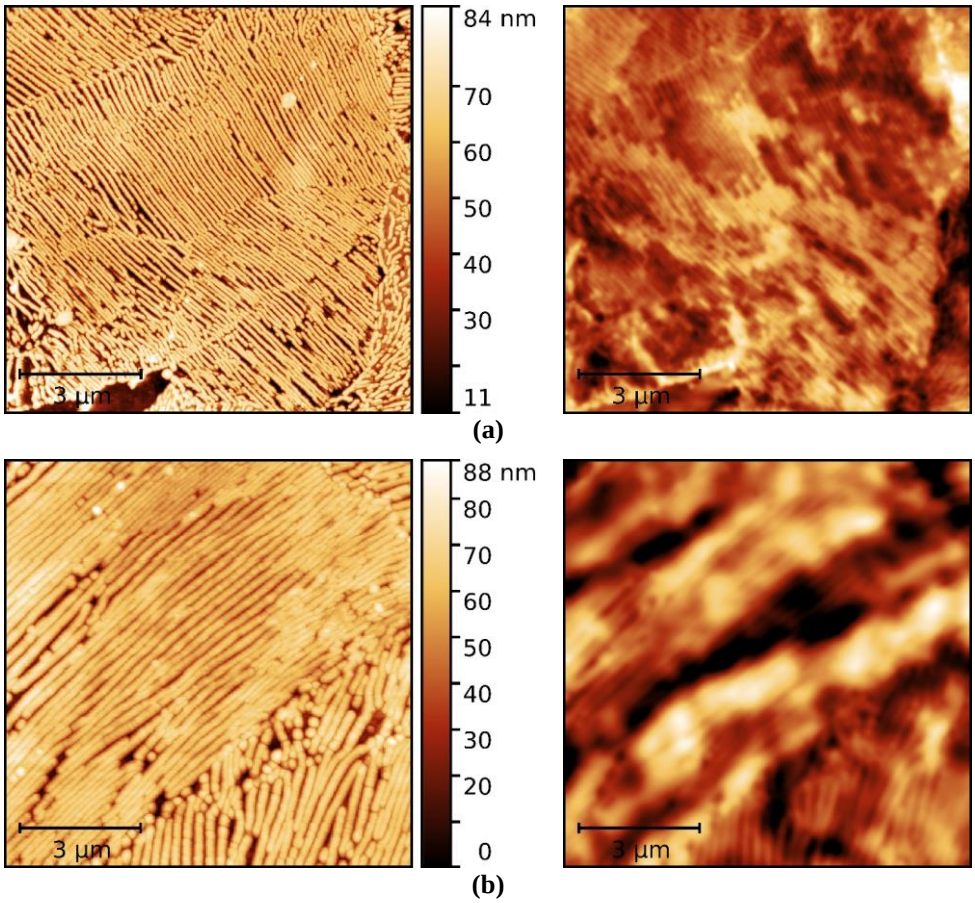

Figure 97: Topographic (right) and MFM images (left) of the eutectoid AISI 1080 samples with (a) fine and (b) coarse lamellar microstructures

A double spike domain structure was observed at a grain boundary between two pearlite colonies with a different orientation, as shown in Figure 98.

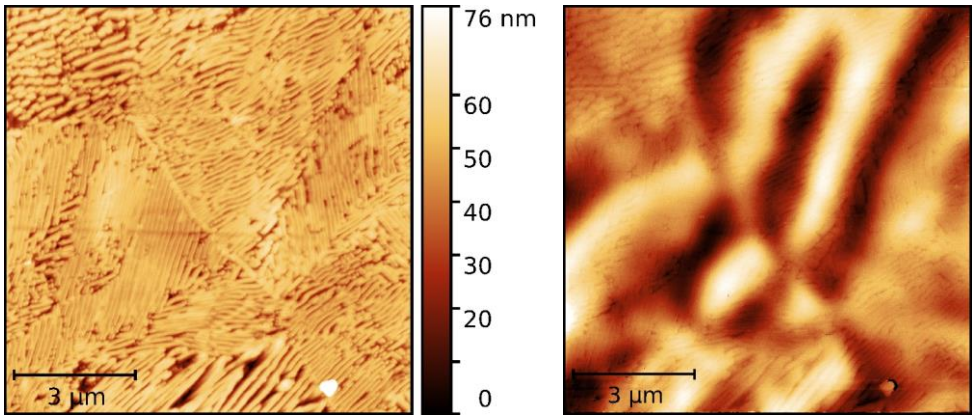

Figure 98: Topographic (right) and MFM images (left) of domain wall interactions with a grain boundary in the pearlitic structure

The following conclusions can be drawn from the imaging of magnetic domains within ferrite-pearlite steels:

- In ferritic steels, the domain walls have been observed to lie along grain boundaries, whose magnetization direction seems to depend on the misorientation between adjacent grains.
- Ferrite grains exhibit larger and well-defined magnetic domain structures than in proeutectoid ferrite-pearlite and fully pearlitic steels.
- The width of magnetic domains has been observed to increase with the increase of the width of ferrite lamellae in pearlitic microstructures.
- These results demonstrated the pinning strength of pearlite, indicating that cementite lamellae are an effective impediment to domain wall motion.

It is important to mention that the interpretation of magnetic domain patterns is not always straightforward because of the complexity of such micromagnetic structures and the problem related to the understanding of third-dimensional interactions from the information contained in strictly two-dimensional images. The evaluation of domains and domain walls properties is generally carried out based on the domain theory models complementing the experimental observations. In this research, however, theoretical calculations could not be deepened, and the domain imaging was carried out for characterizing the micromagnetic configuration of plain carbon steels qualitatively. Despite the difficulties with the appropriate generation and interpretation of domain patterns, a successful investigation of magnetic domain structures of carbon steels was conducted using magnetic force microscopy.

In addition to the MFM analysis, bulk macroscopic magnetic properties of carbon steels were characterized by magnetic hysteresis measurements, as detailed in Chapter 2. Rod-shaped specimens of groups A and B, with 4 mm in diameter and 2.5 cm of length, were employed in this investigation. The steel samples were magnetized along their axial direction at magnetic field strengths varying from ±15 $kA.m^{-1}$, which allowed obtaining a family of hysteresis cycles.

The hysteresis loops or B–H curves given in Figure 99 refers to the hysteresis cycle induced at the maximum applied field strength of 15 $kA.m^{-1}$ for each sample. Besides, normal magnetization curves were determined by coupling the corresponding maximum magnetic flux density and field strength values (B_{max}–H_{max}) of each hysteresis loop.

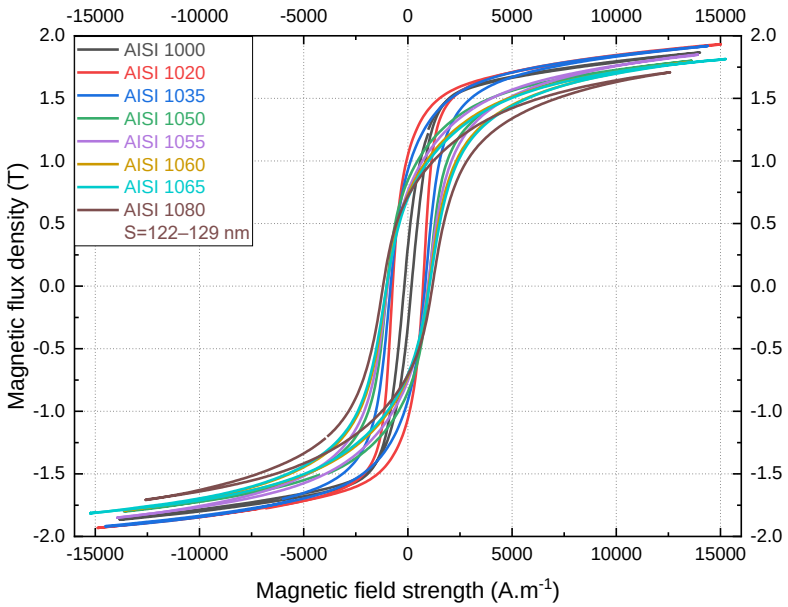

(a)

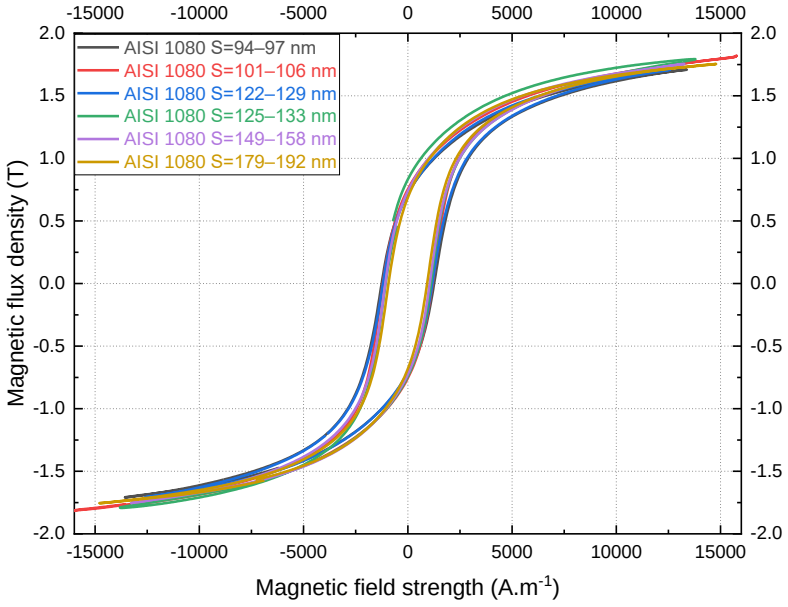

(b)

Figure 99: Comparison of hysteresis loops of the samples of (a) group A and (b) group B, with varying pearlite volume fraction and interlamellar spacing, respectively

Figure 100 shows the normal magnetization curves obtained for the various steels. The shape of the hysteresis loops between the studied samples is notably distinct, becoming smaller and flatter as carbon content increases, which indicates a decrease in the magnetic saturation and a slight increase in the coercivity of the steels. The normal magnetization curves illustrate more clearly the differences in the magnetic behavior of the plain carbon steels, particularly the decrease in the magnetic permeability with the reduction of the amplitude of the curves. It means that the steels become magnetically harder as the carbon content increases.

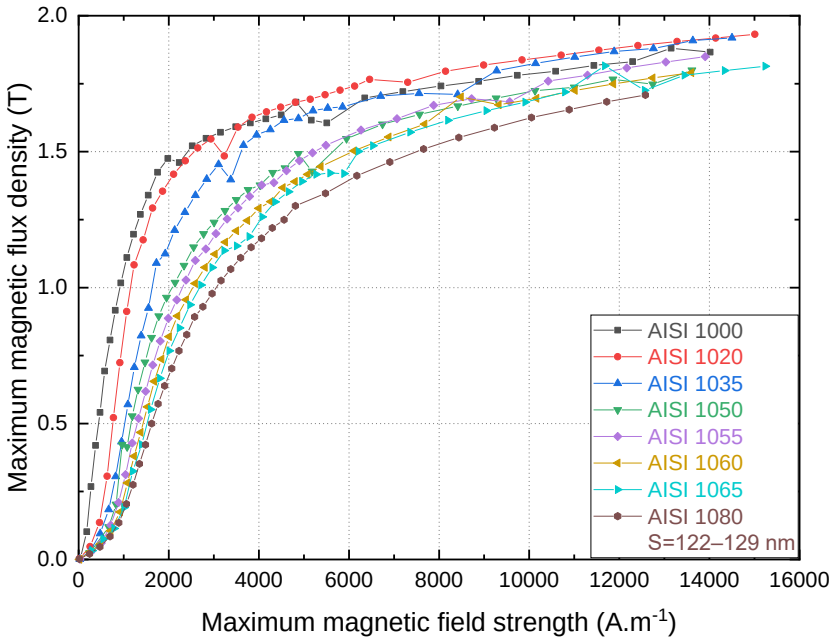

(a)

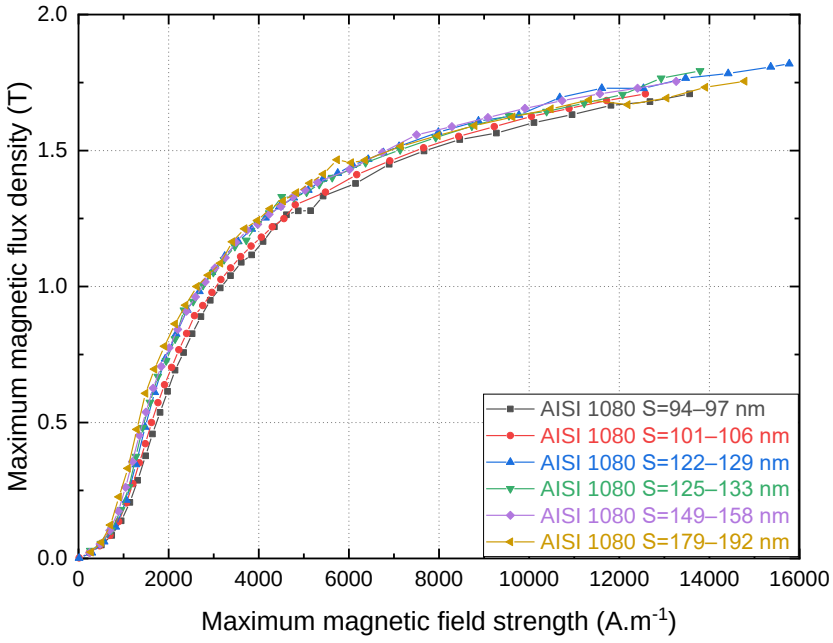

(b)

Figure 100: Normal magnetization curves obtained for the (a) plain carbon steels of group A and (b) eutectoid samples of group B

Based on the B–H loops shown in Figure 99 obtained at 15 kA.m^{-1}, the remanent magnetization, coercivity, magnetic saturation, and hysteresis loss were determined. The relative magnetic permeability was calculated from the normal induction curve data determined experimentally for each sample. A summary of the bulk magnetic properties calculated from the measured hysteresis loops is given in Table 13. Hysteresis loops were obtained three times for each material, and the average results are reported with the respective standard deviations.

Table 13: Magnetic properties of the AISI 1000 series samples corresponding to group A; and the group B composed of 1080 steels with varying lamellar thickness

AISI steel	Coercivity ($A.m^{-1}$)	Remanence (T)	Hysteresis loss ($W.kg^{-1}$)	Magnetic saturation (T)	Maximum relative permeability
Group A					
1000	171 ± 3	0.32 ± 0.01	0.03 ± 0.01	1.95 ± 0.00	941 ± 10
1020	731 ± 2	1.06 ± 0.01	0.24 ± 0.23	1.93 ± 0.00	698 ± 3
1035	841 ± 9	0.91 ± 0.01	0.29 ± 0.07	1.91 ± 0.00	493 ± 9
1050	996 ± 1	0.84 ± 0.00	0.32 ± 0.04	1.83 ± 0.00	399 ± 3
1055	963 ± 8	0.76 ± 0.00	0.32 ± 0.12	1.85 ± 0.00	355 ± 1
1060	1008 ± 1	0.72 ± 0.00	0.33 ± 0.00	1.79 ± 0.00	324 ± 2
1065	1030 ± 3	0.70 ± 0.00	0.33 ± 0.14	1.81 ± 0.00	305 ± 2
1080	1188 ± 3	0.71 ± 0.01	0.36 ± 0.05	1.71 ± 0.00	303 ± 2
Group B 1080					
$\bar{S}$=94–97 nm	1279 ± 25	0.74 ± 0.03	0.38 ± 0.15	1.71 ± 0.00	264 ± 3
$\bar{S}$=101–106 nm	1206 ± 11	0.75 ± 0.00	0.36 ± 0.10	1.71 ± 0.00	276 ± 1
$\bar{S}$=122–129 nm	1188 ± 3	0.71 ± 0.00	0.36 ± 0.05	1.78 ± 0.00	304 ± 2
$\bar{S}$=125–133 nm	1122 ± 7	0.76 ± 0.02	0.35 ± 0.03	1.77 ± 0.02	306 ± 1
$\bar{S}$=149–158 nm	1058 ± 3	0.73 ± 0.00	0.34 ± 0.02	1.76 ± 0.00	310 ± 4
$\bar{S}$=179–192 nm	935 ± 5	0.68 ± 0.00	0.29 ± 0.13	1.75 ± 0.00	329 ± 1

Regarding the plain carbon steels of group A, as the pearlite volume fraction increases, the coercive force and hysteresis losses increase, while the remanent magnetization and the relative permeability are observed to decrease. The magnetic saturation also reduces with the increasing pearlite-proeutectoid ferrite ratio. The results allow concluding that any change in the volume fraction of ferrite, which is a magnetically softer phase than pearlite, may affect the magnetic characteristics of carbon steels. Considering the pearlitic samples of group B, the coercivity and hysteresis losses increase, and the remanence and relative permeability decrease with decreasing pearlite interlamellar spacing. Variations in the magnetic saturation values are not remarkable. On a smaller scale, the pearlite finesse also contributes to the corresponding deterioration of the bulk magnetic performance of the steel samples. The values attained in this investigation are consonant with those reported in the literature [58-60,74,139]. Figure 101 shows the relative permeability as a function of the maximum magnetic field strength of each hysteresis cycle for the various materials.

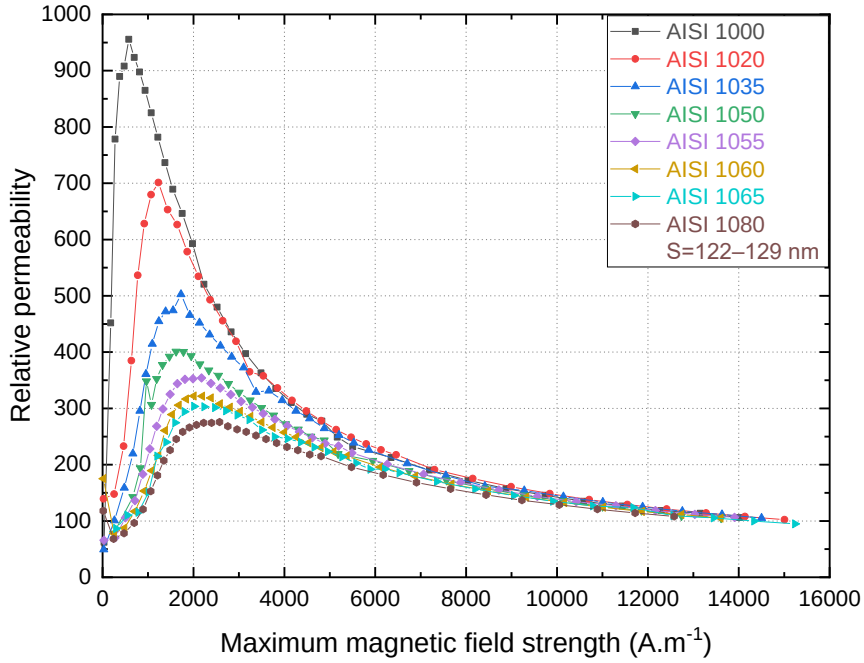

(a)

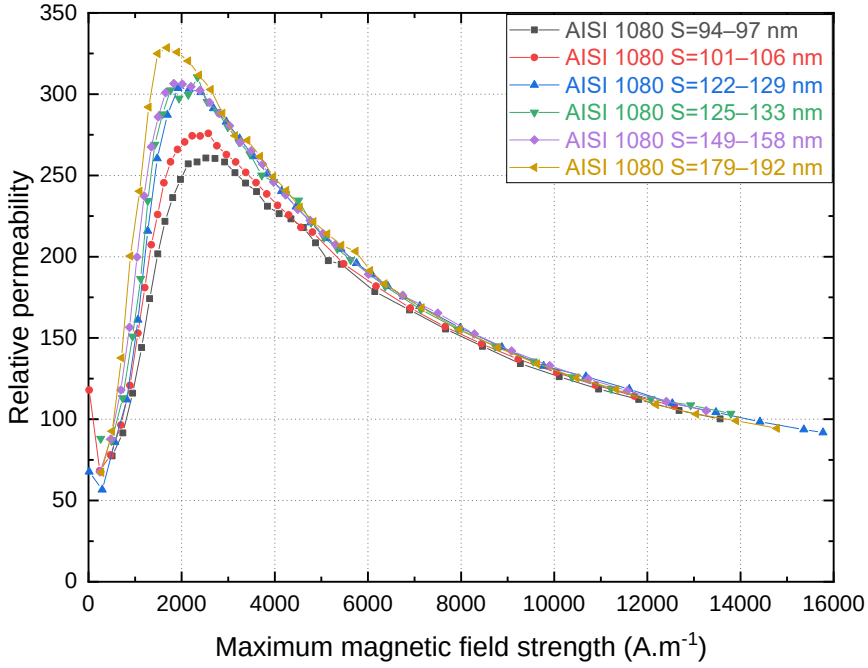

(b)

Figure 101: Variation of the relative permeability as a function of the maximum magnetic field strength of carbon steels of (a) group A and (b) group B

The superposition of the relative permeability curves of the carbon steel of groups A and B is shown in Figure 102. It can be observed that AISI 1080 samples with thicker interlamellar spacing present higher relative permeability values than samples with less carbon amount, for instance, the AISI 1060 and 1065 steels, but showing a thinner lamellae structure. This result confirms the fact that the pearlite morphology may also play a further relevant role in the magnetic behavior of steels.

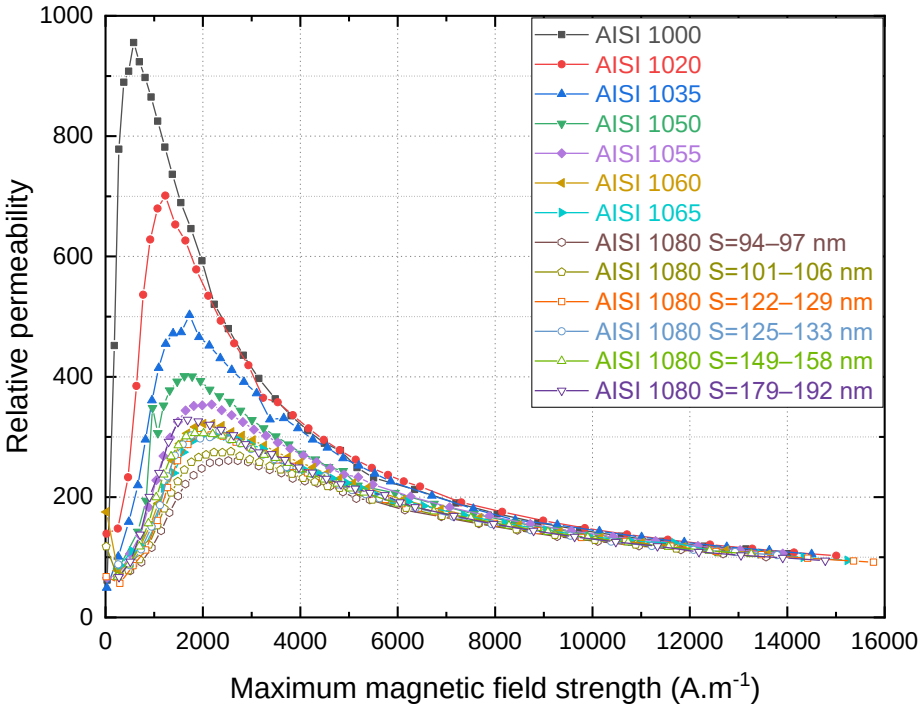

Figure 102: Comparison of relative permeability values for groups A and B

Some additional background knowledge of domain processes is necessary to better understand the macroscopic magnetic behavior dependence of steels on their microstructure. Under the influence of an external magnetic field, the energy equilibrium of the material is modified. Its magnetic microstructure evolves so that the system regains minimal energy, and thus exchange interactions act to align adjacent magnetic moments in the same magnetization direction. The magnetization process is dominated by the displacement of magnetic domain walls that move in a way to enlarge the domains oriented in directions favorable to that of the applied field at the expense of the less favorably orientated domains, which shrink in consequence.

As the $\vec{H}$ field increases, the favorably oriented domains continue to grow, and the magnetic induction $\vec{B}$ rapidly increases. However, domain walls might encounter difficulty in moving inside the crystal due to the presence of lattice defects and strain inhomogeneities. Imperfections such as dislocation, voids, precipitates, or impurity elements inclusions may act like pinning sites to domain walls. As discussed, domain walls and inclusions interactions configure an arrangement that minimizes the wall and the magnetostatic energy states. During magnetization, the domain wall energy is dissipated in heat, giving rise to the phenomena of hysteresis. An additional external field is then required for unpinning the wall from the crystallographic defect, increasing the coercive force, and the hysteresis of the material. Finally, at higher

fields, the saturation region is achieved, and the rotation of the remaining unfavorable aligned domains occurs. At this point, there are no more domain structures. [96,99]

Therefore, bulk magnetic properties can be associated with the disrupted displacement of domain walls when they interact with lattice defects within the material. The differences in the hysteresis loops observed in Figure 99 elucidates the effects of microstructural features on the magnetization of the investigated carbon steels. Group A consists of samples with varying pearlite volume fraction that increases significantly at the expense of proeutectoid ferrite with increasing carbon content in the steels. As a second-phase precipitate, the increasing of cementite lamellae enhances the effective number of domain wall anchorage sites within the material, related to the difference in magnetic parameters between the iron carbide and the ferrite matrix. Besides, the increase of pearlite restricts the proportion of proeutectoid ferrite that can be magnetized in the easy direction [59]. The observed variations in the coercive force and remanent magnetization can be directly related to the phase and structural state of these ferromagnetic materials [140,141]. The ferritic sample presents a low coercivity of 0.17 $kA.m^{-1}$, while the ferrite-pearlite samples with considerable amounts of pearlite and fully pearlitic samples achieve values close to 1 $kA.m^{-1}$. The maximum relative permeability decreases in accordance with the increasing coercive force. The magnetic saturation, considered a phase-sensitive magnetic characteristic [141], presents decreasing values with the increase of pearlite content in the steel. It confirms the sensitivity of this parameter to the phase composition of the heat-treated materials.

In addition to the effect of chemical composition and the consequent phase balance variation in the magnetic behavior of carbon steels, the width of ferrite lamellae affects the structural-sensitive magnetic properties of pearlitic steels. Fully pearlitic samples of group B with coarse and fine lamellar structures present coercive forces of 0.93 and 1.28 $kA.m^{-1}$, respectively. No significant saturation magnetization changes are observed in these eutectoid steels since the phase balance is not altered.

As discussed previously, the increasing amount of carbon made the steels mechanically harder and less ductile. Domain processes can be elucidated by the phenomenon of plasticity, which is based on the movement of the dislocations. Microstructural factors that can prevent this movement, such as dislocations, grain boundaries, precipitates, and other lattice defects, entail a strength hardening of the material. It works in the same way for the domain wall displacement within a solid,

that is, the lattice defects that contribute to the strengthening of steels configure anchorage sites for the domain wall pinning and, hence, make these materials magnetically harder [96].

Figure 103 shows the good correlations between magnetic coercivity and maximum relative permeability, with the mechanical behavior of carbon steels.

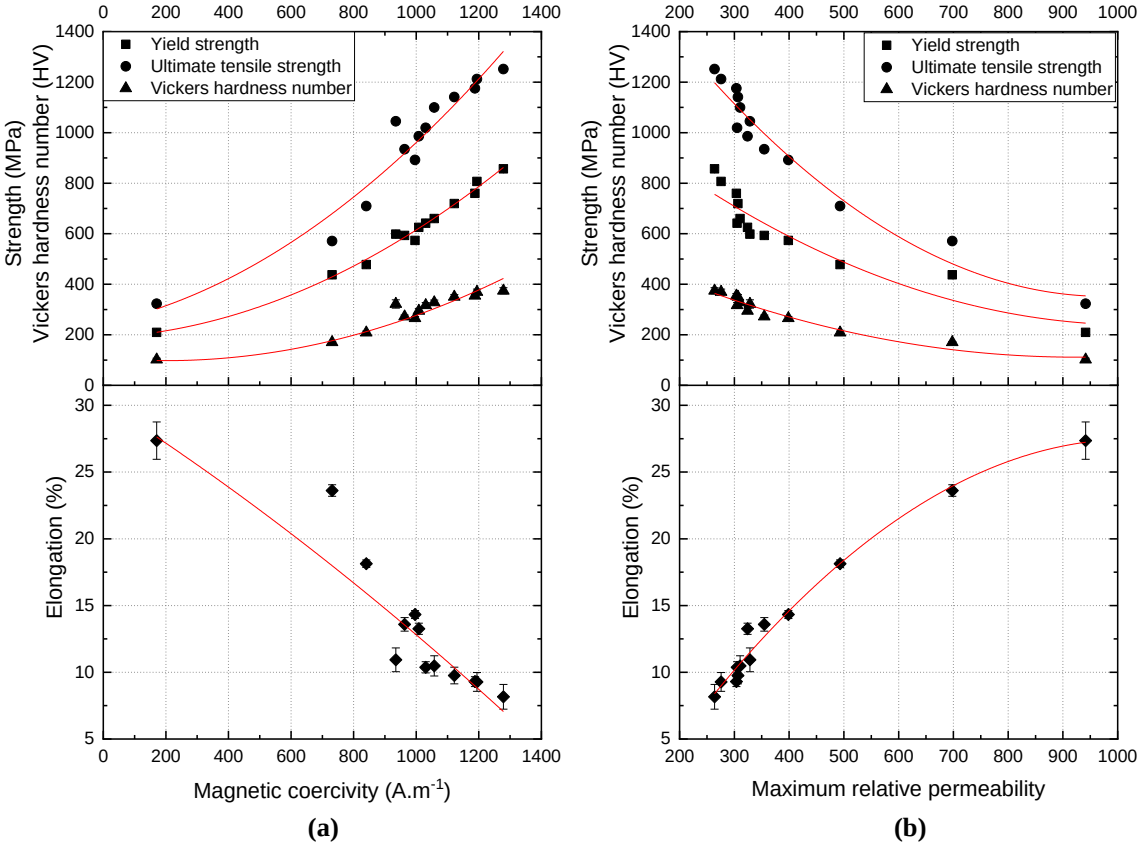

Figure 103: Relations between (a) coercivity, and (b) maximum relative permeability with and the tensile properties and Vickers hardness of the investigated carbon steels

Figure 104 shows the variations of the main bulk magnetic properties with the eddy current inductive voltage signals measured for the investigated samples. The inductive voltage is observed to increase with increasing maximum relative permeability and the corresponding decrease of the coercive force. As the inductive voltage V_L is associated with the imaginary term of the coil's impedance, the reactance X_L, it may depend on the permeability variations of the tested material, as given:

$$V_L = X_L I \tag{44}$$

$$X_L = 2\pi f L = 2\pi f \mu_{material} \left(\frac{N^2 A}{l}\right)_{coil} \tag{45}$$

where f is the frequency, L the coil's inductance, μ is the permeability of the material, N, A, l are the coil's number of turns, cross-section area, and length, respectively.

Indeed, the good correlations between the eddy current outputs and maximum relative permeability (R^2=0.98) and coercivity (R^2=0.96) values confirm the ability of this NDT for indirectly evaluating the magnetic properties of carbon steel wires.

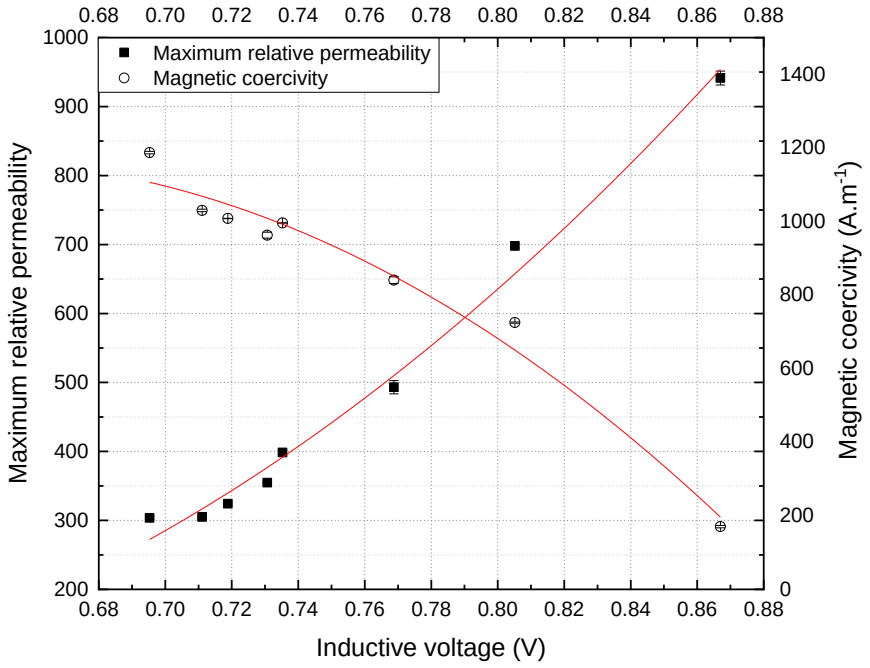

y = Intercept + ∑Bi*x^i (i = 1, 2,...)		
	Maximum relative permeability	Magnetic coercivity
Adj. R-Square	0.9849	0.9631
Intercept	2032.98 ± 2314.7884	-6415.0015 ± 4928.1313
B1	-7746.08 ± 5956.1325	23745.6990 ± 12680.469
B2	7498.9250 ± 3812.1109	-18593.0752 ± 8115.896

Figure 104: Eddy current inductive voltage correlations with the maximum permeability and magnetic coercivity of the studied carbon steels

From the investigation of the effect of carbon concentration on the physical properties of steel wires and eddy current responses, as well as from magnetic domain imaging by MFM, it is possible to list relevant observations:

- The increase in pearlite volume fraction with the increase in carbon concentration was crucial in defining either the mechanical, electrical and magnetic properties of the studied carbon steels.
- The increase of interstitial carbon atoms in the orthorhombic Fe_3C lattice contributes to the covalent character of Fe-C interatomic bonds, reducing the electrical conductivity of the steels. The cementite lamellae act as interfacial barriers for dislocation slip in ferrite, as well as for domain wall displacements within the material, making it mechanically and magnetically harder as the

volume fraction of pearlite increases. Electrical conductivity and magnetic permeability increase in the order of pearlite, pearlite-ferrite, and ferrite microstructures.

- Moreover, the decrease in spacing between lamellae affects the main free-path for the displacement of dislocations; as well as the mobility of free electrons due to the increase of electron scattering events, and magnetic domain walls by increasing the number of effective pinning sites.
- Non-destructive eddy current testing could distinguish the different materials with respect to the chemical composition of steels and morphology of pearlitic lamellar structures. The eddy current responses changed according to the conductivity and permeability variations of each material, which were directly related to changes in the volume fraction and interlamellar spacing of the cementite lamellar phase.

II. EFFECT OF PHASE MORPHOLOGY

II.1. Microstructure and mechanical properties

The eutectoid steel wires with 0.78 wt. % C and 4 mm in diameter were heat-treated at different conditions for the study of the effect of the microstructure morphologies on its mechanical and electromagnetic properties. All materials were austenitized at 950°C and subsequently heat-treated by patenting, quenching, tempering, and spheroidize annealing for producing, respectively, pearlite, martensite, sorbite, and spheroidite microstructures constituting samples of the group C.

Figure 105 shows the SEM micrographs of the various microstructures etched in a 4% Picral solution. Pearlite with fine and coarse lamellar microstructures was obtained by cooling at constant transformation temperatures of 540 and 640°C in a molten lead bath. As introduced in the previous section, the pearlite is a lamellar structure composed of alternating layers of ferrite and cementite phases. The fine lamellar microstructure was characterized by relatively thin distances between the cementite lamellae, included in the 95% confidence interval of 94 and 97 nm, as observed in Figure 105-a. Figure 105-b shows the microstructure of the coarse lamellar pearlite, whose mean true interlamellar spacing increased by a factor of 2 compared with the thinner microstructure, comprised between 179 and 192 nm.

Martensite was obtained after quenching austenite in water at 25°C. In the typical martensite structure obtained from eutectoid steel, the austenite grain gives rise to fine packets with approximately the same habit plane, and each packet contains fine blocks, which are subdivided into laths of the same orientation, as observed in the SEM micrograph of Figure 105-c. Next, after quenching, the sorbite microstructure was obtained by tempering treatment in a molten lead bath at 580°C. Figure 105-d shows the sorbite microstructure consisted of very fine dispersed cementite particles in a matrix of ferrite.

Spheroidite carbides were obtained from the spheroidize annealing treatment of the pearlite microstructure in a furnace at 700°C for soaking times varying from 8, 24, and 72 hours. The obtained microstructures are composed of spherically-shaped cementite precipitates in the ferrite matrix. The different soaking times allowed obtaining spheroidite carbides with various precipitate sizes, as observed in Figure 105-e, Figure 105-f, and Figure 105-g.

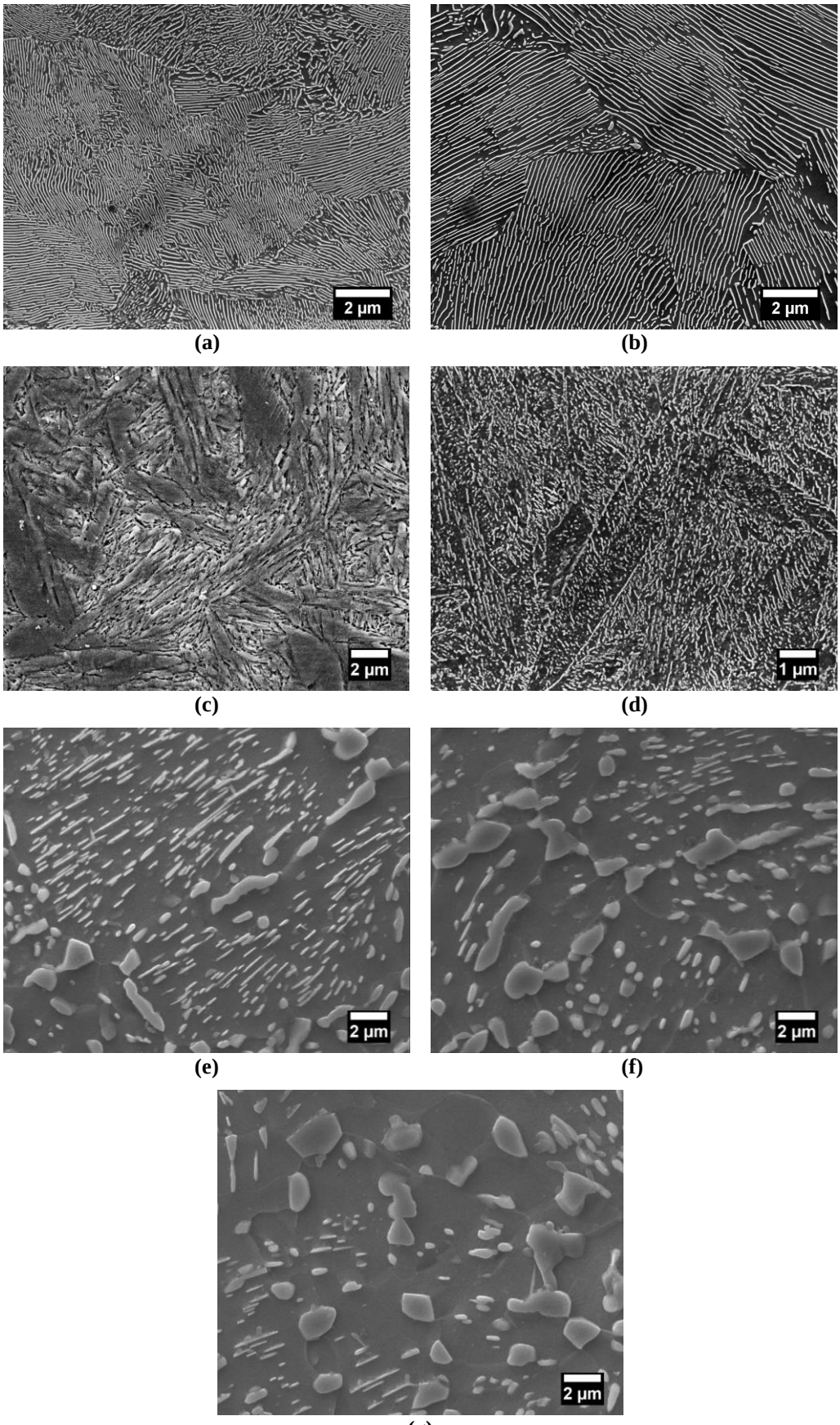

Figure 105: SEM images of (a) fine and (b) coarse lamellar pearlite; (c) martensite; (d) sorbite; (e, f, g) spheroidite microstructures obtained from AISI 1080 steels

The mean size of the spheroidized cementite obtained at each spheroidizing stage is shown in Table 14. The one-way ANOVA test confirmed that the cementite precipitated values are statistically significantly different at the 0.05 level, $F(2, 297)=37.03$, $p=4.37.10^{-15}$, as shown in the box-plot chart of Figure 106. Tukey's post hoc test indicated that all means are significantly different from each other.

Table 14: Estimated precipitate sizes of cementite of the spheroidite samples annealed at different soaking times

AISI steel	Annealing temperature (°C)	Annealing time (h)	Cementite precipitate size (µm)			
			Mean	Standard deviation	95% confidence interval	
					Lower bound	Upper bound
1080	700	8	0.74	0.42	0.66	0.82
1080	700	24	1.10	0.76	0.94	1.25
1080	700	72	1.57	0.80	1.41	1.73

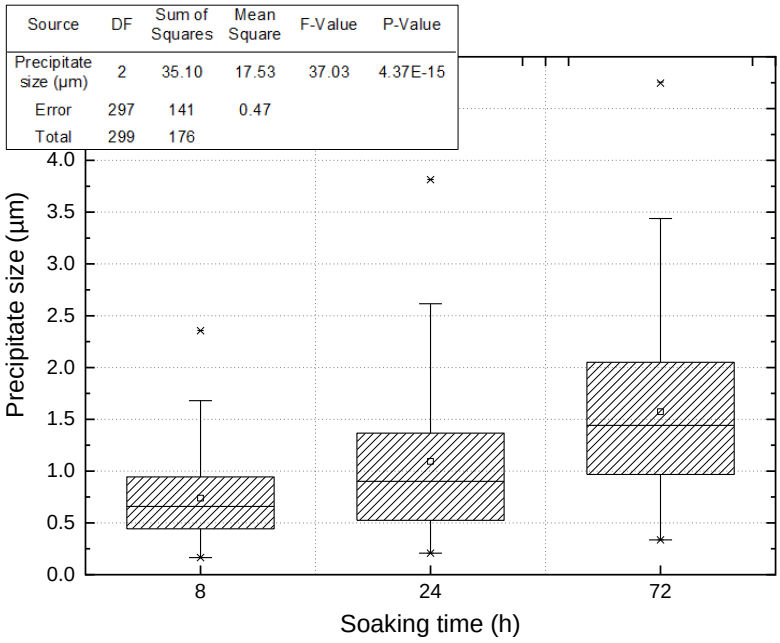

Figure 106: Box-plot chart of one-way ANOVA test (α=0.05) of the cementite precipitate size for the several spheroidized samples

The mechanical properties of the steels of group C were evaluated by tensile tests and Vickers hardness measurements. The data related to the tensile test could not be obtained for the martensitic samples due to the brittleness of such microstructure. The averages and the respective standard deviation values are represented in Table 15 for each type of microstructure.

Table 15: Mechanical properties of the various microstructures of group C

Sample name	Microstructure	Yield strength (MPa)	Ultimate tensile strength (MPa)	Elongation (%)	Reduction of area (%)	Vickers hardness number (HV)
FP	Fine pearlite $\bar{S}$=94–97 nm	857 ± 5	1252 ± 2	8.1 ± 0.9	53.1 ± 0.6	374 ± 12
CP	Coarse pearlite $\bar{S}$=179–192 nm	598 ± 2	1045 ± 1	10.9 ± 0.9	50.4 ± 0.9	322 ± 17
M	Martensite	-	-	-	-	794 ± 10
S	Sorbite	1190 ± 3	1390 ± 2	5.2 ± 0.7	44.3 ± 1	351 ± 11
Sph1	Spheroidite P=0.66–0.83 µm	385 ± 1	641 ± 1	15.9 ± 1.2	60.0 ± 0.9	197 ± 7
Sph2	Spheroidite P=0.94–1.25 µm	349 ± 1	571 ± 1	12.9 ± 2.1	60.5 ± 0.3	184 ± 4
Sph3	Spheroidite P=1.41–1.73 µm	306 ± 2	504 ± 1	16.4 ± 1.3	62.6 ± 0.5	181 ± 5

In the fully pearlitic samples, the strength and hardness of the material increase as interlamellar spacing become thinner, while the ductility decreases accordingly. Both fine and coarse pearlite microstructures present higher strength and hardness values than the spheroidite microstructures due to their plate-shaped lamellar morphology. With annealing treatment at 700°C, the spheroidizing of cementite lamellae took place within the material, forming cementite precipitates with particle sizes that increase with the increasing soaking times. At shorter times, spherical particles start to develop, and plate-shaped lamellae are still present. In further stages of the spheroidizing process, the high densities of very fine particles dissolve in the matrix simultaneously with the coarser precipitates grow. This mechanism is due to the reduction of the ferrite-cementite interfacial energy relative to the spheroidized microstructure. The tensile and yield strengths, as well as Vickers hardness values, decrease with increasing precipitates size, whereas the ductility was observed to increase. The spheroidized samples presented the most ductile and softest condition between the studied steels, which is directly associated with the relatively coarse Fe_3C precipitates dispersed in the continuous ductile ferritic matrix.

Martensite was obtained after rapid cooling from the austenite phase through a displacive transformation that involved the deformation of the austenite lattice without any diffusion of carbon atoms, generating a body-centered tetragonal structure with

interstitial carbon in solid solution. The shear mechanisms and the volume expansion accompanying the transformation of austenite to martensite introduce a high density of dislocations within martensite crystals. As a consequence, this complex structure presents a high Vickers hardness value, indicating the very high strength of martensite. The strength and toughness of martensite are strongly related to packet and block sizes, which depend mainly on the carbon content and the prior-austenite grain size. The latter was measured, and the true mean grain size was estimated between 35–38 µm at a confidence level of 95%, as presented in the previous section. Tempering treatment applied to the martensitic samples allowed to produce a sorbite microstructure, a less hard and brittle structure. The tempering was carried out at a relatively high temperature of 580°C, and, at this stage, the high dislocation density has considerably decreased. The high strength of sorbite is achieved by precipitation hardening due to the very fine Fe_3C particles formed in the resulted microstructure.

II.2. Eddy current testing

Non-destructive eddy current measurements were performed to evaluate their electromagnetic responses of the different microstructure morphologies of AISI 1080 steel wires. ECT was carried out under the same conditions previously described, at room temperature and an excitation frequency of 200 Hz. A considerable number of output signals were obtained by online and off-line measurements, displayed as average and standard deviation values of the multiple measures. Figure 107 shown the graphical outputs of the one-way ANOVA test conducted on the eddy current signals.

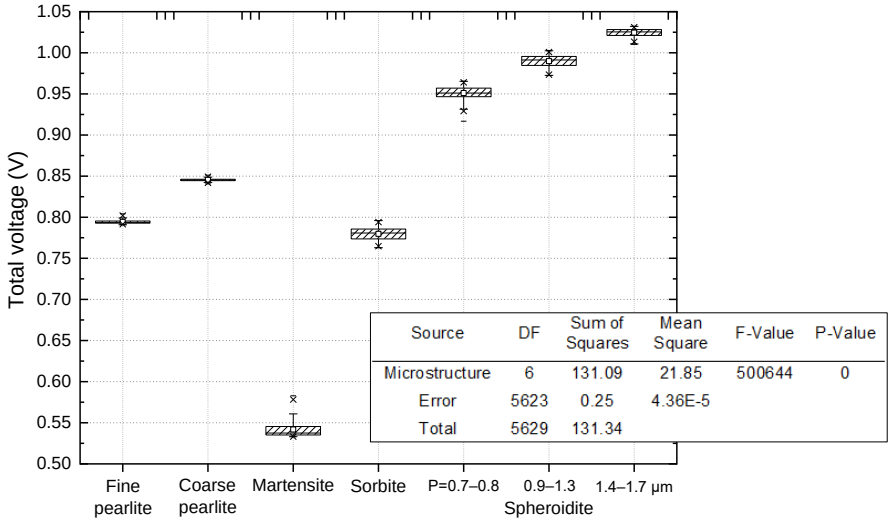

Figure 107: Box-plot chart of one-way ANOVA (α= 0.05) of the mean total voltage signals for the various microstructure morphologies obtained from the AISI 1080 steels

The statistical analysis of variance demonstrated that the total voltage means between the samples are significantly different at the 0.05 level, F(6,5623)=500644, p=0. The differences in the means were also found significant using Tukey's post hoc test. These results indicate that each type of microstructure achieved statistically different electromagnetic responses.

Figure 108 shows the eddy current voltage plane and the total voltage signals in the function of Vickers hardness obtained for the various samples. In the graphs below, the fine and coarse pearlite, martensite, sorbite, and spheroidite morphologies are named, respectively, FP, CP, M, S, Sph1, Sph2, and Sph3 for better visualization.

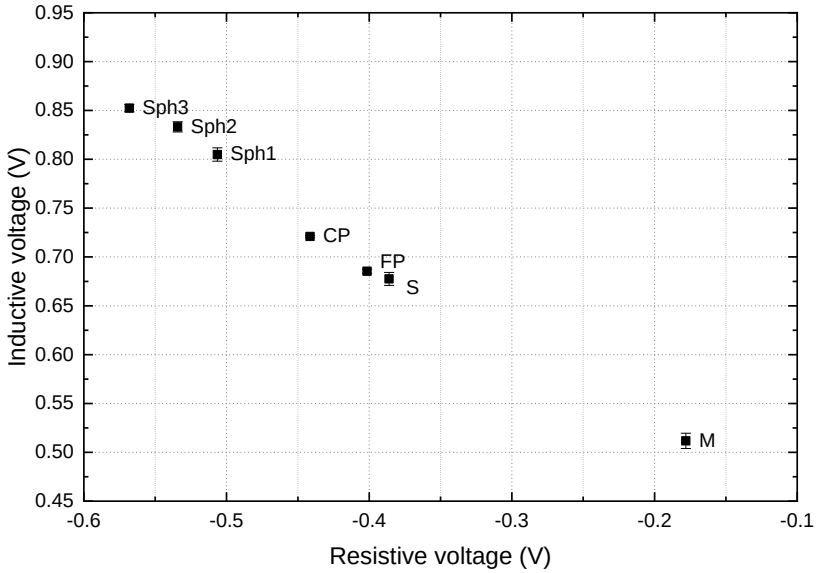

(a)

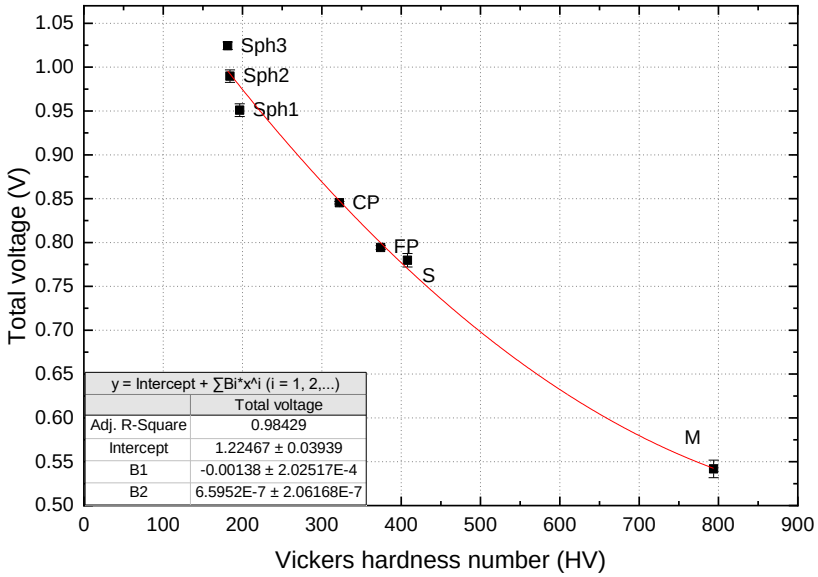

(b)

Figure 108: (a) Eddy current voltage plane and (b) correlation between Vickers hardness and total voltage signals for the various samples of group C

The resistive voltage increases while the inductive voltage decreases in the order of the spheroidite, coarser and fine pearlite, sorbite, and martensite microstructures. The very low standard deviations indicate that the expected values are close to the data set means. Important changes are observed in the total voltage signals to the Vickers hardness values of the several microstructures evaluated. The harder materials present lower responses, indicating that the changes in the microstructure may alter their electrical and magnetic properties.

Figure 109 shows the correlations of total voltage with mechanical properties, excluding only the martensitic steel, whose tensile properties could not be evaluated.

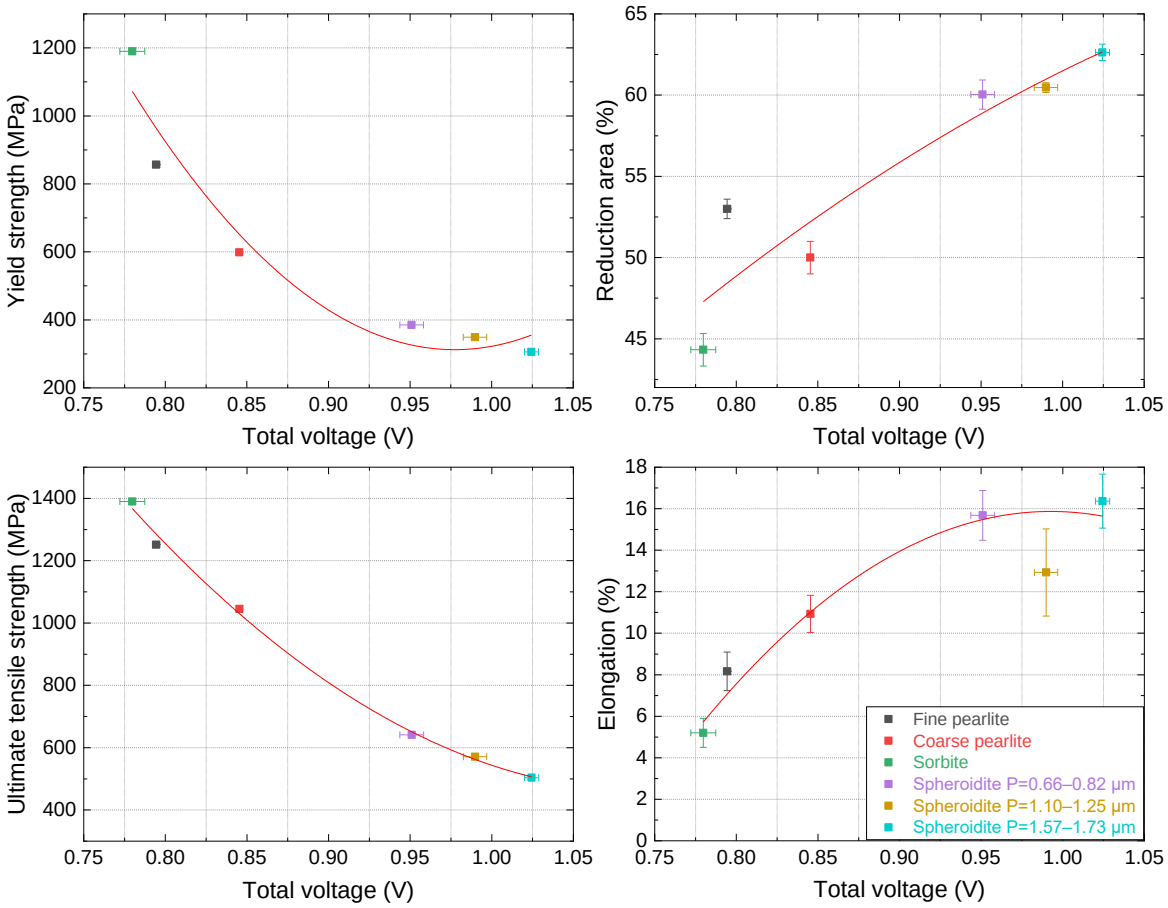

Figure 109: Relations between the total voltage and mechanical properties of the AISI 1080 steels of group C

The good correlations found between eddy current outputs and ultimate tensile strength (R^2=0.99), yield strength (R^2=0.95), reduction in area (R^2=0.86), and percentage elongation (R^2=0.96) evidence the sensitivity of this non-destructive technique to distinguish the different arrangement of microstructures of eutectoid AISI 1080 steel wires.

II.3. Electrical resistivity and bulk magnetic properties

Electrical resistivity measurements were carried out on specimens of 4 mm in diameter and 2.5 cm length, using a four-point probe at a controlled temperature of 35°C to characterize the electrical behavior of the various types of microstructures investigated. The mean resistivity and standard deviation values are given in Table 16.

Table 16: Electrical resistivity measurements of AISI 1080 samples of group C performed at a controlled temperature of 35°C

AISI steel	Microstructure	Electrical Resistivity (µohm.cm)
1080	Fine lamellar pearlite	22.74 ± 0.02
1080	Coarse lamellar pearlite	22.28 ± 0.02
1080	Martensite	33.34 ± 0.01
1080	Sorbite	22.11 ± 0.01
1080	Spheroidite P=0.66–0.83 µm	19.96 ± 0.02
1080	Spheroidite P=0.94–1.25 µm	19.77 ± 0.01
1080	Spheroidite P=1.41–1.73 µm	19.57 ± 0.02

Figure 110 shows the box-plot chart referent to the analysis of variance of the mean resistivity determined for each material.

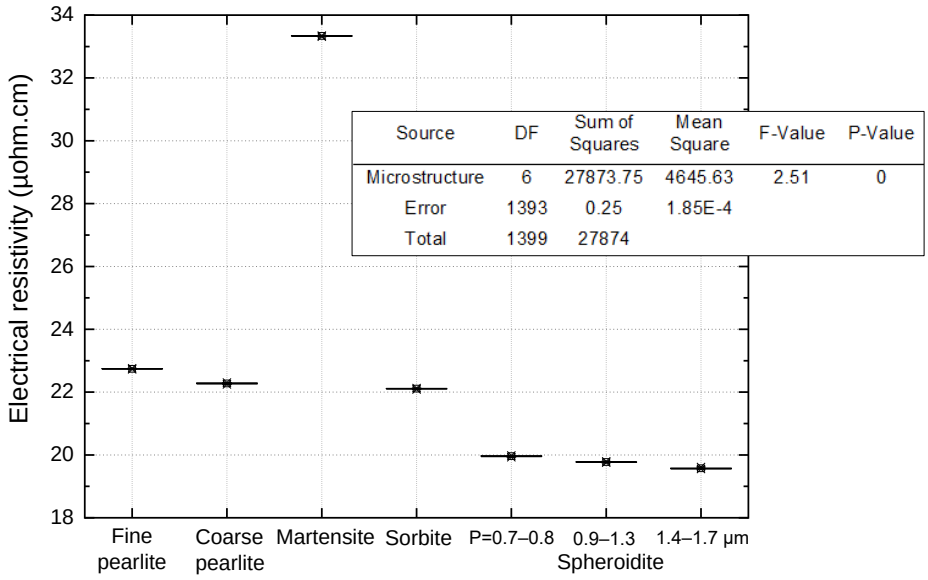

Figure 110: One-way ANOVA test (α=0.05) of resistivity measurements for the various microstructure morphologies of AISI 1080 steel

Levene's test determined that the sample variances are statistically different. However, this homogeneity variance assumption can be ignored once the sample size is equal. The one-way ANOVA test determined that the resistivity means between the different samples are statistically different at the 0.05 level, F(6,1393)=2.51, p=0. The means comparisons carried out through Tukey's test confirmed that the difference of the means is all statistically different from another.

Figure 111 shows the electrical resistivity evolution as a function of the Vickers hardness values of the materials. Resistivity is observed to increase in the order of the spheroidite, coarser and fine pearlite, sorbite, and martensite microstructures.

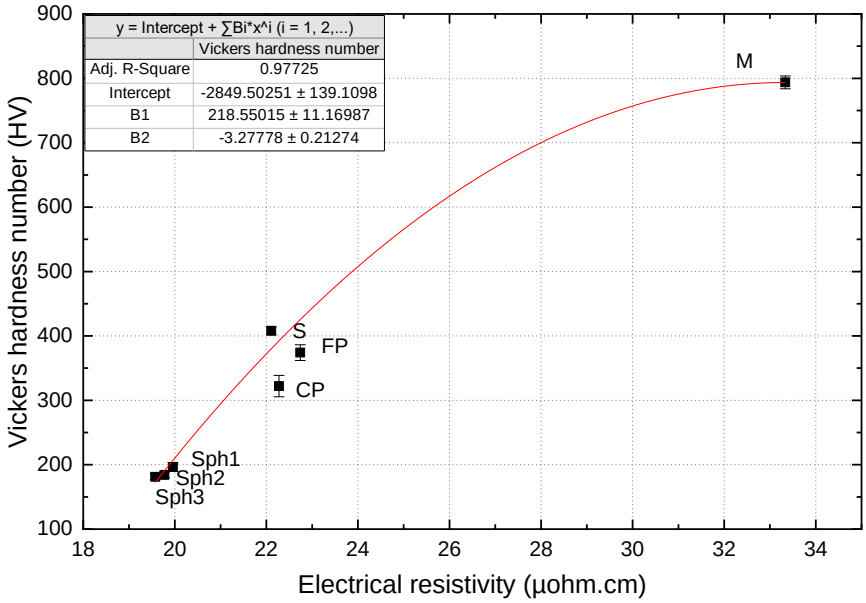

Figure 111: Relation between Vickers hardness and resistivity of the AISI 1080 steels heat-treated at different conditions

These results are explained by the variation of the total interfacial area between ferrite and cementite phases within the material, which alters the frequency of electron scattering events, affecting its mobility. In the spheroidized microstructures, the cementite precipitates in the form of spherical particles in a ferritic matrix resulting in a decrease of α-Fe3C interfaces and a conductive increase, contrary to the cementite lamellae configuration of pearlite. The very fine dispersed precipitates formed in the sorbite microstructure significantly increase scattering events, reducing the conductivity of these microstructures.

The notable differences in the electrical behavior of the martensitic microstructure can be first explained by the tetragonal lattice of martensite. The interstitial atoms of carbon trapped in iron solid solution during quenching strongly

influence the density of the free electrons in the crystal structure. In addition, the needle-like microstructure and the high density of dislocations present in the distorted lattice of martensite difficult the electron mobility. All these factors may explain the poor electrical conductivity of martensite compared to the other microstructures formed in an iron BCC lattice. [142]

Bulk magnetic properties were determined by hysteresis loops measurements performed at the same conditions as mentioned in the previous section and detailed in Chapter 2. Just as for the resistivity experiments, magnetic tests were carried out on specimens of 4 mm in diameter and 2.5 cm of length. The characteristic hysteresis loops obtained at 15 kA.m^{-1} for each sample are shown in Figure 112.

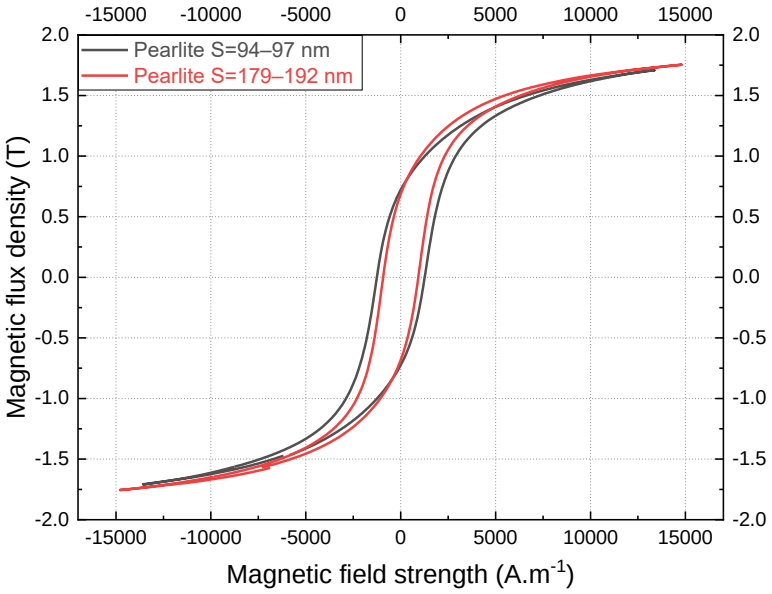

(a)

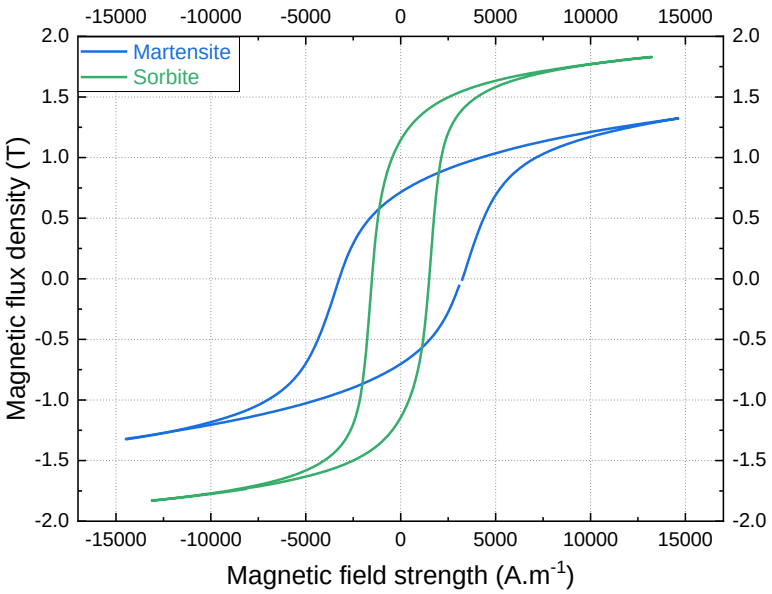

(b)

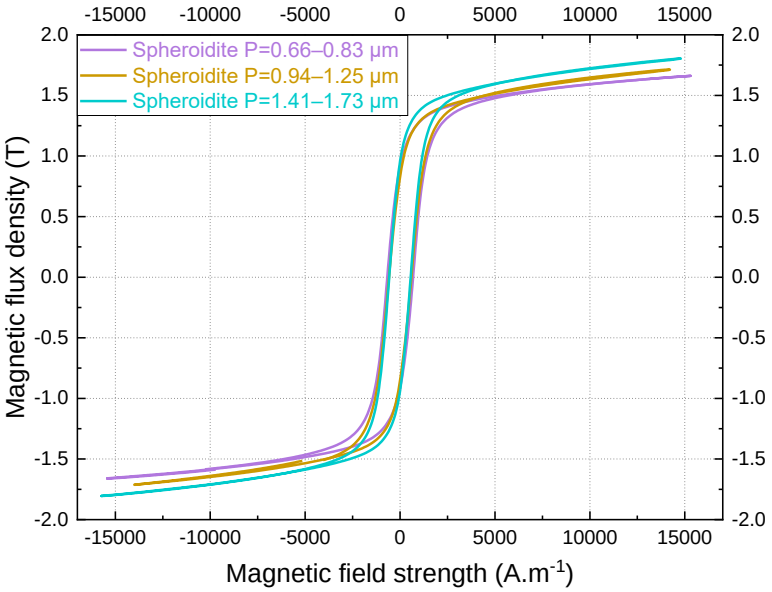

(c)

Figure 112: Comparison of the measured hysteresis loops of (a) fine and coarse lamellae pearlite, (b) martensite and sorbite, and (c) spheroidite microstructures

The hysteresis cycles of the various type of microstructures exhibit different shapes, indicating their distinct magnetic performance. It is notable the magnetic soft behavior of spheroidite presenting a low coercive force. Martensite has a much higher coercivity and is magnetically hard as compared to the other characterized microstructures. Figure 113 shows the normal magnetization curves and the relative permeability referent to hysteresis cycles obtained by varying magnetic field strengths from ± 15 kA.m^{-1} for each material. The magnetic relative permeability increases in the order of the martensite, fine and coarse pearlite, sorbite, and spheroidite.

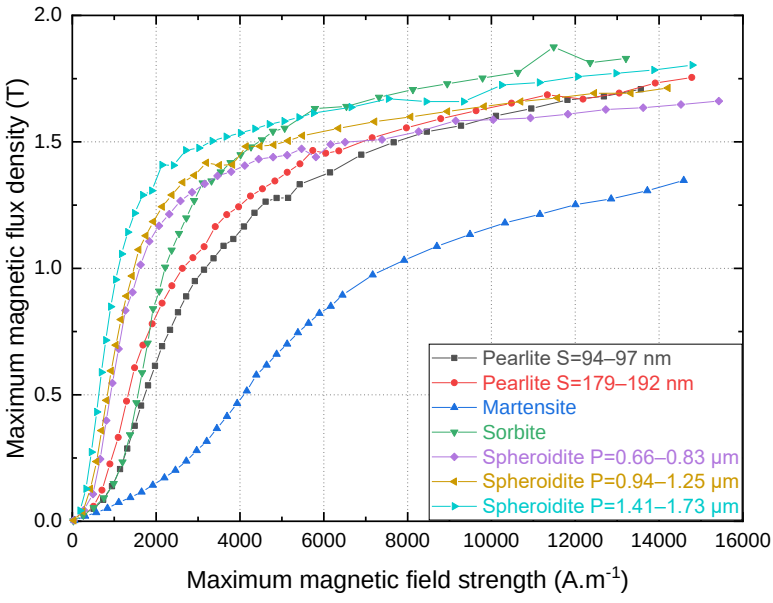

(a)

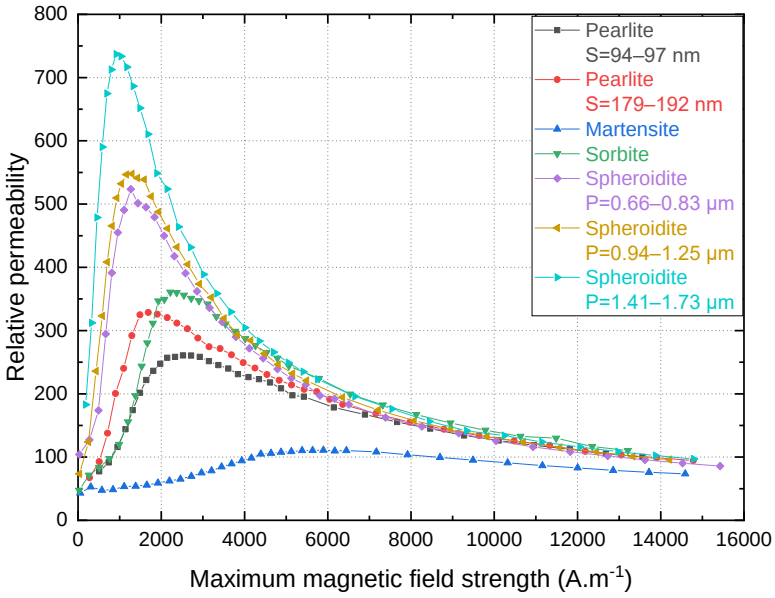

(b)

Figure 113: (a) Normal magnetization curves and (b) relative permeability in the function of the maximum magnetic field strength obtained for group C samples

Table 17 presents the average and standard variation values of the main magnetic properties determined from the hysteresis measurements.

Table 17: Magnetic properties of the several microstructures of AISI 1080 steels

Sample name	Microstructure	Coercivity ($A.m^{-1}$)	Remanence (T)	Hysteresis loss ($W.kg^{-1}$)	Magnetic saturation (T)	Maximum relative permeability
FP	Fine lamellar pearlite	1279 ± 25	0.74 ± 0.03	0.38 ± 0.14	1.71 ± 0.00	264 ± 3
CP	Coarse lamellar pearlite	935 ± 5	0.68 ± 0.00	0.29 ± 0.13	1.75 ± 0.00	328 ± 1
M	Martensite	3231 ± 18	0.70 ± 0.00	0.73 ± 0.09	1.35 ± 0.00	111 ± 1
S	Sorbite	1502 ± 5	1.14 ± 0.00	0.54 ± 0.03	1.83 ± 0.01	359 ± 2
Sph1	Spheroidite P=0.66–0.83 µm	673 ± 6	0.91 ± 0.00	0.24 ± 0.06	1.66 ± 0.00	535 ± 11
Sph2	Spheroidite P=0.94–1.25 µm	609 ± 8	0.84 ± 0.00	0.21 ± 0.05	1.71 ± 0.01	549 ± 1
Sph3	Spheroidite P=1.41–1.73 µm	561 ± 10	0.94 ± 0.00	0.21 ± 0.01	1.78 ± 0.00	730 ± 7

Figure 114 shows the correlations between magnetic properties and Vickers hardness number, displayed as average and standard deviation values. In this study, Vickers hardness is given as an indicator of the microstructure evolution and correspondent mechanical properties variations.

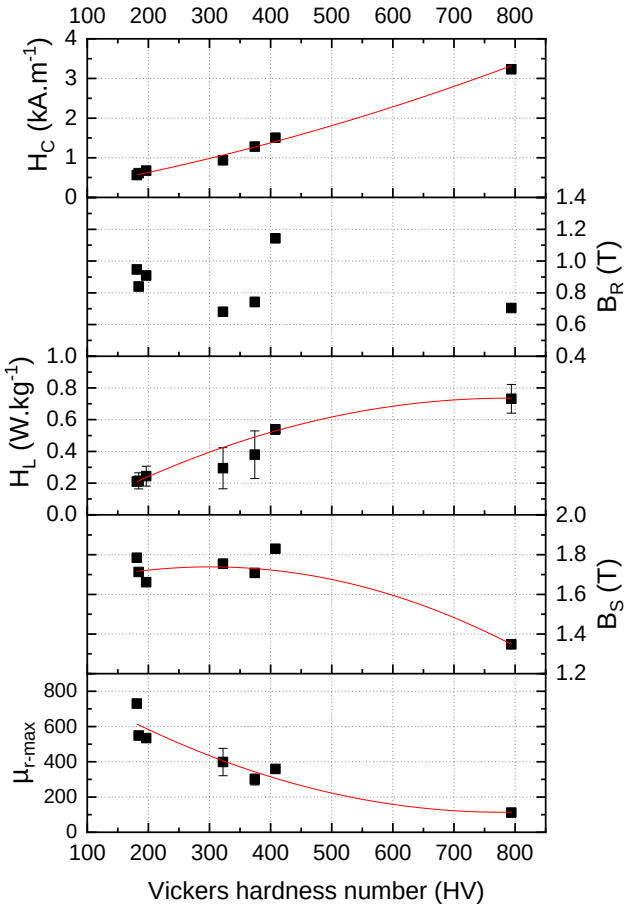

Figure 114: Relations between Vickers hardness and magnetic properties – coercivity (H_C), remanence (B_R), hysteresis loss (H_L), saturation (B_S), and maximum relative permeability ($\mu_{r\text{-}max}$) – of the various samples of group C

As observed, the coercivity and hysteresis losses increase for the mechanically harder microstructures, whereas the maximum relative permeability decrease. Remanent and saturation magnetization does not appear to vary considerably, however, for the martensitic steel, the magnetic saturation decreases markedly.

Spheroidized microstructures exhibit lower coercivity and higher relative permeability values than pearlite, which suggests that spheroidal cementite particles have a weaker pinning effect than continuous lamellae. Besides, sorbite presented a higher coercivity and lower relative permeability than spheroidite, which indicates that the finely dispersed precipitates in the ferrite matrix are more efficient anchorage sites of domain walls than relatively large spherical precipitates. The sorbite morphology is likely to favor precipitation hardening, in the same way, it contributes to the increase of magnetic coercivity as observed. Cementite lamellae become more effective at pinning as the width of ferrite decreases, increasing the number of α-Fe_3C interfaces. Fine lamellar pearlite exhibits worse magnetic properties than coarse microstructures.

The tetragonality of the martensitic lattice structure strongly affects their electromagnetic behavior. The very low relative permeability of such fine and complex needle-like microstructure is associated with the restricted domain wall mobility during magnetization. The high density of dislocations induces stress fields around dislocation lines that act as obstacles to the motion of domain walls within the material [60,65]. The wall movement is small in volume and represents a little increase of the overall magnetization. The magnetization process consists predominantly of domain wall rotations. Indeed, high coercive field strengths of about 3.2 $kA.m^{-1}$ are necessary to reorient the domains in a more favored direction to the applied field and overcome magnetostatic and magnetoelastic energies. Since the domain wall energy is important, the domain structure rearrangement is very limited, and extra magnetostatic energy is introduced to the system. The magnetocrystalline energy is associated with the high shape anisotropy of martensite, in which magnetic domains segregated strictly along specific crystallographic shear planes of BCT unit cell. As well as magnetocrystalline energy, the magnetoelastic energy depends on the deformations of the crystal lattice.

The observed decrease in magnetic saturation is proportional to the volume fraction of the ferromagnetic phase. The value of the saturation magnetization 1.35 T corresponds to the martensitic phase. As previously discussed, the ferrite phase has 1.95 T and ferrite-pearlite steels presented saturation values ranging from 1.70 to 1.90 T, which points out the increase of orthorhombic cementite phase with increasing carbon concentration. The different types of microstructures produced from eutectoid steels and composed of a BCC α-Fe matrix present close saturation magnetization values since no variation in phase composition occurred.

Saquet [143] proposed a schematic representation of the magnetic microstructure of various steel microstructure features, as illustrated in Figure 115.

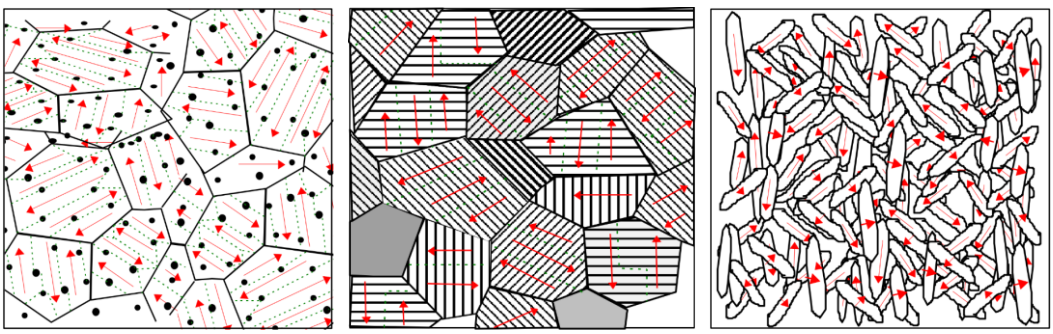

(a) **(b)** **(c)**

Figure 115: Schematic of the magnetic microstructures of (a) cementite precipitates in the ferrite matrix, (b) pearlite, and (c) martensite [143]

The magnetic microstructure of spheroidite tends to become closer to the ferritic configuration, with domain wall anchored at cementite precipitates [60,65,74-76,143]. MFM observations conducted in the present study have shown that the magnetic microstructure of pearlite does not possess a simple sub-lamellar structure, as the α-Fe lamellae are too narrow. The width of magnetic domains increases with the increase of the width of ferrite lamellae, extending across several lamellae. The pearlite domain configuration has also been observed by TEM and Lorentz microscopy [59,66,138]. The magnetic domain arrangement in pearlite depends on the domain wall orientation with respect to the Fe_3C lamellae, lying perpendicular or parallel to it. Domain configuration in martensite microstructures of steels does not seem to be well explored. Based on the work of Beale et al. [144], its domain structure is characterized by very fine single magnetic domains contained within the thin laths. The direction of magnetization within each mono-domain, perpendicular or parallel to the lath, depends on the predominant magnetostatic and magnetoelastic energy of the system [143].

Both electrical and magnetic properties showed significant variations concerning the different microstructures obtained from the eutectoid AISI 1080 steel. Similar relations were found by Jiles et al. [58], Byeon et al. [60], Saquet et al. [65,143] that have investigated the magnetic behavior of various microstructures of steels. Nevertheless, only a few works are found concerning the electrical properties evolution of such materials, among them the work of Klein et al. [140] on the influence of diffusion processes on the thermal and electrical conductivity of heat-treated steels.

Figure 116 shows the relations between physical properties and ECT outputs.

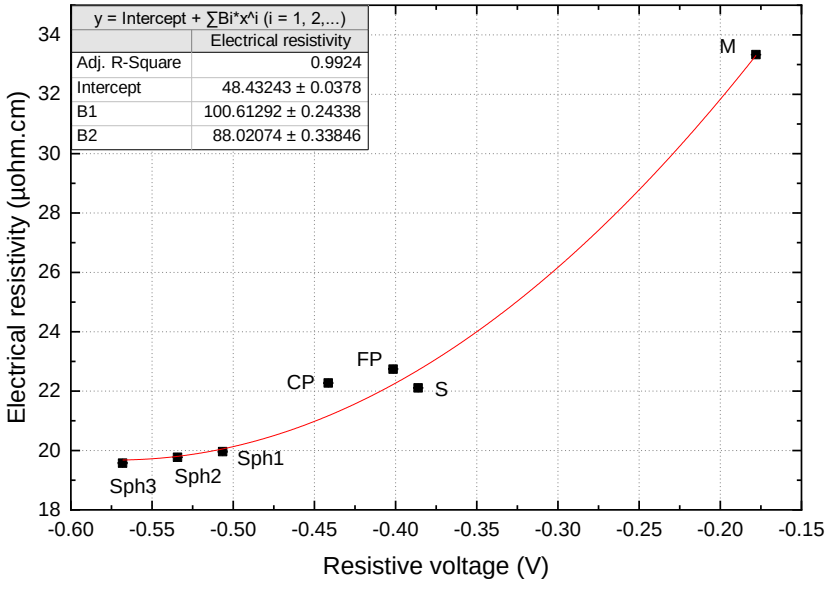

(a)

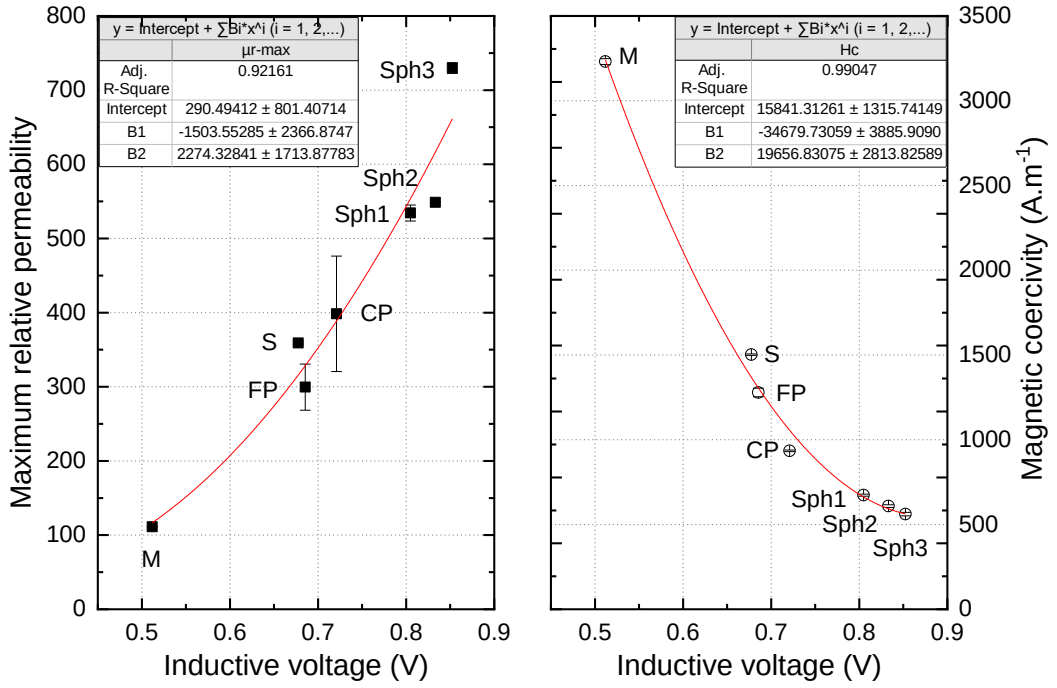

(b)

Figure 116: Correlation between eddy current outputs and (a) electrical resistivity, and (b) magnetic permeability and coercivity of the various samples of group C

As with Vickers hardness, good relations are found between electrical and magnetic properties and the respective resistive and inductive voltages evaluated by eddy current testing. The resistive voltage is observed to increase with increasing electrical resistivity, while the inductive voltage increases with increasing magnetic permeability and decreasing coercive force. These results confirm the sensitivity of the ECT method for distinguishing various carbon steel morphologies.

The electrical and magnetic behavior of eutectoid AISI 1080 steels have been demonstrated to highly depend on their thermo-mechanical history. Some main conclusions can be drawn from this study:

- Besides the strong influence of phase composition discussed in the first part of this chapter, the crystal lattice structure and microstructural morphology are determinant for defining mechanical and physical properties of carbon steels.
- Variation in phase morphology involving the increase of total α-Fe_3C interfacial area has been observed to increase the frequency of electron scattering events, reducing the electrical conductivity. Also, it influences the pinning effect of cementite precipitates on domain walls. Both lamellar and fine dispersed precipitates have shown to be more efficient anchorage sites than

do spheroidal precipitates. Cementite lamellae become more effective at pinning as the width of ferrite decreases. Electrical conductivity and magnetic permeability are observed to increase in the order of the martensite, sorbite, fine and coarse pearlite, and spheroidite microstructures.

- The particular electrical and magnetic behavior of martensite is explained by its tetragonal unit cell supersaturated with carbon atoms, the subsequent needle-like morphology, and the high density of dislocations introduced in the lattice by the diffusionless martensitic transformation.
- The potentiality of eddy current testing was highlighted for characterizing different types of microstructures of eutectoid steels with various morphologies and strengths.

III. EDDY CURRENT TESTING AS A NON-DESTRUCTIVE CHARACTERIZATION TOOL FOR CARBON STEEL WIRES

In this research, a range of plain carbon AISI 1000 series steel wires have been selected and submitted to various thermal treatments for investigating the effects of several microstructural parameters on their electrical and magnetic properties. Moreover, the electromagnetic behavior of such materials was evaluated using an electromagnetic sensor to enlarge the possibilities of such a technique for NDT characterization of carbon steels. The assessment of the capability and limitations of the electromagnetic evaluation of steel wires is presented in this section.

III.1. Interrelationship between eddy current outputs and electromagnetic properties

Eddy current outputs have demonstrated a good correlation with the main electrical and magnetic properties that characterize the electromagnetic behavior of the heat-treated carbon steel wires investigated in this study, as shown in Figure 117.

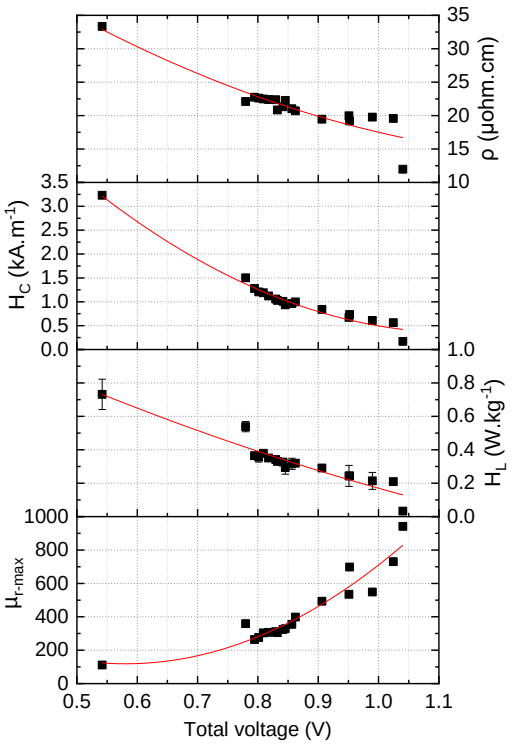

Figure 117: Total voltage dependences of electrical and magnetic properties – resistivity (ρ), coercivity (H_C), hysteresis loss (H_L), and maximum relative permeability ($\mu_{r\text{-}max}$) – of heat-treated plain carbon steels

The electrical resistivity decreases with the increase of total voltage. In the same way, the structure-sensitive magnetic properties, including coercivity and hysteresis losses, is observed to decrease while the maximum relative permeability increases with increasing total voltage. These results confirm that the eddy current responses are strongly related to the electromagnetic behavior of carbon steels. As hitherto discussed, the corresponding variations in their electrical and magnetic characteristics indicate important changes in their phase composition, distribution, and morphology. Hence, the ECT has proved to be capable of evaluating indirectly microstructural parameters of heat-treated carbon steels, including the phase composition of ferrite-pearlite steels and interlamellar spacing of pearlite in fully pearlitic steels. The distinct microstructure morphologies obtained from patenting, spheroidizing, quenching and tempering treatments of eutectoid steels are well distinguished, as well as the tetragonal martensitic structure.

The eddy current voltage plane (Figure 118) shows the average variations of the total voltage signals components, the resistive and inductive voltages, for the several steel wires of 4 mm in diameter studied in this chapter.

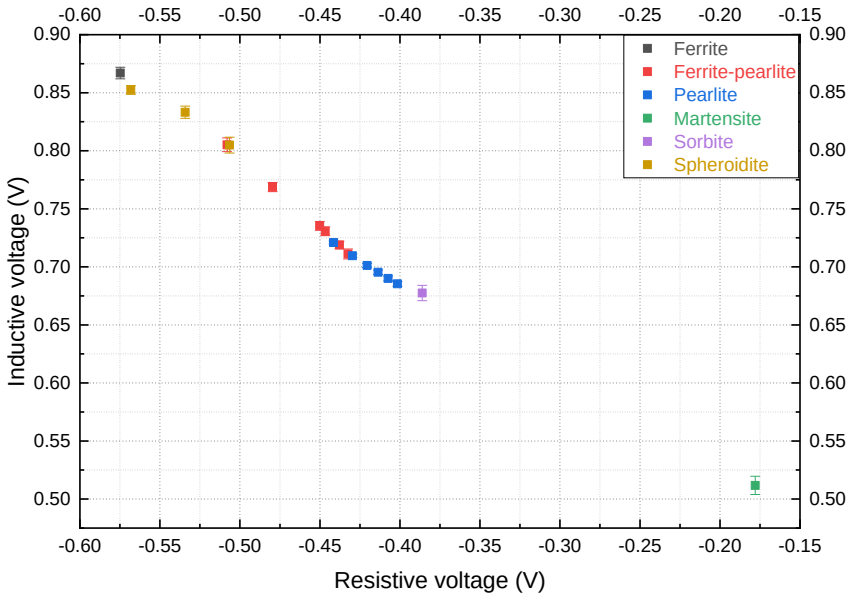

Figure 118: Eddy current voltage plane of the various heat-treated steel samples

Plain carbon steels with carbon concentration ranging from 0.03 to 0.78 wt. %C were used to produce samples with various proeutectoid ferrite-pearlite ratio, as well as fully ferritic and pearlitic steels. The resistive voltage increases and the inductive voltage decreases with the increasing volume fraction of cementite lamellae in the steels. In addition to the changes in the proeutectoid ferrite and pearlite volume

fraction, the carbon concentration increase caused a slight decrease in the interlamellar spacing of pearlite that also contributes to the observed electromagnetic behavior of such materials.

Next, eutectoid steel with 0.78 wt. %C was employed for evaluating the effect of different types of microstructures obtained through various heat treatments. The morphology of the pearlitic microstructure has demonstrated a significant effect on the eddy current responses. Pearlitic steels with a lamellar microstructure present higher resistive voltages and lower inductive voltage values than the microstructures with relatively large spheroidite cementite particles. Besides, fine pearlite samples have higher resistivity and lower inductive voltages than coarse pearlite with a thicker lamellar microstructure. These results demonstrate the effect of α-Fe_3C interfaces on the electromagnetic behavior of such materials. Finally, the influence of crystal lattice structure on the electrical and magnetic properties of steels is evidenced through the investigation of martensitic steels, which achieve very high resistive voltage and very low inductive voltage signals. The sorbite microstructure produced from the tempering of martensite consisted of very fine Fe_3C precipitates dispersed in the ferrite matrix, reinforcing the effect of size and distribution of the cementite phase.

Despite the great potential of eddy current technique for characterizing such a range of materials, it is apparent its limitation on clearly distinguishing different steels exhibiting similar electrical and magnetic behavior and distinct mechanical characteristics. For instance, the coarse lamellar pearlite samples present similar electromagnetic responses than ferrite-pearlite steels having about 2 to 5 % of proeutectoid ferrite. The different interlamellar spacing between the samples counterbalances the effect of proeutectoid ferrite-pearlite balance, and both materials have very close conductivity and magnetic permeability properties. Another example is the eddy current performance of a spheroidite eutectoid steel with relatively small spherical particles and remaining lamellar-like cementite in the ferrite matrix, comparable to that of low-carbon steel with a high amount of proeutectoid ferrite and discontinuous cementite lamellae in pearlite. In this case, even if the steels have different carbon contents, the resembling morphology of cementite with reduced α-Fe_3C interfacial area concentration seems to be a determinant factor affecting their physical properties in a similar way. It is possible to conclude that the macroscopic electromagnetic behavior of steels results from individual contributions of microstructural elements (e.g., chemical composition, phase composition, and

morphology) that are often intrinsically related one to each other. For this reason, a careful interpretation of ECT responses is critical for a proper evaluation.

III.2. Influence of testing parameters on eddy current outputs

Just as electrical conductivity and magnetic measurements are very sensitive to external disturbances, the eddy current testing is susceptible to several parameters other than the material's physical properties variations that can strongly affect the test performance. It includes the test frequency and the coil design and electromagnetic coupling between the electromagnetic sensor and the material (lift-of and fill-factor) that can alter the effective depth and sensitivity of eddy current within the material. Moreover, temperature variations caused by the processing or the eddy currents themselves can affect the conductivity of the material, altering their electromagnetic behavior locally.

Consequently, the calibration of the eddy current measurement system must be performed with reference materials to attenuate undesirable variations and define the more suitable parameters for a specific application. In the present study, ECT was carried out at a low frequency of 200 Hz, which had provided optimum values for discriminating the different materials in the first test calibration. The coupling between coil and wire specimens was regular, once there was no significant cross-section area variation among the materials and the wire sample position within the coil does not oscillate during testing.

In order to verify if the optimum test frequency determined by experimentation was adapted for the characterization of carbon steel wires, the magnetic flux density induced into the materials through eddy current testing was quantitatively evaluated by finite element modeling. The numerical simulations were performed using an open-source finite element analysis software, Finite Element Method Magnetics (FEMM). A solid model of the eddy current system consisted of an excitation copper coil of 281 turns and 10 mm in diameter was configured under an alternate current of 0.5 A and a frequency of 200 Hz. Materials presenting very different electromagnetic behavior were selected for the simulation experiment: ferrite (AISI 1000), pearlite, and martensite (AISI 1080) steel wires of 4 mm in diameter. Their physical properties were assessed taking into account the measured electrical resistivity values and the magnetic properties obtained from magnetization B–H curves for each material. The electromagnetic induction maps acquired for the three different microstructures by the

finite element method are shown in Figure 119. The samples and the electromagnetic coil are represented along their x-axis of symmetry.

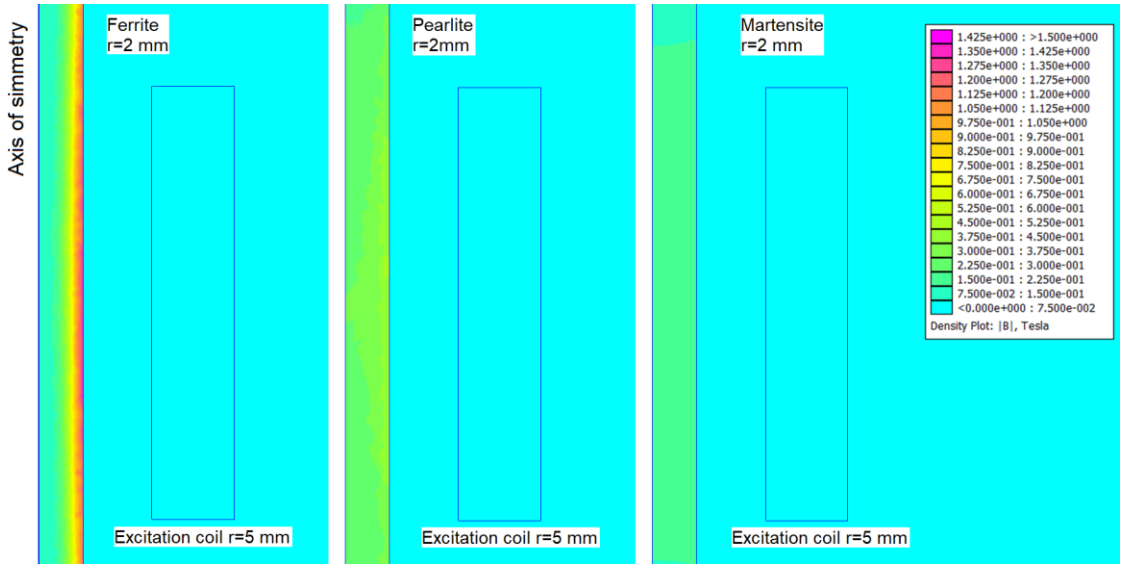

Figure 119: Numerical simulation illustrating the magnetic flux density induced into steel wire samples of 4 mm in diameter by an excitation coil under 0.5 A and 200 Hz

Figure 120 compares the estimated flux density variations between the various microstructures in the function of the depth of penetration of the samples.

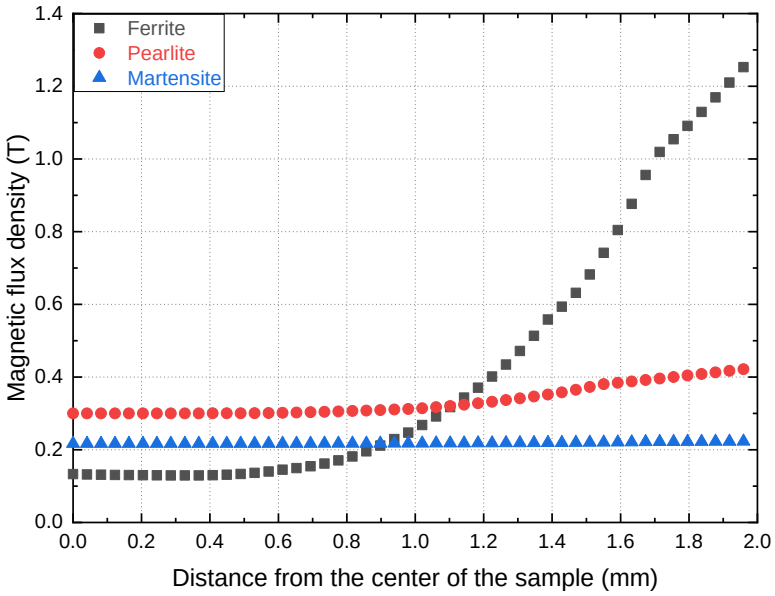

Figure 120: Simulated magnetic flux density in the function of the depth of penetration into different steel sample wires of 4 mm in diameter by eddy currents

It can be observed that the magnetic flux is more concentrated on the surface and decreases in intensity with the distance below the surface in the ferritic sample, which indicates the eddy current skin effect within this soft magnetic material. Pearlite

and martensite steels do not present a significant skin effect, and the magnetic flux is distributed almost homogeneously within the bulk material.

The conductivity of a material is an intrinsic property; however, the magnetic permeability is an extrinsic property that varies in function of an applied field. For this reason, it is of great importance to work at optimum magnetic field ranges in electromagnetic non-destructive testing so that the different magnetic behavior of tested materials may be correctly detected through resistive and inductive voltage signals. Figure 121 shows the relative permeability variation with the maximum magnetic flux density obtained from bulk magnetic measurements and the corresponding ECT outputs obtained for each sample. Based on the numerical simulation, the flux density range induced by eddy current into the core of steel wires at a frequency of 200 Hz is indicated in the graphic, delimited in green.

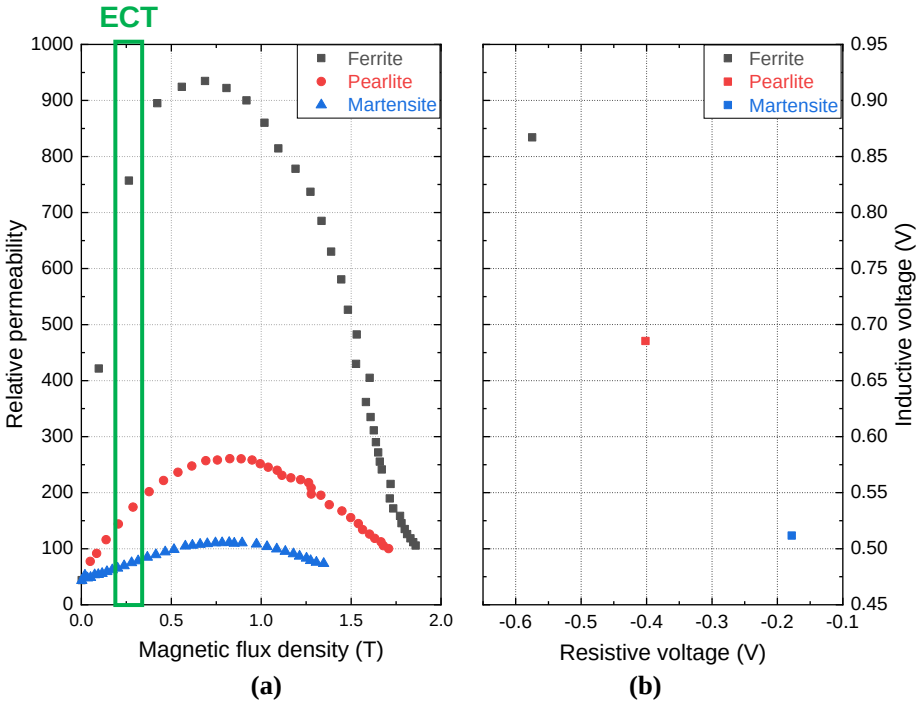

Figure 121: (a) Relative permeability in the function of maximum flux density of the various 4 mm-diameter samples, and (b) their corresponding eddy current outputs

Even with the significant skin effect observed in soft magnetic ferrite, the induced electromagnetic fields at the core of the sample are high enough for evaluating their particular magnetic behavior, as seen in Figure 121-a. Also, it validates the pertinence of determining the maximum permeability, instead of initial permeability in the present work. Since the dimensions of the wires do not change during testing, the variations in flux density and, thus, in ECT signals (Figure 121-b) are purely due to the distinct electromagnetic behavior between the investigated materials.

These results confirm that the test frequency established of 200 Hz for performing ECT evaluation of steel wires allowed to well distinguish the relative permeability between different materials. The very small standard deviations for each group mean suggested the great consistency of ECT values obtained in this investigation. Hence, the effect of external disturbances other than those linked to physical properties is considered negligible on the measurement dispersion.

III.3. Interrelationship between eddy current outputs and mechanical properties

Quantitative correlations were obtained between physical properties and the eddy current signals, demonstrating the potential of this NDT for quantitatively assessing microstructural parameters of carbon steels. To extend this methodology for quality assurance and process monitoring for pearlitic steel wires on an industrial scale, the feasibility of quantitatively predicting mechanical properties, notably ultimate tensile strength, has been evaluated.

The ECT calibration is the first mandatory step. In this context, to complement the primary database consisted of groups A and B, steel batch grades with carbon content varying from 0.03 to 0.78 wt. % C and of 4 mm in diameter were selected. Patenting treatments were then performed by austenitizing at 950°C and cooling at constant temperatures of 540, 560, 580, 600, 620, and 640°C in a lead bath for a few seconds. It resulted in ferrite-pearlite steels with various pearlite fractions, interlamellar spacing, and strengths. ECT was performed in-situ and offline at the same conditions as previously described and correlations between the mean total voltage and mechanical properties are given in Figure 122.

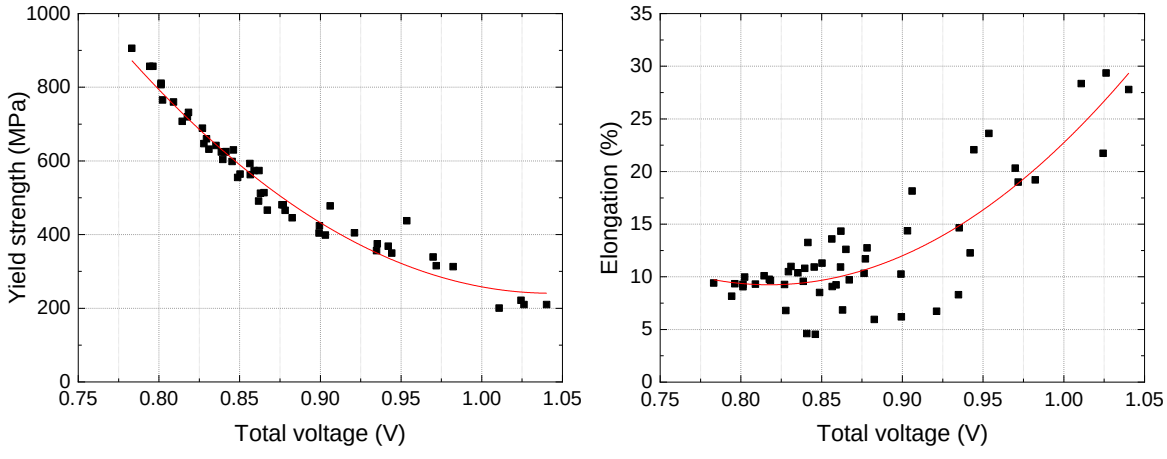

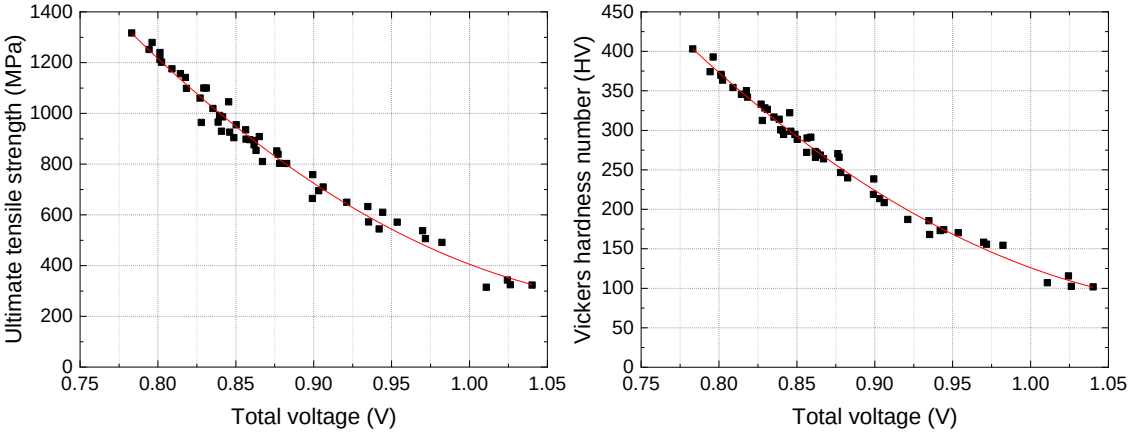

Figure 122: Total voltage variation with mechanical properties of carbon steel wires

The information collected was used for building an empirical model employing multiple regression analysis. In order to predict the ultimate tensile strength of carbon steels, the following key input parameters were considered: carbon content (C), and the eddy current responses, resistive voltage (V_R), inductive voltage (V_L), and total voltage (V_T). The carbon concentration configures the main microstructural parameter determining the phase balance and morphology of the steels, and thus their mechanical properties. The austenitization and transformation temperatures are considered variables with a less incremental impact in the ultimate tensile strength variation. The inputs referents to ECT are the variables that allow directly monitoring steel parts in a non-destructive manner due to interactions between microstructure and their electrical and magnetic properties.

The regression model for predicting ultimate tensile strengths (σ_{UTS}) of ferrite-pearlite steel wires of 4 mm in diameter was built as given:

$$\sigma_{UTS} = 3532 + 476.2\,C + 2610\,V_R + 32089\,V_L - 30965\,V_T + 45248\,V_R V_L - 42182\,V_R V_T \quad (46)$$

where the ultimate tensile strength is in MPa, the carbon content in % weight, and the eddy current outputs in voltage. The relationship between strength and model variables is statistically significant ($p<0.001$), and the coefficient of determination R^2 indicates that the model can explain 99.73% of the variations in strength.

Next, the empirical model was used to directly estimate the strengths by ECT of additional patented wires of AISI 1065, 1080, and 1085 steels of 4 mm in diameter. Samples were also collected for performing conventional tensile tests. The average experimental and predicted σ_{UTS} values are presented in Table 18.

Table 18: Empirical and predicted ultimate tensile strengths of ferrite-pearlite steels wires of 4 mm in diameter

AISI steel	Austenitization/ Transformation temperature (°C)	Experimental	Mathematical model		
		Ultimate tensile strength (MPa)	Ultimate tensile strength (MPa)	95% confidence interval	
				Lower bound	Upper bound
1065	950/ 540	1125 ± 1	1122 ± 7	1107	1136
1065	950 / 580	1050 ± 2	1045 ± 4	1038	1053
1065	950 / 640	937 ± 1	929 ± 4	921	938
1080	950 / 540	1273 ± 2	1274 ± 6	1261	1287
1080	950 / 580	1202 ± 1	1201 ± 4	1192	1209
1080	950 / 640	1078 ± 1	1083 ± 5	1073	1092
1085	950 / 540	1331 ± 1	1344 ± 8	1327	1360
1085	950 / 580	1258 ± 1	1257 ± 6	1244	1270
1085	950 / 640	1110 ± 1	1113 ± 6	1101	1126

Figure 123 illustrates graphically both empirical and predicted ultimate tensile strength, also indicating the confidence interval (0.05 level) of the regression model at the 0.05 level.

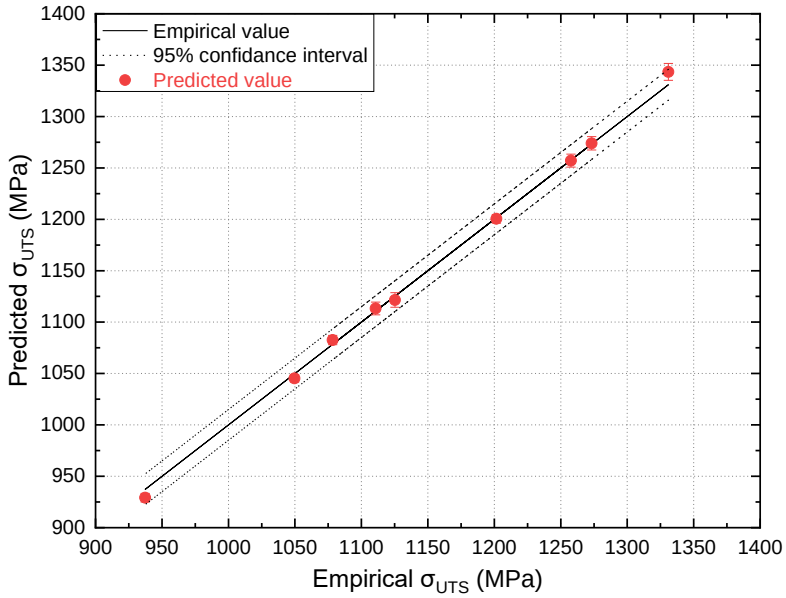

Figure 123: Correlation between the measured and predicted σ_{UTS} values calculated from the empirical model of 4-mm diameter ferrite-pearlite steel wires

A good correlation has been found between the experimental ultimate tensile strength and the estimated values from the regression model. It is important to observe

that the strengths determined from tensile tests have been done from a few wire samples collected after the thermal treatments. Although these measurements have presented very small standard deviations, they are still less representative than the values based on eddy current outputs, which were acquired continuously from a large extent of the material. Nonetheless, a new calibration must be done to define the optimum test parameters and generate an adapted database whenever a new material with different geometry, chemical, and phase compositions need to be tested using the electromagnetic sensor.

These results affirm the great potential of the eddy current testing as a characterization tool for evaluating the microstructural state and mechanical properties of carbon steels and monitoring wire manufacturing processes stability.

IV. SUMMARY

In general, the predominant microstructural factors on the physical properties of plain carbon steels are the result of a combination of the different elements mentioned in this chapter. These relations are illustrated in Figure 124. In order to assess the effect of plastic deformation on the electromagnetic performance of pearlitic steels, the study of their behavior in drawing and cyclic stresses is approached in Chapter 4.

	CARBON STEEL WIRES		PHYSICAL PROPERTIES		NDT
CHEMICAL COMPOSITION	Increase carbon concentration	↑↑ % Pearlite ∴ ↑↑ % Fe_3C ↓ $\bar{S}$ ↑↑ Strength ↓↓ Ductility	↓↓ $\boldsymbol{\sigma}$ * Interstitial C atoms decrease free electrons density * Scattering events increase with increase of α-Fe_3C interfaces	↓↓ $\boldsymbol{\mu}$ · ↑↑ $\boldsymbol{H_C}$ * Strong domain wall pinning effect at Fe_3C lamellae ↓ $\boldsymbol{B_S}$ * Magnetic phase composition change (decrease of ferrite)	↑↑ R · ↓↓ X_L ↓↓ Z ∴ ↑↑ $\boldsymbol{V_R}$ · ↓↓ $\boldsymbol{V_L}$ ↓↓ $\boldsymbol{V_T}$
MICROSTRUCTURAL FEATURES	Lamellar pearlite	↓ $\bar{S}$ ↑ Strength ↓ Ductility	↓ $\boldsymbol{\sigma}$ * Scattering events increase with increase of α-Fe_3C interfaces	↓ $\boldsymbol{\mu}$ · ↑ $\boldsymbol{H_C}$ * Domain wall pinning increase with increasing α-Fe_3C interfaces	↑ R · ↓ X_L ↓ Z ∴ ↑ $\boldsymbol{V_R}$ · ↓ $\boldsymbol{V_L}$ ↓ $\boldsymbol{V_T}$
	Spheroidizing	Spherical Fe_3C particles in ferrite matrix (spheroidite) ↓↓ Strength ↑↑ Ductility	↑↑ $\boldsymbol{\sigma}$ * Reduction of scattering events due to α-Fe_3C interfacial area decrease	↑↑ $\boldsymbol{\mu}$ · ↓↓ $\boldsymbol{H_C}$ * Lower domain wall pinning effect at Fe_3C particles	↓↓ R · ↑↑ X_L ↑↑ Z ∴ ↓↓ $\boldsymbol{V_R}$ · ↑↑ $\boldsymbol{V_L}$ ↑↑ $\boldsymbol{V_T}$
	Martensite	Body-centered tetragonal lattice cell Thin lath morphology ↑↑↑ Strength ↓↓↓ Ductility	↓↓↓ $\boldsymbol{\sigma}$ * Supersaturated solid solution of C atoms decreases free electron density * Scattering events increase with increase of α-Fe_3C interfacial area, lattice distortion, and dislocation density	↓↓↓ $\boldsymbol{\mu}$ · ↑↑↑ $\boldsymbol{H_C}$ * Limited wall displacement (high wall energy) and domain rotation (high anisotropy and magnetostatic energies) ↓↓ $\boldsymbol{B_S}$ * Magnetic phase composition change	↑↑↑ R · ↓↓↓ X_L ↓↓↓ Z ∴ ↑↑↑ $\boldsymbol{V_R}$ · ↓↓↓ $\boldsymbol{V_L}$ ↓↓↓ $\boldsymbol{V_T}$
	Martensite softening	Reduction of martensite tetragonality Very fine Fe_3C precipitates in ferrite (sorbite) ↑ Strength (precipitation hardening) ↑ Ductility	↑ $\boldsymbol{\sigma}$ * Free electron density increases and scattering events decrease with reduction of lattice distortion and Fe_3C precipitation	↑ $\boldsymbol{\mu}$ · ↓ $\boldsymbol{H_C}$ * Lower domain wall pinning at fine Fe_3C precipitates * Reduction of magnetocrystalline anisotropy and magnetostatic energies	↓ R · ↑ X_L ↑ Z ∴ ↓ $\boldsymbol{V_R}$ · ↑ $\boldsymbol{V_L}$ ↑ $\boldsymbol{V_T}$

Figure 124: Diagram summarizing the observed effects of microstructural parameters on the electromagnetic behavior of carbon steel wires

CHAPTER 4

EFFECT OF PLASTIC DEFORMATION ON THE ELECTROMAGNETIC BEHAVIOR OF CARBON STEELS

CHAPTER 4

EFFECT OF PLASTIC DEFORMATION ON THE ELECTROMAGNETIC BEHAVIOR OF CARBON STEELS

Chapter 3 was dedicated to studying the overall effects of microstructural parameters in carbon steels, especially pearlitic steels, and their influences on their mechanical and electromagnetic properties. This chapter is then focused on investigating the effect of plastic deformation on pearlitic steel wires. The first part of this study refers to the impact of cold-drawing on fine and coarse pearlite microstructures at different degrees of deformation, and the influence of cold working on their corresponding electromagnetic behavior.

As this thesis manuscript takes place in the context of an industrial project, the study of phenomena related to fatigue issues of engineering materials, and more particularly of pearlitic steels, is of great interest. The term fatigue refers to a process of progressive localized plastic deformation in a material due to cyclic mechanical stresses, which alters their properties and can lead to mechanical failure. It is considered one of the most common sources of damages to structural components. In this context, the second part of this research investigates the influence of microstructure on the fatigue behavior of fully pearlitic steels and the formation of intrusion-extrusion, which can lead to short cracks initiation and conduct to fatigue failure. Also, the capability of eddy current method for NDT monitoring of structures submitted to cyclic mechanical loadings is investigated. A summary of the main conclusions is presented at the end of the chapter.

I. EFFECT OF WORK-HARDENING DURING COLD-DRAWING

I.1. Microstructure and mechanical properties

Eutectoid AISI 1080 steel wire rods of 6 mm in diameter were first heat-treated for producing fully pearlitic samples with fine and coarse lamellar morphologies. The patented wires were then cold-drawn in a total of ten passes to wires of the diameter of 2 mm. Samples were collected at each pass of drawing with diameters varying from 5.23 to 2 mm, which consists the group D, as detailed in Chapter 2. Also, as-heat-treated samples of 6, 4, and 2 mm of diameter were obtained as reference.

The microstructural evolution during cold-drawing was evaluated by scanning electron microscopy. Figure 125 and Figure 126 show, respectively, SEM micrographs in transversal and longitudinal cross-sections of the cold-drawn pearlite samples, at different deformation degrees. The samples with initial fine pearlite structure are shown on the right images and the ones that were cold-drawn from coarse lamellar pearlite, on the left. The drawing direction (DD) is indicated in the images.

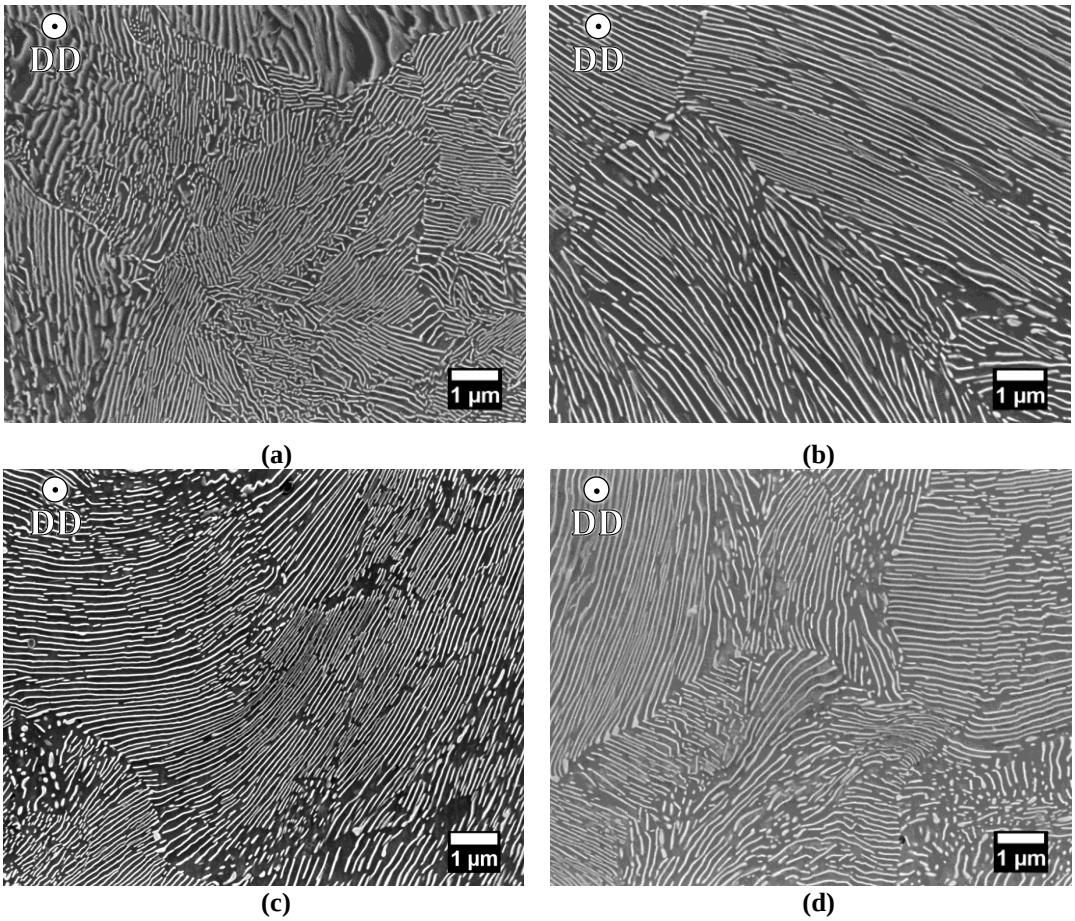

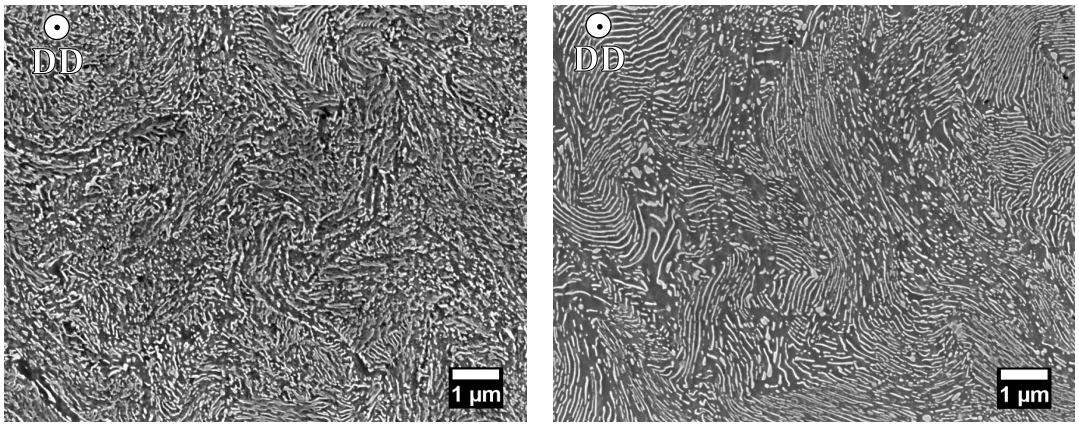

(e) **(f)**

Figure 125: Microstructures of AISI 1080 steels with initially fine (right) and coarse (left) lamellar pearlite observed by SEM in the transverse cross-section after cold-drawing at (a, b) Ɛ=0.27; (c, d) Ɛ=0.81; (e, f) Ɛ=2.20

As discussed in the last chapter, the typical morphology of a non-deformed pearlite structure is characterized by equiaxed colonies and nodules randomly orientated. At the initial stage of cold-drawing, little differences were observed between the cold-drawn samples with initial fine and coarse pearlite structures in the SEM images. Some lamellae exhibited slightly bending around the axis of the wire, as seen in Figure 125-a and Figure 125-b. With increasing drawing strain, deformation bands developed across the cementite lamellae, notably in the samples with initially coarse lamellae. Also, cementite fragmentation was visualized in both microstructures in Figure 125-c and Figure 125-d. At a higher strain of Ɛ=2.20, a curly microstructure morphology is observed in both structures with strongly twisted lamellae and fragmented cementite particles. Nevertheless, the curling effect was more pronounced in the sample with initial fine lamellar pearlite (Figure 125-e), which presented thinner cementite lamellae and a denser fiber microstructure compared to the cold-drawn coarse pearlite (Figure 125-f).

In the longitudinal cross-sections shown in Figure 126, it can be seen that the cementite lamellae become gradually aligned with the wire axis, along the drawing direction due to the stretching and rotation of pearlite colonies. The refinement of the interlamellar spacing and thickness of the ferrite-cementite lamellae was observed following the reductions in the wire diameter of both fine and coarse pearlite steels during the cold-drawing process. The anisotropic behavior of steels is evidenced by comparing the transverse and longitudinal sections.

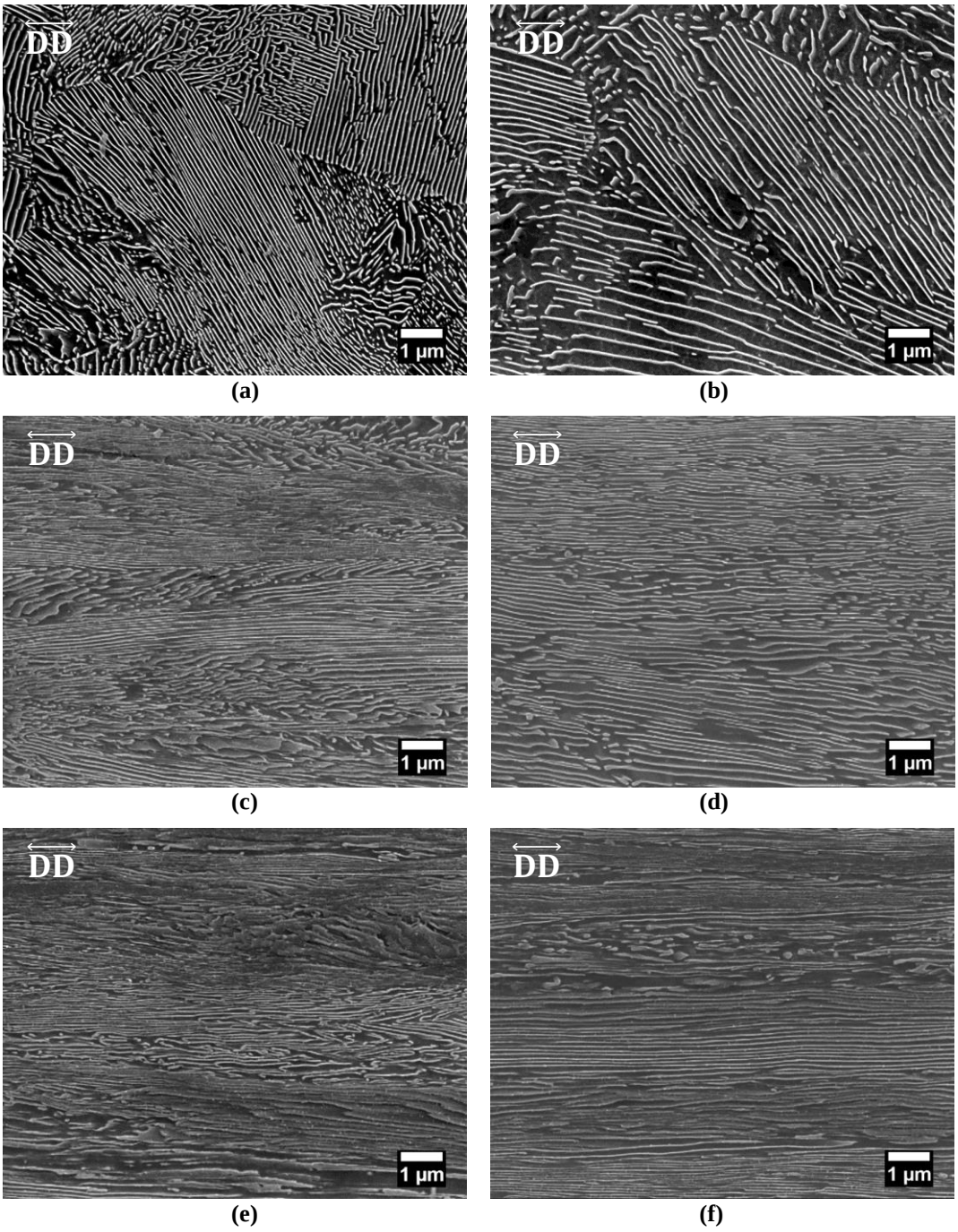

Figure 126: SEM images of longitudinal sections of AISI 1080 steels with fine (right) and coarse (left) pearlite, cold-drawn to strains up (a, b) 0.27; (c, d) 0.81; (e, f) 2.20

As reported by many authors [145-148], the microstructural changes to which the ferrite-cementite lamellae are subjected during drawing involve several mechanisms, depending largely on the original orientation of the lamellae with respect to the direction of drawing and the degree of cold-drawing deformation. It includes the alignment of colonies along the drawing direction, the reduction in the interlamellar spacing, the evolution of ferrite-pearlite interfaces with refinement and fragmentation of cementite lamellae. During the drawing process, the ferrite matrix develops a <110>

fiber crystalline texture [148-152] due to the stretching and alignment of pearlite colonies along the wire axis. The development of a fiber texture along the drawing direction also results in the reorientation of pearlite colonies around their axis to conserve the axial symmetry of the deformation within the wire [148,152,153].

Many authors have studied the evolution of cementite morphology during drawing, among them, Toribio and Ovejero [154], Zhang et al. [155], and Guo et al. [151]. They have proposed evolution mechanisms of pearlite morphology with drawing strain based on the analysis of numerous SEM micrographs at different stages of drawing. The extent of colonies reorientation depends on the orientation of cementite lamellae to the direction of drawing, as shown in Figure 127. The Fe_3C lamellae that lie parallel to the wire axis are elongated and thinned along the drawing direction. The lamellae oriented with an angle to the wire axis progressively rotated to become parallel to the wire axis. In contrast, in colonies consisting of lamellae that are not favorably oriented to the drawing axis, twist and fragmentation can occur, forming nanoscale particles dispersed in the ferrite matrix by severe plastic deformation.

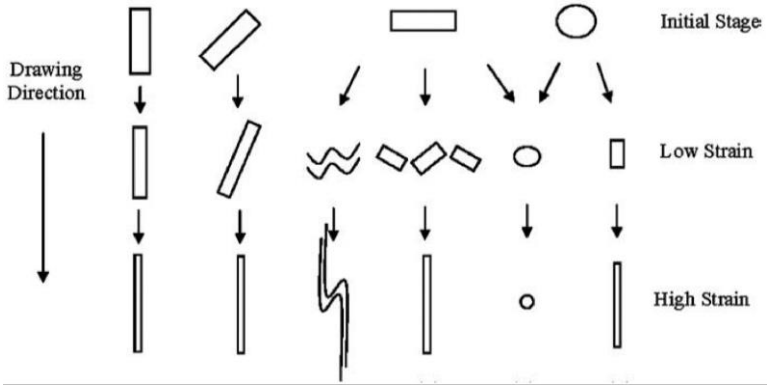

Figure 127: Schematic illustration of the evolution of cementite morphology in the longitudinal section with respect to its orientation to the wire axis during drawing [155]

Besides, deformation bands may appear in the material, formed by either kinking or shearing with increasing drawing strain, because of the locally heterogeneous deformation occurring within pearlite colonies with different spatial orientations [147,148,155-157]. Guo et al. [156] reported that the development of such bands also involved the instability of ferrite-cementite interfaces due to the stress concentration by the increasing density of dislocation pile-ups. Besides, Porter et al. [39] found that shear bands are often observed through growth faults in the lamellae of pearlite colonies (e.g., linear lamellae discontinuities), where the slip distance in the ferrite matrix is locally increased. In addition to the arrangement and density of

dislocations in the ferrite matrix, localized shear and kink deformation bands also contribute to the colony rotation towards the wire axis and reduce the interlamellar spacing of pearlite. Deformation bands were observed to develop across the cementite in both fine and coarse cold-drawn structures, but they were a more common feature in coarse pearlite, as shown in Figure 128.

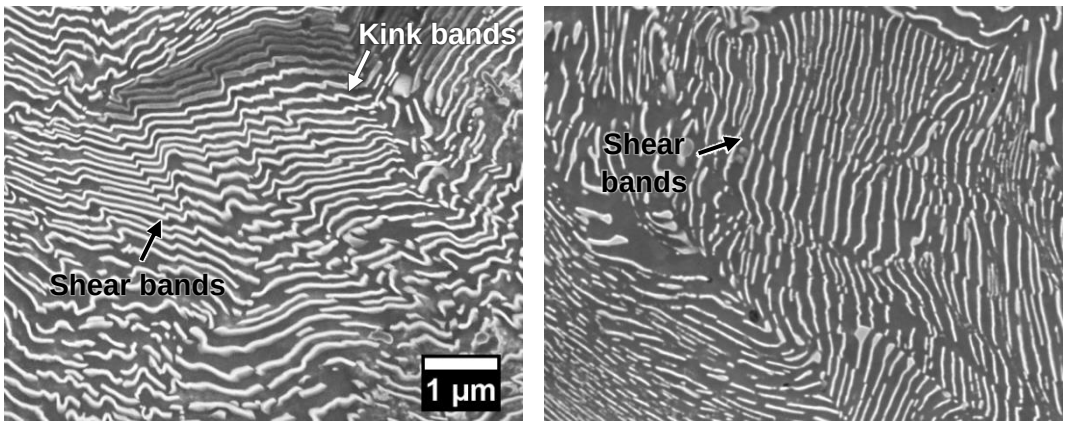

(a) **(b)**

Figure 128: SEM images of transverse sections showing the presence of kink and shear bands on cold-drawn coarse pearlite at (a) ε=0.81 and (b) ε=1.34

At high drawing strains, all the ferrite layers become aligned close to the drawing direction, and a curled-type microstructure is obtained in the transverse section of the wires [147,160]. The cold-drawn pearlite samples obtained at ε=2.2 are shown in detail in Figure 129.

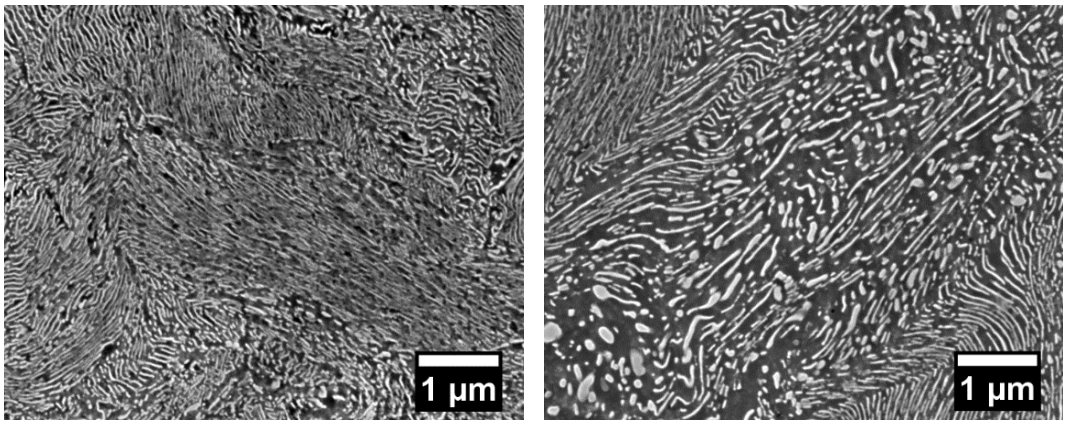

(a) **(b)**

Figure 129: SEM micrographs showing (a) fiber morphology, and (b) fragments of cementite, respectively, in initially fine and coarse lamellar pearlite cold-drawn at Ɛ=2.2

Deformation and fracture of cementite in cold-drawn pearlite are shown more in detail in Figure 130 by electron channeling contrast imaging (ECCI) using an FE-SEM. It can be observed that numerous thin cementite lamellae fragmented after

drawing. The fragmentation of cementite appears to have originated by a ductile necking, indicated by white arrows in the ECCI images below. It seems that the cementite particles broke-up at sections where the lamellae were locally very thin. Langford [150], Porter et al. [39], and Umemoto et al. [159] have reported evidence on the plastic deformability of cementite. Necking of cementite was observed to take place when a highly stressed slip system in the ferrite is nearly parallel to the plane of the lamellae. However, the cementite lamellae fragmentation may also occur by brittle failures promoted by local stress concentration at slip planes [39,159].

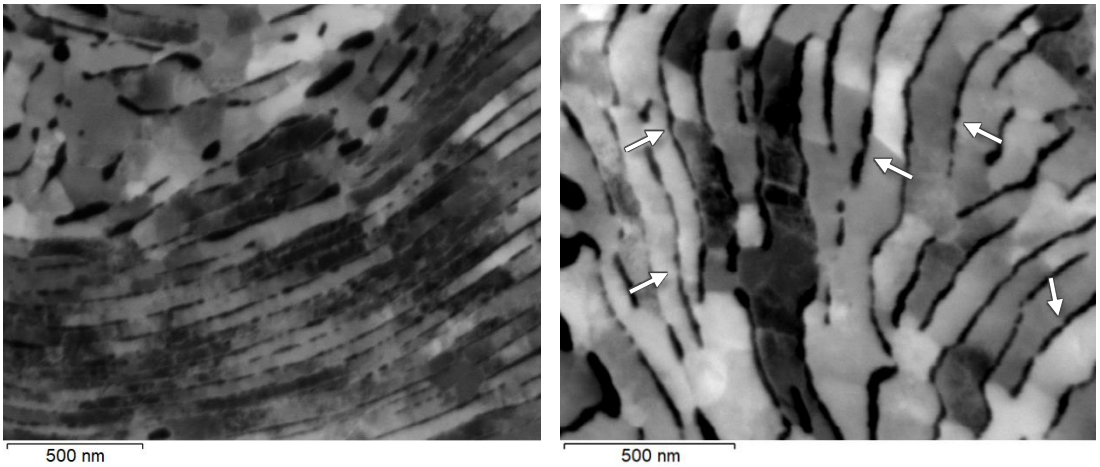

(a) **(b)**

Figure 130: ECCI images on transverse sections showing (a) fragmentation and (b) necking (white arrows) of cementite lamellae in cold-drawn fine pearlite at Ɛ=2.20

The stress-strain curves of the patented and cold-drawn fine and coarse pearlitic wires are in presented in Figure 131.

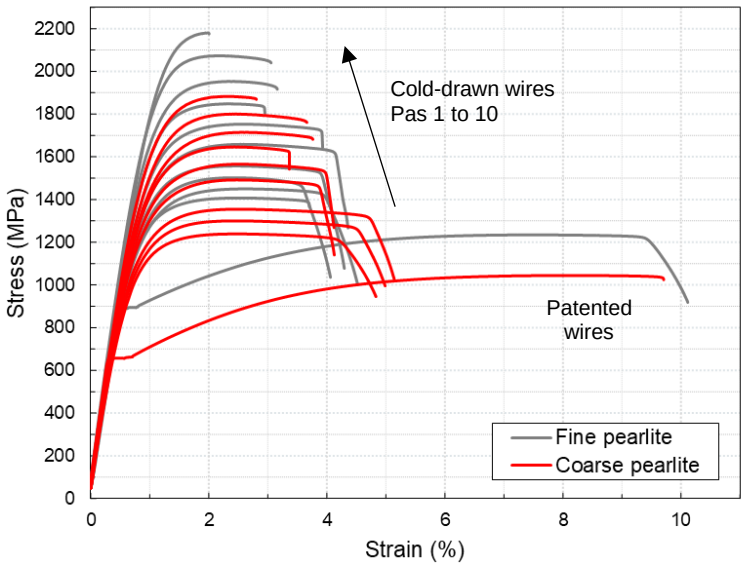

Figure 131: Stress-strain curves of heat-treated and cold-drawn pearlitic wires

Microstructural and mechanical characteristics of the reference patented (Ɛ=0) and cold-drawn steels are shown in Table 19, as mean and standard deviation values.

Table 19: Microstructural and mechanical properties of the AISI 1080 steels after different thermomechanical treatments

Diameter (mm)	Drawing strain	Interlamellar spacing (nm)	Yield strength (MPa)	Ultimate tensile strength (MPa)	Elongation (%)	Vickers hardness values (HV)
Fine lamellar pearlite						
6	0	107.01 ± 17.92	889 ± 7	1230 ± 7	9.3 ± 1.1	378 ± 11
4	0	95.40 ± 9.13	857 ± 5	1252 ± 2	8.2 ± 0.9	374 ± 12
2	0	91.36 ± 12.64	957 ± 4	1307 ± 1	9.8 ± 0.0	382 ± 10
5.23	0.27	93.56 ± 13.73	1206 ± 67	1406 ± 1	4.0 ± 0.3	407 ± 12
4.74	0.47	83.57 ± 9.95	1196 ± 14	1451 ± 1	4.5 ± 0.1	418 ± 9
4.33	0.65	79.94 ± 9.14	1260 ± 5	1503 ± 1	4.3 ± 0.3	422 ± 9
4	0.81	73.04 ± 7.80	1297 ± 18	1557 ± 0	4.4 ± 0.1	432 ± 12
3.49	1.08	-	1384 ± 7	1660 ± 2	4.1 ± 0.5	441 ± 20
3.07	1.34	-	1443 ± 38	1757 ± 7	3.7 ± 0.4	455 ± 30
2.72	1.58	-	1578 ± 9	1848 ± 0	2.9 ± 0.1	462 ± 20
2.44	1.80	-	1654 ± 18	1949 ± 6	3.3 ± 0.2	490 ± 18
2.20	2.01	-	1786 ± 5	2081 ± 10	2.7 ± 0.7	484 ± 16
2	2.20	-	1926 ± 54	2198 ± 25	2.1 ± 0.1	537 ± 19
Coarse lamellar pearlite						
6	0	193.35 ± 42.85	660 ± 5	1042 ± 3	11.3 ± 2.2	312 ± 9
4	0	185.50 ± 37.48	598 ± 2	1045 ± 1	10.9 ± 0.9	322 ± 17
2	0	136.14 ± 28.12	701 ± 12	1119 ± 1	10.6 ± 0.2	325 ± 12
5.23	0.27	164.52 ± 35.47	1034 ± 4	1239 ± 0	4.7 ± 0.3	356 ± 11
4.74	0.47	148.78 ± 29.81	1039 ± 4	1301 ± 1	5.1 ± 0.1	369 ± 10
4.33	0.65	132.86 ± 26.68	1081 ± 6	1354 ± 1	4.3 ± 1.2	376 ± 9
4	0.81	120.22 ± 23.10	1119 ± 5	1410 ± 0	4.3 ± 0.0	386 ± 4
3.49	1.08	109.18 ± 26.60	1191 ± 11	1492 ± 0	4.2 ± 0.0	418 ± 12
3.07	1.34	-	1288 ± 16	1565 ± 1	3.8 ± 0.5	428 ± 13
2.72	1.58	-	1285 ± 23	1650 ± 6	3.7 ± 0.4	439 ± 47
2.44	1.80	-	1362 ± 33	1716 ± 2	3.6 ± 0.2	431 ± 15
2.20	2.01	-	1417 ± 65	1800 ± 1	3.6 ± 0.1	433 ± 19
2	2.20	-	1529 ± 37	1886 ± 4	2.9 ± 0.0	420 ± 17

The interlamellar spacing of pearlite was observed to decrease with increasing drawing strain. However, the mean true interlamellar spacing could only be accurately determined up to a certain degree of deformation, in which the α-Fe_3C lamellae were not heavily distorted and could be distinguished. Both ultimate tensile strength and yield strength increased with a reduction in the cross-section area of the cold-drawn steel wires, whereas the elongation decreased continuously. The cold-drawn fine pearlite exhibited higher strengths and slightly lower percentage elongation values than the coarser structure cold-drawn at the same conditions, as shown in Figure 132.

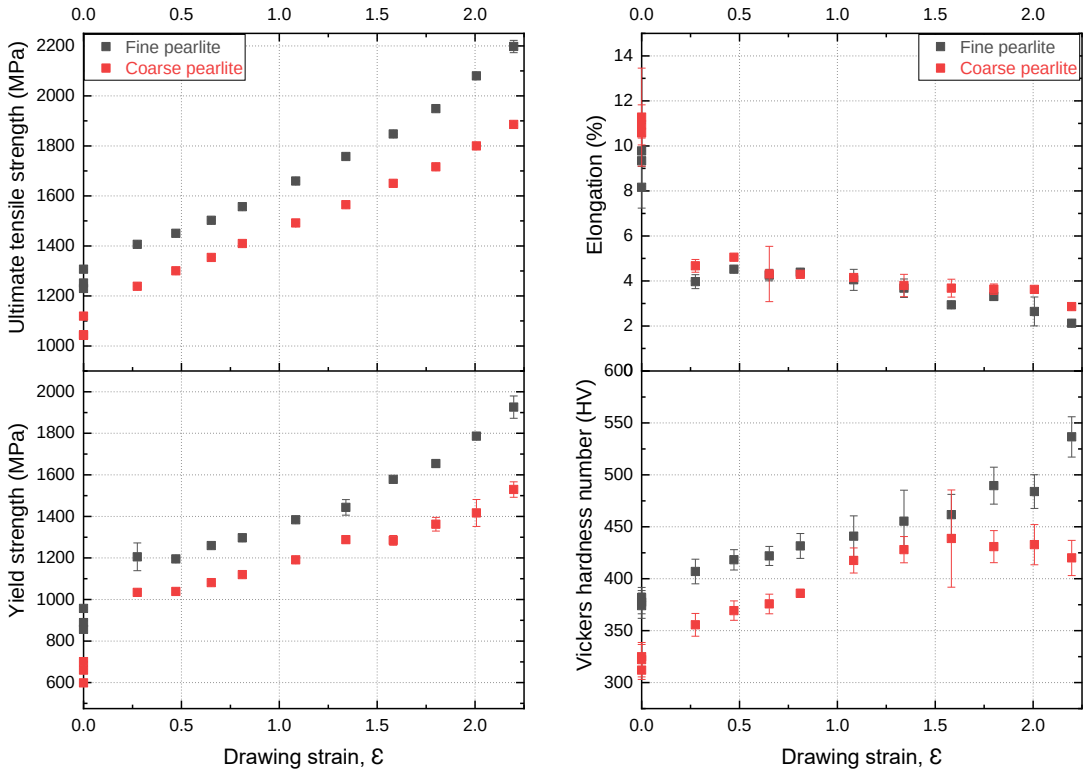

Figure 132: Mechanical properties of as-patented and cold-drawn steel wires with initially fine and coarse pearlite microstructures at various drawing strains

Based on the studies of Embury and Fisher [145], Langford [149,150], and Zhang et al. [147,158,160], the mechanical behavior of cold-drawn microstructures can be analyzed by the contribution of different strengthening mechanisms occurring in the material during drawing. The first mechanism considered is the contribution of Fe_3C lamellae that represents a barrier to dislocation glide such as grain boundaries, the fibre strengthening, also called the Hall-Petch mechanism. The refinement of pearlite interlamellar spacing results in an increase of the α-Fe_3C interfaces that enhance the barrier strength. Besides, the dislocation density and configuration of dislocations storage in the ferrite lamellae may also contribute to the strengthening of

the material. Some authors [147,161-164] have reported that, at larger strains, the cementite may start to decompose, enriching the α-phase in carbon. The interactions between interstitial carbon atoms and dislocations contribute to the strengthening of the heavily cold-drawn material by solid solution hardening. Dispersion hardness by incoherent Fe_3C particles reinforcing the ferrite may also enhance the strength [4].

I.2. Electrical resistivity and bulk magnetic properties

Although the countless works about the microstructure evolution and mechanical behavior of cold-drawn pearlite, investigations on the relation of physical-mechanical properties of such materials during forming processes are still limited. In the present study, resistivity and magnetic measurements were conducted to explore this topic.

Electrical resistivity measurements were carried out using a current of 5 mA at a temperature range from 2 to 300 K in samples of 2 mm in diameter that were patented (ε=0) and cold-drawn at drawing strain of 2.20. The results are shown in Figure 133.

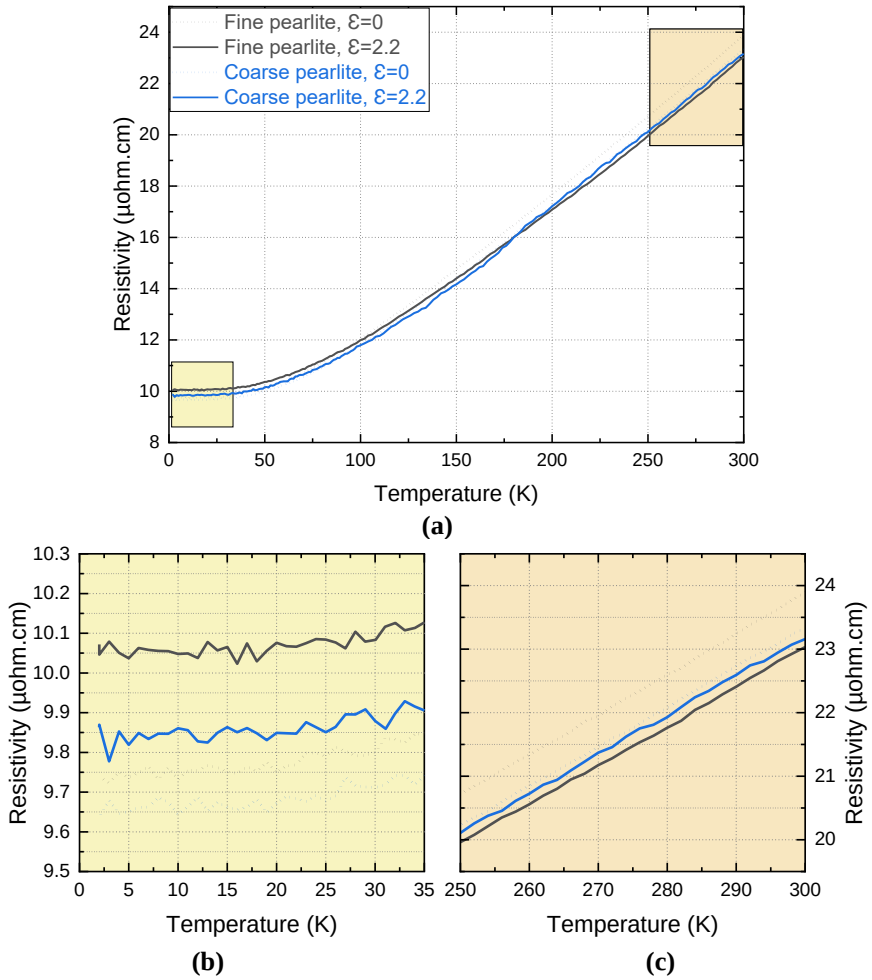

Figure 133: (a) Temperature dependence of resistivity of pearlite steels after different thermomechanical treatments; in detail for regions from (b) 2–35 K and (c) 250–300 K

The resistivity values at shallow temperatures, from 2 to 35 K, are observed in detail in Figure 133-b. One-way ANOVA analysis confirmed that the differences between the mean residual resistivity between the as-patented and cold-drawn samples obtained at a temperature range of 2 to 35 K were statistically significant at the 0.05 level, $F(3,136)=1024$, $p=1.11\ 10^{-91}$, as shown in Figure 134.

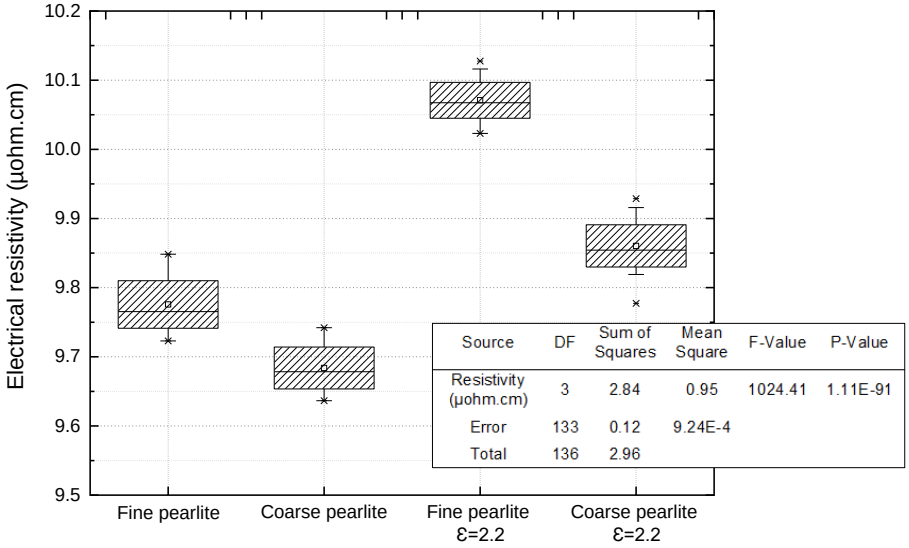

Figure 134: Box-plot of one-way ANOVA test of residual resistivity values for as-heat treated and cold-drawn pearlite samples of 2 mm in diameter

As discussed in Chapter 3, the heat-treated fine pearlite sample presented a higher residual resistivity that the coarse pearlite due to the thinner ferrite-cementite lamellar structure. The steel samples that were cold-drawn from these initial fine and coarse pearlite microstructures presented similar conductive behavior. It can be observed that cold-drawn pearlitic samples exhibited higher resistivity values than the patented steels at temperatures close to 0 K. This is probably due to the increase of density of dislocations and lattice defects generated by plastic deformation. It acts as scattering sources to the motion of free electrons, contributing to the observed growth of the temperature-independent residual resistivity values.

Besides, the cold-drawn fine pearlite steel achieved even higher resistivity values, which may be a response to various mesoscale phenomena. Langford [149,150], Porter et al. [39], and Dollar et al. [40] have studied the micromechanisms of deformation of both fine and coarse pearlite steels. In the pearlite with thicker interlamellar spacing, slipping would occur in large spaced slip planes in ferrite lamellae, as shown in the dislocation model in Figure 135-a. Locally shear stress concentrations cause inhomogeneous deformation, evidenced by dislocation pile-ups

and shear bands in pearlite colonies at higher strains [39,40]. In contrast, cementite is supposed to be predominantly deformed by fibre loading stresses under tensile deformation, due to the higher yield stress of such fine structure that activates many more dislocation sources at the α-Fe_3C interfaces than compared to coarse pearlite [39,149]. Uniform fine slip is believed to occur in fine pearlite, as shown in Figure 135-b. Plastic deformation is considered more homogeneous, resulting in thinning and eventually necking and fragmentation of cementite lamellae.

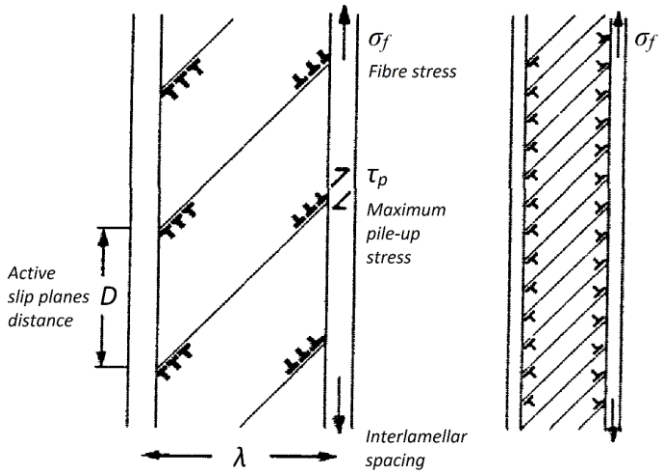

Figure 135: Dislocation model for the deformation of lamellar pearlite aligned parallel to the tensile axis, showing (a) coarse slip and (b) fine slip in the ferrite matrix [38]

In the present work, the cold-drawn fine pearlite sample exhibited a very fine and dense fibrous microstructure that could undergo substantial plastic deformation. Analogously to the restricted motion of dislocations due to fibre strengthening, the increase of α-Fe_3C boundaries reduces the electron mean free path, and dislocation strengthening increases the scattering of conducting electrons at these defects. Therefore, the high mechanical strength of cold-drawn fine pearlite led to a decrease in electrical conductivity.

The better formability of fine pearlite cold-drawn structure demonstrated that the initial pearlite morphology virtually affects their plasticity behavior during drawing, as well as its conductive performance. Moreover, the thinner microstructure of the cold-drawn fine pearlite sample may be more susceptible to the strain-induced dissolution of cementite in conditions of severe plastic deformation [148,161-164]. The decomposition of cementite enriches the BCC lattice with interstitial carbon atoms, strengthening of the material by solid solution and contributing to the deterioration of its electrical conductivity performance.

At higher temperatures, as observed in Figure 133-c, the electrical resistivity increases continuously with temperature indicating the influence of lattice vibration. However, the patented and cold-drawn samples showed very similar values, which makes it difficult to differentiate between the deformation states.

In order to study the electrical behavior of cold-drawn samples at each drawing pass, electrical resistivity measurements were also carried out at a controlled temperature of 35°C. Table 20 shows the average resistivity and standard deviation values of the deformed samples.

Table 20: Electrical resistivity measurements at 35°C of as-patented (Ɛ=0) and cold-drawn AISI 1080 steels

Diameter (mm)	Drawing strain	Reduction in area (%)	Electrical resistivity (µohm.cm)
Fine pearlite			
6	0	-	23.13 ± 0.02
5.23	0.27	24	22.17 ±0.02
4.74	0.47	38	21.74 ± 0.02
4.33	0.65	48	21.52 ± 0.03
4	0.81	56	21.65 ± 0.01
3.49	1.08	66	21.38 ± 0.03
3.07	1.34	74	21.15 ± 0.02
2.72	1.58	79	21.31 ± 0.01
2.44	1.80	83	21.47 ± 0.01
2.20	2.01	87	21.59 ± 0.01
2	2.20	89	
Coarse pearlite			
6	0	-	22.55 ± 0.02
5.23	0.27	24	22.00 ± 0.08
4.74	0.47	38	21.80 ± 0.10
4.33	0.65	48	21.42 ± 0.03
4	0.81	56	21.23 ± 0.03
3.49	1.08	66	20.95 ± 0.02
3.07	1.34	74	21.04 ± 0.02
2.72	1.58	79	21.03 ± 0.01
2.44	1.80	83	21.18 ± 0.01
2.20	2.01	87	21.09 ± 0.01
2	2.20	89	21.35 ± 0.00

Two-way ANOVA analysis evaluated the mean resistivity measured between both fine and coarse pearlite materials at each drawing strain. The mean resistivity values were found to be statistically different at the 0.05 level for both microstructure and deformation state variables. In other words, the mean resistivity of cold-drawn samples was significantly different to characterize the initial fine and coarse pearlite microstructures, $F(1,4699)=10438$, $p=0$; and the population means for each drawing pass could also be significantly distinguished, $F(10,4699)=11058$, $p=0$.

As shown in Table 20, the cold-drawn samples with initially fine lamellar pearlite present a higher resistivity than cold-drawn coarse pearlite for all the deformed states during cold-drawing. Figure 136 shows the average measurements for both cold-drawn fine and coarse pearlite samples after each drawing pass.

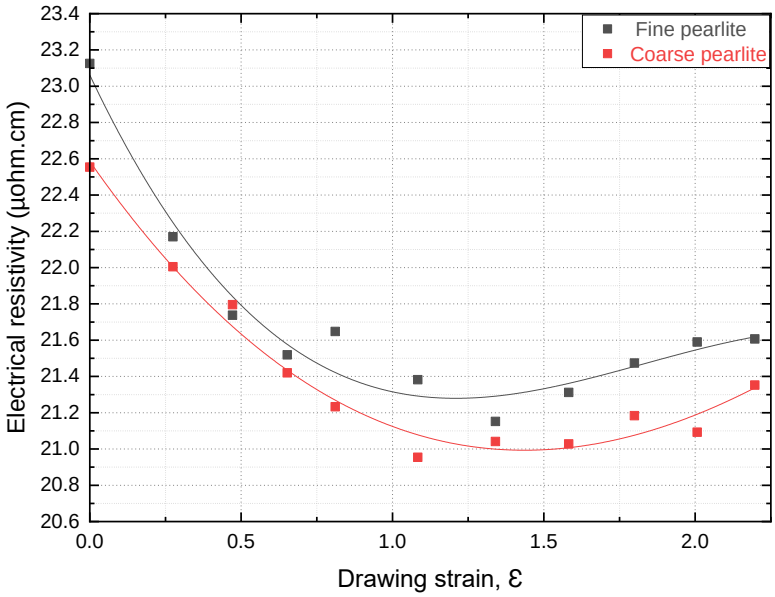

Figure 136: Electrical resistivity variation with drawing strain of cold-drawn pearlitic steel wires with initial fine and coarse microstructures

The electrical resistivity variation of both cold-drawn fine and coarse pearlite steels during the drawing process presents a similar behavior. In the first stages of drawing, the resistivity decreases continuously until $\varepsilon=1.08$, and then the values slightly increase with the increasing drawing strain.

The alignment of pearlite colonies contributed to the increase of the electron mean free paths in ferrite lamellae, reducing the interfacial scattering event and, thus, the resistivity values. In their work on aluminum alloys for high-voltage transmission power lines, Yang et al. [165] demonstrated that grain refinement could improve the mechanical strength of pure metals without harm their electrical conductivity up to a

specific deformation level. Among the few investigations on electrical properties of pearlitic steels, Gorkunov et al. [92] reported similar resistivity changes in cold-drawn pearlitic wires. Therefore, in the first stages of deformation, the spacing between cementite boundaries (i.e., width of ferrite lamellae) is still large enough for the electron mean free path, so the dislocation strengthening contribution to the resistivity seems to be negligible.

At deformations above ε=1.08, a gradual increase in electrical resistivity is observed. After a certain deformation level, the pearlite colonies are mostly aligned along the wire axis, and the lamellar refinement and lattice defects introduced by pile-ups and fibre loading deformation mechanisms probably become significant factors affecting the electrical conductivity of highly deformed pearlitic steels. As discussed, cementite lamellae fragmentation and carbide dissolution at large strains may provide an additional increase in the total resistivity. According to Matthiessen's rule, the total electrical resistivity ρ_{total} can be expressed as:

$$\rho_{total} = \rho_0 + \rho_{gb} + \rho_d + \rho_p + \rho_{ss} \quad (48)$$

where ρ_0 is the residual resistivity of the lattice, ρ_f is the resistivity due to cementite boundaries or fibre strengthening, ρ_d, ρ_p, and ρ_{ss} denote the contribution to electrical resistivity from dislocations, second-phase precipitates, and solute atoms dissolved in the matrix, respectively. Luo et al. [166] investigated the microstructure evolution and physical properties of cold-drawn aluminum wires. They found that the main contributions to the decrease in electrical conductivity were grain boundary and dislocation strengthening. Besides, Gorkunov et al. [92] also proposed that the increase in resistivity can be produced by the gradual accumulation of microcracks within pearlitic steels submitted to deformations above ε=1.5.

Bulk magnetic measurements were determined by hysteresis loops measurements for assessing the magnetic properties resulted from plastic deformation of the pearlitic AISI 1080 steel wires. The magnetic experiments were carried out at room temperature on samples with various diameters and lengths of 2.5 cm at the same conditions already described. Eutectoid steels of 6, 4, and 2 mm in diameter that were patented at the same conditions for obtaining fine and coarse pearlite microstructures were selected, as well cold-drawn fine and coarse pearlite samples at drawing strains of 0.27, 0.81, and 2.20, with corresponding 5.23, 4, and 2 mm in diameter.

Figure 137 shows the characteristic hysteresis loops obtained at 15 $kA.m^{-1}$ for the cold-drawn pearlite at different drawing stages, with strains of 0.27, 0.81, and 2.20,

compared with the as-patented steels of diameters of 6, 4, and 2 mm that were not subjected to stress.

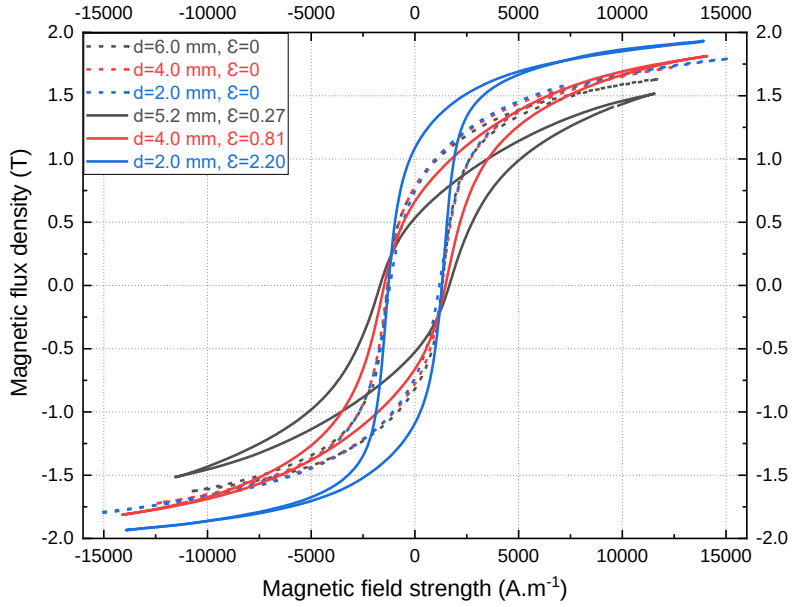

(a)

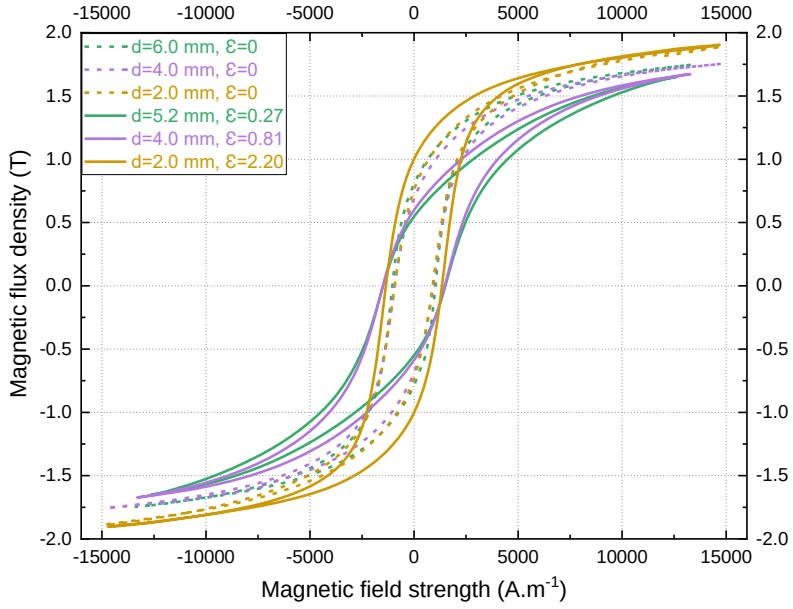

(b)

Figure 137: Comparison of the measured hysteresis loops of patented and cold-drawn pearlitic samples, with initially (a) fine and (b) coarse lamellar microstructures

As can be seen, the hysteresis loops referents to the patented samples exhibit similar magnetic behavior for all the different cross-section areas evaluated. In contrast, the magnetic responses of cold-drawn pearlitic steels alter significantly with increasing of drawing strains. These magnetic behavior changes are even more noticeable in the cold-drawn samples with initially fine pearlite. These differences are

more clearly observed through the normal magnetization curves obtained from the hysteresis loops with a maximum applied field of 15 kA.m^{-1}, as shown in Figure 138.

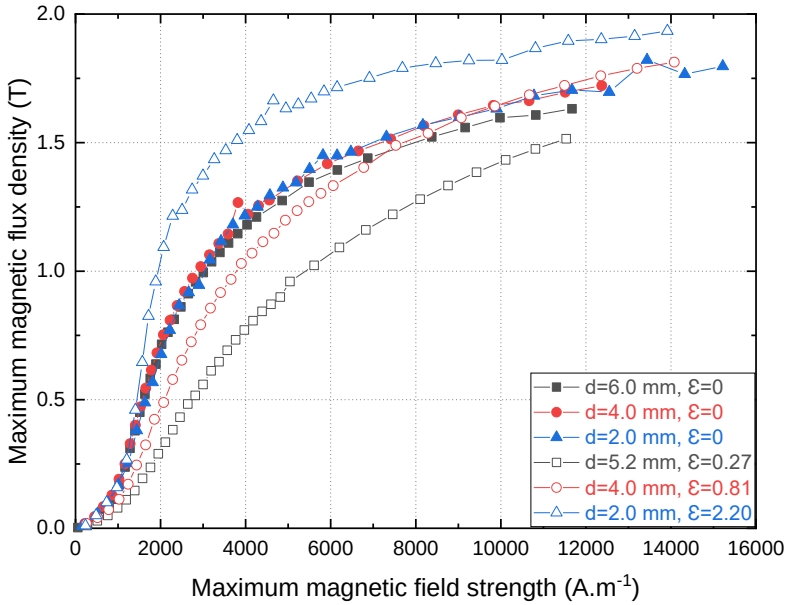

(a)

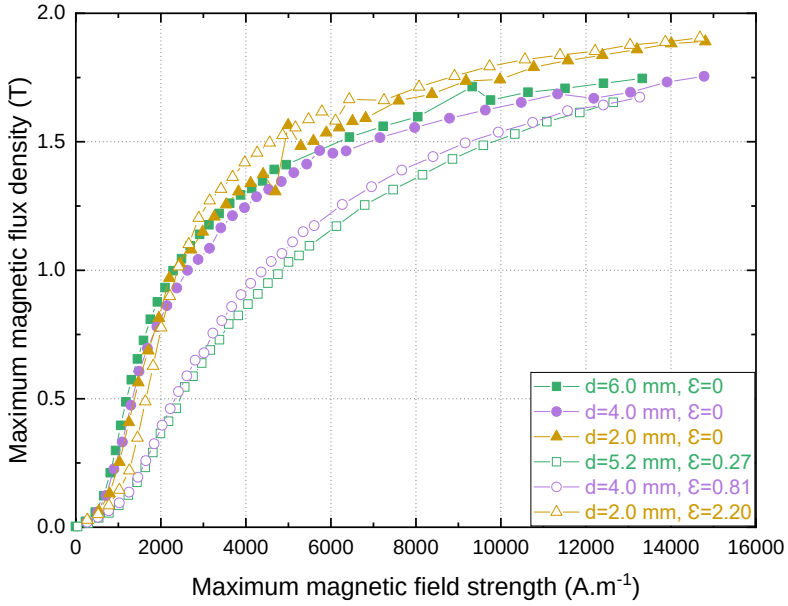

(b)

Figure 138: Normal magnetization curves obtained for patented and cold-drawn pearlitic samples, with initially (a) fine and (b) coarse lamellar microstructure

The bulk magnetic properties determined by analyzing the characteristic hysteresis loops of the studied steels are listed in Table 21 below. Three experiments were conducted on each material, and the values are displayed as average and standard deviation. The relative permeability variation with respect to the maximum magnetic field strength is presented in Figure 139.

Table 21: Magnetic properties of as-patented (Ɛ=0) and cold-drawn AISI 1080 steels

Diameter (mm)	Drawing strain	Coercivity ($A.m^{-1}$)	Remanence (T)	Hysteresis loss ($W.kg^{-1}$)	Magnetic saturation (T)	Maximum relative permeability
Fine pearlite						
6	0	1335 ± 14	0.80 ± 0.02	0.38 ± 0.01	1.63 ± 0.01	281 ± 14
4	0	1314 ± 25	0.78 ± 0.03	0.38 ± 0.00	1.72 ± 0.02	289 ± 3
2	0	1299 ± 32	0.74 ± 0.01	0.37 ± 0.00	1.80 ± 0.01	283 ± 4
5.23	0.27	1664 ± 11	0.53 ± 0.01	0.42 ± 0.01	1.52 ± 0.02	155 ± 1
4	0.81	1470 ± 23	0.66 ± 0.02	0.43 ± 0.02	1.81 ± 0.03	215 ± 2
2	2.20	1254 ± 22	1.10 ± 0.01	0.43 ± 0.03	1.93 ± 0.01	423 ± 1
Coarse pearlite						
6	0	1040 ± 9	0.80 ± 0.01	0.33 ± 0.01	1.75 ± 0.01	368 ± 1
4	0	935 ± 5	0.68 ± 0.02	0.29 ± 0.02	1.75 ± 0.01	329 ± 3
2	0	913 ± 40	0.74 ± 0.01	0.30 ± 0.01	1.89 ± 0.03	351 ± 1
5.23	0.27	1510 ± 9	0.55 ± 0.01	0.42 ± 0.01	1.65 ± 0.01	175 ± 1
4	0.81	1471 ± 13	0.59 ± 0.02	0.43 ± 0.02	1.67 ± 0.02	186 ± 2
2	2.20	1355 ± 1	1.00 ± 0.01	0.47 ± 0.03	1.90 ± 0.01	335 ± 1

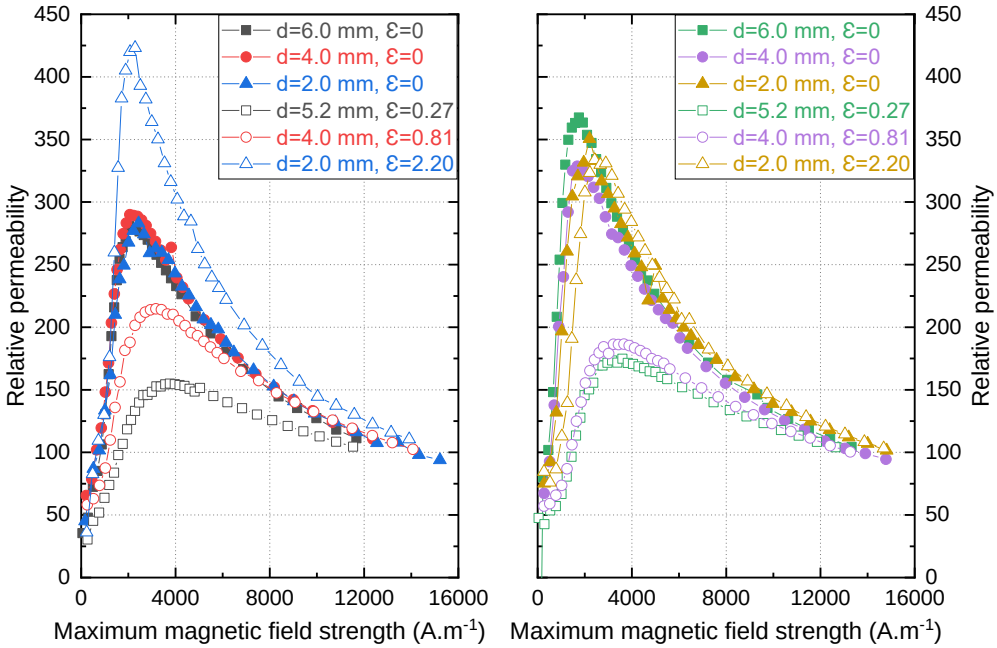

Figure 139: Relative permeability variation with maximum field strength of patented and cold-drawn samples with initially (a) fine and (b) coarse pearlite microstructures

Both the patented fine and coarse pearlite microstructures exhibit similar magnetic behavior between the different diameter wires, which confirms the accuracy

of magnetic measurements. As discussed in Chapter 3, fine pearlite showed harder magnetic characteristics compared to the coarse microstructure.

Concerning the cold-drawn samples, a particular behavior was observed: the magnetic hardening at initial stages of drawing is followed by a noticeable softening with increasing strains. The observed decrease in relative permeability and increase in coercivity of cold-drawn wires at the first stage of drawing (Ɛ=0.27) probably reflects the increasing stress levels, defect and dislocation density in pearlite, as these are physical parameters that strongly depends on the structural state of steels. However, the magnetic permeability is observed to increase while coercivity decreases with the progressive alignment and rotation of pearlite colonies and the development of <110> texture of ferrite with drawing strain. It indicates that the microstructure and crystallographic texture developed during drawing might be responsible for significant magnetic anisotropy changes in the processed pearlitic steels. Both the BCC iron and orthorhombic cementite structures are magnetically anisotropic. Figure 140 shows the easy magnetization axis of a BCC iron is (100), whereas the orthorhombic cementite has easy (001) magnetization direction. The magnetoelastic effect arises from drawing stresses and tends to tends to reorient the magnetic domain arrangement in the <100> crystallographic direction, minimizing the magnetocrystalline energy and favoring the magnetization process in the drawing direction. Changes in the bulk magnetic easy axis related to thermo-mechanical processes of steel components, such as rolling, drawing, extrusion, and recrystallization annealing, are well known [167-171]. Similar observations in pearlitic steels were found by Gorkunov et al. [92], Ul'yanov and Chulkina [172], and Chulkina et al. [173]. In addition, the thinning and fragmentation of Fe_3C lamellae have been observed to facilitate the magnetization process [92].

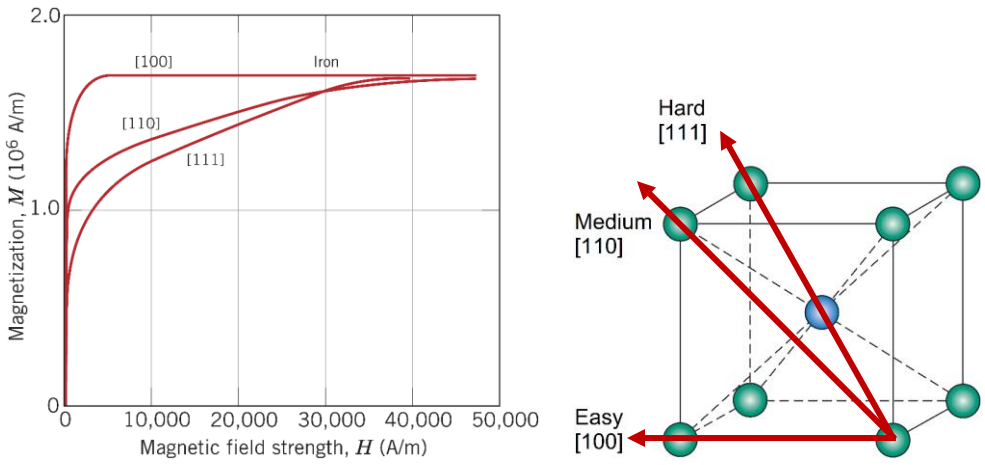

Figure 140: Magnetization curves for single crystals of BCC iron [11-adapted]

The remarkable improvement of magnetic properties observed in the cold-drawn samples at Ɛ=2.20 may also be attributed to the possible decomposition of cementite under large plastic deformation, as reported by Gorkunov et al. [92]. They concluded that the cementite dissolution and the consequent increase in the α-phase concentration cause the growth of magnetic moments, favoring magnetization. In the present work, both fine and coarse cold-drawn pearlite exhibited magnetic saturation close to the values determined for low-carbon AISI 1020 and 1035 steels of about 1.90 T, which may suggest a phase composition variation due to severe plastic deformation. Also, the better magnetic performance observed for the cold-drawn fine pearlite, with an initial interlamellar spacing about two times less than in coarse pearlite, is thought to be related to the intense fiber texture and lamellae fragmentation at high strains.

I.3. Eddy current testing

Eddy current testing was performed by measuring the collected samples at each drawing pass after cold-drawing at the same conditions as previously described, room temperature test at 200 Hz. One-way ANOVA analysis assessed that the mean ECT signals determined for fine and coarse pearlite samples at each drawing step are statistically different at the 0.05 level, F(19,34360)=217283, p=0.

The eddy current voltage plane and total voltage variations with drawing strain of fine and coarse cold-drawn steels are given in Figure 141.

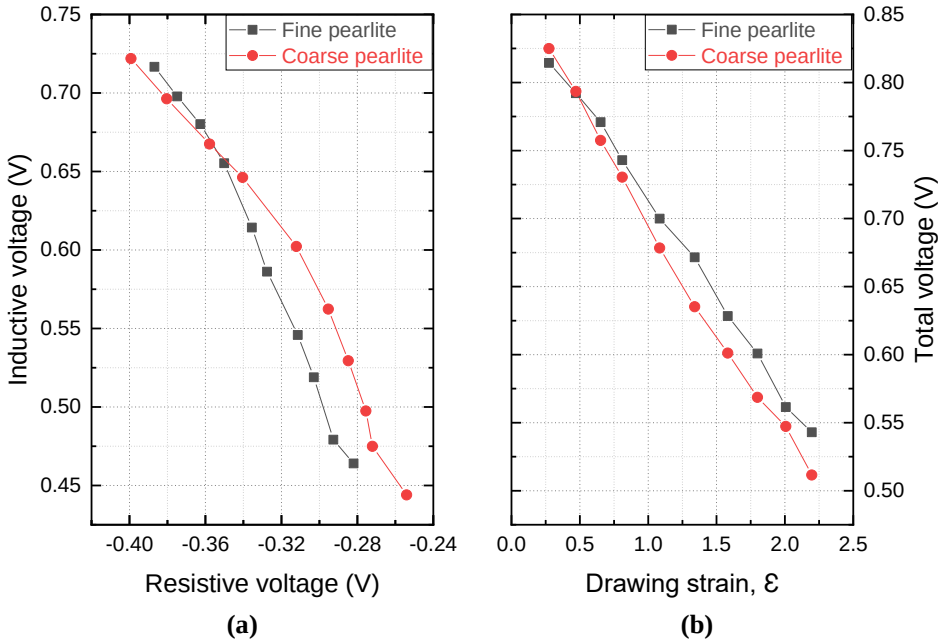

Figure 141: (a) Eddy current plane and (b) total voltage variation with drawing strain of cold-drawn pearlite wires

The inductive voltage is observed to decrease with the increase of drawing strain, while the resistive voltage increases for both fine and coarse pearlite samples. Therefore, the total eddy current voltage signals also decrease with cold-drawing, which would suggest, in a first view, that the materials become continuously less conducive and magnetically harder with the increase of plastic deformation during forming operations.

Nevertheless, the interpretation of these electromagnetic signals is not that straightforward since it involved ECT of steel wires with different geometry dimensions, in which important area reduction of about 20% occurring after each drawing pass. The sample diameter strongly affects the electromagnetic coupling between the electromagnetic coil and the tested material. It alters the induced electromotive force, changing the magnitude of electromagnetic interactions and hence, the measured coil impedance. Also, it affects the material resistance that is indirectly measured by the resistive voltage of the RL circuit. The variation in the physical properties of the different steel wires becomes then a minor factor regarding the eddy current outputs when the sample geometry is not constant.

Regarding this issue, numerical simulations were performed by the finite element method to better understand the influence of sample diameter variations on the electromagnetic signals achieved by eddy current testing under 0.5 A and 200 Hz. Using the FEMM finite element analysis software, the magnetic flux density induced by eddy currents into patented pearlitic AISI 1080 steel wires with 2, 4, and 6 mm in diameter was estimated based on the electrical and magnetic properties measured for each material, the electromagnetic coil geometry, and the defined ECT test parameters.

The electromagnetic induction maps calculated from the solid model constructed for simulating eddy current tests on the various sample wire diameters are shown in Figure 142. The samples and the electromagnetic coil are represented along their x-axis of symmetry. Figure 143 contrasts the estimated flux density variations induced into each pearlitic microstructure in the function of the depth of penetration by eddy currents.

It can be observed that the induced magnetic flux density increases with the decreasing steel wire diameter. Also, at a relatively low excitation frequency of 200 Hz, the skin effect produced by eddy currents is not significant, and sufficient amounts of magnetic flux are induced into the core of the samples. It indicates that ECT allows proper evaluation of the physical properties of bulk pearlitic materials.

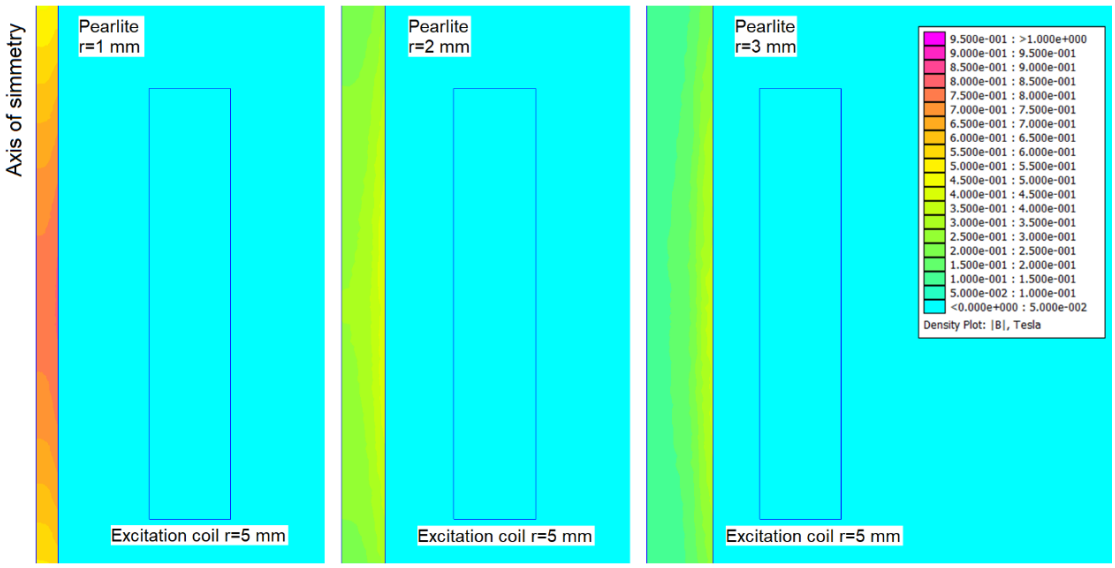

Figure 142: Numerical simulation illustrating the estimated flux density induced into pearlitic wires of diameters 2, 4, and 6 mm by an excitation coil under 0.5 A and 200 Hz

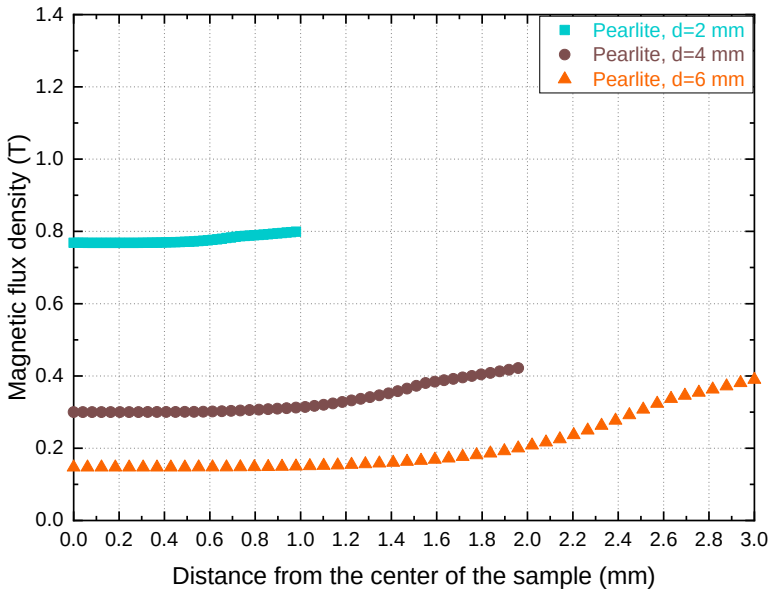

Figure 143: Simulated magnetic flux density in the function of the depth of penetration into patented pearlitic steel wires of 2, 4, and 6 mm in diameter by eddy currents

Figure 144 shows the relative magnetic permeability calculated from the B–H curves in the function of the maximum flux density, and the mean eddy current signals corresponding to the patented samples of 2, 4, and 6 mm in diameter.

As demonstrated in Figure 144-a, the measured relative permeability is characteristic of the pearlite microstructure produced by similar patenting heat-treatments, regardless of the sample diameter. As the estimated flux density induced in the core of 2 mm-diameter wires is of about 0.8 T, the measured relative permeability would be slightly higher than for the evaluated samples of 4 and 6 mm in

diameters, in which the flux density in the core is estimated to reach approximatively 0.15 to 0.3 T. As pointed below, the red and green lines indicate the magnetic flux induced by eddy currents into the core of the several sample diameters, calculated through numerical simulations. In consequence, the total voltage measured by ECT should also present small differences between these samples.

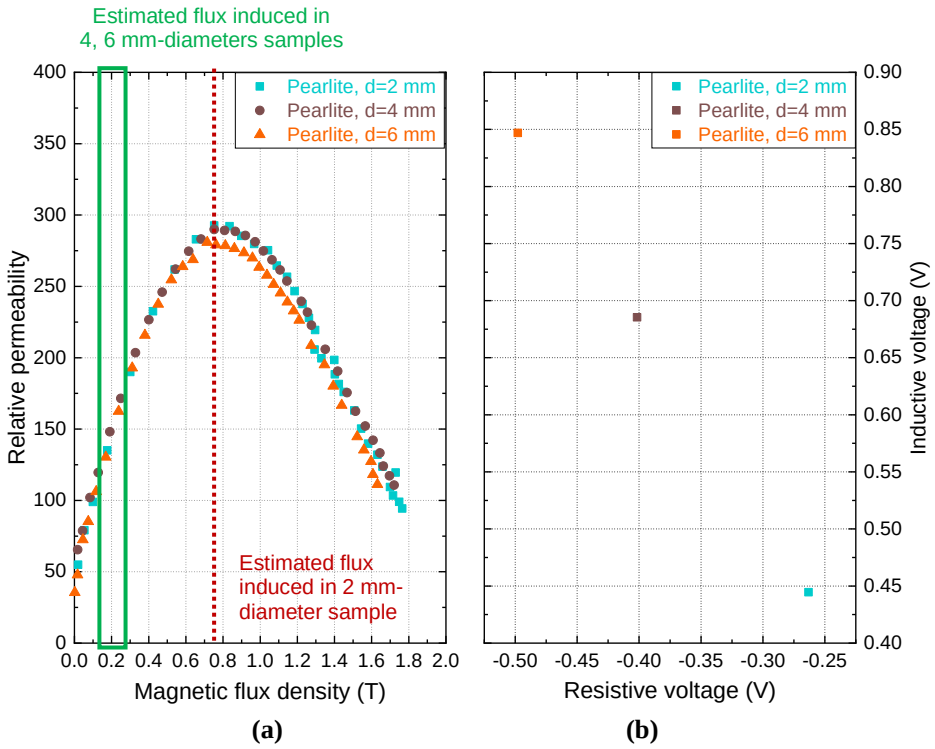

Figure 144: (a) Relative permeability in the function of maximum flux density of pearlite samples of various diameters – red and green lines indicate the estimated induced flux range at the core of respective 2 mm, and 4 and 6-mm diameter samples; and (b) their corresponding eddy current signals

However, Figure 144-b shows that the eddy current resistive voltage increased considerably, while the inductive voltage decreased with decreasing sample diameter, even though the measured electrical and magnetic properties of such materials were quite similar for the described testing conditions. As expected, the diameter reduction causes the material resistance to current flow to increase, contributing to the effective resistance of the coil circuit and, hence, to a rise in the resistive voltage signals. Besides, evaluating a sample with a lower cross-section area implies necessarily in a correspondent increase of the magnetic flux density induced by eddy currents into the bulk material, as confirmed by numerical simulations. Thus, the resulting primary flux of the coil is reduced by the higher opposing flux of the material, decreasing the coil's inductive reactance and the inductive voltage of the RL circuit. These results confirm

that the cross-sectional area changes (reaching almost 90%) substantially affected the eddy current response of the tested materials, which does not reflect the physical properties variation of the studied pearlitic steels. The diameter variation of test specimens configures an important limiting factor for eddy current tests.

Yin et al. [174] and Davis et al. [175] have reported that phase angle, which is the phase shift between voltage and current functions, would remain independent of electromagnetic coupling variations. Considering their work, correlations between phase angles obtained by ECT of cold-drawn samples with respect to drawing strain are shown in Figure 145.

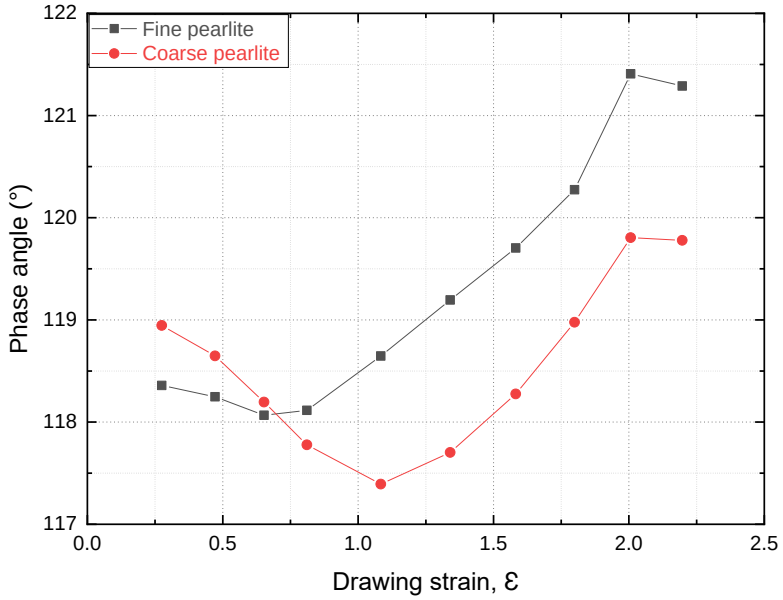

Figure 145: Phase angle response of cold-drawn pearlite samples with drawing strain

The phase angle decreases at the first stages of drawing for both fine and coarse pearlite samples, probably reflecting the decrease in electrical resistivity and magnetic permeability with plastic deformation. Next, the phase angle increase seems to translate the significant raise of permeability and increase of resistivity at higher deformation levels. These results suggest that analyzing the phase shift between voltage and current within the coil system might be useful for assessing the electromagnetic performance of processed carbon steels.

Nevertheless, the correlations of electrical conductivity and magnetic permeability of pearlitic steels with their mechanical behavior during wire manufacturing are not straightforward, as the microstructure evolution encompasses distinct physical mechanisms. In cold-drawing, the strength increased continuously in response to various strengthening mechanisms occurring at different deformation

levels. It includes grain boundary and dislocation strengthening, precipitation hardening with fragmented Fe_3C particles dispersed in the α-phase matrix, as well as solid solution strengthening with the cementite dissolution at severe deformation degrees. All these factors responsible for increase the strength of pearlitic steels tend to impact at different extents their corresponding electrical and magnetic properties.

The ultimate tensile strength evolution of pearlitic steels during the drawing process and the corresponding variations of electrical and magnetic properties are shown in Figure 146 and Figure 147.

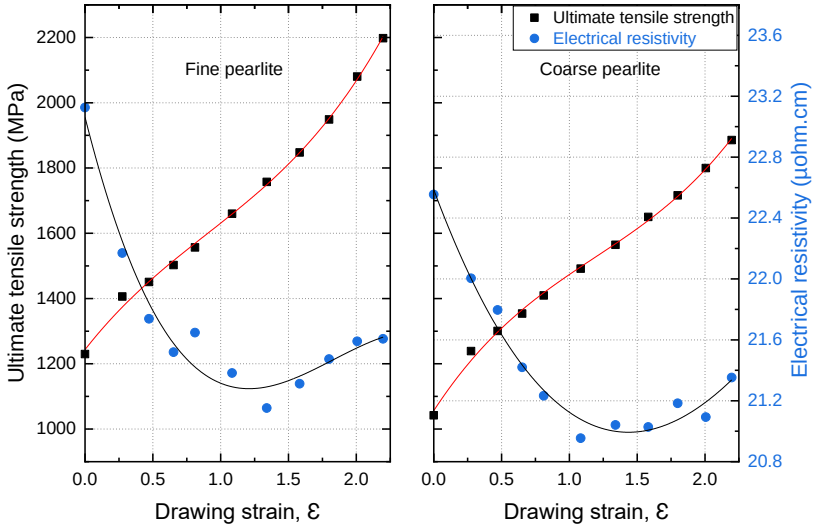

Figure 146: Ultimate tensile strength and electrical resistivity variation with deformation strain of cold-drawn (a) fine and (b) coarse pearlite steels

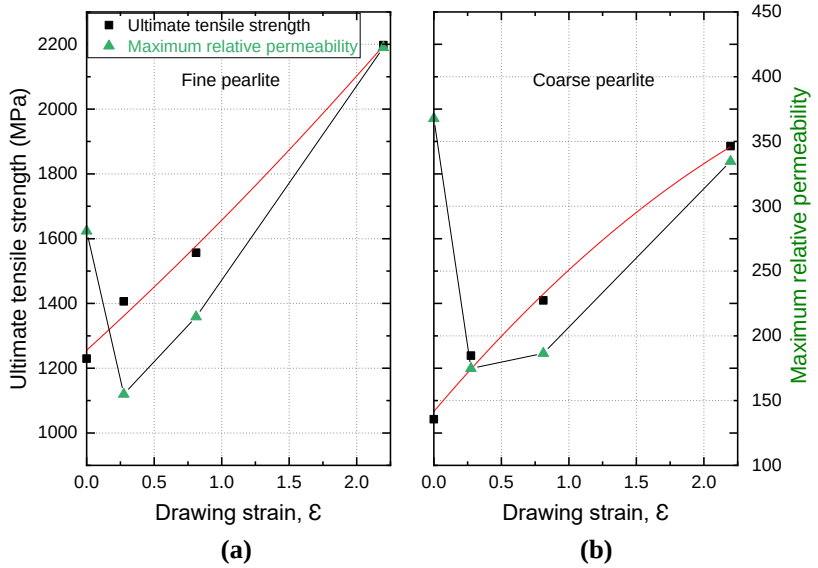

Figure 147: Ultimate tensile strength and magnetic permeability variation with deformation strain of cold-drawn (a) fine and (b) coarse pearlite steels

The alignment of pearlite colonies along with the wire axis increases the electron mean free paths, whereas the microstructure refinement and lattice defects generated during processing have a deleterious effect on the electrical conductivity due to the increase of electron scattering centers.

The magnetic permeability of cold-drawn pearlite decreases at the first stages of drawing due to dislocation strengthening, but it started to increase due to the strong magnetic anisotropy developed along with the drawing direction. Additionally, precipitation and solid solution strengthening may contribute to the permeability improvement at higher deformation levels. Further research is therefore necessary for improving the non-destructive assessment of mechanical properties of cold-drawn pearlite using an electromagnetic sensor.

In the first part of this chapter, the influence of the initial pearlite morphology and the degree of plastic deformation on the electrical and magnetic behavior of cold-drawn pearlitic steels was investigated. The principal conclusions are outlined below:

- The electrical and magnetic behavior of pearlitic steels depends on the stress-strain state developed during the cold-drawing process, at a different extent than their mechanical properties.
- The standard analysis of eddy current voltage outputs is not suitable for characterizing the electromagnetic performance of eutectoid steels due to the significant cross-section area variations affecting the electromagnetic coupling between the coil and the material.
- Eddy current phase angle variations are consistent with the electrical and magnetic properties and are useful for assessing the electromagnetic performance of processed carbon steels.

II. FATIGUE BEHAVIOR OF PEARLITIC STEELS

Structural cables play a significant role in the engineering and design of massive building structures, such as suspension and cable-stayed bridges, glass and membrane roofs, offshore oil and gas platforms, and tensile structures. Cold-drawn pearlitic steel wires are a good option because they exhibit an excellent combination of high strength and formability required for wire strands, ropes, and cables. However, such structures are typically exposed to several damage mechanisms, including fatigue, leading to the progressive degradation of their components. The accurate assessment of fatigue resistance of pearlitic steels is thereby essential to increase the safety and long-term reliability of its applications. In this section, the influence of the microstructure on the fatigue behavior of fully pearlitic steel wires is investigated; in particular, the stress-strain response and fatigue crack initiation and propagation. This section aims to provide an in-depth comprehension of the mechanical and microstructural aspects related to the fatigue performance of such structural materials.

II.1. Materials and experimental methods

The referred AISI 1080 steel rods of 6 mm in diameter patented at transformation temperatures of 540 and 640°C for producing fine and coarse pearlite microstructures were used in the present investigation. Also, an AISI 1070 steel wire of 6 mm in diameter, cold-drawn at a drawing strain of ε=0.45, was selected for this study. Table 22 below gives the chemical composition of the studied materials.

Table 22: Chemical composition of the AISI 1070 and 1080 carbon steels (wt. %)

AISI steel	C	Mn	Si	Cr	Ni	P	S	Fe
1070	0.711	0.612	0.232	0.025	0.021	0.016	0.016	Bal.
1080	0.776	0.587	0.235	0.020	0.020	0.014	0.009	Bal.

SEM micrographs of Figure 148 show the initial microstructures of the 6 mm-diameter wires corresponding to AISI 1070 and 1080 steels submitted to different thermomechanical treatments. The heat-treated eutectoid steels were considered entirely pearlitic. However, the volume fraction of the proeutectoid ferrite of the near-eutectoid AISI 1070 steel could not be estimated by light optical microscopy due to the deformation state of the material. It is considered that this material contained a minimal amount of proeutectoid ferrite phase. The pearlite interlamellar spacing varied

in function of the cold-drawn, fine and coarse pearlite. The non-deformed wires presented an equiaxed microstructure with colonies of pearlite randomly orientated, whereas the cold-drawn sample exhibited colonies slightly bent around the wire axis.

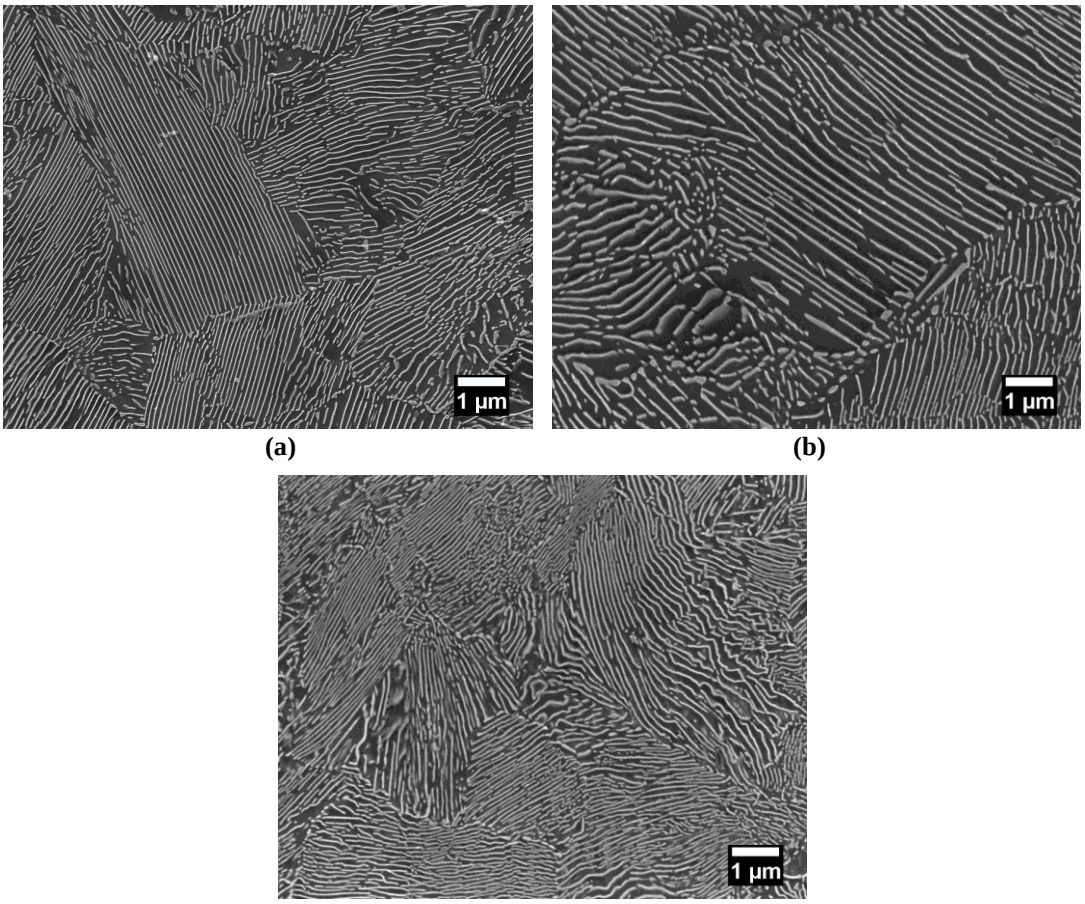

(a) **(b)**

(c)

Figure 148: SEM micrographs of the initial microstructures of (a) fine and (b) coarse pearlite AISI 1080 steels, and (c) cold-drawn pearlitic AISI 1070 steel

Table 23 shows the principal microstructure and mechanical properties of the cold-drawn AISI 1070 and the heat-treated 1080 steel wires, displayed as average and standard deviation values.

Table 23: Microstructural and mechanical properties of the 6 mm-diameter steel wires after different thermomechanical treatments

AISI steel	Microstructure	Diameter (mm)	Drawing strain	Interlamellar spacing (nm)	Vickers hardness values (HV)
1070	Cold-drawn pearlite	6	0.45	84.22 ± 20.51	402 ± 12
1080	Fine pearlite	6	0	107.01 ± 17.92	378 ± 11
1080	Coarse pearlite	6	0	193.35 ± 42.85	312 ± 9

After thermomechanical treatments, the 6 mm-diameter wires were machined for obtaining fatigue specimens of 5 cm in total length, as shown in Figure 149. The gauge section had 2.5 mm in diameter and a length of 16 mm. After machining, the cylindrical specimens were mechanically polished with diamond grinding pastes until roughness of 0.25 µm to remove any machining trace, ensuring a defect-free surface.

Figure 149: Cylindrical fatigue test specimen of AISI 1080 steel

The fatigue tests were carried out in a uniaxial mode at room temperature on an MTS hydraulic fatigue machine. An extensometer Instron was attached directly to the specimen gauge section. Low-cycle fatigue tests were conducted under strain-control to investigate the progressive localized structural damages of pearlitic steels subjected to significant cyclic plasticity. An 8 mm gauge extensometer was used to control strain cycles until failure. The fatigue tests were carried out at a triangular strain waveform at a constant strain rate of 4.10^{-3} s^{-1}, as shown in Figure 150. A minimum strain of 0.1 % was imposed, and the total strain range $\Delta\varepsilon_t$ applied at 0.6, 0.8, 1.2, and 1.6% to each pearlite microstructure. Each testing condition was at least doubled to validate its repeatability.

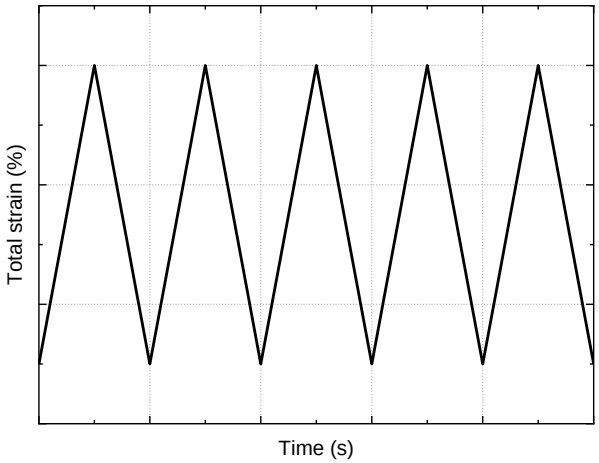

Figure 150: Triangular strain waveform at a constant strain rate

SEM was employed to identify the mechanisms of fracture that occur in pearlitic steels by examination of fracture surface morphologies. Moreover, transmission electron microscopy was used to study the fatigue damage phenomena of pearlitic steels during cyclic loading, particularly the early stage of fatigue crack initiation, with the formation of intrusions and extrusions.

II.2. Strain-controlled fatigue behavior

II.2.1. Cycle accommodation

In order to describe the behavior of the investigated pearlitic steels under low cycle fatigue, the evolution of the maximum and minimum stress with the number of cycles is shown in Figure 151. In addition, Figure 152 shows the evolution of the maximum and minimum stress with the fatigue life fraction.

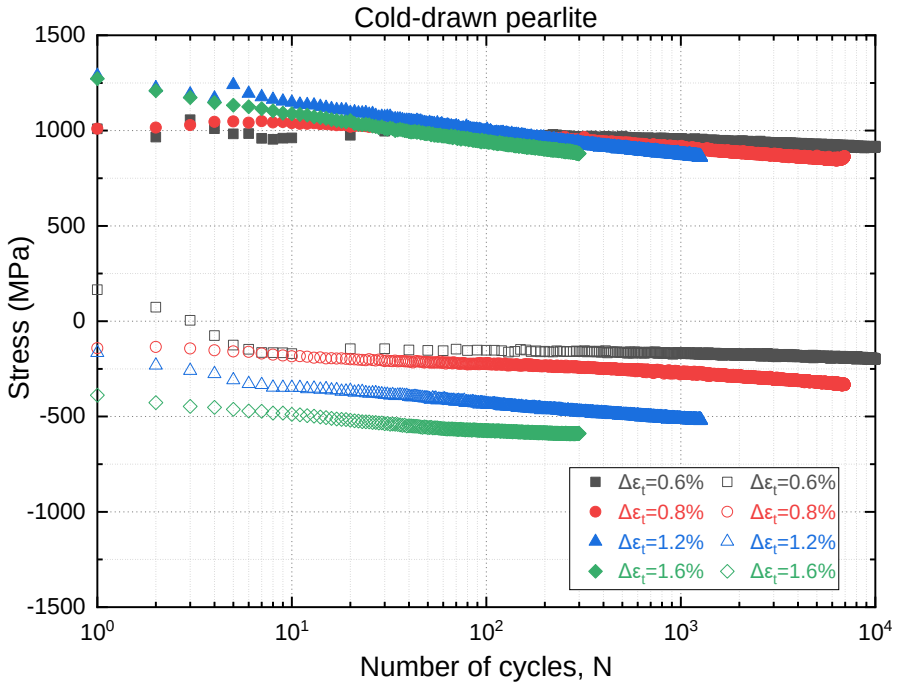

(a)

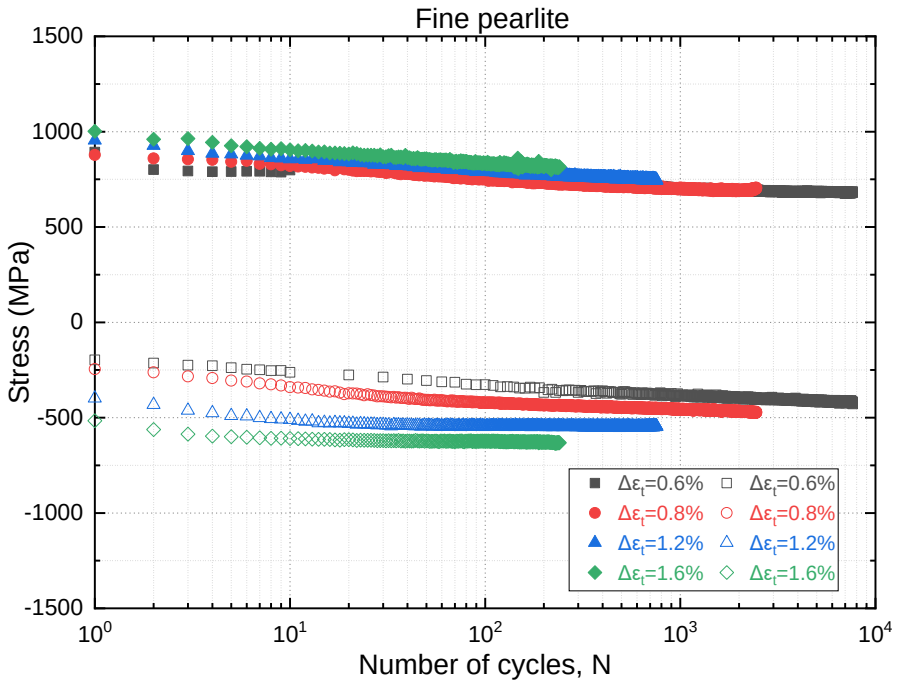

(b)

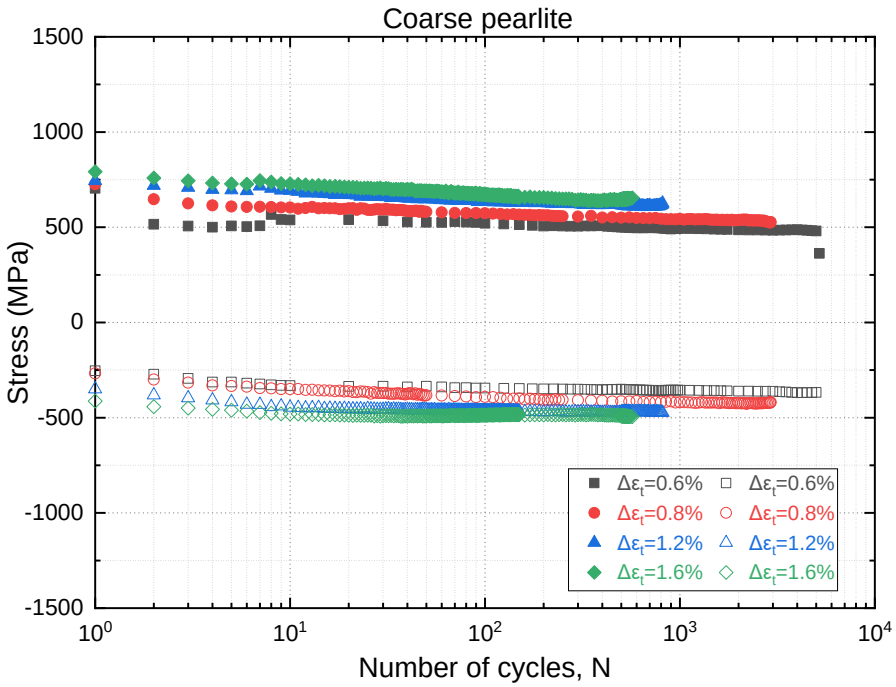

(c)

Figure 151: Evolution of the stress peaks in the function of the number of cycles of (a) cold-drawn, (b) fine, and (c) coarse pearlite specimens at different strain amplitudes

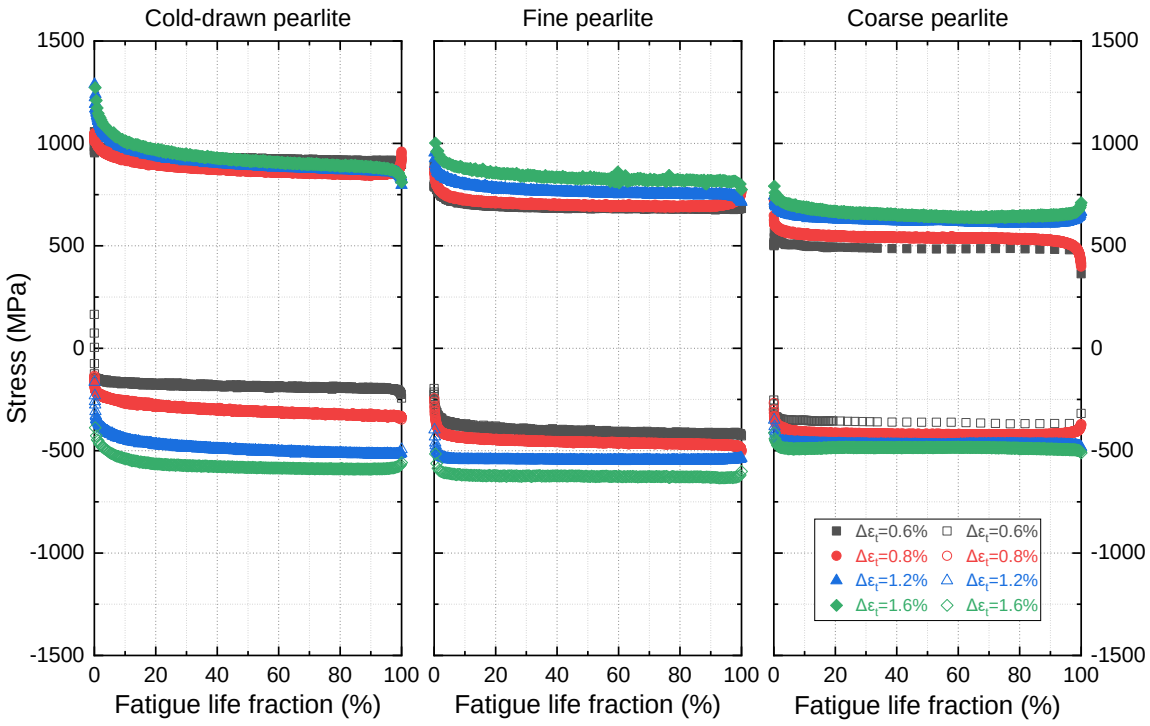

(a) **(b)** **(c)**

Figure 152: Evolution of the stress peak in the function of fatigue life fraction of (a) cold-drawn, (b) fine, and (c) coarse pearlite specimens at different strain amplitudes

Despite the fatigue tests were carried out under uniaxial positive strain, compressive stresses are necessary to be applied to reach the minimum strain targeted value. A tension-compression asymmetry is observed.

For each fatigue test and each material, the maximum stress values measured are always higher than the minimum stress values (in absolute value). However, the difference between the maximum stress value and the minimum stress value for a given test was much larger for the cold-drawn pearlite steel and the fine pearlite steel than for the coarse pearlite steel. The notable decrease in compression with respect to tensile strength confirmed that both heat-treated and cold-drawn pearlitic steels reflect a Bauschinger effect as reported by Toribio et al. [176] on cold-drawn pearlitic steel wires.

The evolution of the stress reached the maximum of applied strain shows that all the materials exhibit a cyclic softening especially marked at the beginning of the fatigue life. This strong primary softening period represents a few percent of the fatigue for the coarse and fine perlite steels but up to 10% for the cold-drawn perlite steels fatigued at the highest strain range. The cold-drawn and fine perlite steels exhibit a secondary softening with a moderate rate while the coarse perlite steel tends to stabilize. The secondary softening is more marked as the applied strain range is high.

The observed softening of cold-drawn, fine, and coarse pearlite specimens during cyclic loading under strain control is evidenced in Figure 153.

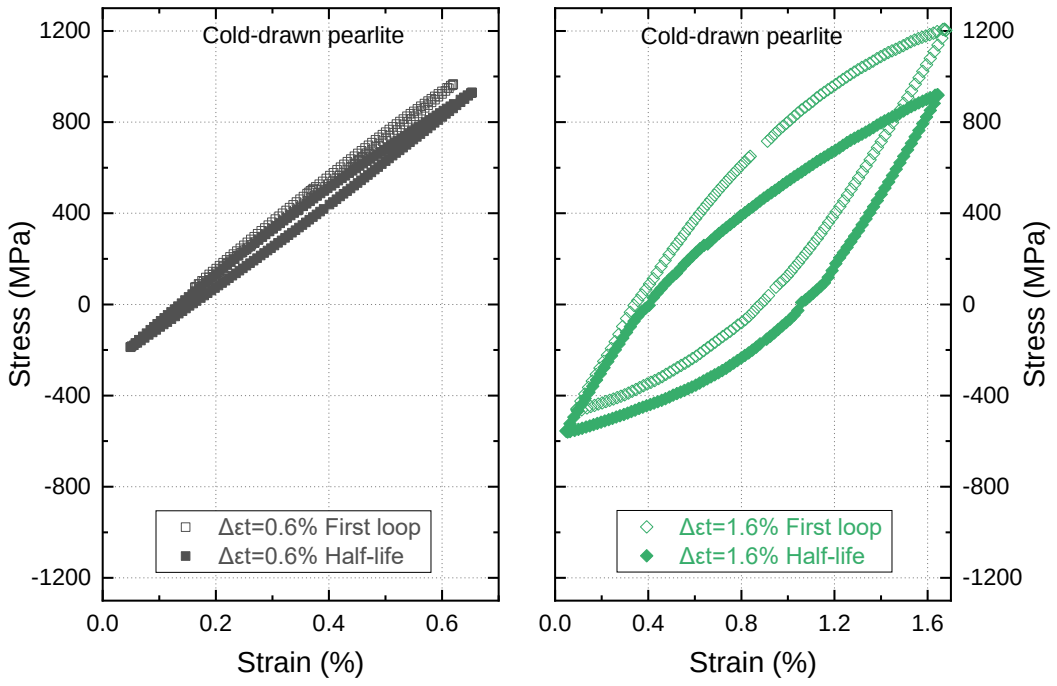

(a)

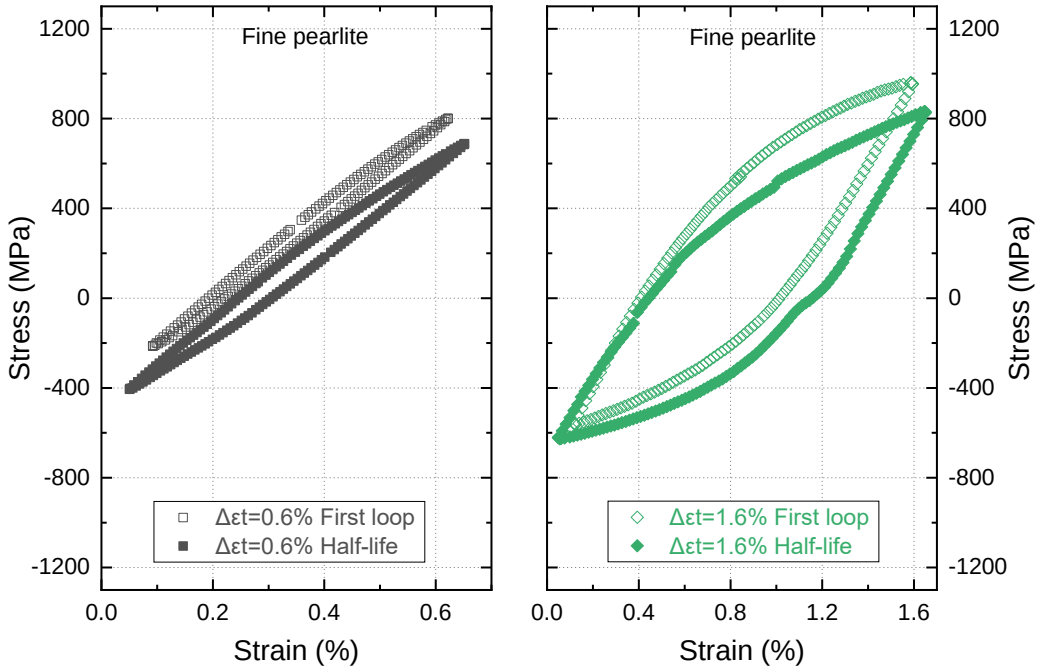

(b)

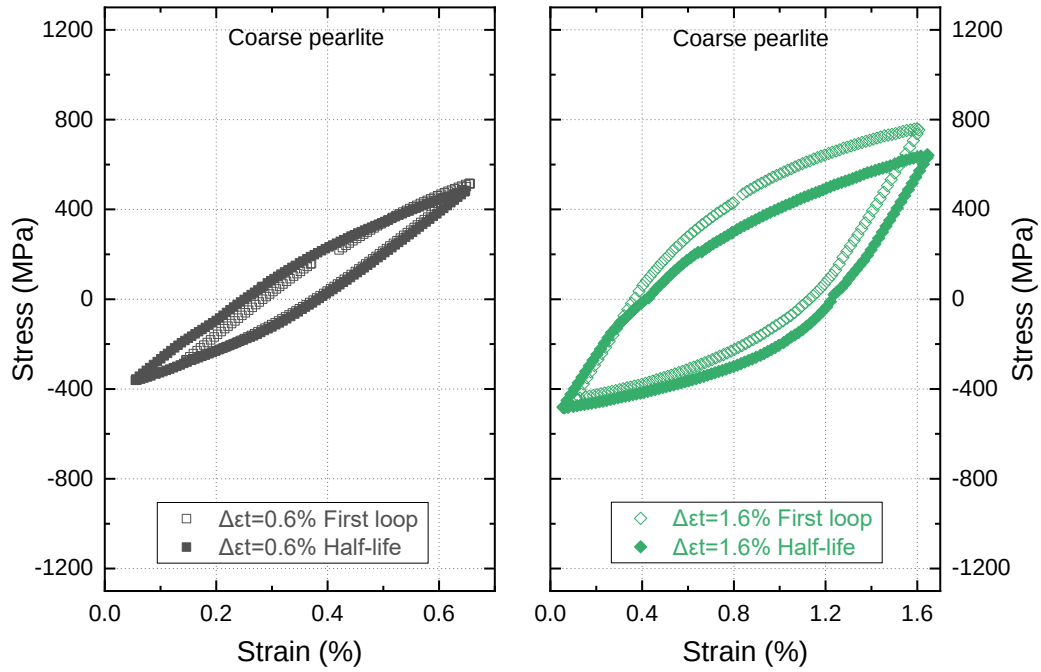

(c)

Figure 153: Comparison of the first and half-life loops of (a) cold-drawn pearlite, (b) fine and (c) coarse pearlite specimens at $\Delta\varepsilon_t$ from 0.6 to 1.6%

II.2.2. Fatigue resistance

For assessing the fatigue resistance of the materials, the Manson-Coffin-Basquin [177-179] relation between the plastic strain amplitudes with the fatigue life have been considered. Because the materials exhibited a significant difference in cyclic stress, the approach proposed by Golos and Ellyin [180] where the strain energy density

describes the fatigue life has also been taken into account. The plastic strain energy dissipated in a load cycle is assumed to be equivalent to the area of the hysteresis loop, which is directly related to the stress amplitude and the variation of plastic deformation during the loading.

Figure 154 shows the strain-life curves and the plastic strain energy dissipation with values measured at half-life calculated for the pearlitic specimens.

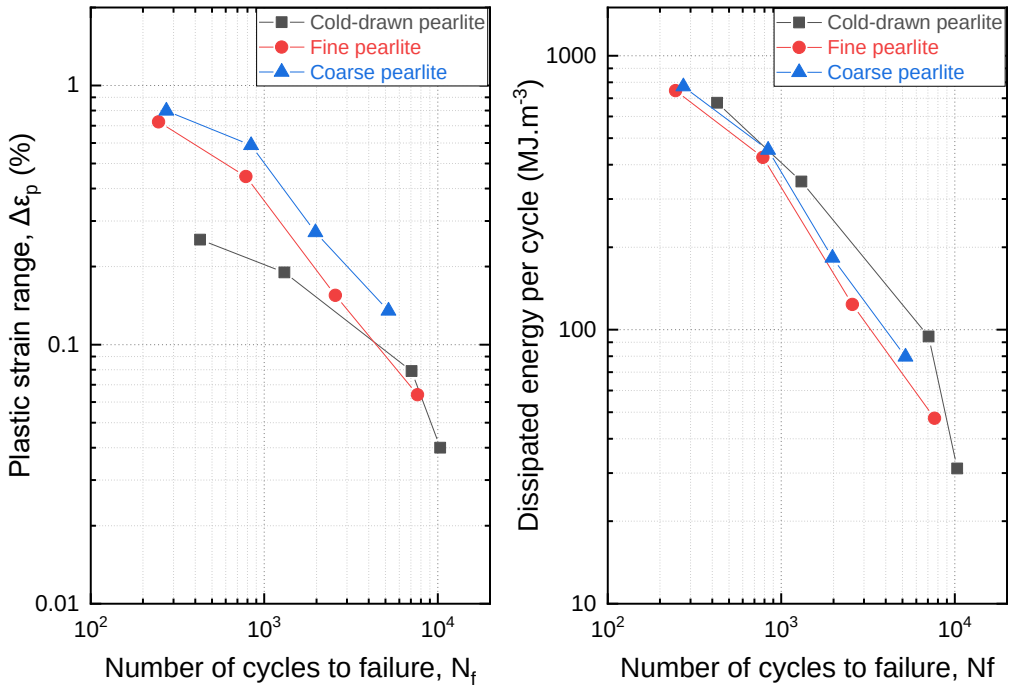

Figure 154: Fatigue strength analysis based on (a) strain-life curves and (b) strain-energy criteria obtained at the half-life of each specimen in the function of fatigue life

The Manson-Coffin curves (Figure 154-a) suggest that the less fatigue resistant material is the cold-drawn steel while the less resistant is the coarse perlite steel. However, with the energy – N_f diagram, the differences between materials vanish. By taking into account this indicator and the fact that the coarse perlite steel is rather stable in terms of cyclic stress during fatigue, coarse pearlite steel seems to combine the best fatigue properties.

II.2.3. Fractographic analysis

Fractographic analysis of the fatigue specimens was achieved by using scanning electron microscopy. Figure 155 shows typical SEM micrographs of the fractured surface observed in the cold-drawn specimens.

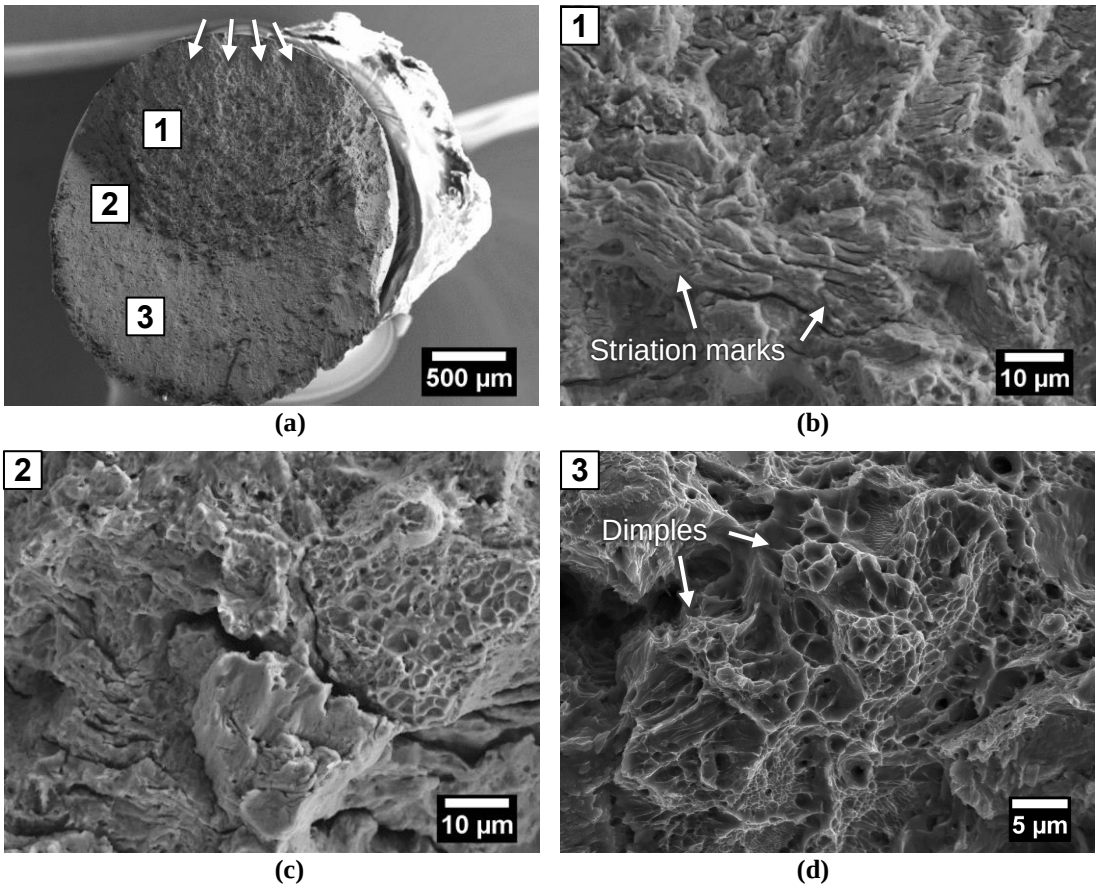

Figure 155: Fractographic analysis of the fractured surfaces in the cold-drawn pearlite specimens at $\Delta\varepsilon_t$=0.8%, showing the (a) fracture surface; (b) fatigue striation marks; (c) intersection between fatigue and final fracture zones; and (d) final ductile fracture

The fracture surface comprises three zones as denoted on the picture of Figure 155-a. Zone 1 is rather perpendicular to the loading axis while zone 3 is very inclined. Between, zone 2 is a transition zone. Zone 1 corresponds to the propagation by the fatigue of the macroscopic crack into the bulk. White arrows indicate the crack initiation site. Striations typical of fatigue crack advance have been observed (Figure 155-b). Zone 3 is the final fracture that occurred during the last cycle in a monotonic way. It contains spherical dimples characteristic of ductile fracture (Figure 155-d). Zone 2 contains a mixture of striations and dimples (Figure 155-c). The fracture surface analysis is in agreement with the behavior of a ductile material.

The fracture surfaces observed by SEM micrographs for both fine and coarse pearlite specimens are shown in Figure 156. The obvious difference at low magnification (Figure 156-a) of these materials and the cold drawn pearlite steel is a less inclined surface in zone 3 (Figure 156-c) . Zone 1 as well contains striation typical of fatigue crack advance (Figure 156-b). At a microscopic level, zone 3 was covered

by cleaved grains with a river pattern (Figure 156-d), typical of brittle transgranular cleavage. Such fracture behavior was observed in the majority of the heat-treated specimens. However, the zone 2 exhibits ductile features as indicated by dimples.

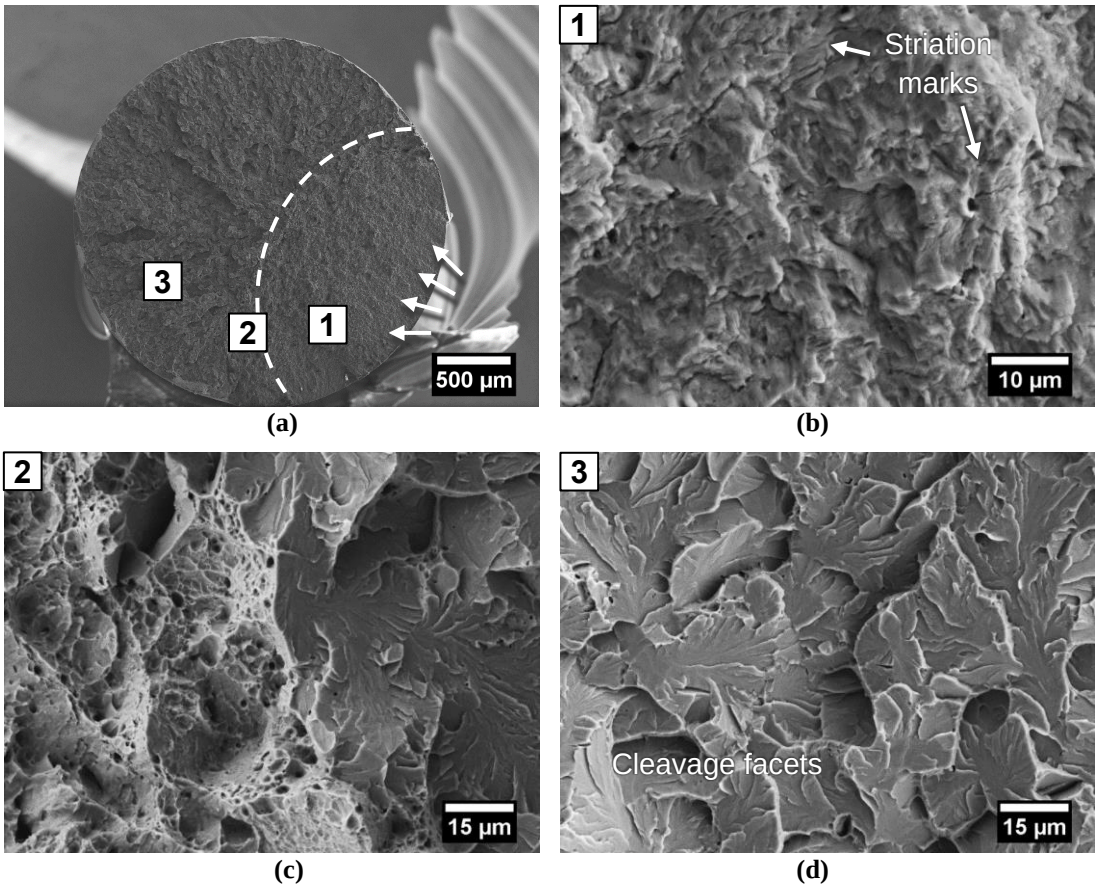

Figure 156: Fractographic analysis of the fractured surfaces in coarse pearlite specimens at $\Delta\varepsilon_t$=0.8%, showing the (a) fracture surface;(b) fatigue striation marks; (c) intersection between fatigue and final fracture zones; and (d) final brittle fracture

The decohesion of pearlite colonies was observed in failure surfaces, particularly in the coarse pearlite specimens, as seen in Figure 157. It probably originates from the accumulation of internal stresses during cyclic loading.

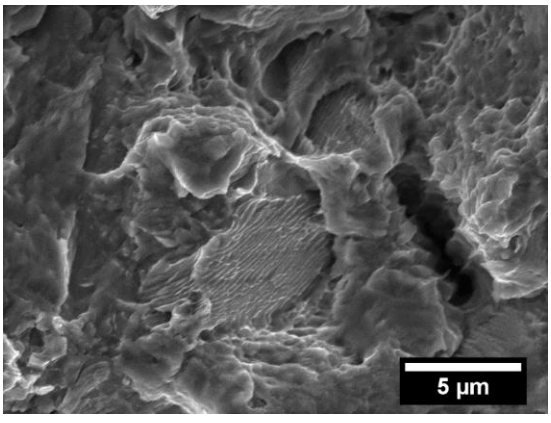

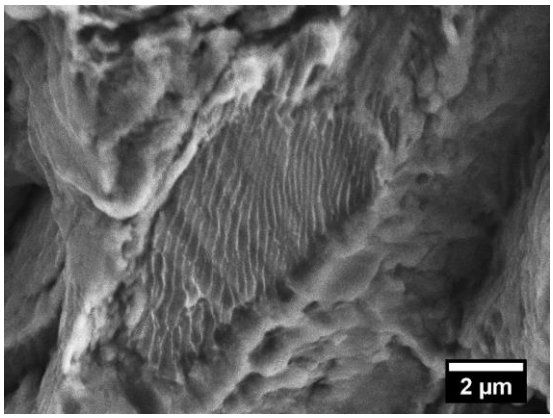

Figure 157: SEM images showing decohesion of pearlite colonies in fracture surfaces of coarse pearlite specimens at $\Delta\varepsilon_t$=0.8%

II.2.4. Second fatigue tests campaign

A non-scheduled experiment involving room temperature aging has been performed. Indeed, fine and coarse pearlite fatigue polished specimens were stored in a conventional desiccator at room temperature for about six months before it was decided to perform a second test campaign. Figure 158 shows the evolution of maximum and minimum stresses with the number of cycles recorded during the first and second test campaign of fine and coarse pearlite specimens at total strain range $\Delta\varepsilon_t$ = 0.8 and 1.2%. Possibly "naturally aged", the second campaign materials exhibit higher stress values than the ones of the first test. The difference was more visible with the highest strain tests ($\Delta\varepsilon_t$ = 1.2%) and more marked in the fine pearlite steel.

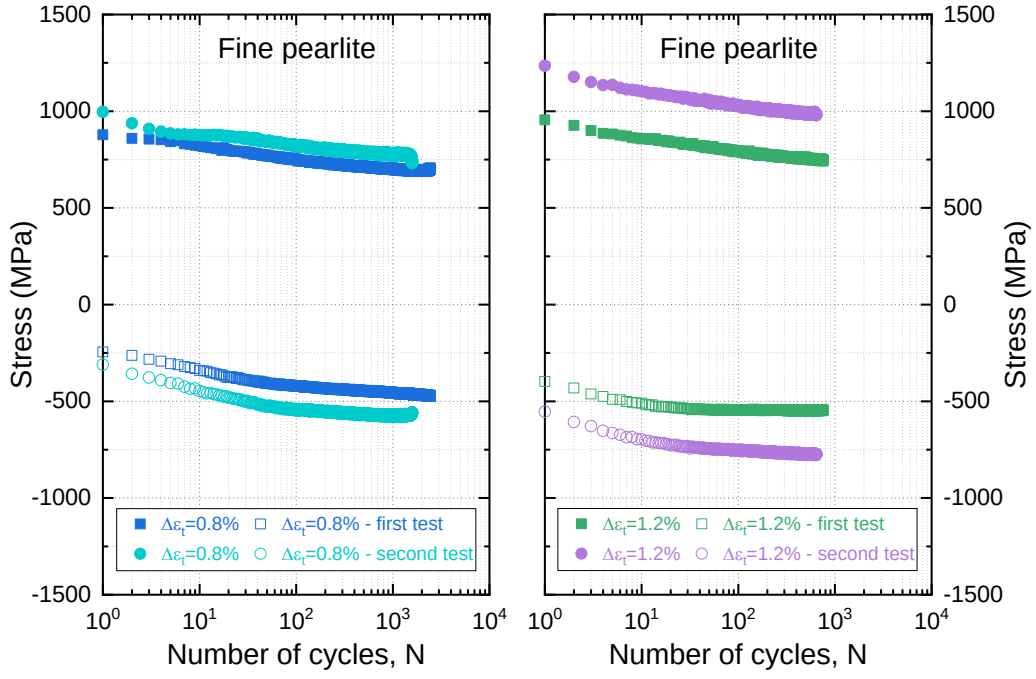

(a)

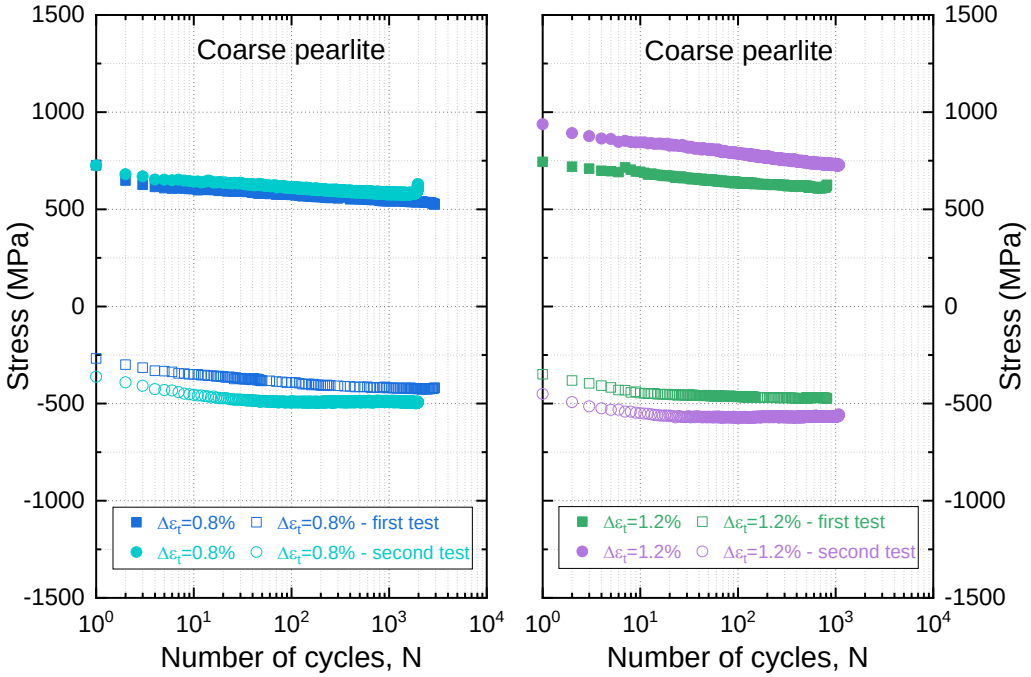

(b)

Figure 158: Comparison of stress evolution in the function of the number of cycles of (a) fine and (b) coarse pearlite specimens at strain amplitudes of 0.8 and 1.2%

Figure 159 shows the stress variations in the function of the fatigue life fraction. If the observed phenomenon is due to the aging of the material tested after 6 months of the first fatigue experiments, it seems not to influence the cyclic softening during cycling except when the tests were performed at $\Delta\varepsilon_t = 1.2\%$

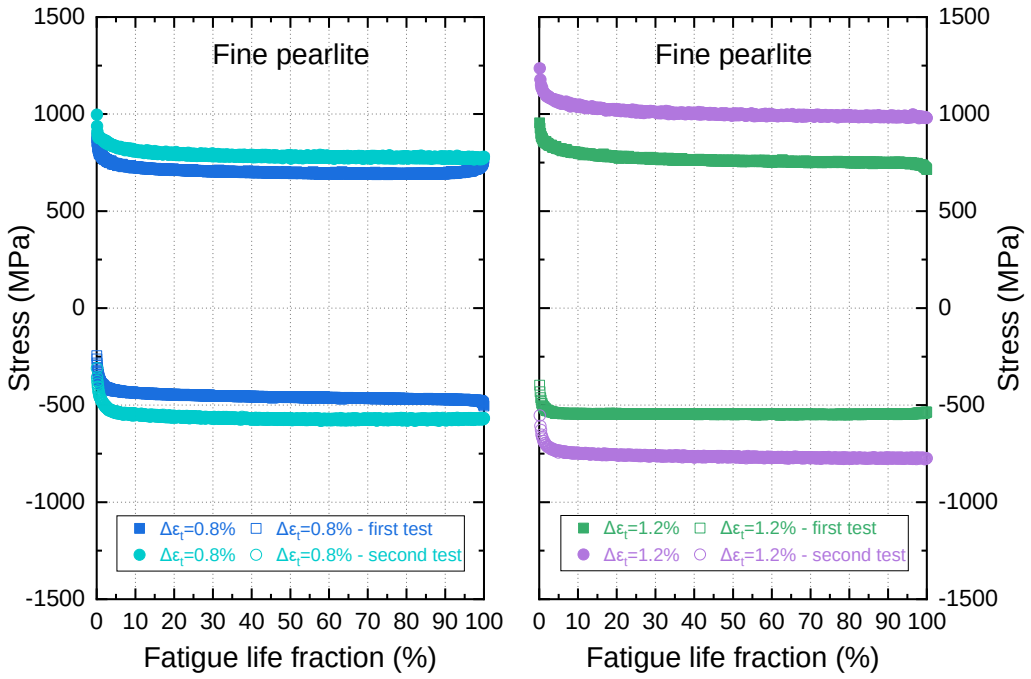

(a)

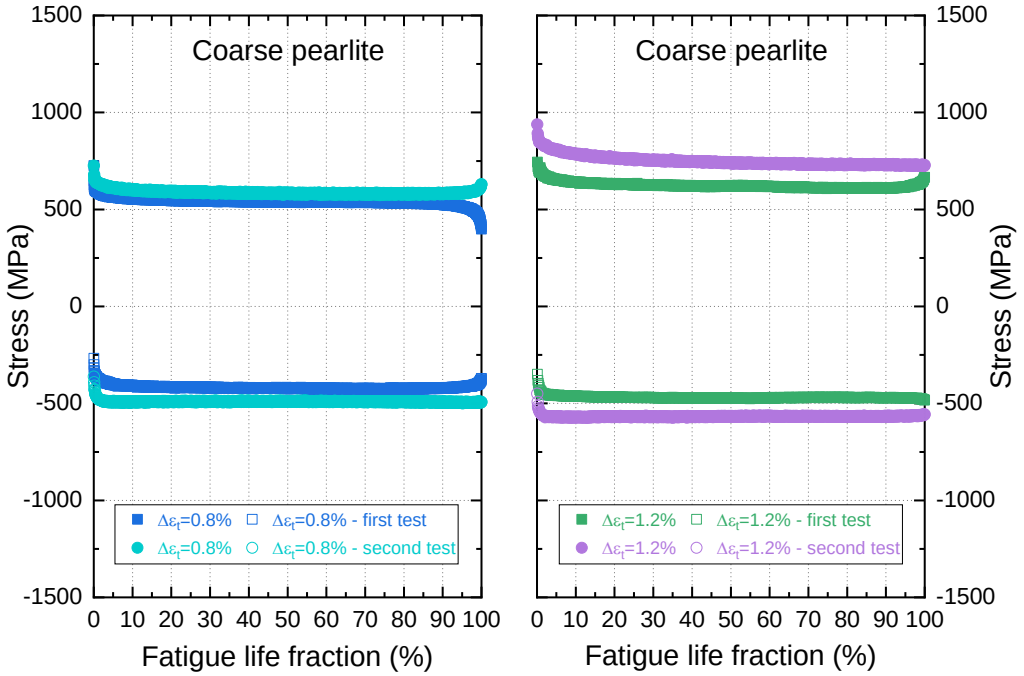

(b)

Figure 159: Comparison of stress evolution in the function of the fatigue fraction life of (a) fine and (b) coarse pearlite specimens at strain amplitudes of 0.8 and 1.2%

Figure 160 shows the plastic strain-life curves for all the strain-controlled cyclic load tests of cold-drawn and heat-treated pearlitic specimens at various total strains. The possible "natural aging" does not affect the fatigue resistance, even though a positive effect seems to appear for the coarse perlite steel.

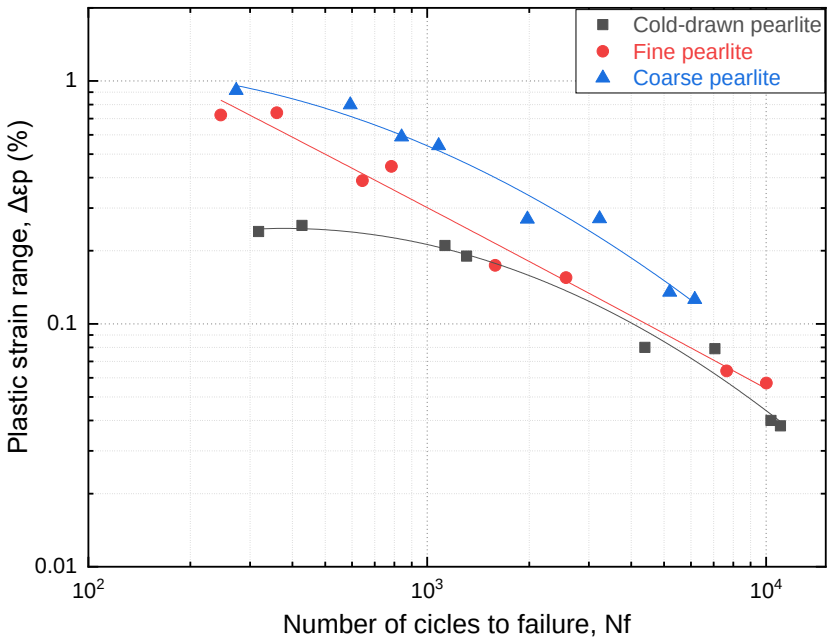

Figure 160: Cyclic strain-stress curves of all test duplicates for cold-drawn and patented pearlite specimens at $\Delta\varepsilon_t$ ranging from 0.6 to 1.6%

Figure 161 shows the SEM micrographs of fracture behavior observed for the specimens of the second campaign.

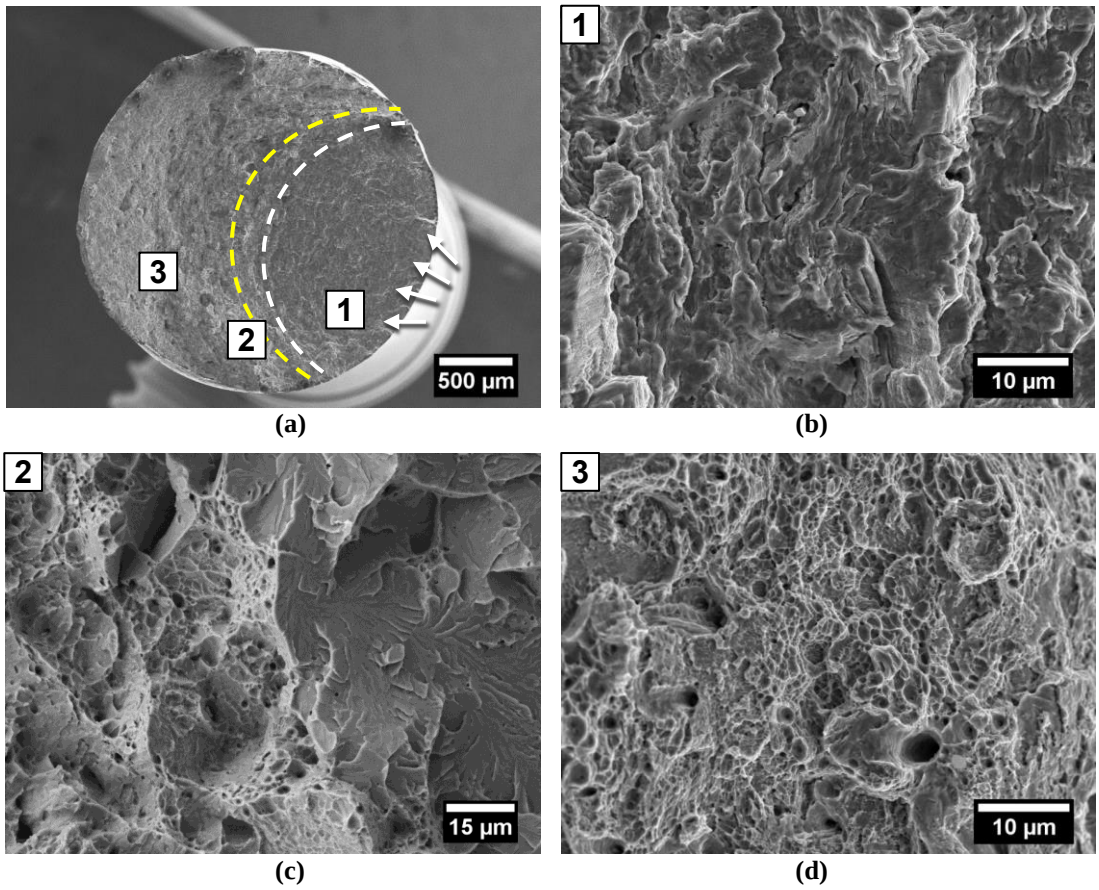

Figure 161: Fractographic analysis of the fractured surfaces in fine pearlite specimens at $\Delta\varepsilon_t$=0.8%, with a brittle transition zone (in yellow) and a final ductile fracture

The low magnification view of the fracture surface in the naturally aged specimen points out again the presence of three zones. However, it suggests a difference with the non-aged specimen – the zone 3 is now inclined instead of flat (Figure 161-a). Zone 1 is still related to the propagation by fatigue into the bulk of the macrocrack as indicated by the striations even though they were more difficult to reveal (Figure 161-b). The most relevant differences concern zone 2 and zone 3. These materials exhibit a narrow brittle transition zone 2 (Figure 161-c) and a final ductile fracture, as observed in Figure 161-d.

These experiments point out the importance of using stabilized microstructure, here possibly resulting from a room temperature aging observed on the fatigue behavior of patented steels. Further tests will be carried out to verify if such differences are due to an aging phenomenon, or if it may be linked to possible inhomogeneities in the steel batches due to variations in composition or thermomechanical processing.

II.3. Fatigue extrusion-intrusion in fully pearlitic steels

Fatigue failure is one of the major causes of many applications of materials. Fatigue life comprises a stage of crack initiation followed by crack propagation and sudden fracture. Crack initiation can occur either under or at the surface. There are several possible sites for fatigue crack initiation such as grain boundaries, twin boundaries, inclusion, persistent slip bands [181]. The presence of interfaces plays a crucial role in fatigue resistance. Cyclic loading above the yield stress results in general in the formation of fatigue slip markings (FSMs) at the external surface of the material. Classical categories of these are the intrusion-extrusion pairs. The evolution of intrusion-extrusion during the cyclic loading leads to the formation of short cracks. Their assessment can serve as quantitative indicators of accumulated fatigue damage [182]. The understanding of the intrusion formation mechanism is, therefore, of prime interest for the development of engineering materials resistant to fatigue. Hence, it is very important to identify very accurately the site of intrusion nucleation in fully pearlitic steel, a material that contains a huge number of α-Fe_3C interfaces.

FSMs developed at the external surface of the materials as a result of cyclic loading above the yield stress, as an indication of the slipping of favorable plans of the crystalline structure due to plastic deformation. FSMs observed at the gauge section of fractured specimens are shown in Figure 162.

The surface relied on consisted of intrusion-extrusion pairs and short cracks. The observation of FSMs revealed the inhomogeneous distribution of cyclic plasticity, with deformed areas adjacent to non-deformed ones. FSMs are observed to increase with the increase in the total strain amplitudes during cyclic loading. The ability to easily plastic deformation is reflected by the higher FSM densities developed at the external surface of coarser lamellar specimens.

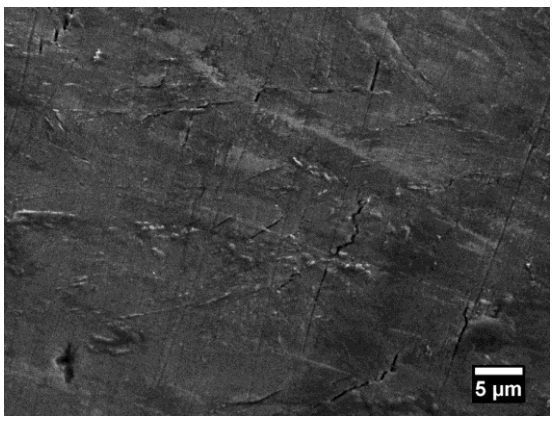

(a)

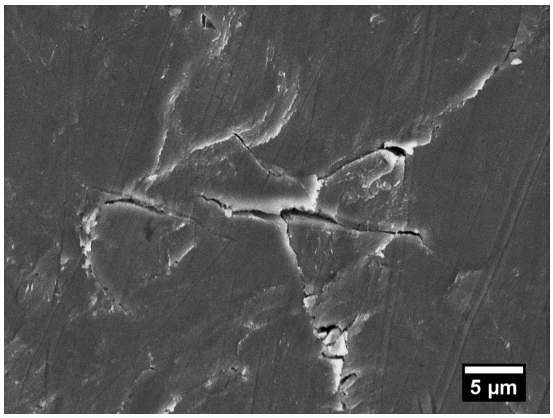

(b)

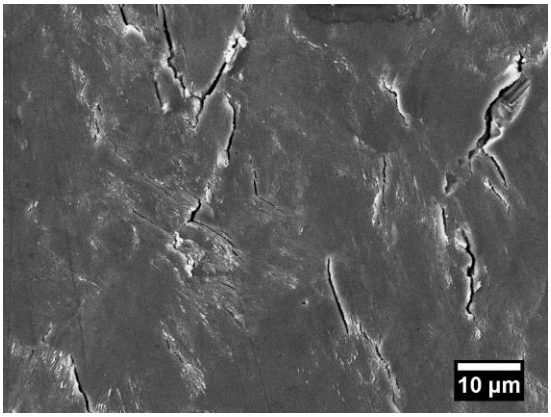

(c)

Figure 162: SEM micrographs of FSMs at the surface of fractured (a) cold-drawn, (b) fine, and (c) coarse pearlite specimens submitted to a total strain amplitude of 1.6%

The extrusion marks were easily identified in the FSMs network. However, it was difficult to distinguish between intrusions and short cracks using SEM. Also, the interactions between short cracks and intrusion-extrusion pairs with the pearlitic microstructure could not be established by a simple observation from the specimen external face. To overcome these difficulties, TEM observations were performed on lamellae extracted directly under the FSMs by FIB, as indicated in Figure 163.

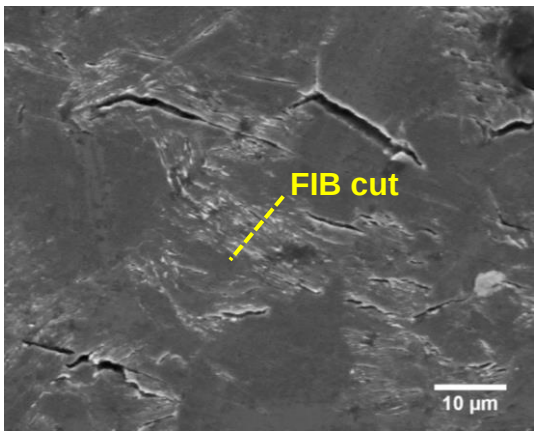

Figure 163: Surface relief induced by cyclic deformation on patented pearlite specimen

The area of interest was covered by two different layers to protect the surface against the ion insertion, a thin layer of carbon deposited by electron bombardment, and a thick layer of platinum about 1 mm sputtered by ion bombardment. Firstly, FIB machined the craters from both sides of the future lamella. Then the lamella was cut and transported on a copper grid and again thinned with a low ion energy beam (5–10 keV) to remove or minimize the damage caused by the previous steps. Imaging was performed on an FEI Titan Themis 300 analytical microscope working at an accelerating voltage of 300 kV. Figure 164 shows TEM images of one extracted lamella under the fatigue slip markings.

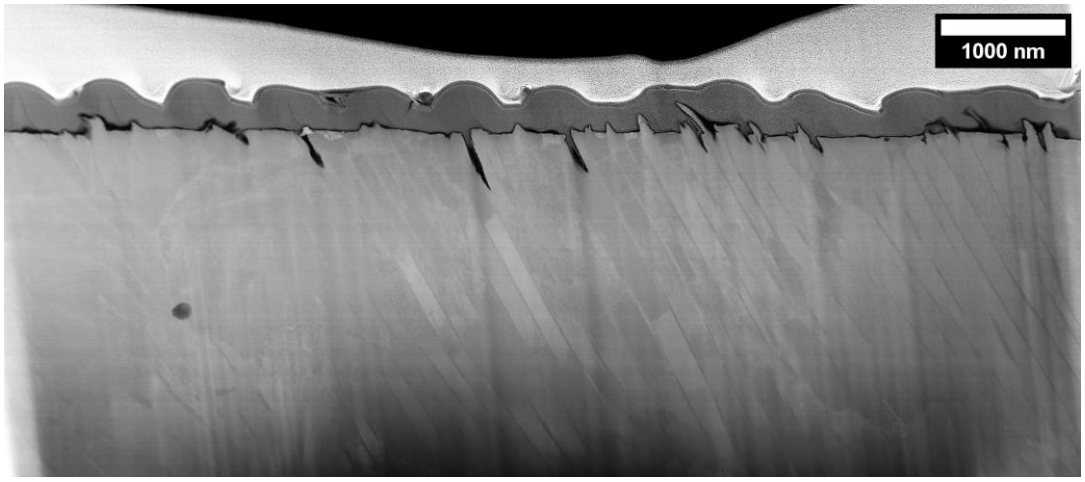

(a)

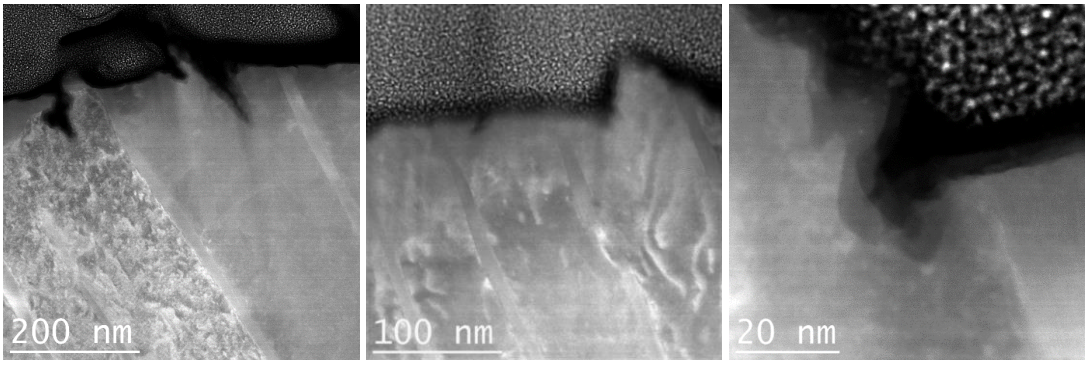

(b)

Figure 164: TEM images of (a) extracted lamella and (b) detail of intrusion-extrusion pairs formed in the lamellae structures after cyclic loading solicitations

It was observed that extrusions and intrusions were formed inside the bands of ferrite, as can be seen in Figure 165. The intrusion evolved into a short crack that propagated inside the α-phase. The image clearly shows that the lip of the microcrack has a serrated shape with inclined dislocation slip traces.

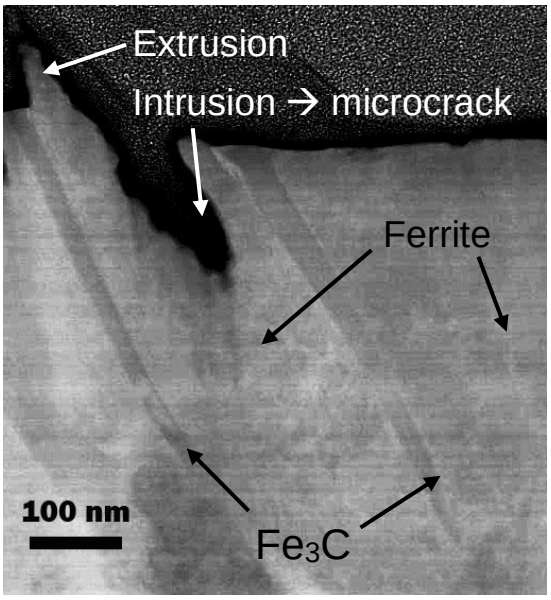

Figure 165: TEM image of the FIB lamella showing an intrusion involving into a short crack and an extrusion in ferrite

Several models of intrusion-extrusion formation have been developed in the literature, e.g., [183-185]. Among them, the model proposed by Polak and Man [184,185] is certainly the most relevant and attractive one. They explained the sequence formation of extrusion and intrusion and the role of point defects, especially vacancies. In annealed copper or solution heat-treated austenitic stainless steel, cyclic straining results in a two-phase dislocation structure consisting of persistent slip bands (PSBs) embedded in a vein matrix. The authors emphasized the role of interface between the PSB and the elastically deformed matrix where an exchange by the migration of vacancies and atoms provokes internal stress in the PSB, which is relaxed by an emerging extrusion.

In BCC steels cycled in the so-called high-temperature regime, dislocations substructures similar to that observed in wavy slip FCC metal can form. Thus, PSBs, walls, and cells can develop as well in equiaxed ferritic grains steels [186] as in elongated laths of martensitic [187] or bainitic steels [186]. Recently the formation of extrusions and intrusions has been approved in a 12Cr martensitic steel [188], taking into account Polak and Man ideas [184,185]. This material exhibits the classical hierarchic microstructure consisting of grains, packets, blocks, and laths. Intrusion-extrusion pairs were indeed observed, and the location of intrusion was unambiguously found at the interface between two laths. It was concluded that the interface between martensitic laths in the 12 Cr martensitic steel behaved as the interface between the PSB and the matrix in other materials. The fully pearlitic steels investigated in this

manuscript exhibited some similarities with this martensitic steel in terms of shape and size of the scanned area by dislocations. As for thin martensite laths, dislocations were indeed observed in the narrow α-ferrite bands. However, they were homogenously distributed but not structured. No dislocation walls nor cells were observed though plastic deformation activity was marked. Dislocation loops were observed to be emitted from the interface between ferrite bands and cementite lamellae. The absence of structuration of dislocations produced by cyclic straining arises from the width of α-ferrite bands. In comparison with large ferritic grains (10 to 50 µm) or with martensite lath (width between 0.4 µm up to 1 µm and length of about 10 µm), the width of α-ferrite bands is much smaller (typically 0.14 µm). Consequently, dislocations cannot glide in the three space directions in agreement with their slip system and their Schmid factor but have an oriented and restricted displacement along with the bands. Nevertheless, the gliding of these dislocations and their interaction can result in high production of vacancies as for other materials. All the conditions are present to form extrusions in α-ferrite bands according to the mechanisms mentioned above [184,185], based on the vacancy's migration toward an interface and atoms moving in the opposite direction.

Regarding the intrusions, they were also observed close to the extrusions and inside the α-ferrite bands. The intrusion was nevertheless expected along α-Fe_3C interfaces, which was not the case. It does not question the importance of the interface on intrusion nucleation but suggests focusing on the interface feature. First, in the investigated martensitic steel, the interface joins materials of the same nature as well in terms of chemical composition, mechanical response as average crystallographic orientation. Indeed, the interface is a low angle boundary. In the pearlitic steel, the situation is precisely the opposite: difference in chemical composition, crystallographic structure, and mechanical response (cementite is much harder than ferrite). Also, the interface is likely to be coherent concerning the literature [189].

Finally, the situation looks like a "composite" with a quasi non plastically deformable phase (cementite) beside a deformable one (ferrite). It turns out that facing a coherent interface could modify the location of vacancies sinks and atom sources. It seems that there exists a band separating the very interface between α-ferrite and Fe_3C and the α-ferrite bands where fatigue plasticity occurs. This band acts as a shield forcing vacancies produced in the active α-ferrite bands to diffuse and accumulate

ahead of the very interface between α-ferrite and Fe_3C cementite. It is also interesting to note that despite cementite is a hard phase. It did not break and nor initiate crack, as observed in a TiB_2-reinforced steel matrix composite [190].

The objective of this study was to evaluate the fatigue behavior of heat-treated and cold-drawn (Ɛ=0.45) pearlitic steels by performing strain-controlled tests at different total deformation levels, 0.6%, 0.8%, 1.2%, and 1.6%.

- A cyclic softening was observed for all the samples. The notable decrease in compression stress is attributed to the Bauschinger effect during tension-compression loading.
- Under cyclic loading, the fully pearlitic steel exhibited well-developed slip markings. Extrusions were easily observable by SEM at the external surface of the specimen. TEM observations on FIB lamellae revealed that both intrusion and extrusion formed in the α-phase. The intrusion initiation site was slightly away from the interface between the ferrite and cementite phases.
- The fractured surface consisted of the crack propagated into the bulk material, revealing a ductile behavior of cold-drawn steels, and brittle cleavage fracture occurring in both fine and coarse pearlite specimens after patenting.
- Unexpected fatigue behavior was observed to happen in the patented specimens tested after an interval of 6 months, possibly due to natural aging. These samples have presented a peculiar fracture behavior with a tiny brittle transition zone between the fatigue failure and the final fracture, and a final ductile fracture. It indicates an improvement of the fatigue behavior of aged pearlitic steels.

III. EFFECT OF CYCLIC LOADING

So far, in this thesis manuscript, the eddy current technique has demonstrated an interesting capability to characterize very complex materials including heat-treated carbon steels and cold-drawn pearlitic wires at different stages of deformation. Applications of eddy current testing have been successfully explored for inspecting fatigue damages in structural engineering materials submitted to cyclic efforts, such as detection of short and deep cracks in multi-layered aircraft structures [191,192], propagation and growth of cracks in steel plates [193], weld connections and coatings of bridge structures [194]. In addition to the prevalent defects inspection, the present research aims to investigate the sensitivity of such NDT to detect and monitor any change in the microstructure of pearlitic steels that can occur in-service conditions.

Fully pearlitic steel wires with fine and coarse lamellar structures were selected for this experiment. Specimens with 6 mm in diameter and 20 cm in length were tested in a Zwick-Roell machine up to failure at a crosshead speed of 30 mm/min for determining the monotonic behavior of each material. The stress-strain curves obtained are shown in Figure 166.

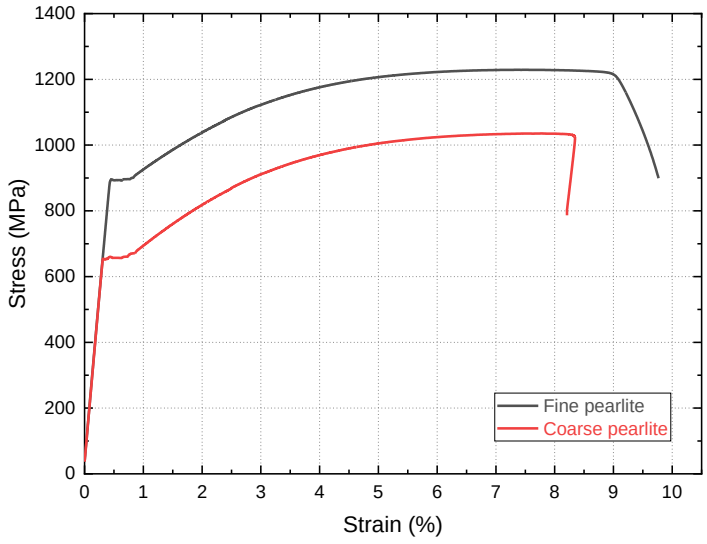

Figure 166: Stress-strain curves of the AISI 1080 steel samples with fine and coarse lamellar pearlite microstructures

In order to perform the cyclic load testing, the contactless eddy current electromagnetic sensor was coupled to the universal testing machine, positioned in the gauge section of the wire specimen, as shown in Figure 167. An extensometer was placed in contact with the specimen extremities. Eddy current testing was carried out

at a low frequency of 200 Hz. The cyclic loading tests were performed under load control resulting in either elastic deformation or elastic and plastic deformation.

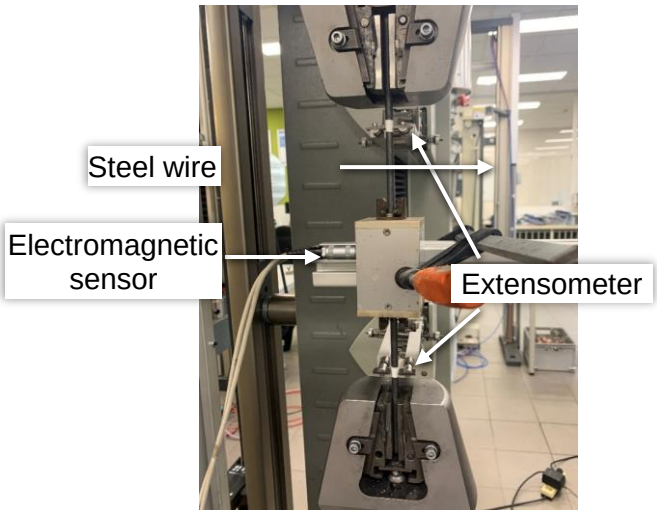

Figure 167: Assembly of the cyclic test experiment with the electromagnetic sensor placed in the gauge section

The effect of cyclic loading on the performance of pearlitic specimens was investigated through tests conducted up to ten cycles, with stress varying between 75 and 400 MPa causing elastic deformation. After cyclic loading, the load was increased to enter the plastic domain. Figure 168 shows the superposition of the curves of the applied stress and the corresponding eddy current responses.

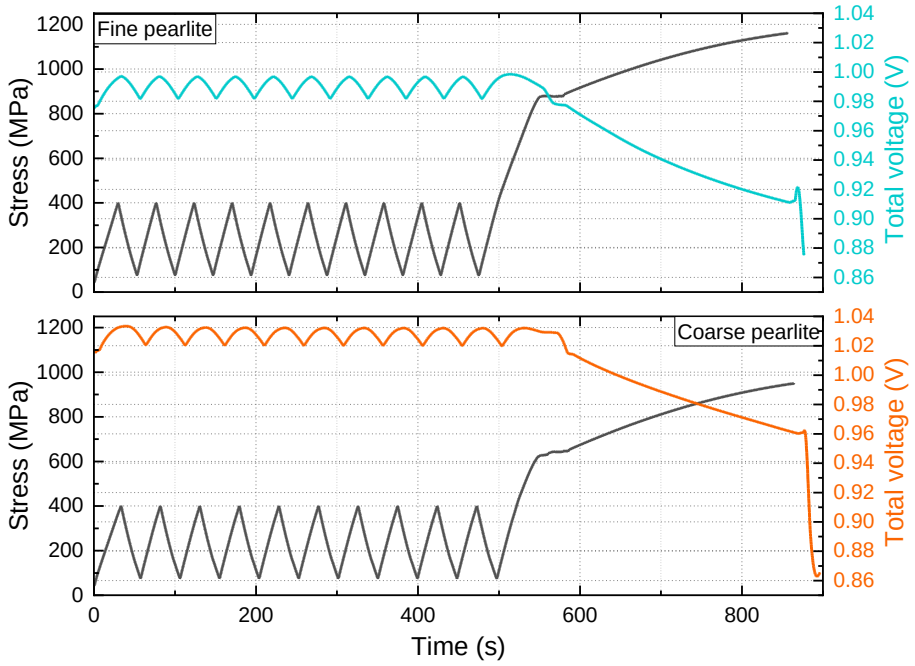

Figure 168: Superposition curves of the applied stresses and eddy current responses during cyclic loading in the elastic regime of fine and coarse pearlite

The shape of the response signals tends to be triangular. In accordance with the applied cyclic elastic loadings, the total voltage values increase with the tensile stresses and decrease when compressive stresses are applied. The crystal lattice structure is distorted during elastic deformation, which affects its electromagnetic properties. As reported by Thompson and Tanner [195], tensile stress enhances the magnetization in a parallel direction to the applied stress due to the positive magnetostriction of iron, while the lattice distortion occurred with compressive stress tends to reduce the overall magnetization.

The total voltage outputs varied at nearly the same range for each material. The fine pearlite steel presented a lower mean total voltage value of approximately 0.9892 V compared to the coarse pearlite sample of about 1.0263 V. The extent of elastic deformation experienced by fine pearlite is smaller than coarse pearlite at the same applied stress, as it presents higher yield stress. It indicates that at the imposed range of cyclic stress, the coarse pearlite is more likely to develop a more significant amount of microplasticity in the nominally elastic region. Therefore, the different mean total voltage obtained between these materials may elucidate the further microplasticity contributions occurring at stresses below to the macroscopic yield point. Microplastic strains are of considerable importance in the study of fatigue. Nonetheless, these strains are rarely defined by standard mechanical methods. Similarly, Esin and Jones [196] and Gajdoš et al. [197] have reported the strain sensitivity of magnetic permeability of steels at low values of stress by means of indirect changes on electrical impedance. The capability for assessing microplasticity strains can be considered a distinctive asset of non-destructive monitoring by eddy current technique.

After the 10 cycles, the increase in stress causes an increase in voltage signals. It exhibited constant signal regions when the yield plateau was reached, indicating Lüder's effect. As the specimens have become further deformed, the voltage signals gradually decrease until the test interruption when the maximum stresses defined for each material have been reached, decreasing significantly during unloading. These responses reflected the strain-stress dependence of the electromagnetic behavior of ferromagnetic materials such as carbon steels.

Next, cyclic loading tests were performed within the plastic regime, at minimum stress of 75 MPa, but maximum stresses established at values approximately 30% higher than the characteristic yield strength of each type of material. It resulted in cycling between 75 MPa and 1100 MPa for the fine pearlite specimen, and between

75 MPa and 900 MPa for the coarse lamellar pearlite sample. The load first increased monotonically until the maximum stress value defined for pearlitic steel, and then, the cyclic tests were conducted up to 200 cycles in the specified stress ranges.

Figure 169 shows the obtained strain-stress curves obtained after the cyclic loading of fine and coarse pearlite specimens.

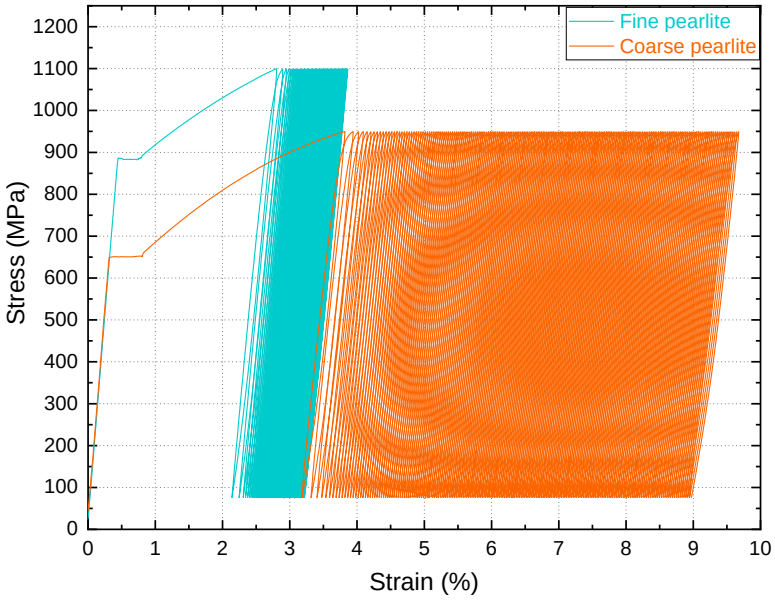

Figure 169: Stress-strain curves recorded after 200 loading cycles of pearlite samples

The uniaxial experiments were carried out under asymmetrical cyclic loading conditions up to 200 cycles. A significant effect of ratcheting is found in the coarse pearlite specimen, compared with fine pearlite. The total plastic strain accumulation increased from about 2% to 3% in the fine pearlite for applied stress of 1020 MPa, whereas, in the coarse pearlite, it ranged from 3 to 9% for applied stress of 825 MPa. It reveals the different mechanisms of cyclic plasticity between fine and coarse pearlite microstructures, reflecting a cyclic softening behavior of these microstructures.

Considering that the materials were not pre-stressed at the same strain levels, the different behavior observed between fine and coarse pearlite after cyclic plastic loading cannot be merely attributed to its microstructural characteristics. At this point, it is important to remind that the objective of the present investigation is not to evaluate the influence of pearlite finesse on the fatigue behavior of such steels but to assess the ability of eddy current technique in monitoring the microstructure evolution of pearlitic steels during cyclic loading.

The superposition curves of applied stress and total voltage responses corresponding to the first five load cycles are shown in Figure 170.

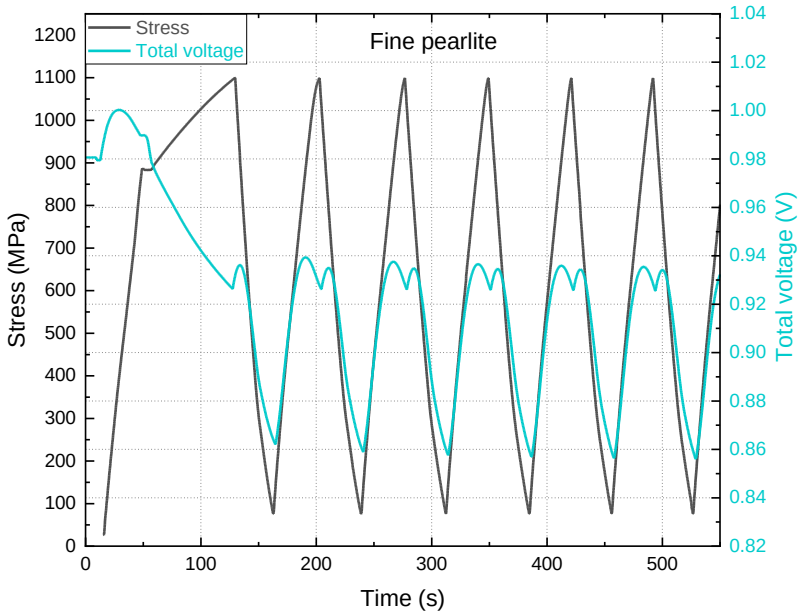

(a)

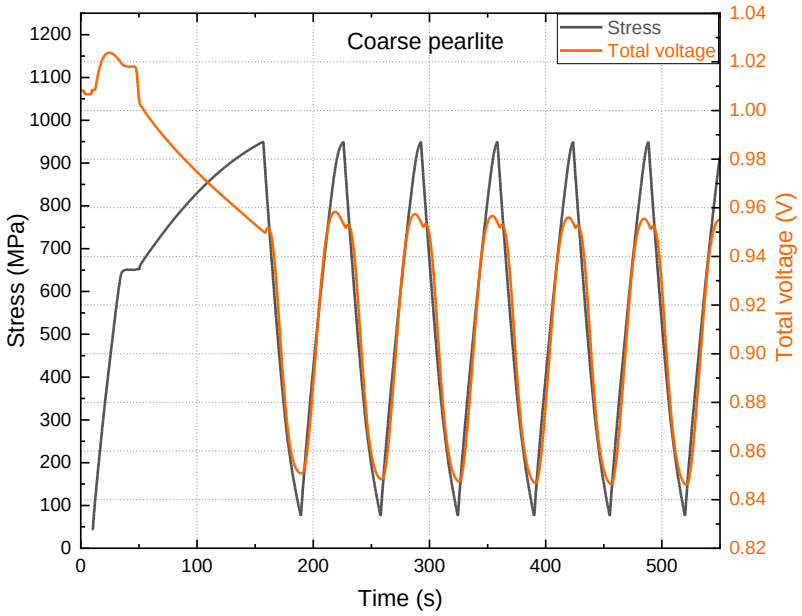

(b)

Figure 170: Superposition curves of the applied stresses and eddy current responses during the first five loading cycles in the plastic regime for the (a) fine and (b) coarse pearlite microstructures

The total voltage is observed to vary in accordance with the cyclic loading, increasing with tensile stresses and decreasing with compressive stresses. The fine pearlite exhibits a smaller amplitude of signal variation than the coarse pearlite, whereas close mean values are observed between the materials. Also, a decrease in the total voltage, followed by a second peak, is produced at the start of loading change from tension to compression. It can be a consequence of the Bauschinger effect related to dislocation interactions (e.g., dislocation-dislocation and dislocation-particle

interactions – grain boundaries, second-phase particles, impurities), and the resulting back stresses generated after load reversal direction [198-201]. The reduction of compressive yield stresses after the load path change probably impacts the electromagnetic response, resulting in the detected signal variations. This effect may contribute to the observed work softening of pearlitic steels.

Figure 171 shows the evolution of total voltage response after 200 loading cycles above the yield stress of both fine and coarse pearlite steels. The amplitude of signal variation does not vary, as the applied stress was constant during the cyclic loading. However, the mean total voltage decreases with cumulative plastic strain during the cyclic loading experiments. This result might reflect the ratcheting and softening behavior observed in Figure 169, notably for the coarse pearlite specimen.

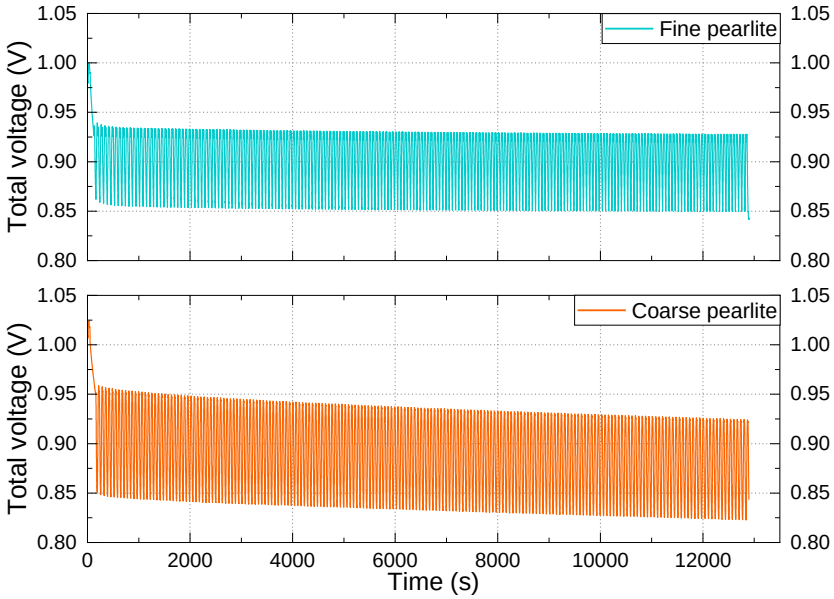

Figure 171: Total voltage signals evolution during cyclic plastic loading of pearlite

After the end of the experiments, the fine pearlite sample showed a slightly lower area reduction than the coarse pearlite specimen, presenting a higher average final total voltage than the coarse pearlite. The one-way ANOVA test confirmed that the mean total voltage values between these materials are statistically different at the 0.05 level, $F(3,8652)=1.47$, $p=0$.

The eddy current voltage planes obtained after cyclic loading of fine and coarse pearlite microstructures are shown in Figure 172. It can be noted that the signal variations in the resistive and inductive voltages due to the cyclic elastic deformation were smaller than compared to cyclic loading above yield strength, where even more prominent signal changes were detected with cumulative plastic deformation. In

addition, the voltage differences between fine and coarse pearlite steels that should suggest different deformation mechanisms of such microstructures.

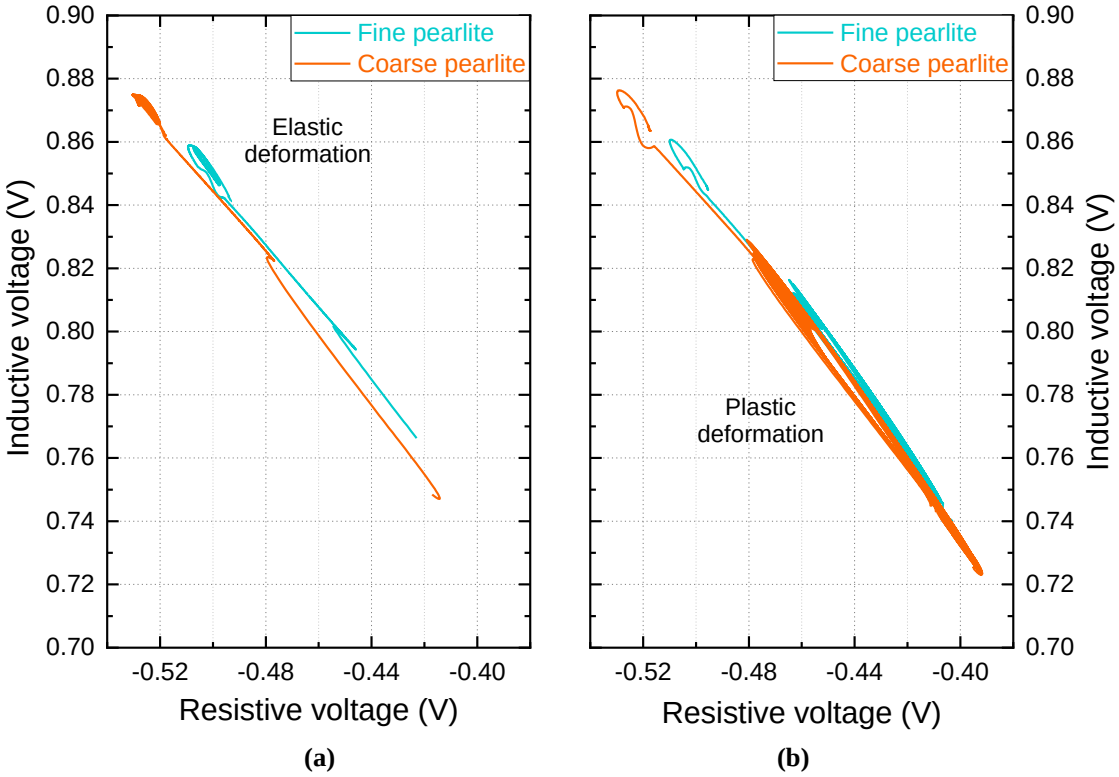

Figure 172: Eddy current voltage plane of fine and coarse pearlite samples after cyclic loading of (a) 10 cycles in the elastic regime, and (b) 200 cycles in the plastic regime

Electrical resistivity and bulk magnetic measurements were performed on the pearlitic samples before and after cyclic loading to evaluate the effect of cyclic plastic deformation on the physical properties of pearlitic steels. Samples of 2.5 cm in length were obtained from the fatigued specimens. The results are shown in Table 24

Table 24: Comparison between the electrical resistivity and main magnetic properties of non-deformed and plastically deformed pearlitic steels

Microstructure	Initial diameter (mm)	Final diameter (mm)	Electrical resistivity (µohm.cm)	Coercivity ($A.m^{-1}$)	Maximum relative permeability
Non-deformed fine pearlite	6	-	23.13 ± 0.02	1299 ± 1	281 ± 14
Fatigued fine pearlite	6	5.76	22.75 ± 0.04	1872 ± 5	160 ± 3
Non-deformed coarse pearlite	6	-	22.55 ± 0.02	1032 ± 3	368 ± 1
Fatigued coarse pearlite	6	5.67	21.97 ± 0.05	1666 ± 1	142 ± 1

The hysteresis loops and magnetization curves of the reference non-deformed and plastically deformed fine and coarse pearlite samples are shown in Figure 173.

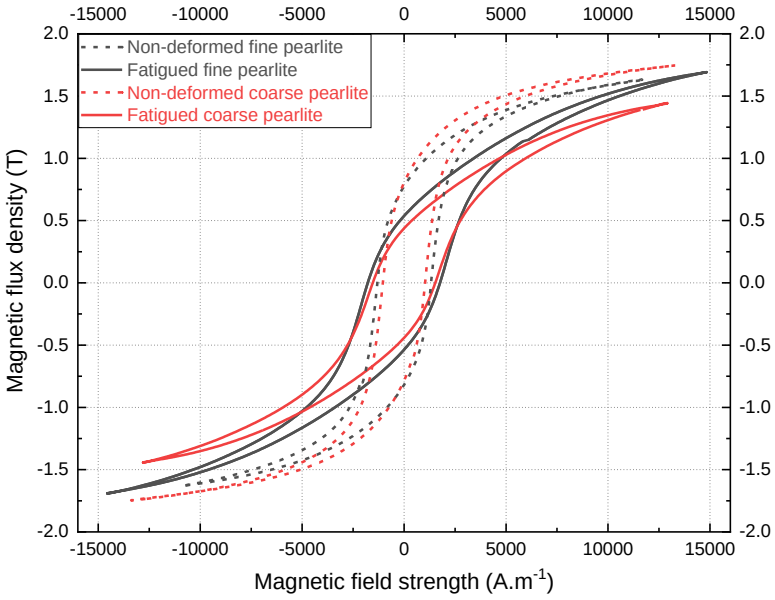

(a)

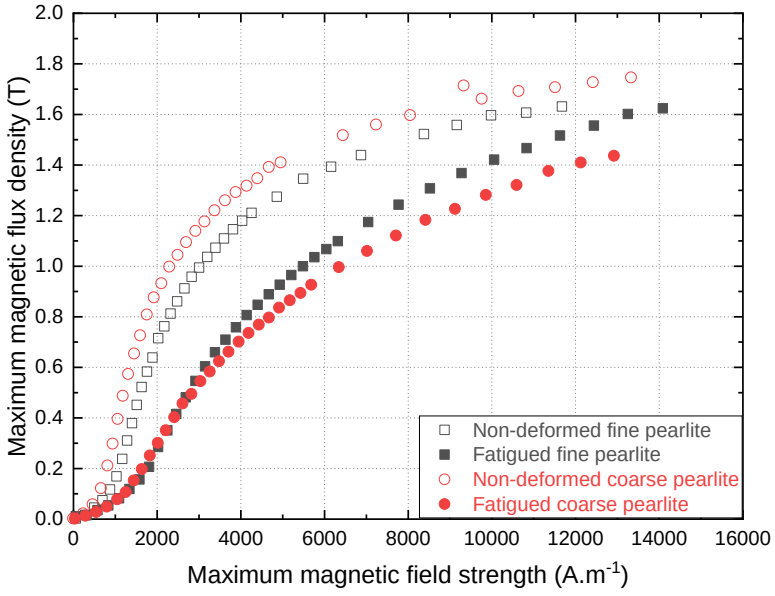

(b)

Figure 173: (a) Hysteresis loops and (b) magnetization curves of the non-deformed and cyclic plastically deformed fine and coarse pearlite microstructures

The cyclically deformed pearlitic steels exhibit a shallow decrease in electrical resistivity when compared to the as-patented microstructures. One-way ANOVA test indicated that the mean differences between the measured resistivity values are statistically different at the significance level of 0.05, $F(3,999)=25592$, $p=0$. Even if the strain sensitivity of resistivity has been indirectly observed by resistive voltage variations during cyclic loading, the interpretation of detected changes in the final

deformed steel merely from resistivity measurements is quite complicated. These results can be due to the orientation of pearlite colonies imposed by the uniaxial stresses, slightly increasing the electrical conductivity, as previously discussed. Also, it may be related to dislocation interactions caused by load path reversion during cyclic deformation that may have influenced the frequency of electron scattering events.

Equivalently to the cold-drawn pearlitic wires at the first drawing stages (Ɛ=0.27), the magnetic permeability values are observed to decrease, whereas the coercivity increases with plastic deformation. The relative permeability of coarse pearlite decreases almost two times more in comparison with fine pearlite. As previously discussed, the degradation of magnetic properties seems to be related to the increase of domain wall pinning at lattice defects generated during cyclic loading, as well as the magnetocrystalline energy associated with the difficulty in magnetizing the materials in directions other than the easy magnetization axis of the BCC crystal lattice. Therefore, the strain-stress dependence of magnetic properties of pearlitic steels submitted to plastic deformations produced by cyclical loadings is comparable to the magnetic behavior observed in the same materials under close total deformation amounts imposed by monotonic stresses.

Figure 174 shows the phase angle outputs relative to the material responses before and after the 200 loading cycles under plastic deformation.

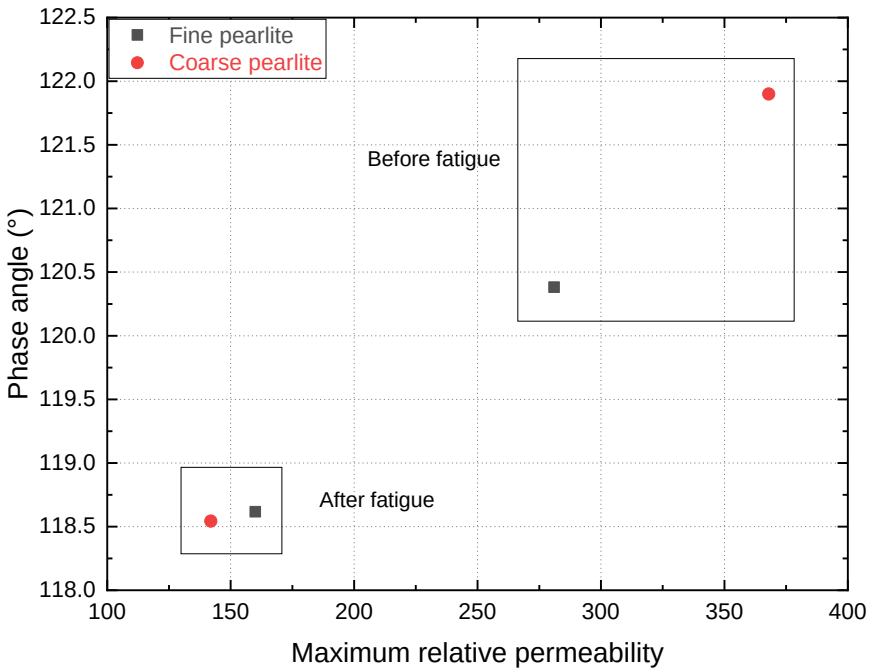

Figure 174: Phase angle variations in the function of maximum relative permeability of pearlitic steels before and after cyclic plastic deformation

The phase angle variations mainly described the magnetic properties changes after cyclic loading, once the electrical conductivity does not present remarkable disparities between the non-deformed and the plastically deformed samples. It is important to mention that the geometric changes of the wire samples were too small (area reduction of less than 10%) to alter the measured eddy current outputs considerably.

In this section, cyclic loading tests were conducted coupled with an electromagnetic sensor for evaluating the response to cyclic elastic and plastic deformations of the pearlitic AISI 1080 steels with different interlamellar spacing.

- Under the elastic regime, the eddy current signal variations between fine and coarse pearlite were attributed to microplasticity contributions at fairly low stresses, relative to the proportional limit stress characteristic of each material.
- Total voltage variations detected after load reversal direction from tension to compression stress was considered as electromagnetic responses to the Bauschinger effect, which might have contributed to the work softening of pearlitic steels.
- The great potential of the eddy current technique was assessed for monitoring cyclic plastic accommodation of pearlitic steels under cyclic loading and the different deformation mechanisms of fine and coarse pearlite microstructures, reflecting the strain-stress dependence of the magnetic permeability.
- Further investigation still necessary for better comprehension and interpretation of the material behavior and the dynamic signal responses occurring during cyclic loading.

IV. SUMMARY

The effect of monotonic and cyclic plastic deformation by cold-drawing and fatigue on the electromagnetic behavior of pearlitic steels are summarized in Figure 175.

	CARBON STEEL WIRES		PHYSICAL PROPERTIES		NDT
COLD-DRAWING	Low plastic deformation $\varepsilon < 1$	Initial bending and rotation of pearlite colonies along the wire axis	$\uparrow \boldsymbol{\sigma}$ * Alignment of pearlite colonies contributes to electron mean free paths increase in the α-phase lamellae, reducing α-Fe_3C scattering events	$\downarrow \boldsymbol{\mu} \cdot \uparrow \boldsymbol{H_C}$ * Domain wall pinning effect increase with dislocation density increase * High anisotropy energy	$\downarrow \varphi$
	Moderate to high plastic deformation $1 < \varepsilon < 2$	Progressive lamellae alignment; fibre texture development in α-phase with drawing strain Deformation bands Thinning, striction, and fragmentation of some Fe_3C lamellae	$\downarrow \boldsymbol{\sigma}$ * Increase of electron scattering events at α-Fe_3C interfaces with increasing fibre and dislocation strengthening	$\uparrow \boldsymbol{\mu} \cdot \downarrow \boldsymbol{H_C}$ * Magnetic anisotropy change * Thinning and fragmentation of Fe_3C lamellae also facilitate the magnetization process	$\uparrow \varphi$
	Severe plastic deformation $\varepsilon > 2$	Thinning, striction, and fragmentation of some Fe_3C lamellae Decomposition of cementite	$\downarrow \boldsymbol{\sigma}$ * Cementite dissolution produces a supersaturated solution in C atoms at ferrite matrix, decreasing free electrons density	$\uparrow \boldsymbol{\mu} \cdot \downarrow \boldsymbol{H_C}$ $\uparrow \boldsymbol{B_S}$ * Magnetic phase composition change (possible cementite dissolution under large deformation)	$\downarrow \varphi$
CYCLIC LOADING: LOW-CYCLE FATIGUE	Final cyclic plastic deformation	Cyclic softening Extrusion-intrusion forms in α-phase Ductile final fracture (cold-drawn and aged pearlite); brittle final fracture (patented pearlite)	$\uparrow \boldsymbol{\sigma}$ * Elongation of pearlite colonies by uniaxial stresses; dislocation interactions due to load-path reversion may alter electron scattering frequency	$\downarrow \boldsymbol{\mu} \cdot \uparrow \boldsymbol{H_C}$ * Domain wall pinning increase at lattice defects generated during cyclic loading * High anisotropy energy	$\uparrow R \ \downarrow X_L \downarrow Z$ $\therefore$ $\uparrow V_R \ \downarrow V_L \downarrow V_T$ $\downarrow \varphi$
	Monitoring cyclic deformation	Microplasticity contribution in the nominally elastic region Cyclic softening - Bauschinger effect during tension-compression (σ_t-σ_c) load reversion - Ratcheting effect	–	–	* Microplasticity: mean signal variation increases in elastic regime * Cyclic loading: σ_t:$\downarrow V_R \uparrow V_L \uparrow V_T$ σ_c:$\uparrow V_R \downarrow V_L \downarrow V_T$ * Bauschinger effect: signal peak at load changing * Ratcheting effect: $\uparrow V_R \downarrow V_L \downarrow V_T$ with cumulative strain

Figure 175: Summary of the observed effects of microstructural parameters on the electromagnetic behavior of carbon steel wires

CONCLUSIONS AND PERSPECTIVES

CONCLUSIONS AND PERSPECTIVES

Pearlite is a common constituent of a large variety of high strength steel grades typically used in many structural engineering applications, which demand a good combination of high strength, toughness, and fatigue properties. With the increasing requirements for product quality and in-service reliability, the non-destructive inspection of defects is giving way to the research of non-destructive evaluation of material properties including methods that rely on electromagnetic principles, such as eddy current testing. ECT comes out as a promising tool for in-situ characterization of ferromagnetic materials such as steels. However, the influence of microstructure on the physical properties indirectly measured by an electromagnetic sensor has not yet been completely elucidated. This implies that the metallurgical mechanisms of microstructure formation and plastic deformation must be studied and understood.

In this context, the purpose of the present work was to understand the relations between microstructure, mechanical properties, and electromagnetic behavior of carbon steel wires submitted to different thermomechanical treatments. It aimed also at improving the knowledge of the physical and mechanical metallurgy of these steels. The effect of microstructure and plastic deformation on the electromagnetic responses of different steel wires with various tensile strengths was investigated through electrical resistivity measurements down to 2 K and bulk magnetic characterization, as well as by ECT. In addition, magnetic domains could be imaged by magnetic force microscopy despite the complex microstructures.

Electrical conductivity and magnetic permeability were observed to increase in the order of martensite, sorbite, pearlite, proeutectoid ferrite-pearlite, spheroidite, and ferrite microstructures. These variations were mainly related to changes in phase composition, and morphology, size, and distribution of the cementite phase within the α-ferrite matrix. The increase of carbon content in the steel enhances the localization of electrons at the atomic sites, assisting the covalent character of interatomic bonds and thereby reducing the conductivity. The consequent increase of pearlite fraction restricts the proportion of proeutectoid ferrite magnetized in easy directions, which contributes to the magnetic permeability decrease. In addition, phase morphology variations involving increasing total α-Fe_3C interfacial area lead to the increase of

scattering events, reducing the conductive behavior. The α-Fe_3C interfaces that behave as a physical barrier for dislocation slip in ferrite, affect as well as magnetic domain walls displacements within the material. Due to the distinct magnetic properties of the orthorhombic cementite and body-centered cubic ferrite phases, Fe_3C precipitates act as nucleation sites for closure and reverse magnetization domains, altering the energetic interactions of the system. The magnetic domain of carbon steels imaged by MFM demonstrated the pinning strength of pearlite, indicating that Fe_3C lamellae become more effective at pinning as the width of the ferrite band decreases.

The weak conductive and magnetic permeability behavior of martensite is explained by its tetragonal unit cell supersaturated with carbon atoms, the subsequent needle-like morphology, and the high density of dislocations introduced in the lattice by the diffusionless martensitic transformation.

Figure 176 summarizes the main microstructural mechanisms affecting the electrical and magnetic behavior of carbon steels.

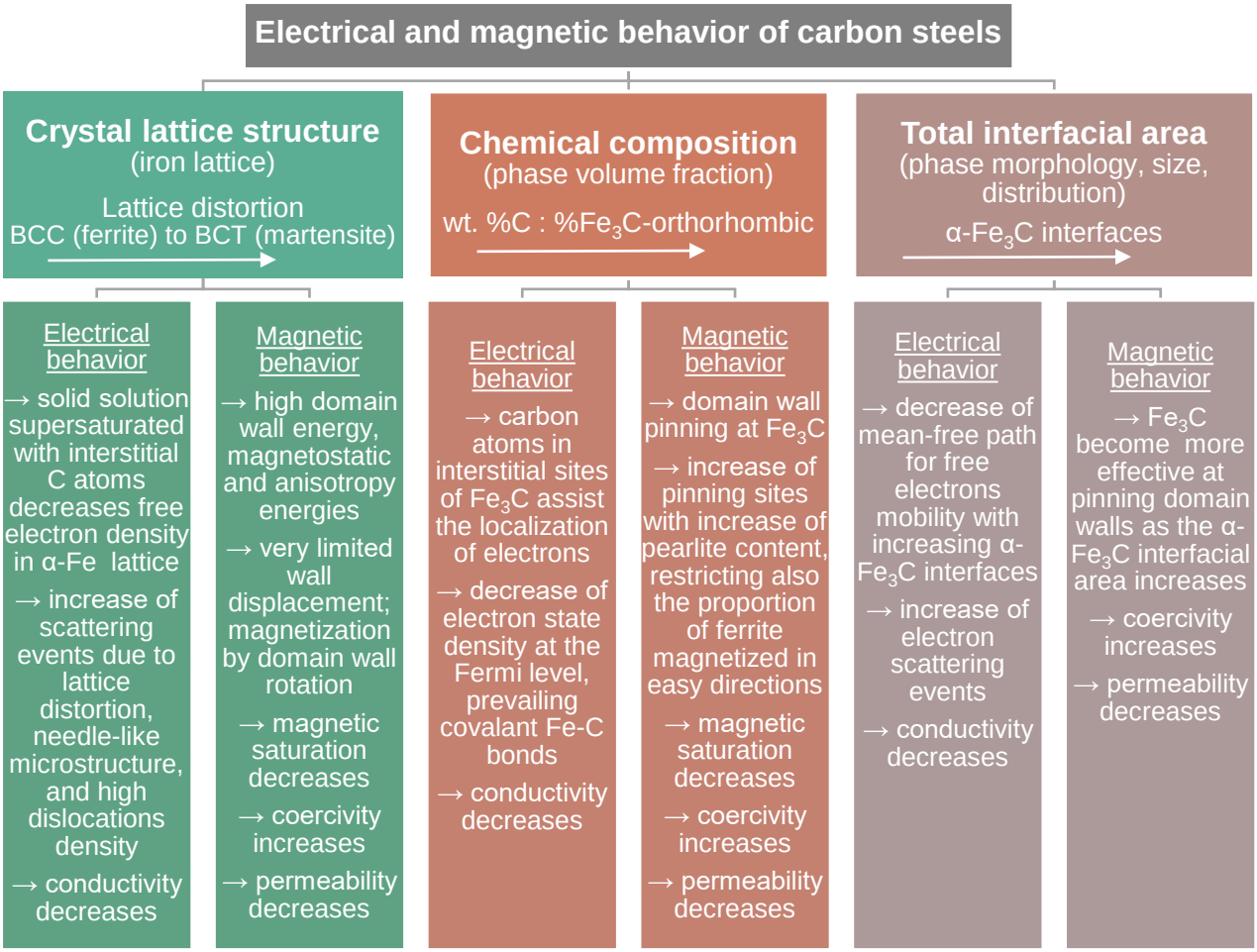

Figure 176: Assessment of the influence of microstructure characteristics on the electrical and magnetic behavior of carbon steels

The comprehension of the mechanisms that affect the electromagnetic behavior of steels allowed to analyze the influence of plastic deformation resulted from the cold-drawing process as well as from in-service applications where fatigue may occur. The strengthening mechanisms responsible for increase the strength of such materials tend to influence at different extents their corresponding electrical and magnetic properties. Also, low-cycle fatigue experiments have pointed out that the resistance can be managed by relevant thermo-mechanical treatments.

The feasibility of using an electromagnetic sensor for the non-destructive evaluation of carbon steel wires was proven. The ECT responses changed according to the electrical conductivity and magnetic permeability characteristic of each material, with respect to their chemical composition, microstructural arrangement, and deformation state.

Figure 177 shows the correlations between the eddy current phase angle with the ultimate tensile strength of the various carbon steel wires submitted to different thermomechanical treatments. The ultimate tensile strength of martensite that could not be directly assessed was estimated based on Vickers hardness characterization.

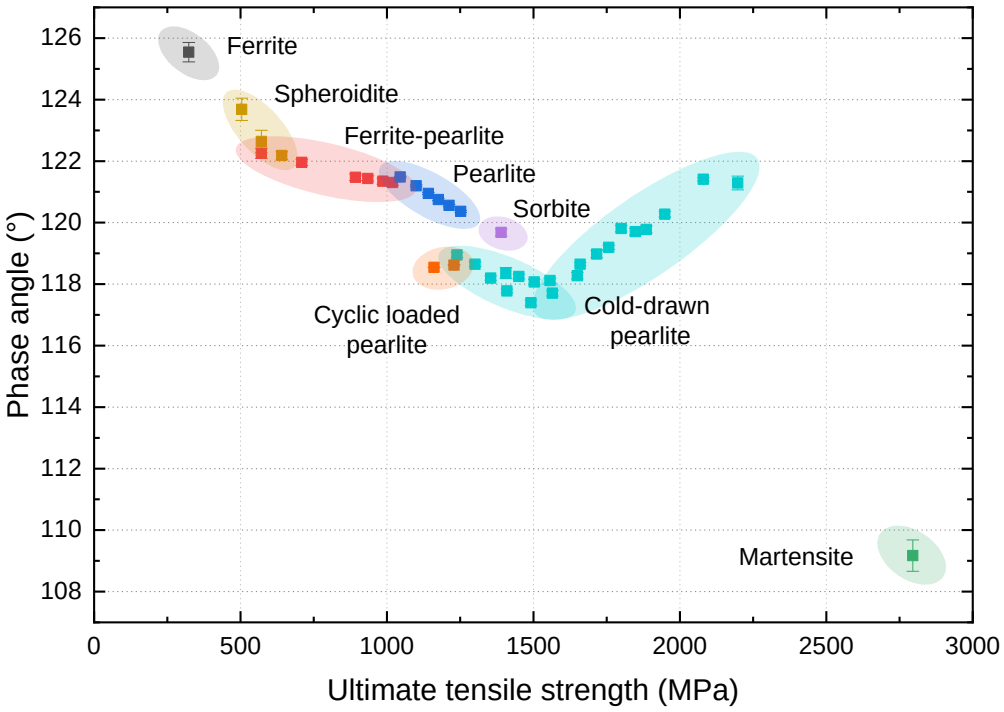

Figure 177: Phase angle variation with the ultimate tensile strength of carbon steel wires after different thermomechanical treatments

The potentiality of ECT was highlighted as an in-situ characterization tool for monitoring wire manufacturing processes stability, providing an accurate evaluation

of the microstructural state and mechanical properties of carbon steels. Good correlations were found between experimental ultimate tensile strengths and predicted values based on ECT outputs of pearlitic steel wires submitted to thermal treatments. Nonetheless, correlations between mechanical and physical properties of plastically deformed pearlitic steels are not straightforward and demand careful interpretation. Finally, the eddy current technique has demonstrated a valuable ability for monitoring cyclic elastic deformation and plastic accommodation of pearlitic steels responding to fatigue-loading conditions.

The perspectives for going even further in the understanding of the phenomena of electromagnetism of plain carbon steels concern a more in-depth investigation of the martensite microstructure in order to better recognize and understand the interactions of dislocations with the micromagnetic microstructure and its influence on the electrical conductivity of these materials. Other complementary topics are the study of the effects of different stages of tempering and the cementite dissolution in cold-drawn pearlitic steel wires in the electromagnetic behavior of steels. Concerning the development of eddy current technique for in-situ characterization of steel wires, assessing of undesirable microstructures such as martensite and bainite by non-destructive means may be the next step. Finally, further exploration can be carried out for the study of microstructure gradients, which can occur during heat-treatment processes, by a multi-frequency eddy current testing, varying the depth of penetration of eddy current into the material.

GRAPHICAL ABSTRACT

Electrical and magnetic behavior of carbon steels

Crystal lattice structure
(iron lattice)

Lattice distortion

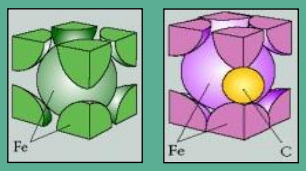

BCC: Ferrite BCT: Martensite

Electrical behavior

→ solid solution supersaturated with interstitial C atoms decreases free electron density in α-Fe lattice

→ increase of scattering events due to lattice distortion, needle-like microstructure, and high dislocations density

→ conductivity decreases

Magnetic behavior

→ high domain wall energy, magnetostatic and anisotropy energies

→ very limited wall displacement

→ magnetization by domain wall rotation

→ magnetic saturation decreases

→ coercivity increases

→ permeability decreases

Chemical composition
(phase volume fraction)

wt. % C : % Fe_3C-orthorhombic

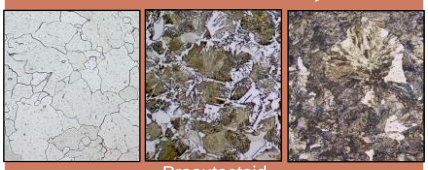

Ferrite | Proeutectoid ferrite-pearlite | Pearlite

Electrical behavior

→ carbon atoms in interstitial sites of Fe_3C assist the localization of electrons

→ decrease of electron state density at the Fermi level, prevailing covalant Fe-C bonds

→ conductivity decreases

Magnetic behavior

→ domain wall pinning at Fe_3C

→ increase of pinning sites with increase of pearlite content, restricting also the proportion of ferrite magnetized in easy directions

→ magnetic saturation decreases

→ coercivity increases

→ permeability decreases

Total interfacial area
(phase morphology, distribution)

α-Fe_3C interfaces

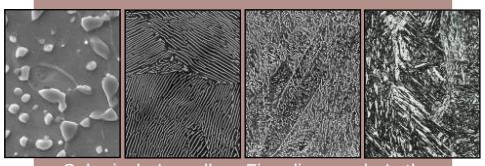

Spherical - Lamellar - Fine dispersed - Lath form precipitates

Electrical behavior

→ decrease of mean-free path for free electrons mobility with increasing α-Fe_3C interfaces

→ increase of electron scattering events

→ conductivity decreases

Magnetic behavior

→ Fe_3C become more effective at pinning domain walls as the α-Fe_3C interfacial area increases

→ coercivity increases

→ permeability decreases

Eddy current testing

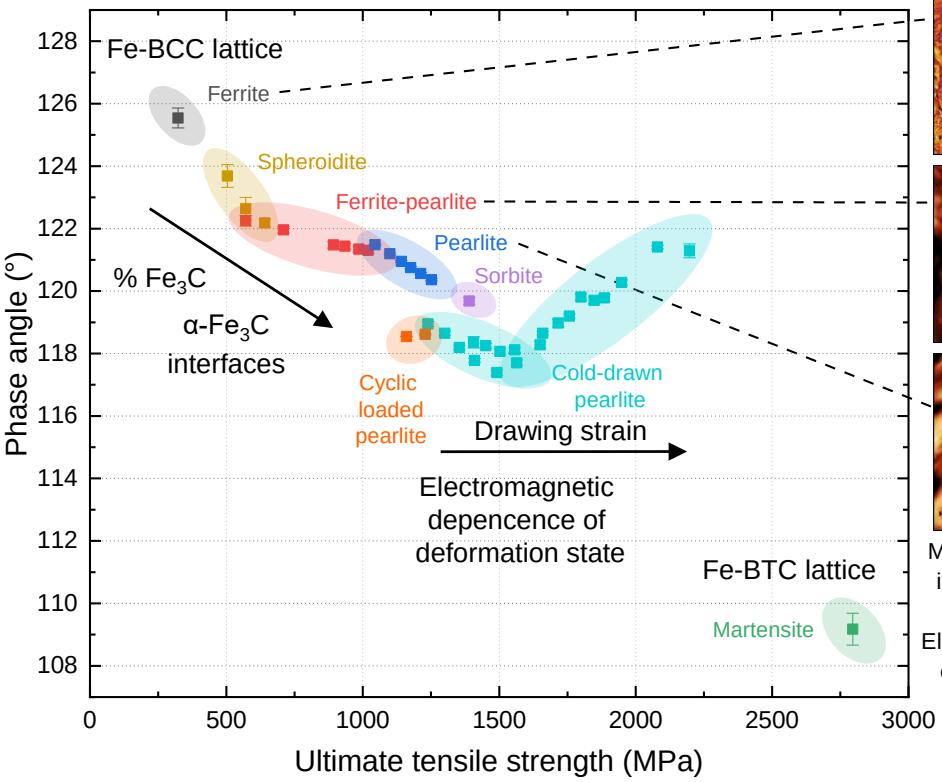

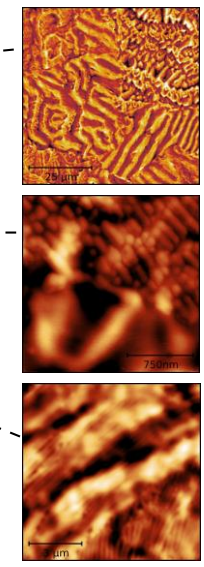

Magnetic domains imaging by MFM

Electrical/ magnetic characterization

BIBLIOGRAPHY

[1] J.D. Cooper, World's longest suspension bridge opens in Japan, ASCE Public Roads. 62 (1998) 32–36. ISSN: 0033-3735

[2] A. Pipinato, Case study: the Akashi-Kaikyō bridge, in: A. Pipinato (Ed.), Innovative Bridge Design Handbook: Construction, Rehabilitation and Maintenance, Elsevier Inc., Amsterdam, NL, 2016, pp. 681–699. DOI:10.1016/B978-0-12-800058-8.00026-8

[3] D. Embury, The formation of pearlite in steels, in: E. Pereloma, D.V. Edmonds (Eds.), Phase Transformations in Steels: Fundamentals and Diffusion-Controlled Transformations, Woodhead Publishing Limited, Oxford, UK, 2012, pp. 276–310. DOI:10.1533/9780857096104.2.276

[4] C. Borchers, R. Kirchheim, Cold-drawn pearlitic steel wires, Progress in Materials Science. 82 (2016) 405–444. DOI:10.1016/j.pmatsci.2016.06.001

[5] Akashi-Kaikyō Bridge, digital photograph, CNN Travel, accessed 4 January 2019, <https://edition.cnn.com/travel/article/suspension-bridges-frightening/index.html>

[6] Cable cross-section of 36,830 individual strands with the 4 km long Akashi-Kaikyō Bridge in the background, digital photograph, Jeffrey Friedl's Blog, accessed 12 May 2020, <http://regex.info/i/JEF_042406.jpg>

[7] D.C. Jiles, Review of magnetic methods for nondestructive evaluation (Part 2), NDT International. 23 (1990) 83-92. DOI:10.1016/0308-9126(90)91892-W

[8] D.C. Jiles, Review of magnetic methods for nondestructive evaluation, NDT International. 21 (1988) 311–319. DOI: 10.1016/0308-9126(88)90189-7

[9] M.K. Devine, The magnetic detection of material properties, Journal of the Minerals, Metals & Materials Society. 44 (1992) 24–30. DOI: 10.1007/BF03223167

[10] G. De Stasio, M. A. Schmitt, S. H. Gellman, Spectromicroscopy at the organic-inorganic interface in biominerals, American Journal of Science. 35 (2005) 673– 686. DOI: 10.2475/ajs.305.6-8.673

[11] W.D. Callister Jr., Materials Science and Engineering: An Introduction, seventh ed., John Wiley & Sons, Inc., New York, USA, 2007. ISBN: 0-471-73696-1

[12] R. Abbaschian, L. Abbaschian, R.E. Reed-Hill, Physical Metallurgy Principles, fourth ed., Cengage Learning, Stamford, USA, 2009. ISBN: 0-495-08254-6

[13] Point defects in crystal structures: interstitial and substitutional atom, vacancy, Frenkel defect, vector image, Wikimedia Commons, accessed 5 October 2018, < https://commons.wikimedia.org/wiki/File:Point_defects_in_crystal_structures.svg>

[14] G. Krauss, Steels: Heat-treatment and Processing Principles, first ed., ASM International, Ohio, USA, 2005. ISBN: 0-87170-817-5

[15] K. Saitoh, Y. Sameshima, M. Takuma, Y. Takahashi, Atomistic simulation of crystal change and carbon diffusion during drawing of pearlitic steel nano-sized wire, Technische Mechanik. 34 (2014) 222–232. DOI: 10.24352/UB.OVGU-2017-064

[16] DoITPoMS – Micrograph Library, light optical microscope images, Department of Materials Science and Metallurgy, University of Cambridge, accessed 15 October 2018, <https://www.doitpoms.ac.uk/miclib/index.php>

[17] C. Zener, Kinetics of the decomposition of austenite, Transactions, American Institute of Mining & Metallurgical Engineers. 167 (1945) 550–595.

[18] M. Hillert, Role of interfacial energy during solidstate phase transformations, Jernkontorets Annaler. 141 (1957) 757–789.

[19] A.N. Kolmogorov, On the statistical theory of crystallization of metals. Izvestia Akademii Nauk USSR - Seria Matematisheskaya. 1 (1937) 355–359.

[20] W.A. Johnson, R.F. Mehl, Reaction kinetics in processes of nucleation and growth, Transactions, American Institute of Mining & Metallurgical Engineers. 135 (1939) 416–442.

[21] M.J. Avrami, Kinetics of phase change, Pt. I – General theory, Journal of Chemical Physics. 7 (1939) 1103–1112.
[22] R.F. Mehl, The structure and rate of formation of pearlite, Metallography, Microstructure, and Analysis. 29 (2015) 423–443. Reprinted from Transactions of the American Society for Metals. 29 (1941) 813–862. DOI: 10.1007/s13632-015-0226-0
[23] H.K.D.H. Bhadeshia, R.W.K. Honeycombe, Steels. Microstructure and Properties, third ed., Butterworth-Heinemann, Oxford, UK, 2006. ISBN: 9780750680844
[24] M. Hillert, The formation of pearlite, in: V.F. Zackay, H.I. Aaronson (Eds.), Decomposition of Austenite by Diffusional Processes, Interscience, New York, USA, 1962, pp. 197–237. DOI: 10.1016/S0036-9748(88)80282-5
[25] R.J. Dippenaar, R.W.K. Honeycombe, The crystallography and nucleation of pearlite, Proceedings of the Royal Society of London, Series A, Mathematical and Physical Sciences. 333 (1973) 455–467. DOI: 10.1098/rspa.1973.0073
[26] M. Pernach, Application of the mixed-mode model for numerical simulation of pearlitic transformation, Journal of Materials Engineering and Performance. 28 (2019) 3136–3148. DOI: 10.1007/s11665-019-04069-0
[27] S. Hamada, D. Sasaki, M. Ueda, H. Noguchi, Fatigue limit evaluation considering crack initiation for lamellar pearlitic steel, Procedia Engineering. 10 (2011) 1467–1472. DOI: 10.1016/j.proeng.2011.04.245
[28] A. Walentek, M. Seefeldt, B. Verlinden, E. Aernoudt, P. Van Houtte, Electron backscatter diffraction on pearlite structures in steel, Journal of Microscopy. 224 (2006) 256–263. DOI: 10.1111/j.1365-2818.2006.01702.x
[29] N. Guo, Q. Liu, Back-scattered electron imaging combined with EBSD technique for characterization of pearlitic steels, Journal of Microscopy. 246 (2012) 221–228. DOI: 10.1111/j.1365-2818.2011.03601.x
[30] A.R. Marder, B.L. Bramfitt, Effect of continuous cooling on the morphology and kinetics of pearlite, Metallurgical Transactions A. 6 (1975) 2009–2014. DOI: 10.1007/BF03161825
[31] F.B. Pickering, B. Garbarz, The effect of transformation temperature and prior austenite grain size on the pearlite colony size in vanadium treated pearlitic steels, Scripta Metallurgica. 21 (1987) 249–253. DOI: 10.1016/0036-9748(87)90207-9
[32] M.M. Aranda, B. Kim, R. Rementeria, C. Capdevila, C. García de Andrés, Effect of prior austenite grain size on pearlite transformation in a hypoeuctectoid Fe-C-Mn steel, Metallurgical and Materials Transactions A. 45 (2014) 1778–1786. DOI: 10.1007/s11661-013-1996-0
[33] H.K.D.H. Bhadeshia, Bainite in Steels. Theory and Practice, third ed., CRC Press, London, UK, 2015. ISBN: 9781909662742
[34] S. B. Singh, Mechanisms of bainite transformation in steels, in: E. Pereloma, D.V. Edmonds (Eds.), Phase Transformations in Steels: Fundamentals and Diffusion-Controlled Transformations, Woodhead Publishing, Cambridge, UK, 2012, pp. 385–416. DOI: 10.1533/9780857096104.3.385
[35] T. Gladman, I.D. McIvor, F.B. Pickering, Some aspects of the structure-property relationships in high-carbon ferrite-pearlite steels, Journal of the Iron and Steel Institute. 210 (1972) 916–930
[36] B. Karlsson, G. Lindén, Plastic deformation of ferrite—pearlite structures in steel, Materials Science and Engineering. 17 (1975) 209–219. DOI: 10.1016/0025-5416(75)90232-3
[37] J.M. Hyzak, I.M. Bernstein, The role of microstructure on the strength and toughness of fully pearlitic steels, Metallurgical Transactions A. 7 (1976) 1217–1224. DOI:10.1007/bf02656606
[38] A.R. Marder, B.L. Bramfitt, The effect of morphology on the strength of pearlite, Metallurgical Transactions A. 7 (1976) 365–372. DOI: 10.1007/BF02642832
[39] D.A. Porter, K.E. Easterling, G.D.W. Smith, Dynamic studies of the tensile deformation and fracture of pearlite, Acta Metallurgica. 26 (1978) 1405–1422. DOI:10.1016/0001-6160(78)90156-6

[40] M. Dollar, I.M. Bernstein, A.W. Thompson, Influence of deformation substructure on flow and fracture of fully pearlitic steel, Acta Metallurgica. 36 (1988) 311–320. DOI: 10.1016/0001-6160(88)90008-9
[41] A.M. Elwazri, P. Wanjara, S. Yue, The effect of microstructural characteristics of pearlite on the mechanical properties of hypereutectoid steel, Materials Science and Engineering A. 404 (2005) 91–98. DOI: 10.1016/j.msea.2005.05.051
[42] H. Yahyaoui, H. Sidhom, C. Braham, A. Baczmanski, Effect of interlamellar spacing on the elastoplastic behavior of C70 pearlitic steel: Experimental results and self-consistent modeling, Materials & Design. 55 (2014) 888–897. DOI: 10.1016/j.matdes.2013.10.062.Strength articles.
[43] Wire Manufacturing Process, digital image, Daeho P&C Co accessed 6 January 2018, <http://www.daehopnc.co.kr/skin/page/process_e.html>
[44] Y. Yamada, Kuwabara T., Materials for Springs, Japan Society of Spring Engineers, Springer, Berlin, Heidelberg, 2007. DOI:10.1007/978-3-540-73812-1
[45] S. Kalpakjian, S.R. Schmid, Manufacturing Engineering Technology, seventh ed., Pearson, New York, USA, 2013. ISBN-10: 0133128741
[46] R.N. Wright, Wire Technology. Process Engineering and Metallurgy, second ed., Butterworth-Heinemann, Oxford, UK, 2016. ISNB: 0128026782
[47] J.G. Wistreich, The Fundamentals of Wire Drawing, Metallurgical Reviews. 3 (1958) 97–141. DOI: 10.1179/mtlr.1958.3.1.97
[48] G.E. Didier, Mechanical Metallurgy, SI metric ed., McGraw-Hill International, London, UK, 1988. ISNB: 0-07-100406-8
[49] S.S. Bargujer, N.M. Suri, R.M. Belokar, Optimization of lead patenting process for high carbon steel wires, Proceedings of the National Academy of Sciences, India Section A: Physical Sciences. 87 (2017) 267–278. DOI: 10.1007/s40010-017-0351-z
[50] S. Tong, Y. von Schirnding, T. Prapamontol, Environmental lead exposure: a public health problem of global dimensions, International Journal of Public Health, World Health Organization. 78 (2000) 1068–1077. PMID: 11019456; PMCID: PMC2560844
[51] X. Luo, K. Chen, G.E. Totten, Fast primary cooling: alternative to lead baths for high-carbon steel wire patenting, Materials Performance and Characterization. 1 (2012) 1–13. DOI: 10.1520/MPC20120006
[52] X.L. George, G.E. Totten, High-carbon steel wire: patenting in lead bath, in: R. Colás, G.E. Totten (Eds.), Encyclopedia of Iron, Steel, and Their Alloys, CRC Press, Boca Raton, USA, 2016, pp.1662–1668. DOI: 10.1081/E-EISA-120048788
[53] C.J. Hellier, Handbook of Nondestructive Evaluation, second ed., McGraw-Hill, New York, USA, 2003. DOI:10.1036/007139947X
[54] Magnetic particle inspection, digital photograph, Sheffield NDT Ltd., accessed 30 April 2020, <http://www.sheff-ndt.com/magnetic-particle-inspection/>
[55] Ultrasonic examination, digital photograph, Yateks, accessed 30 April 2020, <https://yateks.com/what-is-nondestructive-testing/>
[56] J. García-Martín, J. Gómez-Gil, E. Vázquez-Sánchez, Non-destructive techniques based on eddy current testing, Sensors. 11 (2011) 2525–2565. DOI:10.3390/s110302525
[57] C.L. Davis, M. Strangwood, A.J. Peyton, Overview of non-destructive evaluation of steel microstructures using multifrequency electromagnetic sensors, Ironmaking and Steelmaking. 38 (2011) 510-517. DOI: 10.1179/030192311X13135947813816
[58] D.C. Jiles, Magnetic properties and microstructure of AISI 1000 series carbon steels, Journal of Physics D: Applied Physics. 21 (1988) 1186–1195. DOI:10.1016/0308-9126(89)91329-1
[59] S.M. Thompson, B.K. Tanner, The magnetic properties of pearlitic steels as a function of carbon content, Journal of Magnetism and Magnetic Materials. 123 (1993) 283–298. DOI:10.1016/0304-8853(93)90454-A
[60] J.W. Byeon, S.I. Kwun, Magnetic evaluation of microstructures and strength of eutectoid steel, Materials Transactions. 44 (2003) 2184–2190. DOI:10.2320/matertrans.44.2184
[61] A.I. Ul'yanov, E.P. Elsukov, A.A. Chulkina, A.V. Zagainov, N.B. Arsent'eva, G.N.

Konygin, V.F. Novikov, V.V. Isakov, The role of cementite in the formation of magnetic hysteresis properties of plastically deformed high-carbon steels: I. Magnetic properties and structural state of cementite, Russian Journal of Nondestructive Testing. 42 (2006) 452–459. DOI:10.1134/s1061830906070047

[62] S. Kahrobaee, T.-H. Hejazi, A RSM-based predictive model to characterize heat treating parameters of D2 steel using combined Barkhausen noise and hysteresis loop methods, Journal of Magnetism and Magnetic Materials. 433 (2017) 131–140. DOI: 10.1016/j.jmmm.2017.03.015

[63] J. Kameda, R. Ranjan, Non-destructive evaluation of steels using Acoustic and Magnetic Barkhausen signals – I, Effect of carbide precipitates and hardness, Acta Metallurgica. 35 (1987) 1515–1526. DOI: 10.1016/0001-6160(87)90096-4

[64] C.C.H. Lo, C.B. Scruby, G.D. Smith, Dependences of magnetic Barkhausen emission and magnetoacoustic emission on the microstructure of pearlitic steel, Philosophical Magazine. 84 (2004) 1821–1839. DOI: 10.1080/14786430410001663196

[65] O. Saquet, J. Chicois, A. Vincent, Barkhausen noise from plain carbon steels: analysis of the influence of microstructure, Materials Science and Engineering A. 269 (1999) 73–82. DOI:10.1016/s0921-5093(99)00155-0

[66] L. Clapham, C. Jagadish, D. L. Atherton, The influence of pearlite on Barkhausen noise generation in plain carbon steels, Acta Metallurgica et Materialia. 39 (1991) 1555–1562. DOI:10.1016/0956-7151(91)90242-S

[67] V. Moorthy, S. Vaidyanathan, T. Jayakumar, B. Raj, On the influence of tempered microstructure on the magnetic Barkhausen emission in ferritic steels, Philosophical Magazine A. 77 (1998) 1499-1514.DOI: 10.1080/01418619808214266

[68] A. Dhar, L. Clapham, D. L. Atherton, Influence of uniaxial plastic deformation on magnetic Barkhausen noise in steel, NDT&E International. 34 (2001) 507-514. DOI: 10.1016/S0963-8695(00)00079-7

[69] K.M. Koo, M.Y. Yau, D.H.L. Ng, C.C.H. Lo, Characterization of pearlite grains in plain carbon steel by Barkhausen emission, Materials Science and Engineering A. 351 (2003) 310–315. DOI: 10.1016/S0921-5093(02)00859-6

[70] X. Kleber, A. Hug, J. Merlin, M. Soler, Ferrite–martensite steels characterization using magnetic Barkhausen noise measurements, ISIJ International. 44 (2004) 1033–1039. DOI: 10.2355/isijinternational.44.1033

[71] S.P. Sagar, N. Parida, S. Das, G. Dobmann, D.K. Bhattacharya, Magnetic Barkhausen emission to evaluate fatigue damage in a low carbon structural steel, International Journal of Fatigue. 27 (2005) 317–322. DOI:10.1016/j.ijfatigue.2004.06.015

[72] J. Capó Sánchez, M.F. de Campos, L.R. Padovese, Magnetic Barkhausen emission in lightly deformed AISI 1070 steel, Journal of Magnetism and Magnetic Materials. 324 (2012) 11–14. DOI: 10.1016/j.jmmm.2011.07.014

[73] M. Vashista, V. Moorthy, On the shape of the magnetic Barkhausen noise profile for better revelation of the effect of microstructures on the magnetisation process in ferritic steels, Magnetism and Magnetic Materials. 393 (2015) 584–592. DOI: 10.1016/j.jmmm.2015.06.008

[74] L. Batista, U. Rabe, S. Hirsekorn, Magnetic micro- and nanostructures of unalloyed steels: Domain wall interactions with cementite precipitates observed by MFM, NDT&E International. 57 (2013) 58–68. DOI:10.1016/j.ndteint.2013.03.004

[75] L. Batista, U. Rabe, I. Altpeter, S. Hirsekorn, G. Dobmann, On the mechanism of nondestructive evaluation of cementite content in steels using a combination of magnetic Barkhausen noise and magnetic force microscopy techniques, Journal of Magnetism and Magnetic Materials. 354 (2014) 248–256. DOI:10.1016/j.jmmm.2013.11.019

[76] L. Batista, U. Rabe, S. Hirsekorn, Determination of the easy axes of small ferromagnetic precipitates in a bulk material by combined magnetic force microscopy and electron backscatter diffraction techniques, Ultramicroscopy. 146 (2014) 17–26. DOI:10.1016/j.ultramic.2014.05.003

[77] C. L. Davis, M.Ph. Papaelias, M. Strangwood, A. Peyton, Measurement of phase transformation in steels using electromagnetic sensors, Ironmaking and Steelmaking. 29

(2002) 469–476. DOI:10.1179/030192302225004610
[78] R.J. Haldane, W. Yin, M. Strangwood, A.J. Peyton, C.L. Davis, Multi-frequency electromagnetic sensor measurement of ferrite/austenite phase fraction—Experiment and theory, Scripta Materialia. 54 (2006) 1761–1765. DOI:10.1016/j.scriptamat.2006.01.041
[79] M.Ph. Papaelias, M. Strangwood, A.J. Peyton, C.L. Davis, Effect of microstructural variations on smart inductive sensor measurements of phase transformation in steel, Scripta Materialia. 51 (2004) 379–383. DOI:10.1016/j.scriptamat.2004.05.019
[80] D. Mercier, J. Lesage, X. Decoopman, D. Chicot, Eddy currents and hardness testing for evaluation of steel decarburizing, NDT&E International. 39 (2006) 652–660. DOI:10.1016/j.ndteint.2006.04.005
[81] X.J. Hao, W. Yin, M. Strangwood, A.J. Peyton, P.F. Morris, C.L. Davis, Off-line measurement of decarburization of steels using a multifrequency electromagnetic sensor, Scripta Materialia. 58 (2008) 1033–1036. DOI:10.1016/j.scriptamat.2008.01.042
[82] X.J. Hao, W. Yin, M. Strangwood, A.J. Peyton, P.F. Morris, C.L. Davis, Characterization of decarburization of steels using a multifrequency electromagnetic sensor: Experiment and modeling, Metallurgical and Materials Transactions A. 40 (2009) 745–756. DOI: 10.1007/s11661-008-9776-y
[83] S. Ghanei, M. Kashefi, M. Mazinani, Comparative study of eddy current and Barkhausen noise nondestructive testing methods in microstructural examination of ferrite–martensite dual-phase steel, Journal of Magnetism and Magnetic Materials. 356 (2014) 103–110. DOI: 10.1016/j.jmmm.2014.01.001
[84] F. Rumiche, J.E. Indacochea, M.L. Wang, Assessment of the effect of microstructure on the magnetic behavior of structural carbon steels using an electromagnetic sensor, Journal of Materials Engineering and Performance. 17 (2008) 586–593. DOI: 10.1007/s11665-007-9184-2
[85] S. Konoplyuk, Estimation of pearlite fraction in ductile cast irons by eddy current method, NDT & E International. 43 (2010) 360–364. DOI: 10.1016/j.ndteint.2010.01.001
[86] L. Zhou, J. Liu, X.J. Hao, M. Strangwood, A.J. Peyton, C.L. Davis, Quantification of the phase fraction in steel using an electromagnetic sensor, NDT&E International. 67 (2014) 31–35. DOI:10.1016/j.ndteint.2014.06.007
[87] S. Balamurugan, T. Bhattacharyya, D. Gudhae, L. Zhou, C.L. Davis, A.J. Peyton, S. Chandra, Prediction of interlamellar pearlite spacing of tyre bead wires after patenting using electromagnetic techniques, Insight: Non-Destructive Testing and Condition Monitoring. 55 (2013) 132–135. DOI: 10.1784/insi.2012.55.3.132
[88] M. Mansoor, N. Ejaz, Prediction of in-service microstructural degradation of A106 steel using eddy current technique, Materials Characterization. 60 (2009) 1591–1596. DOI:10.1016/j.matchar.2009.09.011
[89] K. Davut, C.H. Gur, Monitoring the microstructural evolution in spheroidized steels by magnetic Barkhausen noise measurements, Journal of Nondestructive Evaluation. 29 (2010) 241–247. DOI 10.1007/s10921-010-0082-4
[90] J.N. Mohapatra, Y. Kamada, Magnetic hysteresis loop as a tool for the evaluation of spheroidization of cementite in pearlitic steels, Journal of Materials Engineering and Performance. 24 (2015) 1551–1557. DOI: 10.1007/s11665-015-1385-5
[91] S. Konoplyuk S, T. Abe, T. Uchimoto, T. Takagi, M. Kurosawa, Characterization of ductile cast iron by eddy current method, NDT & E International. 38 (2005) 623–626. DOI: 10.1016/j.ndteint.2005.02.008
[92] E.S. Gorkunov, S.V. Grachev, S.V. Smirnov, V.M. Somova, S.M. Zadvorkin, L.E. Kar'kina, Relation of physical–mechanical properties to the structural condition of severely deformed patented carbon steels at drawing, Russian Journal of Nondestructive Testing. 41 (2005) 65–79. DOI:10.1007/s11181-005-0131-8
[93] S. Kahrobaee, M. Kashefi, Hardness profile plotting using multi-frequency multi-output electromagnetic sensor, NDT&E International. 44 (2011) 335–338.

DOI:10.1016/j.ndteint.2011.01.005
[94] S. Ghanei, M. Kashefi, M. Mazinani, Eddy current nondestructive evaluation of dual phase steel, Materials and Design. 50 (2013) 491–496. DOI:10.1016/j.matdes.2013.03.040
[95] Amber, digital photograph, Colored Gemstones Guide, accessed 11 March 2020, <http://www.gemstones-guide.com/Amber.html>
[96] R.M. Rose, L.A. Shepard, J. Wulff, The Structure ad Properties of Materials. Volume IV: Electronic Properties, first ed., John Wiley & Sons Inc., New York, USA, 1966. ISBN-10 : 0471106100; ISBN-13 : 978-0471106104
[97] B. Averill, P. Eldredge, General Chemistry: Principles, Patterns, and Applications, Saylor Foundation, Washington, USA, 2011. ISBN 13: 9781453322307
[98] Shapes of s, p, d, and f orbitals, digital image, Oregon Institute of Technology, Chemistry LibretTexts, accessed 18 December 2019, <https://chem.libretexts.org/Courses/Oregon_Institute_of_Technology/OIT%3A_CHE_202_-_General_Chemistry_II >
[99] D. Jiles, Introduction to the Electronic Properties of Materials, second ed., Nelson Thornes Ltd., Cheltenham, UK, 2001. ISBN: 0-7487-6042-3
[100] Electronic band structure, vector image, Wikimedia Commons, accessed 8 Avril 2019, <https://en.wikipedia.org/wiki/Band_gap#/media/File:Solid_state_electronic_band_structure.svg>
[101] Lodestone rocks, digital photograph, Fossilera, accessed 12 January 2020, <https://assets0.fossilera.com/pi/1866/708x500%3E/bulk-magnetic-lodestone-magnetite-5-pieces.jpg>
[102] Naturally magnetic lodestone rock, digital photograph, Bandcamp, accessed 12 January 2020, <https://f4.bcbits.com/img/a1885700589_16.jpg>
[103] A. Hubert, R. Schäfer, Magnetic Domains: The Analysis of Magnetic Microstructures, first ed., Springer-Verlag Berlin Heidelberg, 1998. DOI: 10.1007/978-3-540-85054-0
[104] Magnetic domains behavior at demagnetized state and under applied magnetic field, digital photograph, Skulls in the Stars, accessed 15 January 2020, <https://skullsinthestars.files.wordpress.com/2012/10/domainwallmotion.jpg>
[105] A. Privat-Deschanel, Elementary Treatise on Natural Philosophy, Part 3: Electricity and Magnetism, D. Appleton and Co., New York, USA, 1876, pp. 656.
[106] Electromagnetic induction, digital image, accessed 12 January 2020, <https://d3jc3ahdjad7x7.cloudfront.net/SmjPU75VvfgfSBZcRrEuL0dHnZpZJBvKjcITXdwM1ujmQeQa.pdf>
[107] N. Jain, The rebirth of eddy current non-destructive testing, Quality magazine, acessed 15 January 2020, <https://www.qualitymag.com/articles/92056-the-rebirth-of-eddy-current-nondestructive-testing>
[108] NDT Supply.com, Inc., Technical Manual: Nondestructive Inspection Methods, Basic Theory, 2010.
[109] D.E.T. de Aguiam (2013). Heterodyning non destructive testing electronic system based on eddy currents (unpublished master's thesis). Instituto Superior Técnico, Universidade de Lisboa, Lisboa, Portugal.
[110] G.F. Vander Voort, Metallography, Principles and Practice, first ed., ASM International, New York, USA, 1999. ISBN: 978-0-87170-672-0
[111] L.B. Bramfitt, O.A. Benscoter, Metallographer’s guide: Practices and procedures for irons and steels, ASM International, 2002. ISBN: 978-0-87170-748-2
[112] ASTM E112-13 Standard test methods for determining average grain size, ASTM International, West Conshohocken, PA, 2013.
[113] G.F.V. Voort, A. Róosz, Measurement of the Interlamellar Spacing of Pearlite, Metallography. 17 (1984) 1–17.
[114] O. Idigoras, E. Nikulina, J. M. Porro, P. Vavassori, A. Chuvilin, A. Berger, FEBID fabrication and magnetic characterization of individual nano-scale and micro-scale Co structures, Nanofabrication. 1(2014) 23-34. DOI: 10.2478/nanofab-2014-0003
[115] Measurement quality, image, NDT Resource Center, accessed 11 January 2019,

<https://www.nde-ed.org/GeneralResources/Measurement/MeasurementQuality.gif>
[116] D.C. Montgomery, Design and Analysis of Experiments, eighth ed., John Wiley & Sons, Inc., USA, 2013. ISBN: 978-1-118-09793-9
[117] J.P. Houin, A. Simon and G. Beck. Relationship between structure and mechanical properties of pearlite between 0.2% and 0.8%C. Transactions ISIJ. 1981, 2, 731. DOI: 10.2355/isijinternational1966.21.726
[118] D.C. Jiles. Introduction to Magnetism and Magnetic Materials. 2nd ed. Chapman and Hall, New York, USA. 1991, 179-191. DOI: 10.1007/978-1-4615-3868-4
[119] E.J. Fasiska, G.A. Jeffrey, On the cementite structure, Acta Crystallographica. 19 (1965) 463–471. DOI:10.1107/S0365110X65003602
[120] H.K.D.H. Bhadeshia, Cementite, International Materials Reviews. 65 (2019) 1–27. DOI: 10.1080/09506608.2018.1560984
[121] J. Häglund, G. Grimvall, Electronic structure, x-ray photoemission spectra, and transport properties of Fe_3C (cementite), Physical Review B. 44 (1991) 2914–2919. DOI:10.1103/physrevb.44.2914
[122] W.C. Chiou Jr., E.A. Carter, Structure and stability of Fe_3C-cementite surfaces from first principles, Surface Science. 530 (2003) 87–100. DOI:10.1016/S0039-6028(03)00352-2
[123] H.I. Faraoun, Y.D. Zhang, C. Esling, H. Aourag, Crystalline, electronic, and magnetic structures of θ-Fe_3C, χ-Fe_5C_2, and η-Fe_2C from first principle calculation, Journal of Applied Physics. 99 (2006) 1–8. DOI:10.1063/1.2194118
[124] V.I. Razumovskiy, G. Ghosh, A first-principles study of cementite (Fe_3C) and its alloyed counterparts: Structural properties, stability, and electronic structure, Computational Materials Science. 110 (2015) 169–181. DOI:10.1016/j.commatsci.2015.08.006
[125] A.H. Cottrell, A theory of cementite, Materials Science and Technology. 9 (1993) 277–280. DOI:10.1179/mst.1993.9.4.277
[126] C. Jiang, S.G. Srinivasan, A. Caro, S.A. Maloy, Structural, elastic, and electronic properties of Fe_3C from first principles, Journal of Applied Physics. 103 (2008) 1–29. DOI:10.1063/1.2884529
[127] B.D. Shanina, V.G. Gavriljuk, Effect of carbon and nitrogen on electronic structure of steel, Steel Grips. 2 (2004) 45–52.
[128] V.G. Gavriljuk, V.N. Shivanyuk, B.D. Shanina, Change in the electron structure caused by C, N and H atoms in iron and its effect on their interaction with dislocations, Acta Materialia. 53 (2005) 5017–5024. DOI: 10.1016/j.actamat.2005.07.028
[129] D.P.H. Hasselman, L.F. Johnson, Effective thermal conductivity of composites with interfacial thermal barrier resistance, Journal of Composite Materials. 21 (1987) 508–515. DOI:10.1177/002199838702100602
[130] J.K. Chen, S.F. Chen, Thermal conductivity of an in-situ metal matrix composite - Cast iron, in: John Cuppoletti (Eds.) Metal, Ceramic and Polymeric Composites for Various Uses, IntechOpen , 2011, pp. 211–224. DOI:10.5772/21537
[131] A. Hubert, R. Schäfer, Magnetic Domains: The Analysis of Magnetic Microstructures, third ed., Springer Science & Business Media, New York, USA, 2008. ISBN: 978-3-540-85054-0
[132] M.L. Néel, Nouvelle théorie du champ coercitif, Physica. 15 (1949) 225–234. DOI: 10.1016/0031-8914(49)90047-6
[133] J. Abuthahir, A. Kumar, Magnetic force microscopy studies in bulk polycrystalline iron, Journal of Magnetism and Magnetic Materials. 448 (2018) 107–116 10.1016/j.jmmm.2017.06.107
[134] L.Q. Guo, X.M. Zhao, M. Li, W.J. Zhang, Y. Bai, L.J. Qiao, Annealing effects on the microstructure and magnetic domain structures of duplex stainless steel studied by in situ technique, Applied Surface Science. 259 (2012) 213–218 10.1016/j.apsusc.2012.07.021
[135] M. Gallaugher, N. Brodusch, R. Gauvin, R.R. Chromik, Magnetic domain structure and crystallographic orientation of electrical steels revealed by a forescatter detector and electron backscatter diffraction, Ultramicroscopy. 142 (2014) 40–49. DOI: 10.1016/j.ultramic.2014.03.013

[136] J.B. Goodenough, A theory of domain creation and coercive force in polycrystalline ferromagnetics, Physical Review Journal. 95 (1954) 917–932. DOI:10.1103/PhysRev.95.917.
[137] A.G. Tobin, D.I. Paul, Stability of ferromagnetic domain structures at grain boundaries, Journal of Applied Physics. 40 (1969) 3611–3614. DOI:10.1063/1.1658244
[138] M.G. Hetherington, J.P. Jakubovics, J.A. Szpunar, B.K. Tanner, High-voltage Lorentz electron-microscopy studies of domain-structures and magnetization processes in pearlitic steels, Philosophical Magazine B. 56 (1987) 561–577. DOI:10.1080/13642818708220163
[139] B.K. Tanner, J.A. Szpunar, S.N.M. Willcock, L.L. Morgan, P.A. Mundell, Magnetic and metallurgical properties of high-tensile steels, Journal of Materials Science. 23 (1988) 4534-4540. DOI: 10.1007/BF00551956
[140] S.G. Sandomirskii, Analysis of the structural and phase sensitivity of the relaxation magnetization of steels, Russian Metallurgy (Metally). 3 (2011) 248–252. DOI: 10.1134/S0036029511030153
[141] S.G. Sandomirskii, Structural and phase sensitivity of the maximum differential magnetic susceptibility of steel, Russian Metallurgy (Metally). 7 (2016) 619–624. DOI: 10.1134/S0036029516070144
[142] S. Klein, L. Mujica Roncery, M. Walter, S. Weber, W. Theisen, Diffusion processes during cementite precipitation and their impact on electrical and thermal conductivity of a heat-treatable steel, Journal of Materials Science. 52 (2017) 375–390. DOI:10.1007/s10853-016-0338-1
[143] O. SAQUET. (1997) Caractérisation des aciers par bruit Barkhausen (interaction microstructure cristalline/microstructure magnétique) : optimisation de la mise en œuvre pour un développement industriel : Application au contrôle des traitements superficiels. Institut National des Sciences Appliquées de Lyon, France.
[144] A.D. Beale, J.P. Jakubovics, M.G. Hetherington, C.B. Scruby, B.A. Lewis, K.J. Davies, TEM studies of domains and micromagnetic processes in structural steels, Journal of Magnetism and Magnetic Materials. 104 (1992) 365–367. DOI: 10.1016/0304-8853(92)90836-D
[145] J.D. Embury, R.M. Fisher, The structure and properties of drawn pearlite, Acta Metallurgica. 14 (1966) 147–159. DOI: 10.1016/0001-6160(66)90296-3
[146] J. Toribio, Relationship between microstructure and strength in eutectoid steels, Materials Science and Engineering A. 387–389 (2004) 227–230. DOI:10.1016/j.msea.2004.01.084
[147] X. Zhang, A. Godfrey, X. Huang, N. Hansen, Q. Liu, Microstructure and strengthening mechanisms in cold-drawn pearlitic steel wire, Acta Materialia. 59 (2011) 3422–3430. DOI: 10.1016/j.actamat.2011.02.017
[148] M. Zelin, Microstructure evolution in pearlitic steels during wire drawing. Acta Materialia. 50 (2002) 4431–4447. DOI: 10.1016/S1359-6454(02)00281-1
[149] G. Langford, A study of the deformation of patented steel wire, Metallurgical Transactions A. 2 (1970) 65–77. DOI: 10.1007/BF02811557
[150] G. Langford, Deformation of pearlite, Metallurgical Transactions A. 8 (1977) 861–875. DOI: 10.1007/BF02661567
[151] N. Guo, B. Luan, B. Wang, Q. Liu, Microstructure and texture evolution in fully pearlitic steel during wire drawing, Science China Technological Sciences. 56 (2013) 1139–1146. DOI: 10.1007/s11431-013-5184-7
[152] F. Fang, Y. Zhao, L. Zhou, X. Hu, J. Jiang, Texture inheritance of cold drawn pearlite steel wires after austenitization, Materials Science and Engineering: A. 618 (2014) 618:505–510. DOI: dx.doi.org/10.1016/j.msea.2014.09.061
[153] W.F. Hosford, Microstructural changes during deformation of [011] fiber-textured Metals, Transactions of the Metallurgical Society of AlME. 230 (1964) 12–15.
[154] J. Toribio, E. Ovejero, Effect of cumulative cold drawing on the pearlite interlamellar spacing in eutectoid steel, Scripta Materialia. 39 (1998) 323–328. DOI: 10.1016/S1359-6462(98)00166-3

[155] X. Zhang, A. Godfrey, N. Hansen, X. Huang, W. Liu, Q. Liu, Evolution of cementite morphology in pearlitic steel wire during wet wire drawing, Materials Characterization. 61 (2010) 65–72. DOI: 10.1016/j.matchar.2009.10.007
[156] N. Guo, B. Song, B. Luan, Z. Chen, Q. Liu, Deformation bands in fully pearlitic steel during wire drawing, Science China Technological Sciences. 57 (2014) 796–803. DOI: 10.1007/s11431-013-5434-8
[157] T. Teshima, M. Kosaka, K. Ushioda, N. Koga, N. Nakada, Local cementite cracking induced by heterogeneous plastic deformation in lamellar pearlite, Materials Science & Engineering A. 679 (2017) 223–229. DOI:10.1016/j.msea.2016.10.018.
[158] X. Zhang, A. Godfrey, N. Hansen, X. Huang, Hierarchical structures in cold-drawn pearlitic steel wire, Acta Materialia. 61 (2013) 4898–4909. DOI: dx.doi.org/10.1016/j.actamat.2013.04.057
[159] M. Umemoto, Z.G. Liu, H. Takaoka, M. Sawakami, K. Tsuchiya, K. Masuyama, Production of bulk cementite and its characterization, Metallurgical and Materials Transactions A. 32 (2001) 2127-2131. DOI: 10.1007/s11661-001-0024-y
[160] X. Zhang, N. Hansen, A. Godfrey, X. Huang, Dislocation-based plasticity and strengthening mechanisms in sub-20 nm lamellar structures in pearlitic steel wire, Acta Materialia. 114 (2016) 176–183. DOI: dx.doi.org/10.1016/j.actamat.2016.04.040
[161] Y.J. Li, P. Choi, C. Borchers, S. Westerkamp, S. Goto, D. Raabe, R. Kirchheim, Atomic-scale mechanisms of deformation-induced cementite decomposition in pearlite, Acta Materialia. 59 (2011) 3965–3977. DOI: 10.1016/j.actamat.2011.03.022
[162] V.G. Gavriljuk, Decomposition of cementite in pearlitic steel due to plastic deformation, Materials Science and Engineering A. 345 (2003) 81–89. PII: S0921-5093(02)00358-1
[163] W.J. Nam, C.M. Bae, S.J. Oh, S.-J. Kwon, Effect of interlamellar spacing on cementite dissolution during wire drawing of pearlitic steel wires, Scripta Materialia. 42 (2000) 457–463. DOI:10.1016/S1359-6462(99)00372-3
[164] V.G. Gavriljuk, Comment on "Effect of interlamellar spacing on cementite dissolution during wire drawing of pearlitic steel wires", Scripta Materialia. 45 (2001) 1469–1472. DOI:10.1016/S1359-6462(01)01185-X
[165] Y. Yang, J. Nie, Q. Mao, Y. Zhao, Improving the combination of electrical conductivity and tensile strength of Al 1070 by rotary swaging deformation, Results in Physics. 13 (2019) 102236. DOI: 10.1016/j.rinp.2019.102236
[166] X.M. Luo, Z.M. Song, M.L. Li, Q. Wang, G.P. Zhang, Microstructural evolution and service performance of cold-drawn pure aluminum conductor wires, Journal of Materials Science & Technology. 33 (2017) 1039-1043. DOI: 10.1016/j.jmst.2016.11.018
[167] M. Alberteris Campos, J.Capó-Sánchez, J. Pérez Benítez, L.R. Padovese, Characterization of the elastic–plastic region in AISI/SAE 1070 steel by the magnetic barkhausen noise, NDT & E International. 41 (2008) 656–659. DOI: 10.1016/j.ndteint.2008.03.003
[168] S. Chen, J. Butler, S. Melzer, Effect of asymmetric hot rolling on texture, microstructure and magnetic properties in a non-grain oriented electrical steel, Journal of Magnetism and Magnetic Materials, 368 (2014) 342–352. DOI: 10.1016/j.jmmm.2014.05.054
[169] T.-W. Shyr, S.-J. Huang, C.-S. Wur, Magnetic anisotropy of ultrafine 316L stainless steel fibers, Journal of Magnetism and Magnetic Materials. 419 (2016) 400–406. DOI: 10.1016/j.jmmm.2016.06.047
[170] Y. He, E.J.Hilinski, Skew rolling and its effect on the deformation textures of non-oriented electrical steels, Journal of Materials Processing Technology. 242 (2017) 182–195. DOI: 10.1016/j.jmatprotec.2016.11.033
[171] S. Dutta, A.K. Panda, S. Chatterjee, R.K. Roy, Effect of annealing treatment on magnetic texture of cold rolled ULC steel, Materials Letters. 276 (2020) 128211. DOI: 10.1016/j.matlet.2020.128211
[172] A.I. Ul'yanov, A.A. Chulkina, Magnetic properties of cementite and the coercive force of carbon steels after plastic deformation and annealing, The Physics of Metals and Metallography. 107 (2009) 439–448. DOI: 10.1134/S0031918X09050044

[173] A.A. Chulkina, A.I. Ul'yanov, N.B. Arsent'eva, A.V. Zagainov, E.S. Gorkunov, S.M. Zadvorkin, V.M. Somova, The role of cementite in the formation of magnetic hysteresis properties of plastically deformed high-carbon steels: II. Magnetic properties of patented wire made of steel 70, Russian Journal of Nondestructive Testing. 42 (2006) 460–467. DOI: 10.1134/S1061830906070059
[174] W. Yin, X.J. Hao, A.J. Peyton, M. Strangwood, C.L. Davis, Measurement of permeability and ferrite/austenite phase fraction using a multi-frequency electromagnetic sensor, NDT&E International. 42 (2009) 64–68. DOI: 10.1016/j.ndteint.2008.01.009
[175] C.L. Davis, M. Strangwood, A.J. Peyton, Overview of non-destructive evaluation of steel microstructures using multifrequency electromagnetic sensors, Ironmaking and Steelmaking. 38 (2011) 510-514. DOI: 10.1179/030192311X13135947813816
[176] J. Toribio, V. Kharin, F.-J. Ayaso, M. Lorenzo, B. González, J.-C. Matos, L. Aguado, Analysis of the Bauschinger effect in cold drawn pearlitic steels, Metals. 10 (2020) 114. DOI:10.3390/met10010114
[177] S.S. Manson, Behaviour of materials under cyclic stress, NACA TN 2933, 1953.
[178] L.F. Coffin Jr., A study of the effects of cyclic stresses on a ductile metal, Trans ASME. 1954.
[179] O.H. Basquin, The exponential law of endurance tests, Proceedings of the ASTMJ. 10 (1910) 625-630.
[180] K. Golos, F. Ellyin, A total strain energy density theory for cumulative fatigue damage, ASME Journal of Pressure Vessel Technology. 110 (1988) 36-41. DOI: 10.1115/1.3265565
[181] S.-T. Tu, X.-C. Zhang, Fatigue Crack Initiation Mechanisms Reference Module in Materials Science and Materials Engineering, 2016. DOI:10.1016/B978-0-12-803581-8.02852-6
[182] Ł. Pejkowski, M. Karuskevich, T. Maslak, Extrusion/intrusion structure as a fatigue indicator for uniaxial and multiaxial loading, Fatigue & Fracture of Engineering Materials & Structures. 42 (2019) 1–10. DOI: 10.1111/ffe.13066
[183] U. Essmann, U. Gosele, H. Mughrabi, A model of extrusions and intrusions in fatigued metals l. point-defect production and the growth of extrusions. Philos Mag A. 44 (1981) 405–26. DOI: 10.1080/01418618108239541
[184] J. Polak, J. Man, Experimental evidence and physical models of fatigue crack initiation, International Journal of Fatigue. 91 (2016) 294–303. DOI: 10.1016/j.ijfatigue.2016.02.021
[185] J. Polak, J. Man, Mechanisms of extrusion and intrusion formation in fatigued crystalline materials, Materials Science and Engineering: A. 596 (2014) 15–24. DOI: 10.1016/j.msea.2013.12.005
[186] J.-B. Vogt, S. Argillier, J.-P. Massoud, V. Prunier, Fatigue damage evaluation of a power plant component from analysis of the dislocation structures, Engineering Failure Analysis. 7 (2000) 301–310. DOI: 10.1016/S1350-6307(99)00034-5
[187] K. Kanazawa, K. Yamaguchi, K. Kobayashi, The temperature dependence of low cycle fatigue behaviour of martensitic stainless steels, Materials Science and Engineering. 40 (1979) 89–96. DOI: 10.1016/0025-5416(79)90011-9
[188] G. Seidametova, J.-B. Vogt, I. Proriol Serre, The early stage of fatigue crack initiation in a 12%Cr martensitic steel, International Journal of Fatigue. 106 (2018) 38–48. DOI: 10.1016/j.ijfatigue.2017.09.006
[189] F. Fang, Y. Zhao, P.P. Liu, L. Zhou, X.-J. Hu, X. Zhou, Z.-H. Xie, Deformation of cementite in cold drawn pearlitic steel wire, Materials Science and Engineering: A. 608 (2014) 11–15. DOI: 10.1016/j.msea.2014.04.050
[190] R. Chen, B. Li, Y. Lib, Z. Liu, X. Long, H. Yi, X. Wang, C. Jiang, M. Huang, Revealing the fatigue crack initiation mechanism of a TiB2-reinforced steel matrix composite, International Journal of Fatigue. 130 (2020) 105276. DOI: 10.1016/j.ijfatigue.2019.105276
[191] B. Bohacova, Methodology of short fatigue crack detection by the eddy current method

in a multi-layered metal aircraft structure, Engineering Failure Analysis. 35 (2013) 597-608. DOI: doi.org/10.1016/j.engfailanal.2013.06.009

[192] B. Wincheski, F. Yu, J. Simpon, P. Williams, K. Rackow, Development of SDT sensor based eddy current probe for detection of deep fatigue cracks in multi-layer structure, NDT & E International. 43 (2010) 718-725. DOI: doi.org/10.1016/j.ndteint.2010.08.005

[193] R.A. Savrai, A.V. Makarov, E.S. Gorkunov, L.Kh. Kogan, Eddy-current testing of the fatigue degradation of a surface hardened medium-carbon structural steel, Materials Characterization - ElectroMagnetic Techniques, European Conference on Non-Destructive Testing, 2018.

[194] M. Potthoff, J. Peterseim, W. Thale, Monitoring of low cycle fatigue damage with eddy current, Material Properties, World Conference on Non-Destructive Testing, 2016.

[195] S.M. Thompson, B.K. Tanner, The magnetic properties of specially prepared pearlitic steels of varying carbon content as a function of plastic deformation, Journal of Magnetism and Magnetic Materials. 132 (1994) 71-88. DOI: 10.1016/0304-8853(94)90302-6

[196] A. Esin, W.J.D. Jones, The effect of strain on the a.c. resistance of a metal: a method of studying microplasticity, British Journal of Applied Physics. 9 (1967) 1251–1256. DOI:10.1088/0508-3443/18/9/304

[197] I.Ľ. Gajdoš, I.M. Šperl, J. Kaiser, V. Mentl, Microplastic limit of steels as a means of fatigue limit determination, Procedia Engineering. 66 (2013) 635–642. DOI:10.1016/j.proeng.2013.12.115

[198] A. Abel, H. Muir, The Bauschinger effect and discontinuous yielding, Philosophical Magazine. 26 (1972) 489–504. DOI: 10.1080/14786437208227444

[199] L.M. Brown, Orowan's explanation of the Bauschinger effect, Scripta Metallurgica. 11 (1977) 127–131. DOI:10.1016/0036-9748(77)90291-5

[200] R. Sowerby, D.K. Uko, Y. Tomita, A review of certain aspects of the Bauschinger effect in metals, Materials Science and Engineering. 41(1979) 43–58. DOI:10.1016/0025-5416(79)90043-0

[201] A.G. Kostryzhev, M. Strangwood, C.L. Davis, Bauschinger effect in microalloyed steels: Part I. Dependence on dislocation-particle interaction. Metallurgical and Materials Transactions A, 41 (2010), 1399–1408. DOI:10.1007/s11661-010-0196-4

Relations entre la microstructure, les propriétés mécaniques et électromagnétiques de fils d'acier au carbone traités thermomécaniquement

RÉSUMÉ : La perlite est un constituant de nombreuses nuances d'acier à haute résistance utilisées dans des applications industrielles qui exigent une bonne combinaison de résistance mécanique et de ductilité. Avec les exigences croissantes de qualité des produits et de fiabilité en service, le contrôle non destructif des matériaux permet une évaluation non destructive de leurs propriétés dont les méthodes électromagnétiques, y compris les essais par courants de Foucault (CF). Cependant, l'influence des paramètres microstructuraux sur les propriétés physiques mesurées indirectement par un capteur électromagnétique n'est pas encore complètement élucidée. Le but du présent travail est de comprendre les relations entre microstructure, propriétés mécaniques et comportement électromagnétique de fils d'acier au carbone soumis à différents traitements thermomécaniques. Il vise aussi à améliorer les connaissances en métallurgie physique et mécanique de ces aciers. L'effet des microstructures et de la déformation plastique sur le comportement physique de différents fils d'acier de résistances mécaniques distincts a été étudié à travers de mesures de résistivité jusqu'à 2 K et caractérisations magnétiques, et de contrôle par CF. De plus, les domaines magnétiques ont pu être imagés par microscopie à force magnétique en dépit de microstructures complexes. Les réponses électromagnétiques ont été impactés par des variations de conductivité électrique et de perméabilité magnétique typiques de chaque matériau, principalement liées aux différentes fractions volumiques de phases (cémentite et ferrite), leur distribution et leur morphologie. L'augmentation de la concentration en carbone améliore la localisation des électrons sur les sites atomiques, ce qui contribue au caractère covalent des liaisons interatomiques, réduisant ainsi la conductivité des aciers. En outre, les interfaces α-Fe_3C qui agissent comme une barrière physique pour le glissement de dislocation dans la ferrite, affectent également le déplacement des électrons libres et des parois des domaines magnétiques dans le matériau. La conductivité et la perméabilité ont augmenté dans l'ordre : martensite, sorbite, perlite, ferrite proeutectoïde-perlite, sphéroïdite et ferrite. De plus, il a été observé que le comportement électromagnétique des aciers perlitiques dépendait de l'état de déformation résultant du procédé de tréfilage, ainsi que de l'utilisation en service où l'endommagement par fatigue peut se produire. Des expériences de fatigue oligocyclique ont montré que la résistance peut être contrôlée par des traitements thermomécaniques appropriés. Le potentiel d'évaluation par CF a été mis en évidence en tant qu'outil de caractérisation de l'état microstructural et des propriétés mécaniques des fils d'acier au cours d'un procédé de fabrication ou lors de son usage. Enfin, cette technique a démontré son utilité pour surveiller la déformation élastique cyclique et l'accommodation plastique des aciers perlitiques répondant aux conditions de charge en fatigue.

Mot clés : Perlite ; courants de Foucault ; résistivité ; microscopie à force magnétique ; tréfilage ; fatigue

Relations between microstructure, mechanical and electromagnetic properties of carbon steel wires after thermomechanical treatments

ABSTRACT: Pearlite is a common constituent of a large variety of high strength steel grades typically used in many structural engineering applications, which demand a good combination of high strength and ductility. With the increasing requirements for product quality and in-service reliability, the non-destructive inspection of materials enables the evaluation of their properties including electromagnetic methods, such as eddy current testing (ECT). However, the influence of microstructural parameters on the physical properties indirectly measured by an electromagnetic sensor has not yet been completely elucidated. The objective of the present work is thereby to understand the relations between microstructure, mechanical properties, and electromagnetic behavior of carbon steel wires submitted to different thermomechanical treatments. It aims also at improving the knowledge of the physical and mechanical metallurgy of these steels. The effect of microstructure and plastic deformation on the electromagnetic responses of different steels with various tensile strengths was investigated through resistivity down to 2 K and magnetic measurements, as well as by ECT. In addition, magnetic domains could be imaged by magnetic force microscopy despite the complex microstructures. The electromagnetic responses changed according to the electrical conductivity and magnetic permeability variations of each material, which were mainly related to changes in the volume fraction, distribution, and morphology of the cementite phase within the α-ferrite matrix. The increase of carbon concentration enhances the localization of electrons at the atomic sites, assisting the covalent character of interatomic bonds and thereby reducing the conductivity of steels. Besides, the α-Fe_3C interfaces that act as a physical barrier for dislocation slip in ferrite, affecting as well the main free-path for conductive electrons and magnetic domain walls displacements within the material. Conductivity and permeability increased in the order of martensite, sorbite, pearlite, proeutectoid ferrite-pearlite, spheroidite, and ferrite microstructures. Also, the electrical and magnetic behavior of fully pearlitic steels was observed to depend on the deformation resulted from the cold-drawing and in-service application where fatigue may occur. Low-cycle fatigue experiments have pointed out that the resistance can be managed by relevant thermo-mechanical treatments. The potentiality of ECT was highlighted as a characterization tool of the microstructural state and mechanical properties of steel wires during manufacturing processes or in-service environment. Finally, this technique has been shown to be useful for monitoring cyclic elastic deformation and plastic accommodation of pearlitic steels responding to fatigue-loading conditions.

Keywords: Pearlite; eddy current; resistivity; magnetic force microscopy; wire drawing; fatigue